

**GSFC JPSS CMO
January 20, 2015
Released**

**Joint Polar Satellite System (JPSS) Ground Project
Code 474
474-00056**

**Joint Polar Satellite System (JPSS)
Algorithm Theoretical Basis Document For
the Cross Track Infrared Sounder (CrIS)
Volume II, Environmental Data Records
(EDR)**

For Public Release

The information provided herein does not contain technical data as defined
in the International Traffic in Arms Regulations (ITAR) 22 CFC 120.10.
This document has been approved For Public Release.



National Aeronautics and
Space Administration

**Goddard Space Flight Center
Greenbelt, Maryland**

**Joint Polar Satellite System (JPSS)
Algorithm Theoretical Basis Document (ATBD)
For the Cross Track Infrared Sounder (CrIS)
Volume II, Environmental Data Records (EDR)**

JPSS Electronic Signature Page

Prepared By:

Neal Baker
JPSS Data Products and Algorithms, Senior Engineering Advisor
(Electronic Approvals available online at https://jpssmis.gsfc.nasa.gov/mainmenu_dsp.cfm)

Approved By:

Heather Kilcoyne
DPA Manager
(Electronic Approvals available online at https://jpssmis.gsfc.nasa.gov/mainmenu_dsp.cfm)

**Goddard Space Flight Center
Greenbelt, Maryland**

Preface

This document is under JPSS Algorithm configuration control. Once this document is approved, JPSS approved changes are handled in accordance with Class I and Class II change control requirements as described in the JPSS Configuration Management Procedures, and changes to this document shall be made by complete revision.

Any questions should be addressed to:

JPSS Ground Project Configuration Management Office
NASA/GSFC
Code 474
Greenbelt, MD 20771

Change History Log

Revision	Effective Date	Description of Changes (Reference the CCR & CCB/ERB Approve Date)
Original	05/22/2011	474-CCR-11-0071 : This version baselines D43772, Rev E dated 01/14/2011 as a JPSS document, version Rev -. This is the version that was approved for NPP launch. Per NPOESS CDFCB - External, Volume V – Metadata, doc number D34862-05, this has been approved for Public Release into CLASS. This CCR was approved by the JPSS Algorithm ERB on May 20, 2011.
Revision A	05/23/2012	474-CCR-12-0394 approved by the JPSS Algorithm ERB on May 23, 2012.
Revision B	01/16/2013	474-CCR-12-0472 approved by the JPSS Algorithm ERB on July 25, 2012. 474-CCR-13-0739 approved by the JPSS Algorithm ERB on January 16, 2013. 474-CCR-13-0740 approved by the JPSS Algorithm ERB on January 16, 2013.



Algorithm Theoretical Basis Document For the Cross Track Infrared Sounder (CrIS)

Volume II, Environmental Data Records (EDR)

NOT CLEARED FOR PUBLIC RELEASE

AER Document Number: P1187-TR-I-08
Revision: Version 4.2
Issue Date: October 14, 2005

Original Prepared by

Atmospheric and Environmental Research, Inc.

Northrop Grumman Aerospace Systems Corp. Space Technology One Space Park Redondo Beach, CA 90278			
Revision/Change Record		For Document No. D43772 P1196-TR-I-4-0-ATBD-01-04 P1187-TR-I-08 (for revision C)	
Revision	Document Date	Revision/Change Description	Pages Affected
0	01/31/2004	Original release	All
A	04/30/2004	Modified to be consistent with the CrIMSS EDR algorithm software to be dropped to IDPS on April 30 2004	All
B	11/17/2004	Sec 5.25, 5.27, 5.28: Modified to reflect the implementation of the NWP and rain detection moduels; Sec 5.7.3 Modified to reflect updates in pressure-to-height conversion.	Pp 103-113 Pp 146
C	12/26/2006	Added Appendix G. Mitigation against detector failure and corresponding reference (originally by AER 10/14/2005) Updated EDR descriptions and requirements Updated retrieval strategy under overcast conditions	Pp 304-311 Pp 27-32 Pp 129-132
D	10/27/2010	Changed (Lat>50 and DF1>0.2) to (Lat>50 or DF1>0.2) in Figure 34A Added 8 surface types and deleted Figure 35	Pp 105-106
E	1/14/2011	Added description of handling of RTM random and bias errors in section 5.1.2 Corrected broken links and Microsoft auto formatting errors	P 95-96 All

AER Document Number: P1187-TR-I-08

Version 4.2

Function	Name	Date
Prepared by	Ted Kennelly	10/14/05
Audited by	Scott Zaccheo	10/14/05
Approved by	David Hogan	10/14/05

Contributors:

Jean-Luc Moncet (PDR Algorithm Lead)
Xu Liu (CDR Algorithm Lead)
Ned Snell (Post-CDR Algorithm Lead)

Janusz Eluszkiewicz
Yuguang He
Ted Kennelly
Richard Lynch

Sid Boukabara
Alan Lipton
Hélène Rieu-Isaacs
Gennadi Uymin
Scott Zaccheo

REVISION HISTORY

Version 1.0: Delivered at PDR - May 1999.

Version 1.1: Delivered at SSSR - March 2000.

- Addition of AER, Inc. document numbering on front page.
- Addition of bookmarks and thumbnails in pdf version.
- Modification of Equation 5.11 for transmittance equation in Section 4.2.4.
- Correction of nominal accuracy for OSS selection in Section 4.2.2.
- Correction of Equation 7.7 for transformed retrieval equation in Section 0.

Version 1.2: Delivered in October 2000.

- Section 5.2.7 on the surface pressure determination has been revised.
- Changes were made in Section 6.1.2. They include new information about point selections, validation and methods used (Monte-Carlo vs. sequential search method). Figures which illustrate selection of OSS points and a validation procedure have been added.
- Section 0 has been expanded to discuss approaches to the computation of the Planck function and to include a subsection on trace gas variability.

Version 1.2.2: Delivered in December 2000.

- The main body of the document has been rearranged to follow the structural design of the algorithm.
- Some appendices not referenced in the text have been removed.

Version 1.2.3: Delivered in March 2001.

- Post-DDR version (updated figures).

Version 2.0: Delivered in May 2002.

- Separated trade studies from the descriptions of algorithm modules.
- Incorporated most appendices into the appropriate sections of the ATBD.

- Revised and updated each section.

Version 2.3: Delivered on April 30, 2003.

- Added information with regard to ATMS.
- Added algorithm improvements for cloud-clearing algorithm.
- Added local angle adjustment algorithm description.
- Modifications made to various parts of the ATBD (Overview, Forward Model etc.).

Version 3.0: Delivered on October 30, 2003.

- Rearranged the flow of the ATBD.
- Updated algorithm with regard to ATMS retrievals.
- Updated flow charts to reflect the current state of CrIMSS code.
- Updated scene classification module description.
- Updated description of the joint IR+MW retrievals.
- Updated local angle adjustment algorithm description.
- Updated the post-processing vertical regrid.
- Added validation section.
- Added more trade studies.
- Added more appendices.

Version 4.0: Delivered on January 31, 2004.

- Appendix E added to document addition of transparent clouds to simulation module.
- Appendix F added to document changes in radiative transfer model.
- Overall cleanup of typographic errors; attempt to update some section for clarity based on comments from previous version.

Version 4.2: Delivered on October 14, 2005.

- Version 4.1 included code release only
- Appendix G and corresponding reference was added to describe strategy for detector failure mitigation

Document number was renamed to match current project number P1187

TABLE OF CONTENTS

TABLE OF CONTENTSX

1.0 INTRODUCTION1

2.0 EDR REQUIREMENTS.....3

2.1 Definitions and Requirements..... 3

2.2 Atmospheric Vertical Moisture Profile..... 3

2.3 Atmospheric Vertical Temperature Profile..... 4

2.4 Pressure Profile 6

2.5 EDR Reporting Grid 7

2.6 Timing..... 8

3.0 OVERVIEW OF CrIMSS SENSORS10

3.1 Infrared Instrument 10

3.2 Microwave Instruments 16

3.2.1 Advanced Microwave Sounding Unit (AMSU) 16

3.2.2 Microwave Humidity Sounder (MHS) 16

3.2.3 Advanced Technology Microwave Sounder (ATMS)..... 18

4.0 IMPORTANT ASPECTS IN EDR ALGORITHM DESIGN22

4.1 Apodization Issues Related to FTIR Spectra 23

4.1.1 Apodization Function 24

4.1.2 Instrument Line Shape Function..... 26

4.1.3 Transformation Between ILS Functions..... 28

4.2 Forward Model..... 29

4.2.1 Radiative Transfer Equations 30

4.2.2 Overview of the OSS Method..... 32

4.2.3 Implementation of the OSS Method 34

4.2.4 Radiance Calculations 44

4.3 Inverse Model 56

4.3.1 Linearization Noise..... 59

4.3.2 Non-Linear Inversion Method 60

4.3.3 Inversion of Apodized Spectra 62

4.3.4 Eigenvector Transformation of Retrieved Parameters 64

4.4 Retrieval Strategies Under Cloudy Conditions	76
4.4.1 Cloud-clearing (CC).....	76
5.0 DETAILED DESCRIPTION OF CrIMSS EDR ALGORITHM	77
5.1 Initialization	77
5.1.1 Instrument Specifications and Related Parameters.....	77
5.1.2 Forward Model Parameters.....	77
5.1.3 Topography and Land/Ocean Mask.....	78
5.1.4 Atmospheric/Surface Mean Profiles and Background Covariance	78
5.2 Input and Pre-Processing	79
5.2.1 Microwave SDR	79
5.2.2 Infrared SDR.....	80
5.2.3 Terrain-height Correction for Longitude and Latitude	86
5.2.4 External Data Inputs	87
5.2.5 Precipitation Check.....	87
5.2.6 Surface Type Determination.....	90
5.2.7 Surface Pressure Computation.....	90
5.2.8 NWP Initial Guess	94
5.3 Microwave-Only Retrieval	97
5.3.1 General Description	97
5.3.2 Covariance Stratification	100
5.4 Scene Classification	102
5.4.1 Overview.....	102
5.4.2 Clear FOV Identification	102
5.4.3 Estimating the Number of Cloud Formations.....	104
5.4.4 Formation of FOV Clusters	108
5.5 Joint Microwave and Infrared Retrieval	112
5.5.1 General Description	112
5.5.2 Implementation of the Cloud-clearing Method	116
5.5.3 Channel Selection	120
5.5.4 Trace Gas Variability.....	122
5.5.5 Retrieved Parameters	123

5.6	Quality Control	126
5.6.1	Normalized χ^2	126
5.6.2	Deviation Between MW-Only and Joint MW+IR Retrievals.....	126
5.6.3	MW Quality Control Test.....	127
5.6.4	Flow Diagram	127
5.6.5	Alternative QC Methods.....	128
5.7	Output and Post-Processing	130
5.7.1	Required Outputs	130
5.7.2	Optional Outputs.....	130
5.7.3	Post-Processing.....	131
5.8	Computational Timing	140
6.0	ALGORITHM VALIDATION.....	141
6.1	Validating CrIMSS Algorithm using AMSU Data.....	141
6.1.1	Brief Description of the AER Testbed.....	141
6.1.2	CrIMSS MW Retrieval Performance on Real AMSU Data	142
6.1.3	Future Work.....	145
6.2	Validation of CrIMSS Algorithm Using NAST-I Data	146
6.2.1	Degrading NAST-I Observations to the CrIS Spectral Grid	146
6.2.2	Preliminary Evaluation of the CrIS Forward Model	147
6.2.3	CAMEX-3 Retrievals	149
6.2.4	Future Work.....	153
7.0	TRADE STUDIES	154
7.1	Impact of Inversion Method.....	154
7.2	Determination of the Number of Cloud Formations.....	162
7.3	Impact of Apodization	165
7.4	Impact of Channel Selection.....	171
7.5	Impact of Trace Gas Variability	176
7.6	Application of QC to Scanline Retrievals.....	184
7.7	Error Analysis for the Slant-to-Vertical Conversion	189
7.8	Impact of Switching from AMSU/MHS to ATMS.....	195
7.8.1	Impact of ATMS Noise Amplification on Homogeneous Scenes.....	195

7.8.2	Impact of ATMS Remapping Under Inhomogeneous Conditions	206
7.8.3	ATMS Inhomogeneity Studies Using NOAA-88 Profiles	220
7.9	Impact of the Zeeman Effect on AMSU Radiances.....	231
7.10	Impact of Sub-FOV Cloud Variability/Edge-of-Scan Effects	233
7.10.1	Cloud Data.....	233
7.10.2	Ray-tracing Model.....	234
7.10.3	Retrieval Results.....	235
7.10.4	Summary.....	238
APPENDIX A: Monte-Carlo Approach to the OSS Model		239
A.1	Introduction	239
A.2	Determinant Control	241
A.3	Statistical Control	242
APPENDIX B: MM5 Simulations to Generate Realistic Scenes		244
B.1	Overview of MM5 Simulations	244
B.2	Application to Simulated CrIS Retrievals	252
APPENDIX C: CrIS FOV Naming Convention and Local Angles for Each FOV		255
APPENDIX D: ATMS SDR Remapping Issues		259
D.1	Relative Scan Geometry of CrIS and ATMS	259
D.2	Calculation of ATMS Noise Reduction Factor (NRF).....	265
D.3	Differences from NGES Noise Amplification Memo	269
APPENDIX E: Simulation of Transparent Clouds		271
E.1:	Introduction.....	271
E.2:	Input Files	271
E.3:	Discussion	272
APPENDIX F: Radiative Transfer Model Upgrade.....		273
F.1:	Introduction.....	273
F.2:	Code Configuration for Testing	273
F.3:	OSS Radiative Transfer Changes.....	274
F.3.1:	Impact of Layering	277
F.3.2:	Impact of Temperature Interpolation.....	278
F.3.3:	Treatment of Absorption Coefficients	280

F.3.4: Additional Changes to the Radiative Transfer..... 285

F.4: OSS Node Selection and Validation 286

F.5: Changes in Retrieval Results Due to RT Changes..... 294

F.6: Changes to Algorithm Computational Time 299

APPENDIX G: Mitigation against Detector Failure300

G.1: Description of Changes 300

G.2: Performance Analysis..... 304

G.3: Modifications to Local Angle Adjustment 307

REFERENCES.....308

LIST OF ACRONYMS313

LIST OF TABLES

Table 1: AVMP Requirements.....	4
Table 2: AVTP Requirements.....	5
Table 3: Pressure Profile Requirements.....	6
Table 4: AVMP Vertical Reporting Grid.....	7
Table 5: AVTP Vertical Reporting Grid.....	7
Table 6: Deleted.....	8
Table 7: Spectral Band Characteristics as Defined by the CrIS SDR.....	10
Table 8: AMSU (1 to 15) and MHS (16 to 20) Channel Set.	17
Table 9: Characteristics of ATMS Channel Sets.	19
Table 10: Number of OSS Points in LWIR.	38
Table 11: Number of OSS Points in MWIR.	38
Table 12: Number of OSS Points in SWIR.	38
Table 13: Number of Spectral Points Selected for AMSU/MHS.	43
Table 14: Number of Spectral Points Selected for ATMS.	44
Table 15: Parameters Retrieved in the Microwave.....	99
Table 16: Retrieval Flags and Associated Retrieval Strategies	112
Table 17: Parameters Retrieved in the Joint MW+IR Retrieval.....	123
Table 18: Vertical grids employed in the CrIMSS algorithm.....	133
Table 19: Timing (in seconds) for the RT Model and the Joint MW+IR Retrieval.	140
Table 20: NAST-I Instrument Specifications	146
Table 21: Timing Results for 1305 Channels.	168
Table 22: Timing Results for 937 Channels.	169
Table 23: Timing Results for 346 Channels.	169
Table 24: Selected Channels for CrIS.....	172
Table 25: ATMS Noise Characteristics	196
Table 26: Recommended ATMS Noise Characteristics	201
Table 27: Noise Amplification Factors (NAFs) for ATMS Matched to CrIS.	213
Table 28: Scene Noise Amplification Factors Relative to CrIS FOR.	215
Table 29: Scene Noise Amplification Factors relative to CrIS FOR (Left / Right Halves).	216

Table 30: Scene Noise due to 10% Temperature Inhomogeneities.222

Table 31: Scene Noise due to 10% Water Vapor Inhomogeneities.....223

Table 32: Scene Noise due to 10% Skin Temperature Inhomogeneities.....224

Table 33: Scene Noise due to 10% Cloud Inhomogeneities.....224

Table 34: Scene Noise due to 10% Coastline Inhomogeneities.225

Table 35: Nominal FOV/FOR Parameters.....255

Table 36: CrIS Scan Angles.....258

Table 37: Comparison of CrIS and ATMS Geometry Characteristics.261

Table 38: NRF as a Function of FOR Size (relative to ATMS) and Scan Angle.266

Table 39: Pressure levels for 101 level vertical grid.....277

LIST OF FIGURES

Figure 1: Processing timeline for the CrIMSS algorithm.	9
Figure 2: Example of simulated clear-sky brightness temperatures in the CrIS spectral bands.	11
Figure 3: Temperature (top) and water vapor (bottom) weighting functions in LWIR.	13
Figure 4: Temperature (top) and water vapor (bottom) weighting functions in MWIR.	14
Figure 5: Temperature (top) and water vapor (bottom) weighting functions in SWIR.	15
Figure 6: AMSU/MHS FOV Configuration.	17
Figure 7: Channel positions for AMSU (1 to 15) and MHS (16 to 20).	18
Figure 8: ATMS footprint sizes relative to CrIMSS field-of-regard (FOR). Note that the 15 th FOR occurs just to the left of nadir relative to the along-track satellite velocity vector. The solid circles represent the 9 CrIS FOVs and the dotted circles represent the 3 different ATMS FOV sizes. The individual points show the ATMS footprint centers for three successive scanlines (each of which includes 3 cross-track ATMS scans and 1 cross-track CrIS scan).	21
Figure 9: CrIMSS EDR Algorithm Flow Diagram.	23
Figure 10: Apodization functions used in the CrIS EDR algorithm.	25
Figure 11: ILS functions corresponding to the apodization functions in Figure 10.	28
Figure 12: Number of spectral points per channel selected for <i>sinc</i> ILS in the LWIR band.	38
Figure 13: RMS differences between OSS-generated and true radiances for <i>sinc</i> ILS in LWIR.	39
Figure 14: (a) The RMS difference between the radiances generated using direct <i>Hamming</i> OSS coefficients and the radiances generated using the <i>sinc</i> to <i>Hamming</i> transformation. (b) The RMS difference between the radiances generated using direct <i>Blackman</i> OSS coefficients and the radiances generated using the <i>sinc</i> to <i>Blackman</i> transformation.	41
Figure 15: Comparison OSS/Central Frequency (Maximum Differences).	44
Figure 16: Numbering convention for the atmospheric layers used by OSS.	48
Figure 17: Planck function tabulation error as a function of the number of temperature nodes in the tabulation array. The curves are labeled by the number of frequency nodes (in intervals of 50). The diamond marks the point where the tabulation error drops below 0.01 K.	54

Figure 18: Absolute value of tabulation error as a function of frequency at selected temperatures between 150 and 350 K for the diamond point in Figure 17. The diamonds in this figure mark the maximum errors at each temperature.....	55
Figure 19: Inversion flowchart.....	57
Figure 20: First 6 EOFs of the NOAA-88 temperature profiles. SV stands for “singular value” (equal to the square root of the eigenvalue).....	67
Figure 21: Bias and RMS representation errors of NOAA-88 temperature profiles using 20 EOFs.	68
Figure 22: Layer-mean representation errors of NOAA-88 temperature profiles.	68
Figure 23: The original NOAA-88 temperature profile (solid line) and the profile reconstructed using 20 EOFs (stars). The plot on the right is the difference.	69
Figure 24: Mean and RMS errors when twenty NOAA-88 EOFs are used to reconstruct TIGR temperature profiles.	70
Figure 25: First 6 EOFs of the NOAA-88 moisture profiles.	71
Figure 26: Bias and RMS errors of the reconstructed NOAA-88 moisture profiles using 10 eigenvectors.	71
Figure 27: Layer-mean representation errors of NOAA-88 moisture profiles.	72
Figure 28: Example of the original and reconstructed moisture profiles and the difference between them.	72
Figure 29: Bias and RMS error when eigenvectors of the NOAA-88 moisture profiles are used to reconstruct the TIGR moisture profiles.	73
Figure 30: MW-only and MW+IR retrieval RMS statistics and convergence rate as a function of temperature EOFs.	74
Figure 31: MW-only and MW+IR retrieval RMS statistics and convergence rate as a function of moisture EOFs.	75
Figure 32: Eigenvalues based on nighttime simulations sorted by decreasing amplitude. The first 20 EOFs were used in the regression analysis.	84
Figure 33: Uncertainty versus wavenumber for maximum scan angle. The largest radiance errors resulting from scan angle differences will occur at the edge-of-scan. Here, the brightness temperature uncertainty under nighttime conditions (computed based on the full set of 240	

scanlines) is illustrated before (red) and after (green) the radiance adjustment and in comparison to the noise (blue).....	85
Figure 34: Band 1 averaged uncertainty as a function of scan angle. Brightness temperature errors are shown before LAA (red) and after LAA (green) for 15 FORs and 8 off-center FOVs. These errors impact the retrievals when equal to or greater than the noise amplitude (i.e., scan angles greater than 20 degrees). Applying LAA reduces errors to a level below the noise.	86
Figure 35: NOAA/NESDIS Day-1 precipitation detection algorithm (for AMSU).....	89
Figure 36: Surface pressure for the Tibetan Plateau/India region at 0.1°-resolution. Top: Calculated using the method described in this section. Bottom: Obtained from a direct interpolation of NWP data.	94
Figure 37: Functional Flow Diagram for MW Retrieval.	97
Figure 38: Flowchart for the covariance stratification scheme employed in the retrieval.....	101
Figure 39: Flow Diagram of the Scene Classification Module.....	104
Figure 40: First 6 EOFs resulting from PCA.	106
Figure 41: Magnitudes of singular values (equal to the square root of eigenvalues λ).	107
Figure 42: Left: The RSD test as a function of n for the scene described in the text. Right: The χ^2 test for the scene described in the text.	107
Figure 43: Flow diagram for the surface classification scheme.	109
Figure 44: Clustering pattern when the number of estimated cloud formations is between 1 and 3. The four FOVs enclosed in the box are grouped into a cluster. Similar clusters are formed in the three other corner locations within the FOR. This clustering scheme is used when <i>iclsmode</i> = 1. See text for details.....	110
Figure 45: Flowchart for the Joint Microwave and Infrared Retrieval.	116
Figure 46: Quality Control Flow Diagram.....	128
Figure 47: Pressure Profile Uncertainty.....	132
Figure 48: Flow diagram of the AMSU testbed.....	142
Figure 49: Performance of the CrIMSS MW retrieval algorithm.	143
Figure 50: Total precipitable water retrieval from AMSU.	143
Figure 51: Total precipitable water retrieval from the MRF model.	144

Figure 52: Difference in TPW between AMSU retrieval and MRF model.....	144
Figure 53: CrIMSS-retrieved TPW from AMSU data.....	145
Figure 54: AMSU TPW retrieval from the NOAA website.	145
Figure 55: Top: NAST-I measurement Bottom: NAST-I degraded to CrIS resolution and with a Blackman apodization applied.....	147
Figure 56: Bias correction, in brightness temperature, applied to NAST-I observations before retrievals are performed. This correction has been obtained by comparing CrIS OSS with a model that includes more layers and more absorbers.	148
Figure 57: Difference between LBLRTM-generated radiances with and without certain trace gases included. The gases are indicated in the region where they have significant spectral features. The blue curve is for nadir calculations while the red curve is for calculations performed assuming a 45° observation angle.	149
Figure 58: Flight path of ER-2, location of radiosonde launch and locations of dropsondes for CAMEX-3 on September 13-14.	150
Figure 59: Comparison of NAST-I retrievals with radiosonde launched from Andros Island (left) and dropsonde dropped from the DC-8 (right).	151
Figure 60: Moisture retrieval pattern, on a log scale, as the ER-2 flies on a pass close to the island, far from the island and then back close to the island. The wide gaps in the retrievals represent flight turns while the narrow gaps are caused by clouds and a small island (see Figure 58). CrIS retrievals, performed on a sparse pressure grid, have been interpolated to generate a continuous plot.	152
Figure 61: GOES water vapor channel image of the Andros Island region taken on September 13 and 23:45 UTC.....	153
Figure 62: Algorithm retrieval rates and χ^2 values versus iteration number for clear-sky land and ocean cases (microwave first guess). Results obtained using the DRAD, Levenberg-Marquardt, and Maximum Likelihood methods are shown. The upper plots describe the number of retrievals that meet the radiance convergence criterion ($\chi^2 < 2$). The lower plots show average χ^2 values for profiles that converged in 8 iterations.	156
Figure 63: Algorithm retrieval rates and χ^2 values versus iteration number for clear-sky land and ocean cases (microwave first guess). Refer to Figure 62.....	157

Figure 64: Temperature and water vapor RMS errors for 200 clear-sky land profiles retrieved using the DRAD algorithm.	157
Figure 65: Similar to Figure 64, but for the Levenberg-Marquadt algorithm.	158
Figure 66: Similar to Figure 64, but for the Maximum Likelihood algorithm.	159
Figure 67: Similar to Figure 62, but for climatology first guess.	159
Figure 68: Temperature and water vapor RMS errors for 200 clear-sky land profiles retrieved using the DRAD algorithm and a climatology first guess.	160
Figure 69: Similar to Figure 68, but for the Levenberg-Marquadt algorithm.	161
Figure 70: Similar to Figure 68, but for the Maximum Likelihood algorithm.	161
Figure 71: Frequency of correct determination of the number of cloud formations N_{CF} as a function of the tuning parameters γ_1 and γ_2 (upper and lower panel, respectively). The red curves are for scenes in which the true $N_{CF} \leq 1$, while the blue lines are for scenes in which the true $N_{CF} = 2$ (see text for the definition of true N_{CF}). The solid and dashed lines are for <i>Blackman</i> and <i>sinc</i> , respectively.	163
Figure 72: Application of PCA to estimate the number of cloud formations for the weather product testbed scanlines. Sixteen scans with 30 FORs per scan with 9 FOVs. From top to bottom: Number of estimated cloud formations, cloud-top pressures, average cloud fraction for cloud 1 and average cloud fraction for cloud 2.	164
Figure 73: EDR performance using error covariance matrices for <i>Hamming</i> and <i>Blackman</i> apodizations computed self-consistently using Equation (0.60).	166
Figure 74: Impact of ignoring off-diagonal elements, while relaxing the noise variance, on the EDR retrieval accuracy for <i>Hamming</i> and <i>Blackman</i> . Results for <i>sinc</i> are shown for reference.	167
Figure 75: Water vapor derivatives and selection thresholds. Channels for which the absolute values of water vapor derivatives exceed the threshold are excluded from the entropy-based channel selection for temperature.	173
Figure 76: Trace gas derivatives and selection thresholds. Channels for which the absolute values of trace gas derivatives exceed the threshold are excluded from the channel selection for temperature, water vapor, and surface parameters.	174
Figure 77: Typical Temperature Entropy (δS) per Channel.	174

- Figure 78: Selected channels for temperature T (with and without MWIR), water vapor, and the surface parameters as a function of the total number of channels. The temperature channels selected in MWIR are based on information in all three bands (non-weighted S_e).175
- Figure 79: RMS errors for temperature and water vapor for 200 clear-sky ocean scenes. Results from second stage retrievals performed using all IR channels and subsets of 150, 300, and 400 channels are shown.176
- Figure 80: Trace gas profiles used in evaluating the sensitivity of the CrIS retrieval to trace gas variability. The ozone profiles are from the NOAA-88 database, while the profiles of N₂O, CO, and CH₄ are from the MOZART model. The black lines represent reference profiles from the U.S. Standard Atmosphere.178
- Figure 81: Radiative effects of variable ozone. The red and blues lines show the maximum positive and maximum negative radiance differences (relative to the standard profile) in each CrIS channel for a set of 200 land profiles under clear-sky conditions. Black lines represent CrIS instrument noise. Only results for the LWIR and SWIR bands are shown (note the very different vertical scales for the two bands), as the impact of variable ozone is below the noise level in MWIR.179
- Figure 82: Radiative effects of variable N₂O. The impact of variable N₂O is near-zero in LWIR. 180
- Figure 83: Radiative effect of variable CO. For CrIS, the radiative impact of variable CO is only significant in the portion of the SWIR band shown here.181
- Figure 84: Radiative effect of variable CH₄.181
- Figure 85: Scatter plots of retrieved vs. true column amounts (in non-dimensional units) for N₂O and CH₄ (red and blue dots, respectively). The results in this figure have been obtained for warm clear-sky land profiles using (a) modified column retrieval for N₂O and CH₄ and (b) standard column retrieval for N₂O and CH₄. The numbers in each panel give the RMS error for each species.182
- Figure 86: Effect of trace gas variability and apodization on EDR retrievals. The results shown in this figure have been obtained for 200 land profiles under clear-sky conditions, with the trace gas profiles from the NOAA-88 and MOZART databases (see Figure 80). The solid lines show the retrieval results in the baseline case of no trace gas variability.183
- Figure 87: Location of scanlines.184

- Figure 88: From top to bottom: average cloud-top pressure, average cloud fraction (the vertical lines divide the 16 scanlines), and maximum cloud contrast for each FOR.....185
- Figure 89: Top: Absolute value of the difference in the average lower tropospheric temperature for each FOR. Bottom: Same, but with the rejection criterion applied - negative numbers refer to applicable rejection criteria (see text).186
- Figure 90: (a) Error in the lower tropospheric temperature for each FOR (sequenced from small to large), (b) χ^2 plotted in the same sequence as (a), (c) χ^2 MW plotted in the same sequence as (a), (d) σ plotted in the same sequence as (a).187
- Figure 91: RMS error for temperature and moisture. Results with and without QC are presented. With QC implemented, 129 profiles out of 480 were rejected (27%).188
- Figure 92: Temperature (upper panels, contour interval 1 K) and moisture (lower panels, contour interval 0.1 in the \log_{10} of water vapor mass mixing ratio in g/kg) for March 20th, 2001 over the Great Lake Region. On the left are the fields simulated by the MM5 model, with the corresponding fields from the ETA model shown on the right. The red dots in the lower right panel represent locations of CrIS footprints at the surface (excluding cloudy FOVs).190
- Figure 93: RMS error for the slant-to-vertical conversion in a 2 km thick layer centered at 450 hPa for the moisture field simulated by the MM5 model as a function of the number of Fourier components used to represent the field. Lower curve: recursive filter; upper curve: slant = local vertical approximation.....191
- Figure 94: Layer-mean RMS errors for temperature and moisture simulated by the ETA model. Dashed lines: local vertical = slant; solid lines: local vertical obtained from the application of the recursive filter. The upper and lower panels are for 1 and 9 reports per FOR, respectively.194
- Figure 95: Analogous to Figure 94, but for the MM5 model. The RMS error profiles in this figure are taken as representative of the error budget in the slant-to-vertical conversion...194
- Figure 96: ATMS noise amplification factors based on NGES Backus-Gilbert calculations.197
- Figure 97: Noise amplitude for ATMS simulations computed from simulations of 400 random FORs. The baseline noise model assumes a noise reduction of one-over-root-nine.198
- Figure 98: MW retrieval performance for the baseline (one-over-root-nine) noise model and based on the NGES Backus-Gilbert noise amplification estimates.198

Figure 99: MW retrieval performance based on four noise models. BG-1-22 used Backus-Gilbert noise estimates for channels 1 to 22. BG1-2 and BG16-22 used Backus-Gilbert noise estimates for channels 1 to 2 and 16 to 22, respectively, and used baseline noise estimates for the other channels.....	199
Figure 100: Difference in water vapor performance with respect the baseline noise model as a function of FOR (i.e., scan angle). The difference is less than 2% and there is little variation with scan angle.....	200
Figure 101: Noise amplitude for simulations based on the baseline ATMS noise and including the ATMS noise amplification factors computed by NGES.....	202
Figure 102: MW and MW/IR retrieval performance statistics based on simulations with the baseline ATMS noise (1) and with ATMS noise amplification factors computed by NGES (2).....	203
Figure 103: MW and MW/IR retrieval performance statistics based on simulations with the baseline ATMS noise including channels 1 and 2 (1) and excluding channels 1 and 2 (2).	203
Figure 104: Noise amplitude for simulations based on the baseline ATMS noise and including the ATMS noise amplification factors computed by AER (for FOR #1).....	204
Figure 105: MW and MW/IR retrieval performance statistics based on simulations with the baseline ATMS noise (1) and with ATMS noise amplification factors computed by AER (2). The simulations are at edge-of-scan (FOR #1).	205
Figure 106: NGES and AER noise amplification factors comparison.	205
Figure 107: Performance based on AER noise amplification estimates (2) compared to baseline (1) for 700 mbar cloud and for FOR #1.....	206
Figure 108: Performance based on AER noise amplification estimates (2) compared to baseline (1) for 700 mbar cloud and for FOR #14.....	206
Figure 109: Surface pressure as a function of latitude and longitude showing the extent of the 2 km and 15 km resolution MM5 scenes. Simulations and retrievals were based on the 2 km scene. The covariance was computed based on data from the 15 km scene merged with data from the NOAA-88 profile database.....	209
Figure 110: Air temperature below 100 mbar for a slice through the MM5 scene. The green line indicates surface pressure.	210

Figure 111: Water vapor for one slice through the MM5 scene. The green line indicates surface pressure.	210
Figure 112: Selected ATMS and CrIS gridpoints and footprints used in the simulations. Black dots represent ATMS sampling at nadir. Blue dots represent CrIS sampling at nadir. The 3 ATMS footprint sizes at nadir are shown as concentric black circles. The small blue circle (top) represents CrIS field-of-regard (FOR) size at nadir. The larger blue circles represent the CrIS FOR plus 1.1 degrees and CrIS FOR plus 2.2 degrees. The set of nine blue circles (bottom) represent the CrIS FOVs at nadir. The extent of the MM5 scene is shown as a pink rectangle.	211
Figure 113: Simulated radiances in ATMS channels 1 (left) and 2 (right) based on the 2 km MM5 scene (at nadir). The sizes of the CrIS and ATMS footprints are indicated.	212
Figure 114: Simulated radiances in ATMS channels 10 (left) and 15 (right) based on the 2 km MM5 scene (at nadir). The sizes of the CrIS and ATMS footprints are indicated.	212
Figure 115: Simulated radiances in ATMS channel 16 (left) and 22 (right) based on the 2 km MM5 scene (at nadir). The sizes of the CrIS and ATMS footprints are indicated.	212
Figure 116: Sensor and total noise for entire MM5 scene based on nadir geometry.	214
Figure 117: Sensor and total noise for left and right halves of MM5 scene based on nadir geometry.	214
Figure 118: MW and MW/IR retrievals based on MM5 scene showing the effect of decreased resolution on 50 GHz ATMS bands. The lines labeled Mw0 and Ir0 correspond to retrievals based on ATMS SDRs matched to the CrIS FOR. The lines labeled Mw1 and Ir1 and Mw2 and Ir2 correspond to retrievals based on ATMS SDRs matched to the CrIS FOR + 1.1 degree and CrIS FOR + 2.2 degree footprints, respectively.	218
Figure 119: MW and MW/IR retrievals based on MM5 profiles showing the effect of decreased resolution on the 23 and 31 GHz ATMS bands. The lines labeled Mw0 and Ir0 correspond to retrievals based on ATMS SDRs matched to the CrIS FOR. The lines labeled Mw1 and Ir1 and Mw2 and Ir2 correspond to retrievals based on ATMS SDRs matched to the CrIS FOR + 1.1 degree and CrIS FOR + 2.2 degree footprints respectively.	220
Figure 120: Circles representing the CrIS FOR (A: 3.3 degrees) and ATMS FOR (A,B,C: 5.2 degrees) are shown (left). The scene is bisected into two parts representing different	

conditions. The plot (right) shows the difference in contribution of the shaded area to the	
ATMS and CrIS footprints as a function of position in the scene.	221
Figure 121: 2K Temperature inhomogeneity over land – clear (left), cloudy (right).....	225
Figure 122: 2K Temperature inhomogeneity over ocean – clear (left), cloudy (right).	226
Figure 123: 50% Water vapor inhomogeneity over land – clear (left), cloudy (right).....	226
Figure 124: 50% Water vapor inhomogeneity over ocean – clear (left), cloudy (right).	227
Figure 125: 5 K Skin temperature inhomogeneity over land – clear (left), cloudy (right).....	227
Figure 126: 5 K Skin temperature inhomogeneity over ocean – clear (left), cloudy (right).	227
Figure 127: Cloud inhomogeneity over land – clear (left), cloudy (right).	228
Figure 128: Cloud inhomogeneity over ocean – clear (left), cloudy (right).....	228
Figure 129: 10% Coastline inhomogeneity over ocean – clear (left), cloudy (right).	229
Figure 130: 5% Coastline inhomogeneity over ocean – clear (left), cloudy (right).	229
Figure 131: Histogram of errors caused by the omission of the Zeeman effect using the five latitude-stratified atmospheric profiles.	232
Figure 132: (a) Example of an inhomogeneous cloud scene from the Southern Great Plains ARM site on June 23, 1997. The color map represents the distribution of the cloud-top height in kilometers (with the scale given on the right). Ground footprints of 9 CrIS FOVs corresponding to the scan angle of 45° are represented by the black dots, with each FOV represented by approximately 100 individual dots (rays or pixels). (b) Positions of the rays in the vertical projection. The red crosses mark the points of intersection with the clouds.	234
Figure 133: Impact of sub-FOV cloud-top variability and edge-of-scan effect. The three curves in this figure correspond to the case of variable cloud height (as in Figure 132), as well as cloud height fixed at 10 and 5 km (for these two cases, the variability in the cloud-top pressure results purely from geometrical effects at off-nadir scan angles).	237
Figure 134: Flow diagram for the MC approach to the OSS model.	239
Figure 135: Horizontal domain for the 15 km run. The green lines represent the distribution of column-integrated hydrometeor amount (cloud water, cloud ice, snow, and graupel) used in the definition of cloudiness (see below).	245
Figure 136: Horizontal domain for the 2 km run.	246
Figure 137: Fields of temperature at 850 mbar, wind speed and geopotential height at 300 mbar, surface pressure, and relative humidity at 0000Z, August 3, 2003, from the Eta analysis..	247

Figure 138: Ground temperature from the 15 km MM5 simulation.	248
Figure 139: Mean profiles and standard deviation for temperature and water vapor in the NOAA-88 database (black) and the MM5 simulation (red).	249
Figure 140: Visible image obtained by the GOES-8 satellite at August 2, 2002, 18 UTC (the beginning of the MM5 simulation).	250
Figure 141: Infrared image obtained by the GOES-8 satellite at August 3, 2002, 00 UTC (the end of the MM5 simulation).	251
Figure 142: Cloud-top pressure in the 2- and 15 km MM5 simulations (color contours and circles, respectively).	252
Figure 143: Nominal FOV/FOR parameters have been adopted from the August 2002 CrIS Sensor Specifications and based on discussions with ITT. In the current design, the extent of the FOR is equal in the in-track (indicated by the arrow) and cross-track directions (i.e., 3.300 degrees). The FOV footprint size (0.963 degrees) and FOV sampling (1.100 degrees) are also equal in the two directions. The numbering convention for the FOVs is indicated in the plot.	256
Figure 144: The top plot shows the numbering convention for the CrIS FORs as seen from above. The direction of the satellite is indicated by the arrow at zero scan angle (nadir). FORs are numbered 1 through 30 from left to right with scan angles ranging from +48.333 to -48.333 degrees. The FOV locations are shown for selected FORs in order to illustrate the rotation of the FOV pattern. The lower two plots show the FOV numbering convention at FOR #1 and #30. For these FORs, the FOV pattern is rotated by +48.333 and -48.333 degrees, respectively.	257
Figure 145: Comparison of beam diameters and CrIS FOR.	260
Figure 146: Example of CrIS FOR (FOR #15 corresponds to the 15 th FOR and occurs just to the left of nadir relative to the along-track satellite velocity vector).	262
Figure 147: CrIS FORs.	264
Figure 148: Footprint characteristics for FOV #8.	268
Figure 149: Absorption coefficients generated using MIE code for $R_{\text{eff}}=15\mu\text{m}$ for both water and ice.	272
Figure 150: Total brightness temperature errors with old scheme	275
Figure 151: Total brightness temperature errors with new scheme	276

Figure 152: The OSS absorption coefficient temperature grid (*) superimposed on the set of 52 ECMWF standard temperature profiles.....	279
Figure 153: Brightness temperature differences between linear interpolation and the 3-point Lagrange interpolation.....	280
Figure 154: Sample spectral region for test.....	282
Figure 155: Brightness temperature errors for the "old" treatment of water vapor absorption. Note that for this test water was the sole absorber.....	283
Figure 156: Brightness temperature errors for the "new" treatment of water vapor absorption. Note that for this test water was the sole absorber.....	283
Figure 157: Error obtained when assuming that fixed gases optical depth does not vary with water vapor concentration.....	284
Figure 158: Error obtained when accounting for the impact of water vapor concentration on the fixed gases optical depth.....	285
Figure 159: Number of points selected for finite-width Blackman apodization.....	287
Figure 160: Number of points selected for Blackman apodization extending to the edges of the band.....	288
Figure 161: Number of points selected for finite-width Hamming apodization.....	288
Figure 162: Number of points selected for Hamming apodization extending to the edges of the band.....	289
Figure 163: Number of points selected for sinc-function ILS extending to the edges of the band.....	289
Figure 164: Dependent validation of OSS node selection for finite-width Blackman apodization.....	290
Figure 165: Dependent validation of OSS node selection for Blackman apodization extending to the edges of the band.....	290
Figure 166: Dependent validation of OSS node selection for finite-width Hamming apodization.....	291
Figure 167: Dependent validation of OSS node selection for Hamming apodization extending to the edges of the band.....	291
Figure 168: Dependent validation of OSS node selection for sinc-function ILS.....	292
Figure 169: Independent validation of OSS node selection for Blackman apodization extending to the edges of the band.....	293
Figure 170: Independent validation of OSS node selection for Hamming apodization extending to the edges of the band.....	293

Figure 171: Independent validation of OSS node selection for sinc-function ILS.....	294
Figure 172: The top plot shows the brightness temperature and the bottom plot shows the radiometric differences (given in units of brightness temperature, K) between the 40-level model and the 101-level model for a single atmospheric profile.....	295
Figure 173: Ocean scenes: (a) 40-level retrieval results and (b) 101-level retrieval results.....	297
Figure 174: Land scenes: (a) 40-level retrieval results and (b) 101-level retrieval results.....	298
Figure 175: Left. In clear or overcast conditions, retrievals are based on the average of available information for all FOVs. Middle. Option A for cloudy conditions eliminates any FOV impacted by detector failure. Right. Option B for cloudy conditions eliminates FOVs that are impacted by failures in bands 1 or 2 and eliminates band 3 for all FOVs if a failure occurs in that band.	302
Figure 176: Performance degradation owing to Band 1 detector failure for FOV 1, 5, and 8 with iClssMode = 3. Results are based on the scheme to eliminate FOVs impacted by detector failure.	306
Figure 177: Performance degradation owing to Band 3 detector failure for FOV1, 5, and 8 with iClssMode = 3. Results are based on the option to eliminate band 3 and perform retrievals using bands 1 and 2 only (Option B).	307
Figure 178: Performance degradation owing to Band 1 detector failure for FOV 1, 5, and 8 with iClssMode = 1. Differences in performance relative to the baseline are largely due to differences in scene classification (i.e. FOV clustering).	307

1.0 INTRODUCTION

This algorithm theoretical basis document (ATBD) describes the theoretical background and functional implementation of the environmental data record (EDR) retrieval algorithm for the Cross Track Infrared and Microwave Sounder Suite (CrIMSS). The algorithm has been developed by Atmospheric and Environmental Research, Inc. (AER) in support of the National Polar-orbiting Operational Environmental Satellite System (NPOESS). The mission of the CrIMSS payload is to produce both Sensor Data Record (SDR) and EDR in support of the NPOESS mission requirements. The SDR processing is described in the companion SDR ATBD (Lachance *et al.* 1999). The EDRs allocated to CrIMSS include atmospheric vertical temperature, moisture, and pressure profiles. The CrIMSS payload consists of infrared and microwave components. Differing in their sensitivity to clouds, the microwave components provide data in situations of full overcast as well as first guess information for the infrared component. In partly cloudy and clear situations, the infrared component provides the highest quality EDRs. Under overcast conditions, the infrared component provides retrievals above cloud-top while the microwave component provides retrievals below cloud. The infrared component is the Cross Track Infrared Sounder (CrIS) to be procured by NPOESS with nominal characteristics defined by the ITT CrIS system specification. During most of the algorithm development work, the microwave components have been assumed to include the Advanced Microwave Sounding Unit (AMSU) and the Microwave Humidity Sounder (MHS). However, the actual flight unit for the microwave components will be the Advanced Technology Microwave Sounder (ATMS) supplied by NASA. The current version of the CrIMSS science code (version 3.0) incorporates the full functionality of the ATMS as the microwave component. The ATMS has a similar channel set as AMSU/MHS, but the footprint sizes and scan geometries are different. There is no significant difference in performance if the ATMS is fully mapped to the CrIS field-of-regard (FOR) and the noise performance is similar to that of AMSU/MHS. Since the footprint size for ATMS channels 1 and 2 are 5.2 degrees, which is larger than that of the AMSU, it has some impact on algorithm performance and this will be discussed in the trade study, Section 0 in this ATBD.

The organization of this document is as follows. The EDR thresholds and objectives allocated to CrIMSS are presented in Section 2.0, followed by an overview of the sensor suite in Section 3.0. A top-level EDR algorithm overview and key aspects of the CrIMSS algorithm are presented in Section 4.0. These key aspects are: 1) treatment of apodization functions for FTIR sensors such as CrIS, 2) detailed description of our radiative transfer model, 3) our general approach to the inverse problem, and 4) an overview of retrieval strategies under cloudy conditions. Section 5.0 provides detailed descriptions of the individual modules in the CrIMSS algorithm. The initialization of the retrieval process is described in Section 5.1, followed by a description of input and pre-processing in Section 5.2. Section 6.0 describes the microwave-only retrieval, followed by a description of the scene classification in Section 6.1 and of the joint microwave and infrared retrieval in Section 6.2. Quality control and post-processing are discussed in Sections 6.3 and 6.4, respectively. The timing results are summarized in Section 6.5. Section 6.6 discusses algorithm validation. The main document concludes with a description of trade studies in Section 7.0, which provides information on algorithm performance under various conditions. The appendices provide supplemental information about forward model training, a description of high-resolution scenes used to test the ATMS performance, CrIS viewing geometry, and ATMS remapping issues.

2.0 EDR REQUIREMENTS

2.1 Definitions and Requirements

Three NPOESS EDRs are produced from CrIMSS: Atmospheric Vertical Moisture Profile (AVMP), Atmospheric Vertical Temperature Profile (AVTP) and atmospheric pressure profile.

Atmospheric temperature EDR above 0.5 mb will be obtained from Conical-scanning Microwave Imager/Sounder (CMIS). Specification of horizontal cell size or and vertical resolution for temperature above 0.5 mb is specified in the CMIS payload. For an EDR for which horizontal cell size is specified only at nadir, cell size is allowed to grow away from nadir as a normal function of the looking angle.

“Clear” refers to cases in which the average fractional cloudiness within one CrIS FOR is up to 50%. The instrument shall be capable of meeting “clear” sounding requirements in situations where none of the individual spots are totally cloud-free. “Cloudy” refers to cases in which the average fractional cloudiness is in the range from 50% to 100% (e.g., totally overcast). The “average fractional cloudiness” is determined from the sensor’s view angle, not from a local vertical. “Cloud-free” represents conditions in which no clouds are present within a CrIS FOR.

The following tables present ITT’s guaranteed performances for the primary EDRs and the requirements for timing.

2.2 Atmospheric Vertical Moisture Profile

The requirements for AVMP are specified in NPOESS System Specification, Appendix D (document number: SY15-0007):

40.2.1 * Atmospheric Vertical Moisture Profile (AVMP)

An AVMP is a set of estimates of average mixing ratio in three-dimensional cells centered on specified points along a local vertical. The mixing ratio of a sample of air is the ratio of the mass of water vapor in the sample to the mass of dry air in the sample. Up to three EDRs are produced for AVMP, depending on sensor data availability: a combined EDR which uses data from CrIMSS and CMIS, a CrIMSS EDR that does not use CMIS data, and a CMIS EDR that

does not use CrIMSS data. Whether a cell is clear or cloudy will be determined for the combined EDR and the CrIMSS EDR by comparing the radiance from CrIS spectral bands. The CMIS EDR will use the cloud mask generated from VIIRS data to determine whether a cell is clear or cloudy. The AVMP performance guaranteed by CrIMSS without CMIS is the same as the performance specified below for CrIMSS plus CMIS.

Table 1: AVMP Requirements

Paragraph	Subject	Specified Value	NPP Exclusion
	a. Horizontal Cell Size		
40.2.1-1a	1. Clear	14 km @ Nadir	
40.2.1-1b	2. Cloudy [165 - 183 GHz ATMS Channels]	16 km @ Nadir	
40.2.1-2	b. Horizontal Reporting Interval at Nadir	1 to 9 per 45 km x 48 km Area	
40.2.1-3	c. Vertical Cell Size	2 km or less	
	d. Vertical Reporting Interval		
40.2.1-4	1. Surface to 850 mb	20 mb	
40.2.1-5	2. 850 mb to 100 mb	50 mb	
40.2.1-6	e. Horizontal Coverage	Global	
40.2.1-7	f. Vertical Coverage	Surface to 100 mb	
40.2.1-8	g. Measurement Range	0 - 30 g/kg	
	h. *Measurement Uncertainty Averaged Over HRI		
40.2.1-9	1. *Clear, Surface to 600 mb	14.10%	
40.2.1-10	2. Clear, 600 mb to 300 mb	13.80%	
40.2.1-11	3. Clear, 300 mb to 100 mb	11.7% (or 0.05g/kg)	
40.2.1-12	4. *Cloudy, Surface to 600 mb	15.80%	
40.2.1-13	5. Cloudy, 600 mb to 300 mb	17.10%	
40.2.1-14	6. Cloudy, 300 mb to 100 mb	16.4% (or 0.05g/kg)	
40.2.1-15	i. Mapping Uncertainty, 3 Sigma	1.5 km	
40.2.1-16	j. Maximum Local Average Revisit Time	8 hrs	X
40.2.1-18	k. Latency	See Appendix E	
40.2.1-19	l. Long-term Stability (C)	2%	

2.3 Atmospheric Vertical Temperature Profile

The requirements for AVTP are specified in NPOESS System Specification, Appendix D (document number: SY15-0007):

40.2.2 *Atmospheric Vertical Temperature Profile (AVTP)

An AVTP is a set of estimates of the average atmospheric temperature in three-dimensional cells centered on specified points along a local vertical. Up to three EDRs are produced for AVMP, depending on sensor data availability: a combined EDR which uses data from CrIMSS and CMIS, a CrIMSS EDR that does not use CMIS data, and a CMIS EDR that does not use CrIMSS data. Whether a cell is clear or cloudy will be determined for the combined EDR and the CrIMSS EDR by comparing the radiance from CrIS spectral bands. The CMIS EDR will use the cloud mask generated from VIIRS data to determine whether a cell is clear or cloudy. The AVTP performance guaranteed by CrIMSS without CMIS is the same as the performance specified below for CrIMSS plus CMIS except that CrIMSS does not provide measurements at atmospheric pressures below 0.5 mb.

Table 2: AVTP Requirements

Paragraph	Subject	Specified Value	NPP Exclusion
	a. Horizontal Cell Size		
40.2.2-1a	1. Clear, Nadir, Surface to 0.5 mb	14 km	
40.2.2-2	3. Clear, Edge of Swath, Surface to 0.5 mb	50 km	
40.2.2-3	4. Cloudy, Nadir, Surface to 0.5 mb	40 km	
40.2.2-4	5. Cloudy, Edge of Swath, Surface to 0.5 mb	200km	
40.2.2-5	b. Horizontal Reporting Interval at Nadir	One to Nine per 45 km x 48 km Area	
	c. Vertical Cell Size		
40.2.2-6a	1. Clear, Surface to 300 mb	1 km	
40.2.2-6b	2. Clear, Surface to 700 mb	N/A	
40.2.2-6c	3. Clear, 700 mb to 300 mb	N/A	
40.2.2-7	4. Clear, 300 mb to 30 mb	3 km	
40.2.2-8	5. Clear, 30 mb to 1 mb	5 km	
40.2.2-9	6. Clear, 1 mb to 0.5 mb	5 km	
40.2.2-10	8. Cloudy, Surface to 700 mb	1 km or Less	
40.2.2-11	9. Cloudy, 700 mb to 300 mb	1 km or Less	
40.2.2-12	10. Cloudy, 300 mb to 30 mb	3 km or Less	
40.2.2-13	11. Cloudy, 30 mb to 1 mb	5 km or Less	
40.2.2-14	12. Cloudy, 1 mb to 0.5 mb	5 km or Less	
	d. Vertical Reporting Interval		
40.2.2-15	1. Surface to 850 mb	20 mb or Less	
40.2.2-16	2. 850 mb to 300 mb	50 mb or Less	
40.2.2-17	3. 300 mb to 100 mb	25 mb or Less	
40.2.2-18	4. 100 mb to 10 mb	20 mb or Less	
40.2.2-19	5. 10 mb to 1 mb	2 mb or Less	
40.2.2-20	6. 1 mb to 0.5 mb	0.2 mb or Less	
40.2.2-22	e. Horizontal Coverage	Global	
40.2.2-23	f. Vertical Coverage	Surface to 0.5 mb	

40.2.2-24	g. Measurement Range	180-335K [Earth Scene], 180-310K [Black Body]	
	h. Measurement Uncertainty		
40.2.2-26a	1. *Clear, Surface to 300 mb	0.9 K / 1 km Layer	
40.2.2-27	4. Clear, 300 mb to 30 mb	0.98 K / 3 km Layer	
40.2.2-28a	5. Clear, 30 mb to 1 mb	1.45 K / 5 km Layer	
40.2.2-29	8. Clear, 1 mb to 0.5 mb	3.5 K / 5 km Layer	
40.2.2-30	10. *Cloudy, Surface to 700 mb	2.0 K / 1 km Layer	
40.2.2-31	11. Cloudy, 700 mb to 300 mb	1.4 K / 1 km Layer	
40.2.2-32	12. Cloudy, 300 mb to 30 mb	1.3 K / 3 km Layer	
40.2.2-33a	13. Cloudy, 30 mb to 1 mb	1.45 K / 5 km Layer	
40.2.2-34	16. Cloudy, 1 mb to 0.5 mb	3.5 K / 5 km Layer	
40.2.2-35	i. Mapping Uncertainty, 3 Sigma	3 km	
40.2.2-36	j. Maximum Local Average Revisit Time	8 hrs	X
40.2.2-38	l. Latency	See Appendix E	
40.2.2-39	m. Long Term Stability (C)	Trop Mean 0.05 K, Strat Mean 0.1 K	

2.4 Pressure Profile

The requirements for AVTP are specified in NPOESS System Specification, Appendix D (document number: SY15-0007):

40.3.5 Pressure Profile

A pressure profile is a set of estimates of the atmospheric pressure at specified altitudes above the earth's surface. The requirements below apply under both clear and cloudy conditions.

Table 3: Pressure Profile Requirements

Paragraph	Subject	Specified Value	NPP Exclusion
40.3.5-1	a. Horizontal Cell Size, HCS [CMIS Guarantee]	25 km	X
40.3.5-2	b. Horizontal Reporting Interval [CMIS Guarantee]	25 km	X
40.3.5-3	c. Vertical Cell Size [CMIS Guarantee]	0 km	X
	d. Vertical Reporting Interval		
40.3.5-4	1. For Altitude 0 – 2 km [CMIS & CrIMSS Guarantee]	1 km	
40.3.5-5	2. For Altitude 2 – 5 km [CMIS & CrIMSS Guarantee]	1 km	
40.3.5-6	3. For Altitude > 5 km [CMIS & CrIMSS Guarantee]	1 km	
40.3.5-7	e. Horizontal Coverage [CMIS & CrIMSS Guarantee]	Global	
40.3.5-8	f. Vertical Coverage [CMIS & CrIMSS Guarantee]	0 - 30 km	
40.3.5-9	g. Measurement Range [CMIS & CrIMSS Guarantee]	10 -1050 mb	
	h. Measurement Accuracy for HCS		
40.3.5-10	1. For Altitude 0 – 2 km [CMIS Guarantee]	3%	X

40.3.5-11	2. For Altitude 2 – 10 km [CMIS Guarantee]	3%	X
40.3.5-12	3. For Altitude 10 – 30 km [CMIS Guarantee]	5%	X
40.3.5-13	i. Measurement Precision for HCS [CMIS Guarantee]	3 mb	X
40.3.5-14	j. Mapping Uncertainty, 3 Sigma [CMIS Guarantee]	3 km	X
40.3.5-15	k. Maximum Local Average Revisit Time	8 hrs	X
40.3.5-17	l. Latency	See Appendix E	

2.5 EDR Reporting Grid

It should be pointed out that in the system requirement specs document it does not explicitly define the exact vertical reporting grid for both moisture and temperature EDRs. Currently the CrIMSS EDR algorithm will produce these two EDRs on the grids defined in Table 4 and Table 5 for AVMP and AVTP, respectively.

Table 4: AVMP Vertical Reporting Grid

Layer Index	Pressure (mb)	VCS (km)	Layer Index	Pressure (mb)	VCS (km)	Layer Index	Pressure (mb)	VCS (km)
1	100	2	10	550	2	19	910	2
2	150	2	11	600	2	20	930	2
3	200	2	12	650	2	21	950	2
4	250	2	13	700	2	22	970	2
5	300	2	14	750	2			
6	350	2	15	800	2			
7	400	2	16	850	2			
8	450	2	17	870	2			
9	500	2	18	890	2			

Table 5: AVTP Vertical Reporting Grid

Layer Index	Pressure (mb)	VCS (km)	Layer Index	Pressure (mb)	VCS (km)	Layer Index	Pressure (mb)	VCS (km)
1	0.5	5	16	150	3	31	750	1
2	0.7	5	17	175	3	32	800	1
3	0.9	5	18	200	3	33	850	1

4	1	5	19	225	3	34	870	1
5	3	5	20	250	3	35	890	1
6	5	5	21	275	3	36	900	1
7	7	5	2;2	300	3	37	920	1
8	9	5	23	350	3	38	940	1
9	10	5	24	400	3	39	960	1
10	30	3	25	450	3	40	980	1
11	50	3	26	500	1	41	1000	1
12	70	3	27	550	1	42	1020	1
13	90	3	28	600	1			
14	100	3	29	650	1			
15	125	3	30	700	1			

Table 6: Deleted

2.6 Timing

Any initialization of operational EDR algorithms that is unique to specific satellite, sensor data, or orbital conditions shall take no more than 1 minute following receipt of the first segments of CrIS SDRs. The SDRs transmitted to EDR algorithms shall be broken into segments and processed in blocks (each block being equivalent to 1 minute worth of data). Processing of one SDR data block in operational algorithms into an EDR data block shall be completed and handed off as a user output prior to processing of the next data block. Processing time associated with each data block shall be 1 minute or less. SDR data resulting from 1.25 orbits of data collection shall be fully processed into EDRs in under 18 minutes when scientific code is converted to operational code running on forecast 2007 desktop computers. Figure 1 presents the processing timeline for the combined SDR+EDR algorithm.

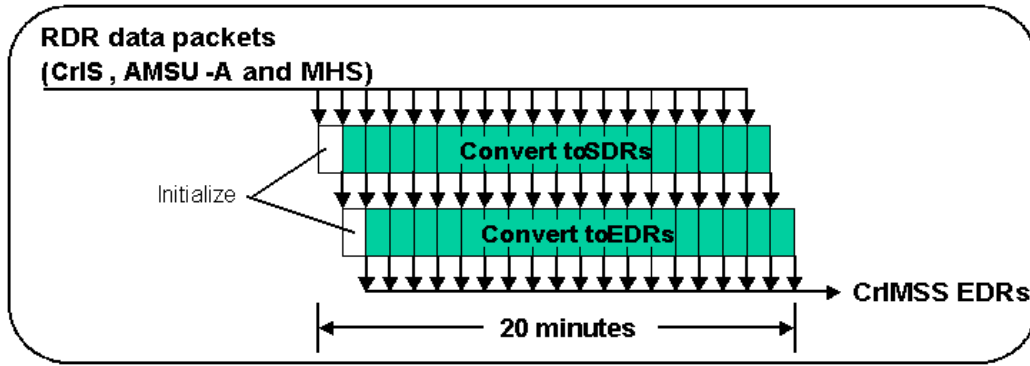


Figure 1: Processing timeline for the CrIMSS algorithm.

3.0 OVERVIEW OF CrIMSS SENSORS

3.1 Infrared Instrument

The CrIS (Cross Track Infrared Sounder) instrument is a Michelson interferometer covering the spectral range of approximately 3.9 to 15.4 μm . CrIS provides cross-track measurements of top-of-atmosphere (TOA) radiances to permit the calculation of vertical distributions of temperature and moisture in the Earth's atmosphere. The nominal spectral resolution is defined as $1/2L$, where L is the maximum optical path difference of the interferometer. The frequency range adopted in the current design of the CrIS instrument is listed in Table 7. There are three bands in the CrIS spectral range: long-, mid-, and short-wave (denoted as LWIR, MWIR, and SWIR, respectively). Each band has different spectral resolutions. Figure 2 shows an example of simulated clear-sky radiances in the CrIS bands. The radiances are expressed in brightness temperature units. The emission in the spectral region 650-800 cm^{-1} is mainly from atmospheric CO_2 and is used for atmospheric temperature sounding. The atmospheric window region in LWIR extends from 800 to 950 cm^{-1} and provides sounding channels for the surface properties and the lower troposphere temperatures. The main emission band of O_3 is centered around 1050 cm^{-1} . The main emission in MWIR is due to atmospheric moisture, although there are some contributions from methane and nitrous oxide near 1250 cm^{-1} . MWIR contains most of the CrIS atmospheric moisture sounding channels. The main feature in SWIR is the emission from the 4.18- μm band of CO_2 that is also used for atmospheric temperature sounding.

Table 7: Spectral Band Characteristics as Defined by the CrIS SDR.

Band	Frequency Range	Resolution (1/2L)	# Channels
LWIR	650-1095 cm^{-1}	0.625 cm^{-1}	713
MWIR	1210-1750 cm^{-1}	1.25 cm^{-1}	433
SWIR	2155-2550 cm^{-1}	2.5 cm^{-1}	159
Total			1305

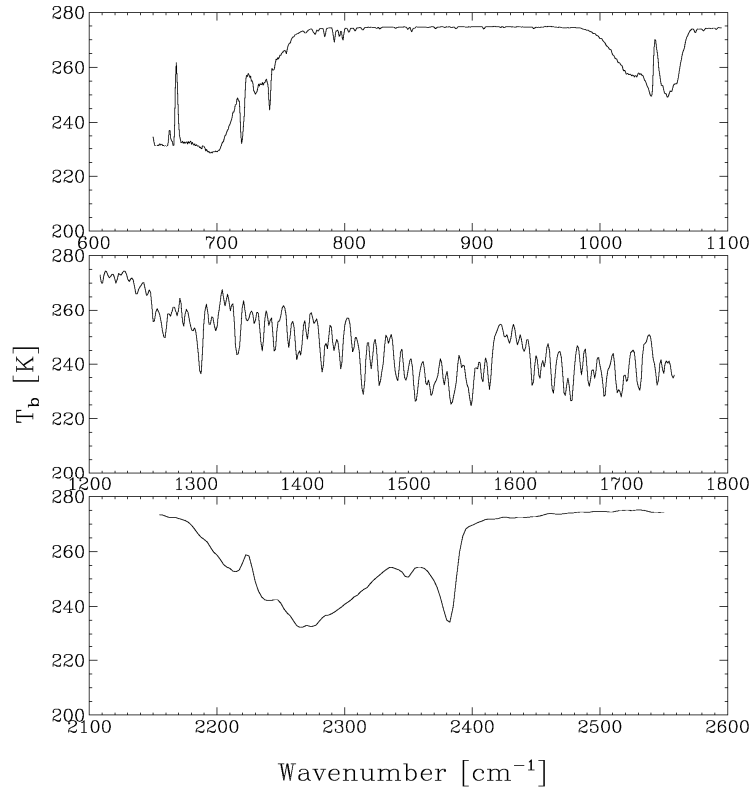


Figure 2: Example of simulated clear-sky brightness temperatures in the CrIS spectral bands.

Figure 3, Figure 4, and Figure 5 show temperature and water vapor derivatives (weighting functions) normalized by the CrIS instrument noise in the 3 CrIS bands. A mid-latitude atmospheric profile was used in generating the weighting functions. The centers of the CO₂ bands are responsible for the sounding of upper atmospheric temperature. For channels away from the center of a CO₂ band, the peak of the weighting function shifts down in altitude, allowing for sounding of the atmosphere below 1 mb. The width of the weighting function is a good indicator of the vertical resolution of the sounding instrument. For the CrIS instrument the vertical resolution increases with decreasing altitude. It should be mentioned that MWIR is very sensitive to lower atmospheric temperatures. The weighting functions have narrower width compared to LWIR and SWIR. However, channels in MWIR are also sensitive to atmospheric moisture and they should not be used as the primary temperature sounding channels if temperature and moisture are retrieved sequentially. In the current version of the code, all geophysical parameters are retrieved simultaneously and therefore MWIR also contributes to the lower atmospheric temperature retrievals.

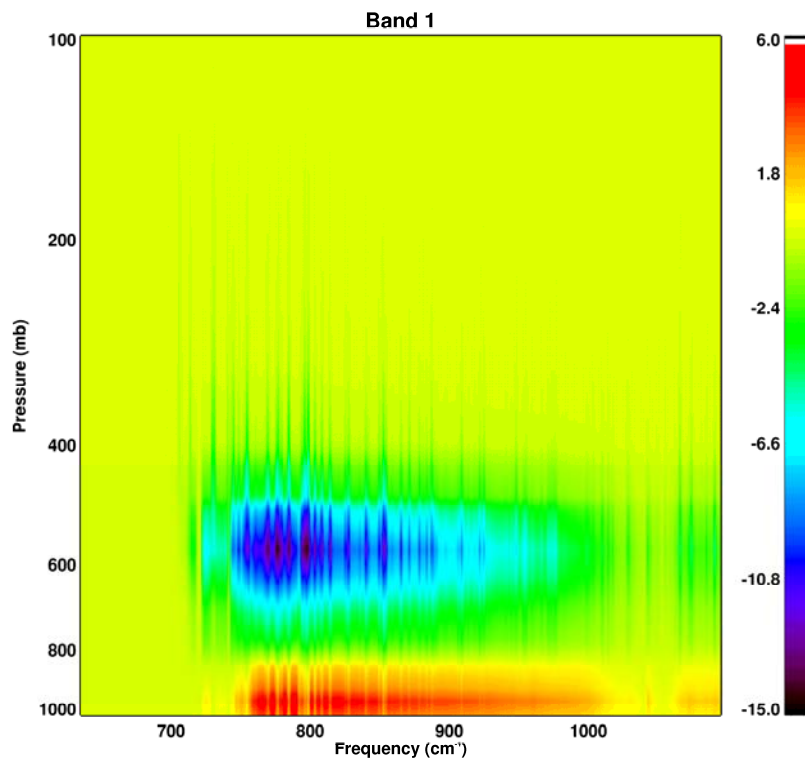
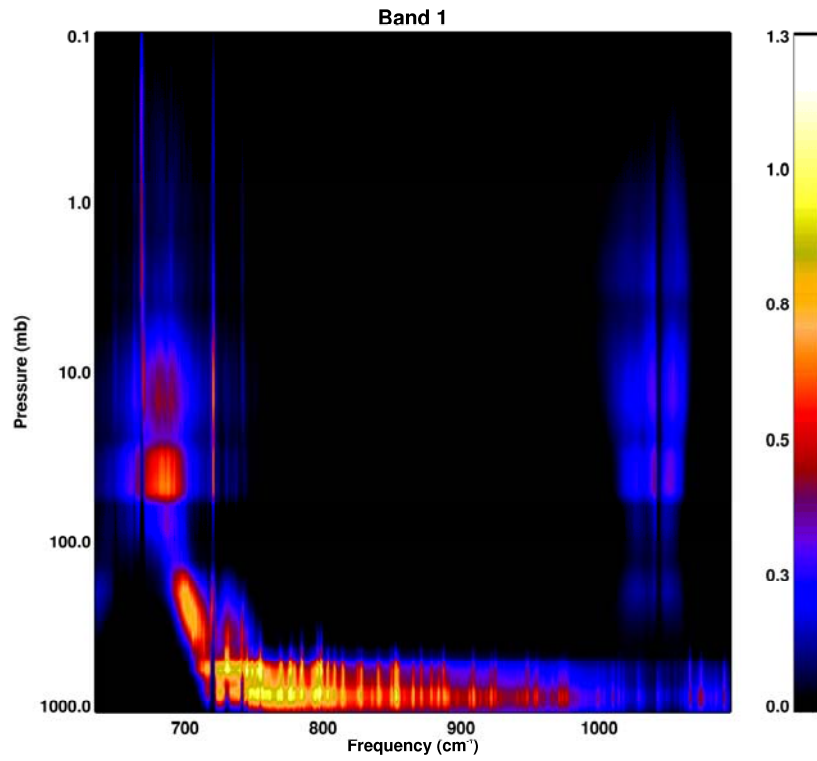
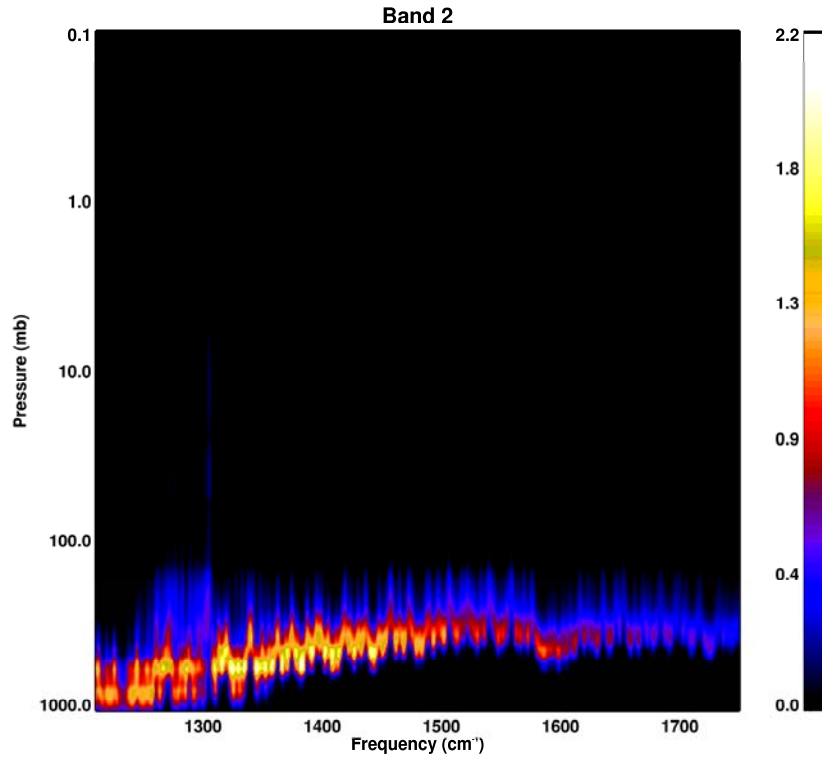


Figure 3: Temperature (top) and water vapor (bottom) weighting functions in LWIR.



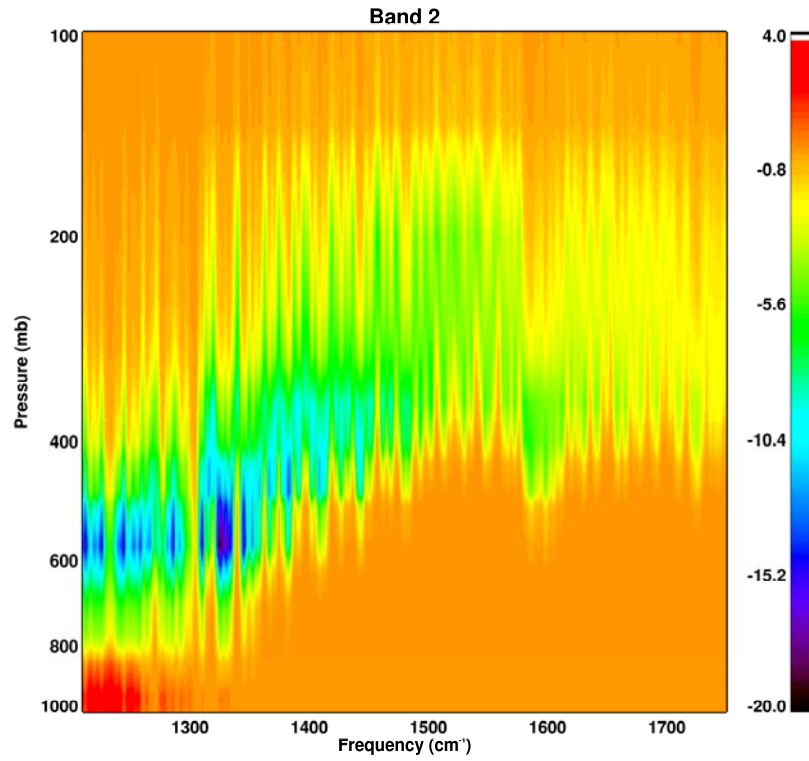


Figure 4: Temperature (top) and water vapor (bottom) weighting functions in MWIR.

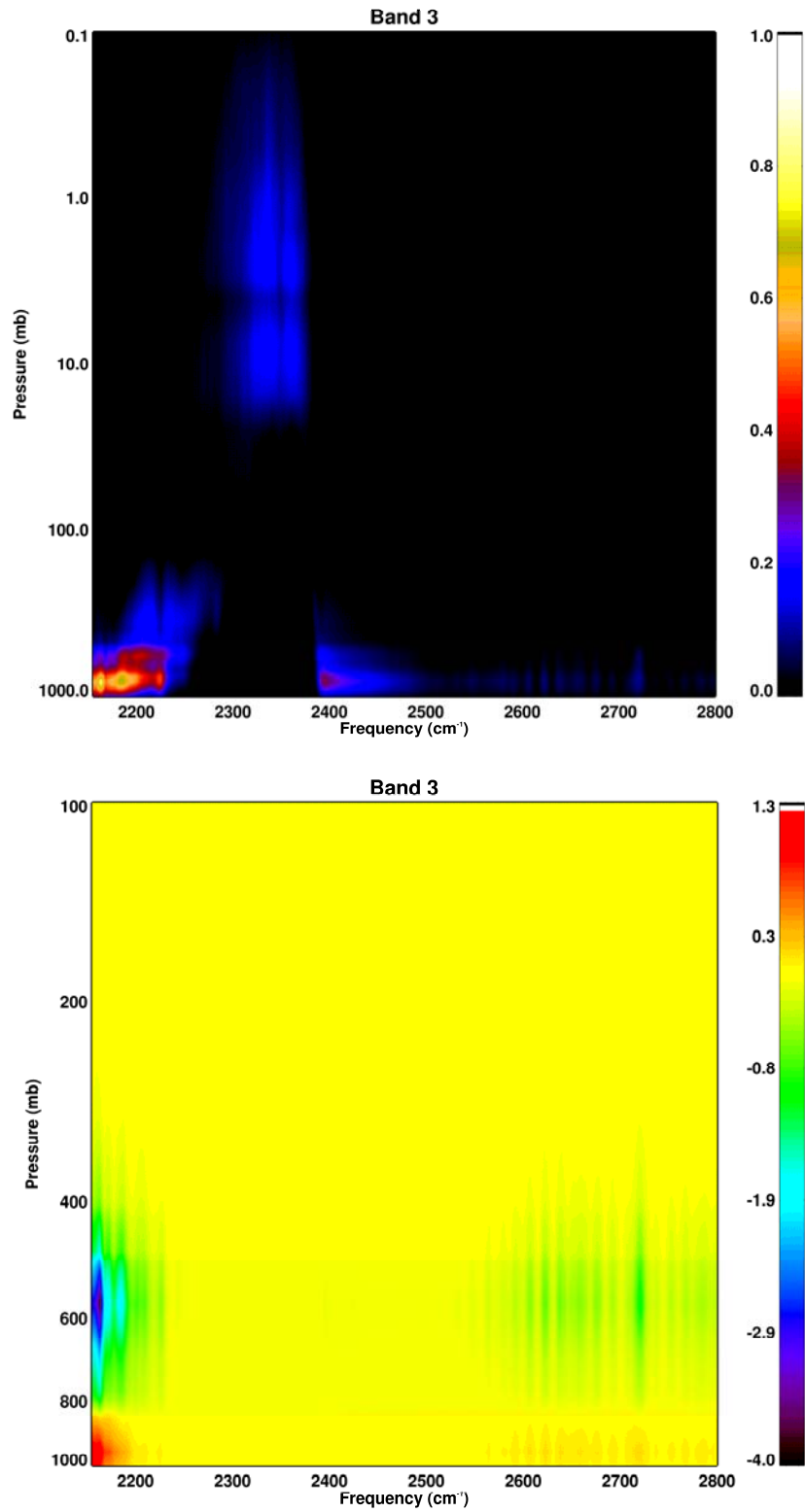


Figure 5: Temperature (top) and water vapor (bottom) weighting functions in SWIR.

3.2 Microwave Instruments

The initial algorithm design and trade studies were conducted using the AMSU (Advanced Microwave Sounding Unit) and MHS (Microwave Humidity Sounder) microwave radiometers. For NPOESS, however, ATMS (Advanced Technology Microwave Sounder) will be the microwave portion of CrIMSS. Starting from CrIMSS algorithm Version 2.3, ATMS has been included. The current version of the CrIMSS EDR algorithm assumes ATMS as the default MW sensor. But for users to better understand the characteristics and sounding capability of ATMS, the heritage instruments (AMUS and MHS) are also briefly described here.

3.2.1 Advanced Microwave Sounding Unit (AMSU)

AMSU is a cross-track scanning microwave radiometer with 15 spectral channels (23 GHz - 89 GHz). The AMSU channels and their specifications are given in Table 8 (channels 1 to 15). AMSU consists of 12 channels within the 50-60 GHz portion of the oxygen band to provide temperature and precipitation information. In addition, AMSU contains three window-channels at 24, 31, and 89 GHz to provide total precipitable water, cloud liquid water content, and precipitation measurements, respectively. These channels can also be used to provide information on sea-ice concentration and snow cover. The 3-dB beam diameter of AMSU is 3.3°, corresponding to about 48 km at nadir. This beam is co-located with the CrIS field-of-regard (FOR). Each cross-track scan produces 32 sets of measurements (30 Earth looks, 1 dark space calibration, and 1 internal blackbody radiometric calibration). The scan repeats every 8 seconds.

3.2.2 Microwave Humidity Sounder (MHS)

MHS is a cross-track scanning microwave radiometer with 5 spectral channels (89 GHz - 183 GHz). The MHS channels and their specifications are given in Table 8 (channels 16 to 20). Like AMSU, MHS contains a channel at 89 GHz to provide precipitation information (but at a higher spatial resolution). MHS has one window-channel at 150 GHz to obtain high-resolution measurements of precipitation, snow cover, and sea-ice. Three additional channels in the 183

GHz water vapor line are used to retrieve atmospheric humidity profiles. The 3-dB beam diameter of an MHS FOV is 1.1° , corresponding to about 16 km at nadir. Each cross-track scan produces 92 sets of measurements (90 Earth looks, 1 dark space calibration, and 1 blackbody calibration). The scan repeats every $8/3$ seconds. One AMSU FOV contains 9 (3x3) MHS FOVs, as shown in Figure 6.

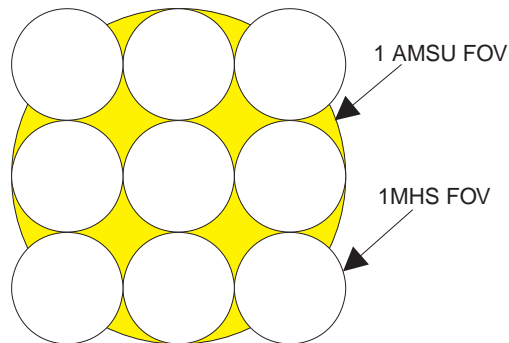


Figure 6: AMSU/MHS FOV Configuration.

Table 8: AMSU (1 to 15) and MHS (16 to 20) Channel Set.

Channel	Central Frequency	Side Band	Bandwidth	Primary Use
1	23.800	0.0	270	TPW
2	31.400	0.0	180	CLW
3	50.300	0.0	180	Temperature
4	52.800	0.0	400	Temperature
5	53.596	± 0.115	170	Temperature
6	54.400	0.0	400	Temperature
7	54.940	0.0	400	Temperature
8	55.500	0.0	330	Temperature
9	57.290	0.0	330	Temperature
10	57.290	0.217	78	Temperature
11	57.290	$\pm 0.322 \pm 0.048$	36	Temperature
12	57.290	$\pm 0.322 \pm 0.022$	16	Temperature
13	57.290	$\pm 0.322 \pm 0.010$	8	Temperature
14	57.290	$\pm 0.322 \pm 0.0045$	3	Temperature
15	89.000	0.0	6000	CLW
16	89.000	± 0.9	1000	CLW
17	150.000	± 0.9	1000	Water vapor
18	183.310	± 1.0	500	Water vapor
19	183.310	± 3.0	1000	Water vapor

20	183.310	± 7.0	2000	Water vapor
----	---------	-----------	------	-------------

Figure 7 shows the locations of the AMSU and MHS channels on the microwave water vapor and oxygen absorption spectrum.

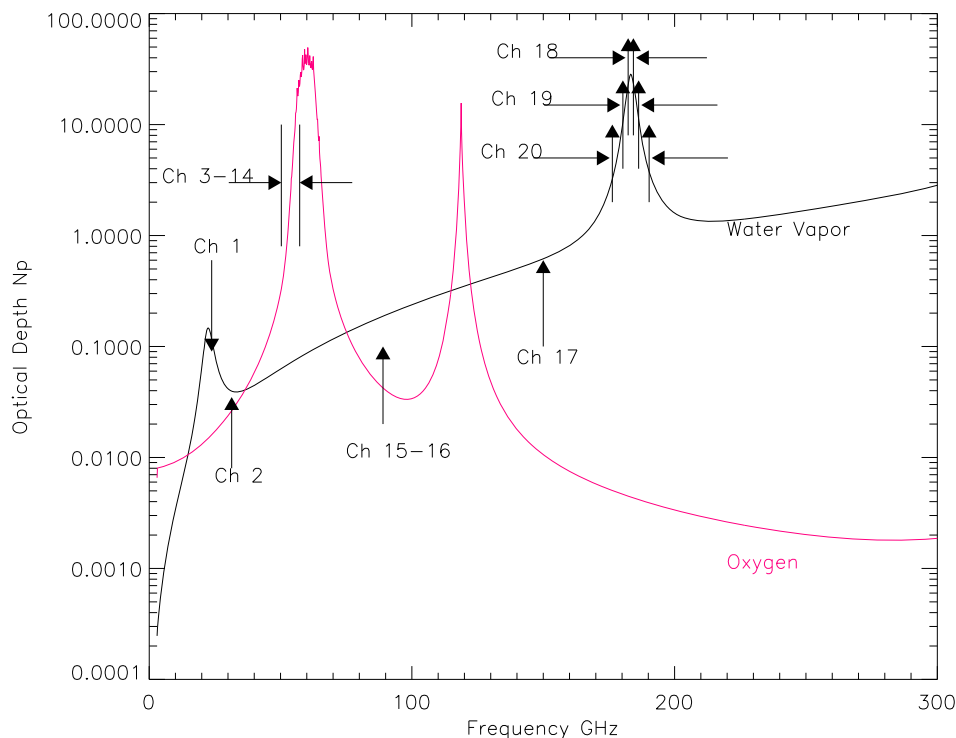


Figure 7: Channel positions for AMSU (1 to 15) and MHS (16 to 20).

3.2.3 Advanced Technology Microwave Sounder (ATMS)

As mentioned in the introduction, ATMS is the actual microwave component for the NPOESS CrIMSS. The current algorithm uses ATMS as the default microwave component although it still retains the capability of using AMSU/MHS.

Instead of having two separate microwave instruments, AMSU and MHS, the ATMS combines both temperature and moisture sounding components in one compact instrument. The channel set is very similar to the AMSU/MHS combination, although ATMS contains two additional

channels in the 183 GHz region for enhanced water vapor profiling and one additional temperature sounding channel at 57 GHz. AMSU/MHS have two 89 GHz channels with different spatial resolutions (3.3° and 1.1°) while ATMS only has one 89 GHz channel with spatial resolution of 2.2°. Table 9 lists the characteristics of the ATMS channels.

The scanning geometry and footprint sizes of ATMS are somewhat different from that of AMSU and MHS. Channels 1 and 2 have a beam width of 5.2°, which corresponds to a footprint size of 74.8 km at nadir. Channels 3-16 have a beam width of 2.2°, which corresponds to a footprint size of 31.6 km at nadir. Channels 17-22 have a beam size of 1.1°, which corresponds to a footprint size of 15.8 km. The footprints are shown in Figure 8. Because the ATMS scans at a rate of 8/3 seconds per scan, the scan pattern overlaps, but does not match exactly, the scan pattern of CrIS. For the operational implementation, the ATMS SDR algorithm will re-sample the ATMS SDRs to match the CrIS FOR configuration prior to ingestion by the CrIMSS EDR retrieval algorithm. Detailed discussion on the resampling of the ATMS SDRs can be found in Appendix D.

Table 9: Characteristics of ATMS Channel Sets.

CHANNEL	CENTER FREQUENCY (GHz)	MAXIMUM BANDWIDTH (GHz)	CENTER FREQUENCY STABILITY (MHz)	NASA TEMPERATURE SENSITIVITY (K) NEdT	NGES TEMPERATURE SENSITIVITY (K) NEdT	STATIC BEAMWIDTH B (degrees)	QUASI-POLARIZATION	CHARACTERIZATION AT NADIR (REFERENCE ONLY)
1	23.8	0.27	10	0.9	0.5	5.2	QV	water vapor
2	31.4	0.18	10	0.9	0.6	5.2	QV	window
3	50.3	0.18	10	1.20	0.7	2.2	QH	window
4	51.76	0.40	5	0.75	0.5	2.2	QH	window
5	52.8	0.40	5	0.75	0.5	2.2	QH	surface air
6	53.596 ± 0.115	0.17	5	0.75	0.5	2.2	QH	4km ~700mb

7	54.40	0.40	5	0.75	0.5	2.2	QH	9km ~400mb
8	54.94	0.40	10	0.75	0.5	2.2	QH	11km ~250mb
9	55.50	0.33	10	0.75	0.5	2.2	QH	13km ~180mb
10	57.290334	0.33	0.5	0.75	0.75	2.2	QH	17km ~90mb
11	57.290334 ± 0.217	0.078	0.5	1.20	1.0	2.2	QH	19km ~50mb
12	$57.290334 \pm 0.3222 \pm 0.048$	0.036	1.2	1.20	1.0	2.2	QH	25km ~25mb
13	$57.290334 \pm 0.3222 \pm 0.022$	0.016	1.6	1.50	1.50	2.2	QH	29km ~10mb
14	$57.290334 \pm 0.3222 \pm 0.010$	0.008	0.5	2.40	2.2	2.2	QH	32km ~6mb
15	$57.290334 \pm 0.3222 \pm 0.0045$	0.003	0.5	3.60	3.60	2.2	QH	37km ~3mb
16	88.2	2.0	200	0.5	0.3	2.2	QV	H ₂ O 150mm
17	165.5	3.0	200	0.6	0.6	1.1	QH	H ₂ O 18mm
18	183.31 ± 7	2.0	30	0.8	0.8	1.1	QH	H ₂ O 8mm
19	183.31 ± 4.5	2.0	30	0.8	0.8	1.1	QH	H ₂ O 4.5mm
20	183.31 ± 3	1.0	30	0.8	0.8	1.1	QH	H ₂ O 2.5mm
21	183.31 ± 1.8	1.0	30	0.8	0.8	1.1	QH	H ₂ O 1.2mm
22	183.31 ± 1	0.5	30	0.9	0.9	1.1	QH	H ₂ O 0.5mm

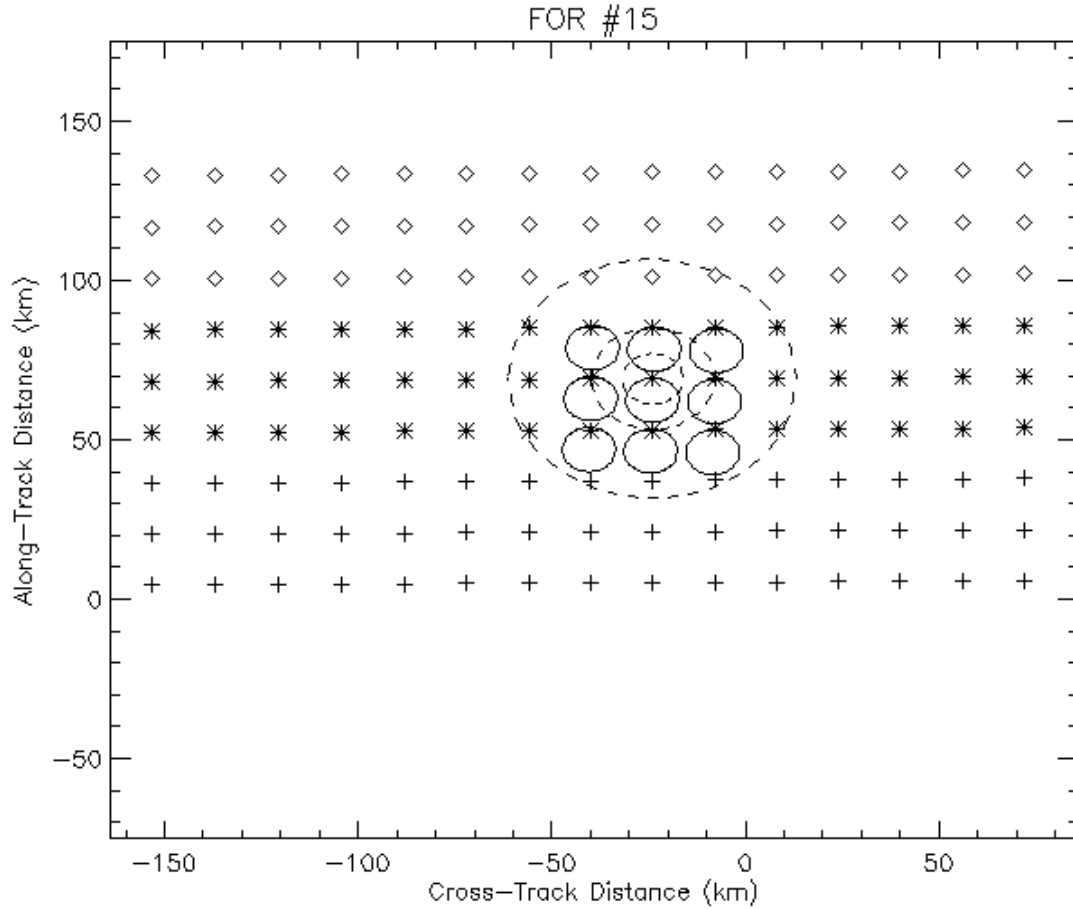


Figure 8: ATMS footprint sizes relative to CrIMSS field-of-regard (FOR). Note that the 15th FOR occurs just to the left of nadir relative to the along-track satellite velocity vector. The solid circles represent the 9 CrIS FOVs and the dotted circles represent the 3 different ATMS FOV sizes. The individual points show the ATMS footprint centers for three successive scanlines (each of which includes 3 cross-track ATMS scans and 1 cross-track CrIS scan).

4.0 IMPORTANT ASPECTS IN EDR ALGORITHM DESIGN

Figure 9 presents the top-level flow diagram for the CrIMSS retrieval algorithm. The algorithm consists of seven modules (shown enclosed in rectangular boxes in Figure 9):

1. Initialization
2. Input and pre-processing
3. Microwave-only retrieval
4. Scene classification
5. Joint microwave and infrared retrieval
6. Quality control
7. Output and post-processing (includes a slant-to-vertical conversion program executed outside of the FOR loop)

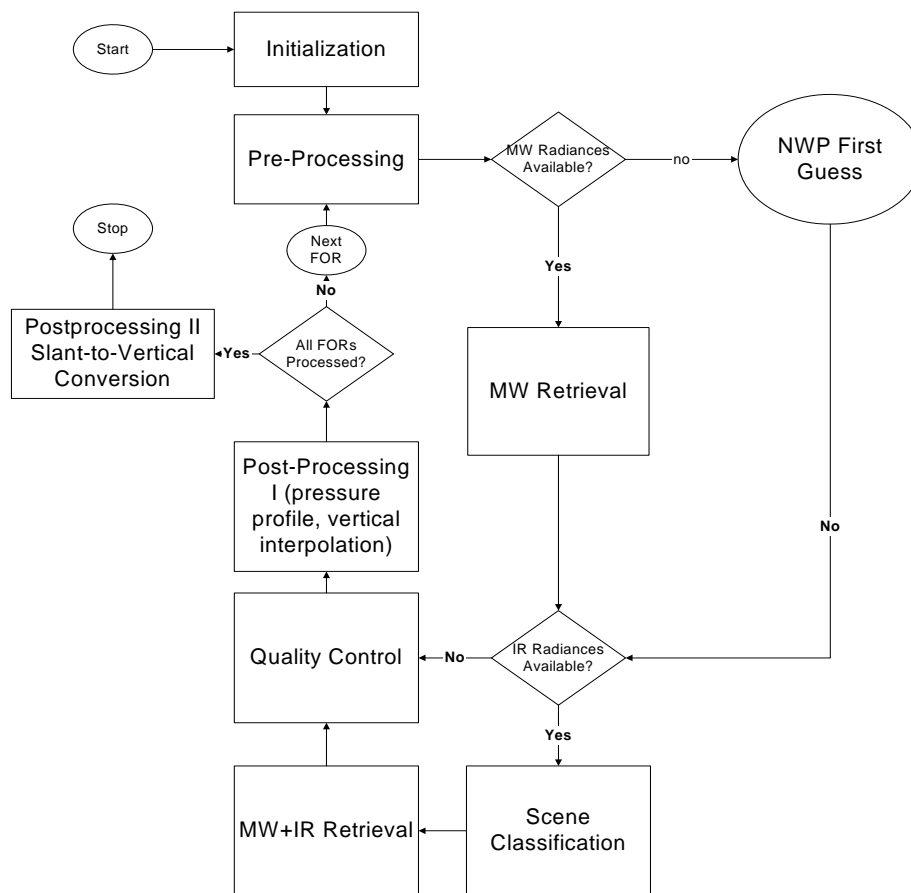


Figure 9: CrIMSS EDR Algorithm Flow Diagram.

The CrIMSS EDR algorithm can be divided into three parts (in order to make the CrIMSS science code modular and flexible, each part of the algorithm consists of several modules). The initialization and pre-processing modules constitute the first part. This part of the algorithm prepares the SDRs and auxiliary data needed to generate EDR output. The microwave-only retrieval, the scene classification, and the IR+MW joint retrieval constitute the second part of the EDR algorithm. This part takes the SDRs along with auxiliary data and performs several physical retrievals to handle cloud effects and to invert SDRs into EDRs. The last part consists of quality control and post-processing modules. It checks the quality of the retrieved product and converts the EDRs into the required reporting format.

Since the CrIMSS instrument has more than 1000 channels of data, it provides a large amount of information with regard to clouds, atmospheric temperature and moisture profiles, and surface properties. Since these quantities are related to the SDRs in a non-linear way, a retrieval algorithm based on regression may not provide optimal EDR output. The CrIMSS algorithm utilizes a physical retrieval approach to simultaneously retrieve all relevant geophysical parameters. Two key elements of this algorithm are a fast radiative transfer (forward) model and a robust inversion algorithm, both of which share common features between the microwave and infrared parts of the retrieval. Their general description is presented in Sections 4.2 and 4.3, respectively. Since the CrIS instrument is a Fourier transform type instrument and the physical retrieval algorithm is closely related to the instrument apodizations, Section 4.1 provides general information about apodization of FTIR spectra. Another critical consideration in the design of an infrared retrieval algorithm concerns the treatment of clouds and a brief overview of retrieval strategies under cloudy conditions is provided in Section 4.4. Section 5.0 of this ATBD is devoted to the description of the individual modules of the CrIMSS algorithm. Section 6.0 discusses algorithm validation, while results from trade studies related to the design of individual modules are presented in Section 7.0.

4.1 Apodization Issues Related to FTIR Spectra

As mentioned above, the CrIS sensor is a Michelson Fourier Transform Infrared spectrometer. Owing to the finite length of the sampled interferogram, the resulting Instrument-Line-Shape (ILS) function will exhibit ringing if no damping (or apodization) is applied to the interferograms. The damping on the other hand will introduce correlations between adjacent channels. Therefore, there are two issues related to the CrIMSS EDR algorithm when dealing with the ILS functions of the CrIS sensor:

1. How to effectively model both the localized (strong apodization) and the non-localized (weak apodization) ILS in the forward model.
2. How to take into account the interchannel noise correlation when inverting an apodized spectrum.

These two issues will be discussed in Sections 4.2 and 4.3, respectively. In this section, we will briefly describe the apodization functions and ILS functions available in the CrIMSS EDR algorithm. The relationship between ILS and apodization functions will also be discussed. For a more detailed description of these topics, the reader is referred to Barnett *et al.* (2000).

4.1.1 Apodization Function

For an FTIR instrument such as CrIS, several factors affect the ILS. The first is the instrument self-apodization caused by the finite field-of-view of the optical system and different geometric locations of the individual detectors relative to the optical axis. The second factor is the imperfect alignment of the interferometer, which causes degradation of the modulations. The CrIS SDR algorithm corrects for these two effects, so that the forward model used by the EDR algorithm does not have to model the 9 FOVs differently with regard to the ILS. The third factor contributing to the ILS is the finite length of the interferogram. Since the FFT is supposed to be performed from minus infinity to plus infinity with respect to Optical Path Difference (OPD), the finite Maximum Optical Path Difference (MPD) sampled by the CrIS interferometer causes ringing and the ILS has the form of a *sinc* function (see below). To minimize the ringing effect, the measured interferograms are multiplied by an apodization function before being transformed into the spectral domain. Usually the apodization function has a value of 1 at zero OPD and gradually decreases to a very small value at the MPD. Figure 10 shows three apodization functions used in the CRIMSS algorithm: *Boxcar*, *Hamming* and *Blackman*. When the

interferograms are multiplied by an apodization function that has a value of 1 near zero OPD and approaches 0 near the MPD, the effect of the finite extent of the interferogram is reduced and the ILS in the spectral (frequency) domain is much more localized. Among the apodization functions in Figure 10, the *Blackman* apodization is the strongest and therefore its ILS is the most localized in the spectral domain.

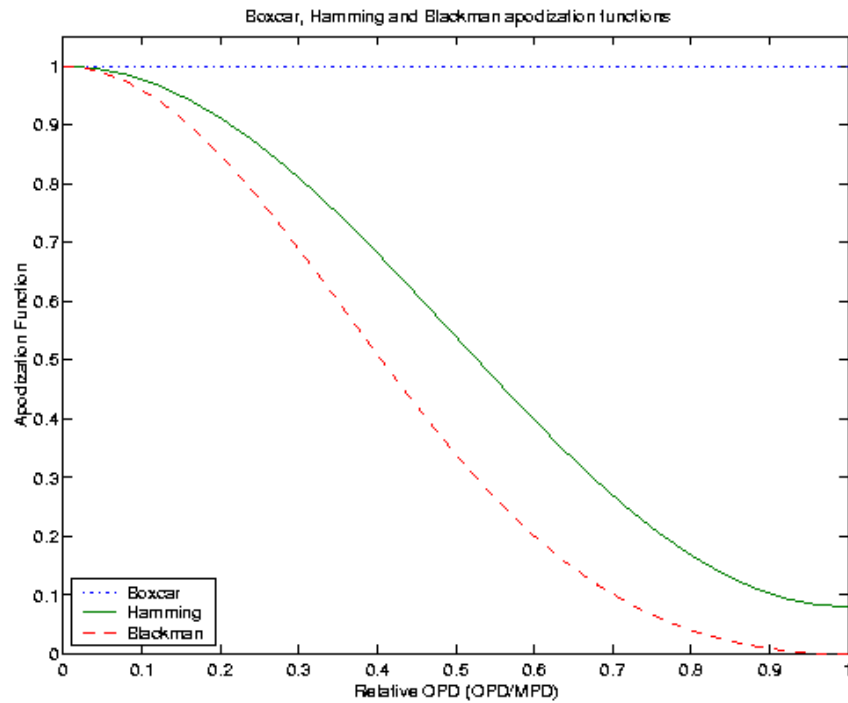


Figure 10: Apodization functions used in the CrIS EDR algorithm.

The *Boxcar* apodization (or unapodized) function is defined as:

$$A(x) = \begin{cases} 1 & \text{for } |x| \leq MPD \\ 0 & \text{for } |x| > MPD \end{cases} \quad (0.1)$$

where x is the OPD. The *Hamming* apodization function is defined as

$$A(x) = \begin{cases} 0.54 + 0.46 \cos\left(\pi \frac{x}{MPD}\right) & \text{for } |x| \leq MPD \\ 0 & \text{for } |x| > MPD \end{cases} \quad (0.2)$$

The *Blackman* apodization function is defined as

$$A(x) = \begin{cases} 0.42 + 0.5 \cos\left(\pi \frac{x}{MPD}\right) + 0.08 \cos\left(2\pi \frac{x}{MPD}\right) & \text{for } |x| \leq MPD \\ 0 & \text{for } |x| > MPD \end{cases}. \quad (0.3)$$

Both the *Hamming* and *Blackman* apodizations are special cases of cosine apodization functions, which have the following general form

$$A(x) = \begin{cases} a_0 + 2 \cdot \sum_{k=1}^{K-1} a_k \cos\left(k\pi \frac{x}{MPD}\right) & \text{for } |x| \leq MPD \\ 0 & \text{for } |x| > MPD \end{cases}. \quad (0.4)$$

For the *Hamming* apodization, $K=2$, $a_1=0.23$, $a_0=(1-2a_1)$, whereas for *Blackman*, $K=3$, $a_1=0.25$, $a_2=0.04$, $a_0=(1-2a_1-2a_2)$.

In Section 7.3 of this document, pre-launch trade studies comparing the *Blackman* and *Hamming* apodizations are described and discussed.

Another example of a cosine apodization function is the three-term *Blackman-Harris* apodization (Harris, 1978). Expressed in the form of Equation (4.4), a three-term ($K=3$) *Blackman-Harris* apodization that very strongly reduces sidelobes in the transform of the interferogram has $a_0=0.42323$, $a_1=.49755/2$, $a_2=.07922/2$ (Harris, 1978). The *Blackman-Harris* is the apodization in use in the operational CrIMSS algorithm code.

For a fuller discussion of apodizations in the context of the use of CrIS instrument data, see Section 3.7 of the CrIS SDR ATBD (NASA, 2011).

4.1.2 Instrument Line Shape Function

The CrIS channel radiance $Y(\nu)$ is given by a convolution of the ILS function $\phi(\nu)$ with the monochromatic radiance $Y_0(\nu)$ at the entrance to the interferometer:

$$Y(\nu) = Y_0(\nu) \otimes \phi(\nu) = \frac{\int_{\Delta\nu'} Y_0(\nu') \phi(\nu - \nu') d\nu'}{\int_{\Delta\nu'} \phi(\nu - \nu') d\nu'} \quad (0.5)$$

The ILS function $\phi(\nu)$ is defined as the Fourier transform of the apodization function. For an unapodized (i.e., *boxcar*-apodized) interferogram, the resulting ILS has a *sinc* form

$$\phi_U = \text{sinc}(2MPD \cdot \nu) \equiv \frac{\sin(2\pi MPD \cdot \nu)}{2\pi MPD \cdot \nu} \quad (0.6)$$

where ν is proportional to the frequency separation from the channel center. As shown in Figure 11, this function has large side-lobes that alternate in sign and fall off slowly with increasing frequency separation. The first four side-lobes have heights of -21.7%, +12.8%, -9.1%, and +7.1% with respect to the central lobe. The zero crossings occur at

$$\nu - \nu_0 = \pm n / (2MPD) \quad (0.7)$$

where ν_0 is the channel center frequency and n is an integer. The Full Width at Half Maximum (FWHM) of the *sinc* function is $1.21/(2 MPD)$. For the *Hamming* apodization, the ILS function has the following form

$$\begin{aligned} \phi_H(\nu) = & 0.54 \text{sinc}(2\pi MPD \cdot \Delta\nu) \\ & + 0.23 [\text{sinc}(2\pi MPD \cdot \Delta\nu - \pi) + \text{sinc}(2\pi MPD \cdot \Delta\nu + \pi)] \end{aligned} \quad (0.8)$$

with FWHM = $1.8152/(2 MPD)$ (i.e., 50% larger than for *sinc*). The *Blackman* ILS has the form

$$\begin{aligned} \phi_B(\nu) = & 0.42 \text{sinc}(2\pi MPD \cdot \Delta\nu) \\ & + 0.25 [\text{sinc}(2\pi MPD \cdot \Delta\nu - \pi) + \text{sinc}(2\pi MPD \cdot \Delta\nu + \pi)] \\ & + 0.04 [\text{sinc}(2\pi MPD \cdot \Delta\nu - 2\pi) + \text{sinc}(2\pi MPD \cdot \Delta\nu + 2\pi)] \end{aligned} \quad (0.9)$$

with $\text{FWHM} = 2.274/(2MPD)$ (88% larger than for *sinc*). The general form for a cosine ILS function is

$$\begin{aligned} \phi(\nu) = & a_0 \text{sinc}(2\pi MPD \cdot \Delta\nu) \\ & + \sum_{k=1}^{K-1} a_k [\text{sinc}(2\pi MPD \cdot \Delta\nu - k\pi) + \text{sinc}(2\pi MPD \cdot \Delta\nu + k\pi)] \end{aligned} \quad (0.10)$$

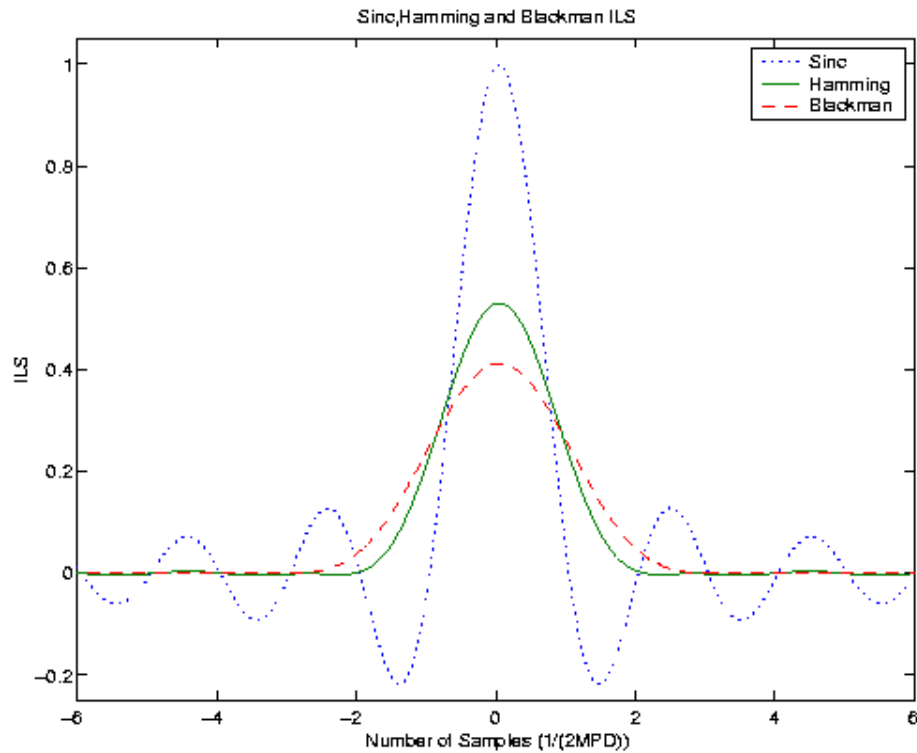


Figure 11: ILS functions corresponding to the apodization functions in Figure 10.

4.1.3 Transformation Between ILS Functions

An important feature of the cosine apodization functions (such as *Hamming* or *Blackman*) is that the apodized radiances are linear combinations of the unapodized radiances, provided the Nyquist channel spacing of $\Delta\nu = 1/(2MPD)$ is used. Because of this linear relationship, the information content of unapodized and apodized radiances is identical. *Hamming*-apodized radiances for channel i are a 3-point running mean of neighboring unapodized radiances

$$Y_H(i) = 0.54Y_U(i) + 0.23[Y_U(i-1) + Y_U(i+1)] \quad (0.11)$$

whereas *Blackman*-apodized radiances are a 5-point average

$$Y_B(i) = 0.42Y_U(i) + 0.25[Y_U(i-1) + Y_U(i+1)] + 0.04[Y_U(i-2) + Y_U(i+2)]. \quad (0.12)$$

The general form for transforming an unapodized ILS into a cosine ILS is

$$Y_{\cos}(i) = (1 - 2\sum_{k=1}^{K-1} a_k) \cdot Y_U(i) + \sum_{k=1}^{K-1} a_k [Y_U(i-k) + Y_U(i+k)] \quad (0.13)$$

For *Blackman* apodization, the corresponding ILS is strongly localized. This property simplifies the forward model parameterization. The *Hamming* function has a moderately localized ILS and a narrower FWHM than *Blackman*. It also has a simple analytic inverse so that it can be transformed into other apodization functions (e.g., Barnet *et al.* 2000). The CrIS forward model is capable of modeling all 3 apodization functions efficiently. This will be discussed in the next section.

4.2 Forward Model

One of the most critical components of a remote sensing retrieval algorithm is the radiative transfer model (also referred to as the forward model). The forward model computes radiances corresponding to a given atmospheric and geophysical state (temperature, water vapor and ozone profiles, surface properties, cloud properties, etc.), as well as derivatives (Jacobian) of radiances with respect to atmospheric and surface parameters, for use by the inversion module. The forward model must be able to accurately model the Instrument Line Shape (ILS) function or Spectral Response Function (SRF). In addition to being accurate, the forward model must also meet stringent requirements on computational time. The Optimal Spectral Sampling (OSS) technique developed at AER forms the basis of an accurate and efficient forward model for the CrIMSS EDR algorithm. Being monochromatic, the OSS technique has the advantage over other fast forward models in providing the required derivatives analytically, with little extra

computation time. It provides orders of magnitude improvement in computational efficiency compared with line-by-line (LBL) radiative transfer codes. In Section 4.2.1, the basic radiative equations relating top-of-atmosphere (TOA) radiances to the atmospheric temperature and moisture profiles and the surface properties are given. Section 4.2.2 presents an overview of the OSS radiative transfer model. Section 4.2.3 describes the implementation of the OSS method, while in Section 4.2.4, a detailed description of calculating TOA radiances is provided.

4.2.1 Radiative Transfer Equations

The radiative transfer equation relates TOA radiances observed from space to the atmospheric and surface emissions and the transmittance of the atmosphere. The atmospheric transmittance is related to the atmospheric temperature, moisture and trace gas profiles. By inverting the radiative transfer equation, the EDRs can be derived from the CrIMSS-observed radiances. Sections 4.2.1.1 and 4.2.1.2 describe the RT equations in microwave and infrared spectral regions, respectively. It should be mentioned that the radiances discussed in this section are monochromatic and they need to be convolved with the instrument ILS or SRF to match radiances observed by the CrIMSS sensors (see Section 4.1.2).

4.2.1.1 Microwave

The radiative transfer equation used in the microwave region treats the atmosphere as an inhomogeneous, plane-parallel, non-scattering medium. The brightness temperature R_ν at frequency ν is computed using the Rayleigh-Jeans approximation:

$$R_\nu \cong \varepsilon_\nu \Theta_s T_{s,\nu} + \int_{p_s}^0 \Theta(p) \frac{\partial T_\nu(p, \theta_u)}{\partial p} dp + (1 - \varepsilon_\nu) T_{s,\nu} \left[\int_0^{p_s} \Theta(p) \frac{\partial T_\nu^*(p, \theta_d)}{\partial p} dp + T_\nu^*(0, \theta_d) \Theta_c \right] \quad (0.14)$$

where $\Theta(p)$ is the atmospheric temperature at pressure p , $T_\nu(p, \theta_u)$ is the total transmittance due to molecular species and cloud liquid water from pressure p to space at the satellite viewing

angle θ_u , $T_v^*(p, \theta_d)$ is the transmittance from surface to pressure p at computational angle θ_d , ε_v is the surface emissivity, and Θ_c is the cosmic radiation term

$$\Theta_c = \frac{kv e^{hv/2.73k} + 1}{2k e^{kv/2.73k} - 1}. \quad (0.15)$$

In the microwave, over both land and ocean, the surface is treated as specular, i.e. $\theta_d = \theta_u$. The OSS forward model allows θ_d to be set to any desired value.

4.2.1.2 Infrared

The general form of the RTE in the infrared for an inhomogeneous, plane-parallel, non-scattering medium can be written as:

$$\begin{aligned} R_v = & \varepsilon_v B_v(\Theta_s) T_{s,v} + \int_{p_s}^0 B_v(\Theta(p)) \frac{\partial T_v(p, \theta_u)}{\partial p} dp \\ & + \alpha T_{s,v} \int_0^{2\pi} \int_0^{\pi/2} f_v(\theta_u, \phi_d; \theta, \phi) \left[\int_0^{p_s} B_v(\Theta(p)) \frac{\partial T_v^*(p, \theta)}{\partial p} dp \right] \sin \theta \cos \theta d\theta d\phi \quad (0.16) \\ & + \rho_v T_{s,v} T_v(p_s, \theta_{sun}) F_{0,v} \cos \theta_{sun} \end{aligned}$$

where $B_v(\Theta(p))$ is the Planck function emission, α is the surface albedo, $f_v(\theta_u, \phi_u; \theta, \phi)$ is the surface bidirectional reflectance function, θ and ϕ are zenith and azimuth angles, respectively, $F_{0,v}$ is the solar irradiance, θ_{sun} is the solar zenith angle, $T_v(p_s, \Theta_{sun})$ is the transmittance of the atmosphere long the solar refracted path, and ρ_v is the solar bi-directional surface reflectance. The third term in Equation (0.16) represents the downwelling thermal radiation reflected from the surface.

A proper treatment of the angular integral in Equation (0.16) would require information about the anisotropy in the downwelling radiances caused by the anisotropy in the reflective properties

of the surface. In practice, because of the non-homogenous nature of the atmosphere and the fact that bi-directional reflectance distribution functions (BRDF) for natural land surfaces are poorly known, the usefulness of such a level of sophistication for a 1-D retrieval problem is uncertain. At the present stage of development of the CrIS EDR algorithm, the following form of RTE is used to address the case of specular and Lambertian surfaces

$$R_v \cong \varepsilon_v B_v(\Theta_s) T_{s,v} + \int_{p_s}^0 B_v(\Theta(p)) \frac{\partial T_v(p, \theta_u)}{\partial p} dp + (1 - \varepsilon_v) T_{s,v} \int_0^{p_s} B_v(\Theta(p)) \frac{\partial T_v^*(p, \theta_d)}{\partial p} dp + \rho_v T_{s,v} T_v(p_s, \theta_{sun}) F_{0,v} \cos \theta_{sun} \quad (0.17)$$

where $\theta_d = \theta_u$ and $\theta_d \approx 53^\circ$ for specular and Lambertian surfaces, respectively. The Lambertian case corresponds to the use of a single “diffusivity” angle that provides a good approximation to the explicit angular integral when the downwelling radiance field is isotropic. The surface albedo is assumed to be $(1 - \varepsilon_v)$.

The single-angle integration is valid over ocean, where the specular assumption is approximately valid, and for densely vegetated land surfaces, for which the BRDFs are nearly isotropic. However, more complex land surface types, such as sand, snow, senescent vegetation, as well as inhomogeneous pixels (e.g. mixture of land and water bodies) often display highly non-Lambertian characteristics (Snyder *et al.* 1998). As a future enhancement to the current algorithm, a separate retrieval of thermal reflectivity over land and coastal regions should be considered. Appropriate constraints will be used to tie the spectral thermal reflectivity to the emissivity as a function of geographical location, season, and surface/vegetation type.

4.2.2 Overview of the OSS Method

Optimal Spectral Sampling (OSS) is a general approach to radiative transfer that is applicable from the microwave through the ultraviolet regions of the spectrum and that can be used with any ILS (or SRF). In this approach, the TOA radiance for each instrument channel is represented

as a linear combination of radiances computed at selected monochromatic locations within the domain spanned by the ILS

$$R_{\Delta\nu}(\nu) = \frac{\int_{\Delta\nu} \phi(\nu - \nu') R(\nu') d\nu'}{\int_{\Delta\nu} \phi(\nu - \nu') d\nu'} = \sum_i w_i R_{\nu_i} + err \quad (0.18)$$

where ν_i belongs to some spectral interval $\Delta\nu$ around the “central” frequency ν and $\phi(\nu - \nu')$ is the ILS function (assumed to vanish when ν' is outside the interval $\Delta\nu$). For a *sinc* ILS, $\Delta\nu$ extends from the low frequency limit to the high frequency limit of each of the CrIS spectral bands. For the ATMS (or AMSU/MHS), $\Delta\nu$ is very localized (equal to the band width). The optimal selection of the frequencies ν_i and weights w_i is performed off-line by comparing radiances derived from the OSS formulation with those obtained using a reference line-by-line model. The optimization procedure minimizes RMS differences between the reference and approximate radiances for an ensemble of globally representative atmospheric profiles and the full range of satellite viewing angles. The error term on the right-hand side of Equation (0.18) expresses the degree of approximation in this scheme and determines the number of points used in Equation (0.18) for each channel (per CrIMSS EDR algorithm requirements, this term is set to 0.1 K).

For a localized ILS or SRF, the following constraints are applied to ensure a physical solution

$$\begin{aligned} w_i &> 0 \\ \sum_i w_i &= 1 \end{aligned} \quad (0.19)$$

The positive coefficient constraint serves as a sign control that prevents the instability of the selection process. In their paper describing the Exponential Sum Fitting Transmittance (ESFT) approach, Wiscombe and Evans (1977) pointed out that the appearance of a negative coefficient indicates linear dependence of some selected points and can lead to ill-conditioning in the least-squares fitting process. However, for a non-localized ILS the sign control is not a good constraint, since negative coefficients are physically allowed for spectral regions in which the

side-lobes of the non-localized ILS are negative. An alternative approach to avoiding ill-conditioning relies on controlling the value of the determinant of the inversion matrix in the least squares fitting process and is combined with a statistical Monte-Carlo search described in Appendix A. It is flexible and allows control of the determinant values and of statistically rejecting configurations of points characterized by small values of the determinant.

Two methods have been adopted for selecting the monochromatic spectral points and their associated weights. For a localized ILS (such as *Blackman* for CrIS or SRF for AMSU/MHS), a sequential search, similar to that used by Wiscombe and Evans (1977) for ESFT, is implemented with constraints listed in Equation (0.19). However, this method is not practical for a non-localized ILS (such as *Hamming* or *sinc*), since the sign control needs to be replaced in this case by determinant control and this results in a significant increase in the number of points required to fit the “true” radiances. Because of this, for a non-localized ILS the sequential search has been replaced by the more efficient Monte-Carlo method. This method can be used for both localized and non-localized ILS.

Note that if the second constraint in Equation (0.19) is not explicitly enforced, it can still be approximately realized with a fairly high accuracy for a localized ILS. For example, when modeling apodized radiances without this constraint for *Blackman*, the sum rule is still valid with an accuracy of about 10^{-3} . However, the situation changes dramatically when the number of side-lobes reaches a few tens. For the *Hamming* instrument function with 40 side-lobes, the value of the sum ranges between 0.7 and 1.3 if the sum rule is not enforced explicitly. For the *sinc* ILS, the sum can even turn negative values for some instrument channels. Consequently, we have chosen to work with the sum rule, as expressed in Equation (0.19), but without confining the coefficients to positive values. Instead, we use the determinant control (see Appendix A).

4.2.3 Implementation of the OSS Method

Important Note: Prior to Version 4.0 of the CrIMSS EDR algorithm, the forward model used a 40-level atmospheric profile on which to compute the radiative transfer. This was adequate for sensor sensor simulation studies but not for the application to “real” data. In addition,

improvements were made to the way in which molecular absorption coefficients are stored and accessed for a particular atmospheric profile. These changes are discussed in Appendix F. Note that all trade studies and performance estimates discussed in this ATBD were conducted with the 40-level model unless noted specifically otherwise.

This section describes the application of the OSS method to the modeling of CrIMSS radiances. The number of points selected for each instrument channel will be discussed and results of validation studies for the OSS forward model will be presented. It should be noted that the RMS differences shown in this section do not include errors due to optical depth interpolation with respect to temperature. These errors can be made arbitrarily small by increasing the number of temperature entries in the optical depth look-up tables (see Section 4.2.4.1).

4.2.3.1 Infrared

In the infrared, the OSS approach is applicable to calculating both apodized and unapodized radiances. Other fast forward models, such as the rapid transmittance algorithm, require that the channel transmittances T_i be physical (i.e. $0 \leq T_i \leq 1$). Since the *sinc* ILS has large negative side-lobes as shown in Figure 11, this requirement cannot always be met. Furthermore, the *sinc* ILS extends over the whole spectral band so the assumption that the Planck function is constant for a particular channel is not valid. Barnett *et al.* (2000) used a rapid transmittance algorithm to calculate the channel radiance for an apodized ILS and transformed apodized radiances to unapodized radiances using a transformation matrix. McMillin *et al.* (1997) used a linear combination of five localized radiances for each unapodized channel radiance. Both methods avoid the limitations mentioned above, but are significantly slower than modeling the non-localized ILS directly. The OSS approach takes advantage of the fact that the selection depends mainly on the local features in the radiance spectrum and the information about the shape of the ILS is carried mostly by the weights. Once the pre-selection is done for a localized ILS at a given spectral resolution, the channel radiances for both apodized and unapodized ILS are simply linear combinations of these pre-selected monochromatic radiances. The total number of monochromatic spectral points needed to represent the channel radiances in a particular spectral

band should be similar for different apodization functions. However, for an unapodized ILS a potential increase in computational time can be caused by two factors: 1. A larger number of selected points are needed to reconstruct a given channel, and 2. The assumption that the Planck function is constant over the interval spanned by the ILS is no longer valid (see Section 4.2.4.4 for a description of the treatment of the Planck function in the OSS forward model). Results show that the OSS algorithm takes about 70% more computational time to model a *sinc* ILS (compared with *Hamming* or *Blackman*).

A training set of 49 atmospheric profiles (provided by Prof. Larrabee Strow of the AIRS team) has been used to select OSS spectral locations and weights. In order to simulate variable surface emissivity, emissivities at 20 hinge points for each of the CrIS spectral bands have been assigned random values between 0.85 and 0.98 and the emissivities at frequencies located between the hinge points have been obtained by linear interpolation. The line-by-line radiative transfer model adopted as reference in the infrared is the LBLRTM model (Clough *et al.* 1992). LBLRTM is originally based on FASCODE and has been extensively validated against atmospheric measurements (Snell *et al.* 1995). Numerical simulations have been performed with a strongly localized ILS (*Blackman*), an “intermediate” ILS (*Hamming*), and a non-localized ILS (*sinc*). Test studies have shown that the contributions of *Blackman* side-lobes beyond the central peak are negligible, as are the contributions from *Hamming* side-lobes beyond 40. On the other hand, the side-lobes of *sinc* only become negligible outside of the CrIS bands, with the result that near the band edges, the shape of a *sinc* ILS is strongly asymmetric.

For each ILS, before the final selection of OSS points and their weights using the MC method, several pre-selections are performed sequentially using a *Boxcar* ILS. At each pre-selection step, the accuracy threshold is kept at 0.025 K. In LWIR, for example, the initial monochromatic frequency spacing in the LBL calculations is 10^{-4} cm^{-1} . The initial pre-selection is made for a *Boxcar* ILS with a width of $5 \times 10^{-3} \text{ cm}^{-1}$ and is followed by three hierarchical steps. At each step, five adjacent *Boxcars* are joined together to form the *Boxcar* for the next step. Some of the combined points in the new *Boxcar* are eliminated during the next pre-selection step. The fitted radiances of the new *Boxcar* are defined as averages over predecessors. Upon completion of the three hierarchical steps, a set of spectral points and weights is selected to represent a *Boxcar* ILS

with $\text{FWHM} = 0.625 \text{ cm}^{-1}$. It should be noted that in order to save computational time, the pre-selection is performed assuming a constant value of surface emissivity. This is reasonable since the pre-selection provides more monochromatic points than needed for the final selection. The final selection can adjust the weights to account for reflected radiation. A set of monochromatic transmittances at the selected monochromatic frequency points is saved and monochromatic radiances with variable surface emissivity values are calculated from these transmittances.

The final selection for each channel is both ILS- and emissivity-dependent and is performed within a spectral range that covers the entire ILS (e.g., for a *sinc* ILS, all points in CrIS LWIR are used). The accuracy threshold adopted in the final selection is 0.05 K to ensure the forward model accuracy meets the specification. The output from this process includes the selected frequencies and the associated weights for each channel. Optical depth tables of various atmospheric gases at different atmospheric temperatures and at the selected frequencies are then generated using a LBL model. Section 4.2.4 describes how the CrIMSS forward model calculates infrared and microwave radiances using information resulting from this procedure.

Figure 12 shows the number of monochromatic spectral points per channel needed to model the *Sinc* ILS in the LWIR band. In the window spectral region, only a few points are required, but within strong absorption bands the number of points per channel can exceed 15. In general, the non-localized ILS requires more monochromatic spectral points per channel than an apodized ILS, but this is mitigated by the common spectral points selected for different channels, with the result that the total number of independent spectral points needed to model a non-localized ILS is only slightly larger than for a localized ILS. The numbers of points selected in the three CrIS bands are summarized in Table 10 through Table 12.

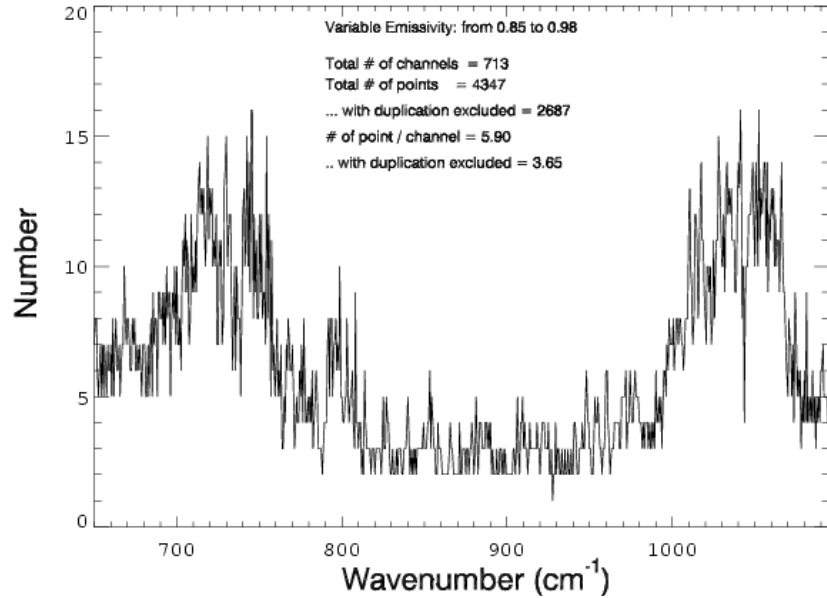


Figure 12: Number of spectral points per channel selected for *sinc* ILS in the LWIR band.

Table 10: Number of OSS Points in LWIR.

ILS	Number of Channels	Number of Points per Channel	Number of Points per Channel without Duplication
<i>Blackman</i>	713	4.97	3.34
<i>Hamming</i>		5.00	3.29
<i>sinc</i>		5.90	3.65

Table 11: Number of OSS Points in MWIR.

ILS	Number of Channels	Number of Points per Channel	Number of Points per Channel without Duplication
<i>Blackman</i>	433	5.63	3.77
<i>Hamming</i>		5.58	3.65
<i>sinc</i>		6.65	4.12

Table 12: Number of OSS Points in SWIR.

ILS	Number of Channels	Number of Points per Channel	Number of Points per Channel without Duplication
<i>Blackman</i>	159	5.33	3.69
<i>Hamming</i>		5.46	3.82
<i>sinc</i>		8.81	5.00

A set of 100 atmospheric profiles from the TIGR database (Chedin *et al.* 1985), which are independent of the profiles used in the OSS training process, has been used to validate the OSS model. The validation involves a comparison between radiances generated using the OSS model for these profiles at randomly selected scan angles and radiances obtained by convolving the appropriate ILS with the monochromatic radiances. To minimize the errors due to different radiative transfer schemes used by LBLRTM and by OSS, the monochromatic radiances are obtained by performing calculations using the OSS RT routine and using optical depths generated by LBLRTM. Figure 13 shows the RMS differences between the two sets of radiances for *sinc* ILS in LWIR (results for *Blackman* and *Hamming* are very similar). The errors in Figure 13 are smaller than the required accuracy threshold of 0.1 K, but for some channels within strong absorption bands this has only been achieved after an additional selection. Specifically, channels with validation errors larger than 0.1 K after the original training based on the 0.05-K threshold are re-trained using a lower threshold of 0.045 K. For channels that have RMS errors larger than 0.1 K after the 0.045-K selection, another selection is performed with a threshold of 0.04 K, etc. and the process is repeated until the validation errors for all channels are less 0.1 K. Since only a small number of channels exceed the 0.1-K threshold after the original selection, the overall number of points increases by less than 5% when the threshold is lowered in selected channels.

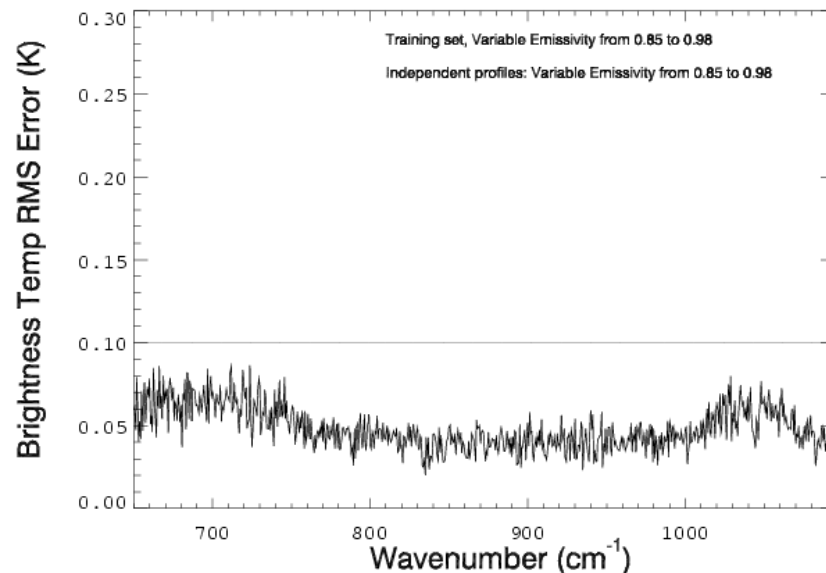


Figure 13: RMS differences between OSS-generated and true radiances for *sinc* ILS in LWIR.

Another approach to the validation of the OSS model utilizes the linear transformation between apodized and unapodized spectra described in Section 4.1.3. In this approach, the radiances for an apodized ILS are expressed using radiances computed for an unapodized ILS and compared with radiances computed directly for the apodized ILS. The RMS difference between the radiances generated using direct *Hamming* OSS coefficients and the radiances generated using the *sinc* to *Hamming* transformation is shown in Figure 14a. Similarly, the RMS difference between the radiances generated using direct *Blackman* OSS coefficients and the radiances generated using the *sinc* to *Blackman* transformation is shown in Figure 14b. The differences are about 0.05 K and this can be interpreted in two ways. If it is known (from an independent validation) that the OSS method for *sinc* is accurate to 0.05 K, then the results shown in Figure 14 validate the method for *Blackman* and *Hamming* (in general, the transformation errors are sensitive to the truncation of the side-lobes). Alternatively, if *Blackman* or *Hamming* are independently validated, then the results shown in Figure 14 validate the OSS selection for *sinc*. This validation approach is especially useful near the edges of the bands, where a direct validation such as that presented in Figure 13 can mask edge effects present in both OSS- and LBL-calculated radiances for a particular ILS function.

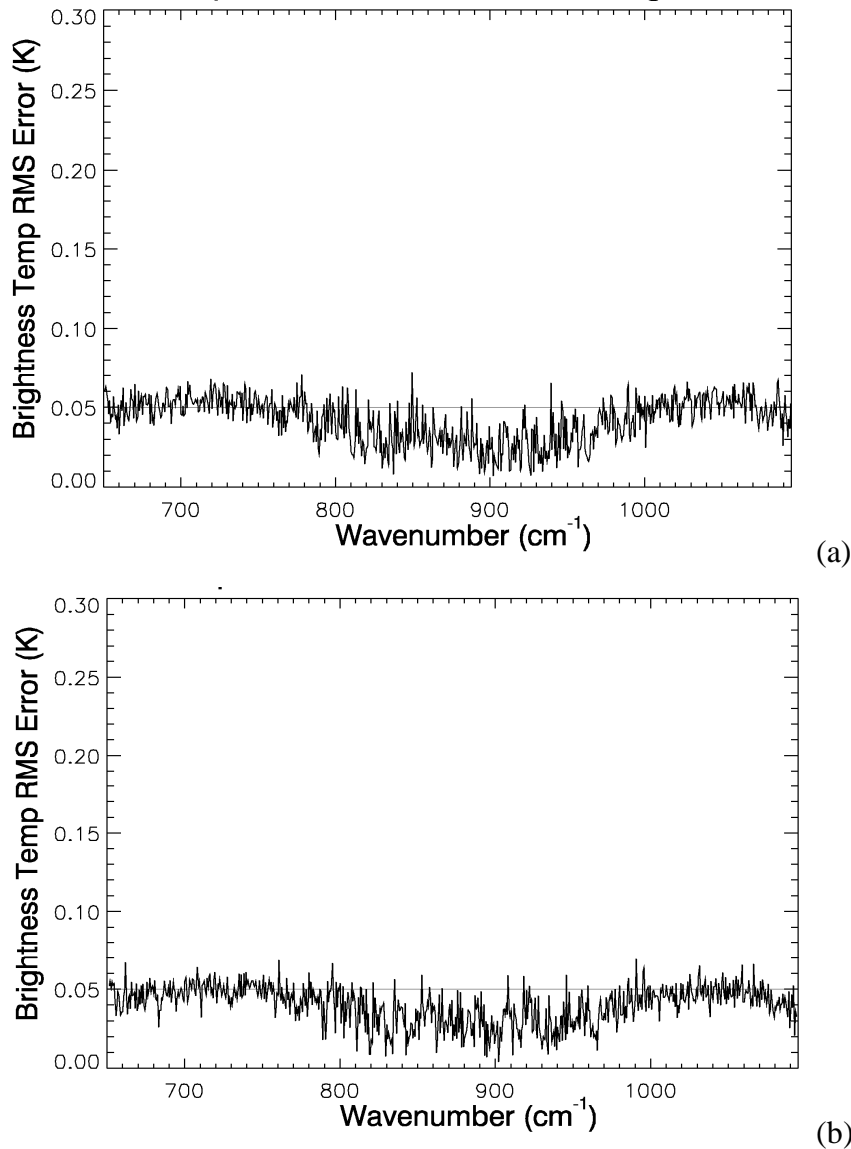


Figure 14: (a) The RMS difference between the radiances generated using direct *Hamming* OSS coefficients and the radiances generated using the *sinc* to *Hamming* transformation. (b) The RMS difference between the radiances generated using direct *Blackman* OSS coefficients and the radiances generated using the *sinc* to *Blackman* transformation

4.2.3.2 Microwave

In the microwave, the OSS forward model has been trained using the line-by-line radiative transfer model of Rosenkranz (1995). This model has a slightly different treatment of water continuum compared to that of LBLRTM in the microwave region and includes a complete

treatment of the Zeeman effect. However, the results presented in this section have been obtained without including this effect, with the impact of this omission discussed in Section 0. Since the sensor spectral response functions (SRFs) are localized, a sequential search method is used to perform the OSS selection.

As discussed in Section 3.2, initial algorithm studies were conducted for the AMSU/MHS channel set. Therefore we will start the description of MW OSS models from the AMSU/HSB instruments, although the current code will no longer be used to process such data. The following sections discuss the OSS forward model as it is applied to the characteristics of these sensor configurations.

4.2.3.2.1 OSS for AMSU/MHS Channels

The number of OSS points used in the modeling of AMSU and MHS radiances is given in Table 13. The average RMS error resulting from validation of the point selection using an independent set of profiles is 0.0135 K, which is much smaller than the 0.05 K threshold set in the selection process. It should be mentioned that the actual RMS errors resulting from the selection process using the training profiles are much smaller than the 0.05 K threshold because the instrument SRF is smaller than the spectral features. Consequently the spectral variations within the SRF are relatively small and 1 to 3 optimally selected monochromatic spectral points can represent the true radiances with very high accuracy. The total number of monochromatic points needed to model all 20 channels is 48 (2.4 points per channel).

Figure 15 compares brightness temperatures in the AMSU (1 to 15) and MHS (16 to 20) channels obtained with the OSS approach and the “central frequency” approximation with the “exact” calculations from Rosenkranz’s model.

Table 13: Number of Spectral Points Selected for AMSU/MHS.

Channel Number	Center Frequency (GHz)	Number of OSS Nodes	RMS
1	23.800	1	0.0009
2	31.400	1	0.0019
3	50.300	1	0.0060
4	52.800	3	0.0042
5	53.596	3	0.0049
6	54.400	3	0.0016
7	54.940	3	0.0263
8	55.500	3	0.0168
9	57.290	1	0.0188
10	57.290	3	0.0221
11	57.290	3	0.0310
12	57.290	3	0.0290
13	57.290	3	0.0258
14	57.290	3	0.0378
15	89.000	2	0.0006
16	89.000	2	0.0005
17	150.000	2	0.0025
18	183.310	2	0.0164
19	183.310	3	0.0066
20	183.310	3	0.0166

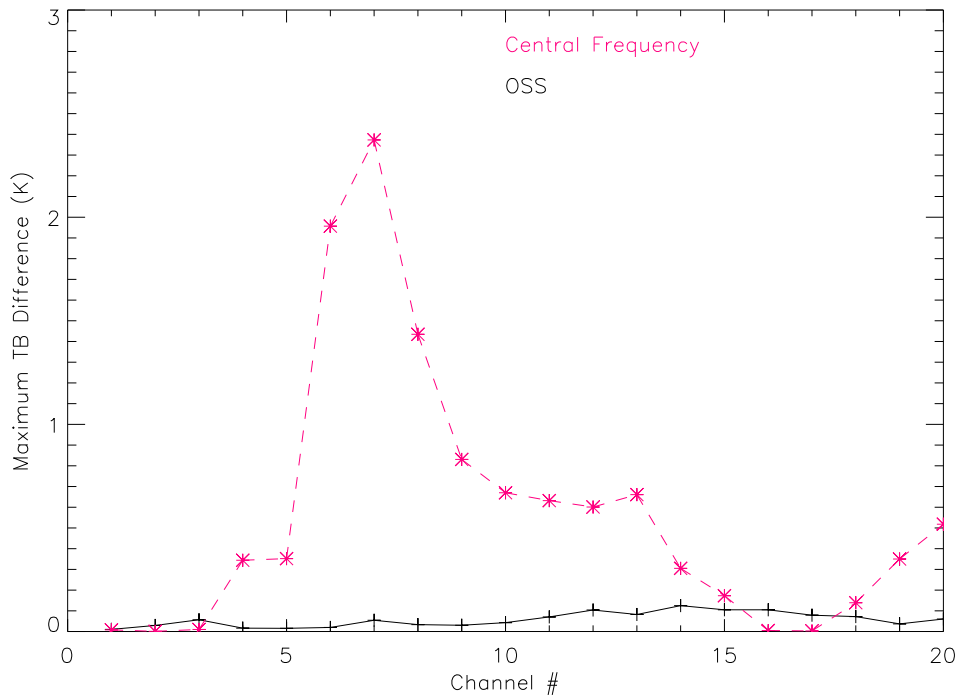


Figure 15: Comparison OSS/Central Frequency (Maximum Differences).

4.2.3.2.2 OSS for ATMS Channels

The number of OSS points used in the modeling of ATMS radiances is given in Table 14. The average RMS error resulting from validation of the point selection using an independent set of profiles similar to that of AMSU/MHS configuration described above. The total number of monochromatic points needed to model all 22 channels is 52, which results in the same number of average points needed to model on ATMS channel (i.e. 2.4 points/channel).

Table 14: Number of Spectral Points Selected for ATMS.

Channel Number	Center Frequency (GHz)	Number of OSS Nodes	RMS
1	23.800	1	0.0009
2	31.400	1	0.0019
3	50.300	1	0.0060
4	52.800	3	0.0167
5	51.760	3	0.0042
6	53.596	3	0.0049
7	54.400	3	0.0016
8	54.940	3	0.0263
9	55.500	1	0.0168
10	57.290	3	0.0188
11	57.290	3	0.0221
12	57.290	3	0.0310
13	57.290	3	0.0290
14	57.290	3	0.0255
15	57.290	2	0.0305
16	88.200	2	0.0009
17	165.50	1	0.0238
18	183.31±7	3	0.0166
19	183.31±4.5	3	0.0231
20	183.31±3	3	0.0066
21	183.31±1.8	4	0.0017
22	183.31±1	1	0.0389

4.2.4 Radiance Calculations

Important Note: Prior to Version 4.0 of the CrIMSS EDR algorithm, the forward model used a 40-level atmospheric profile on which to compute the radiative transfer. This was adequate for sensor sensor simulation studies but not for the application to “real” data. In addition, improvements were made to the way in which molecular absorption coefficients are stored and accessed for a particular atmospheric profile. These changes are discussed in Appendix F. Note that all trade studies and performance estimates discussed in this ATBD were conducted with the 40-level model unless noted specifically otherwise.

Computation of radiances and derivatives with the OSS method uses a generic recursive scheme developed for the modeling of upward, downward-looking and limb-viewing instruments and used in atmospheric retrievals from CIRRIS (Miller *et al.* 1999).

4.2.4.1 Optical Depth Tables

To compute transmittances and radiances, the OSS model makes use of pre-computed monochromatic layer optical depths for the relevant atmospheric gases at the frequency locations selected by the OSS method. The gases are split into two groups, those that have a fixed molecular amount and those that are variable. Because a single optical depth represents the fixed gases, this grouping reduces storage requirements for the optical depth tables. For each species, the optical depths are stored at a set of temperatures for each pressure layer used in the discrete radiative transfer model. For each layer this temperature range spans the temperatures expected for that layer based on the profiles in the TIGR and NOAA-88 databases.

The optical depth tables are calculated using the LBLRTM radiative transfer model along with the molecular amounts from the U.S. Standard Atmosphere profile (Anderson *et al.* 1986). Because of the formulation adopted for the water vapor continuum in the LBLRTM model (Clough *et al.* 1989), the method of optical depth calculation has been modified slightly for water vapor, since the self-broadened component of the water vapor continuum contains a quadratic dependence on the number density. As such the self-broadened component is separated from the water lines and the foreign-broadened component of the continuum. Absorption coefficients of

water vapor lines and foreign broadened continuum are grouped together in one table since they linearly depend on water partial pressure. A second table contains absorption coefficients of the self-broadened water vapor continuum.

For a given layer, each optical depth is linearly interpolated to the layer temperature. The correct optical depths for the variable species are then obtained by multiplying the temperature-interpolated optical depth by the ratio of the actual layer amount to the standard amount. This is equivalent to multiplying the species' molecular absorption coefficients by their molecular amounts. Of minimal impact, and thus neglected in the current formulation, is the difference in the self-broadened component of the water line shape between the standard density used to compute the stored optical depths and the actual layer density. This approximation will be eliminated in the next version of the forward model.

In the infrared, the total optical depth τ_l^o for layer l at nadir is computed as the sum of contributions from the fixed and variable gases

$$\tau_l^o = \tau_{\text{fix}}(\bar{p}_l, \Theta_l) + [k_{H_2O}(\bar{p}_l, \Theta_l) + k_{H_2O}^{\text{self}}(q_{H_2O}, \Theta_l)\omega_{H_2O}] \omega_{H_2O} + k_{O_3}(\bar{p}_l, \Theta_l)\omega_{O_3} + \tau_{CH_4}(\bar{p}_l, \Theta_l) + \tau_{CO}(\bar{p}_l, \Theta_l) + \tau_{N_2O}(\bar{p}_l, \Theta_l) \quad (0.20)$$

where κ is the absorption coefficient, ω is the absorber amount, p is the layer pressure, and Θ is the temperature. The current set of optical depths is stored at selected monochromatic spectral points for 39 pressure layers and 10 temperatures. Linear interpolation is performed to obtain optical depth for a given atmospheric temperature for each pressure level. The interpolation error decreases as the number of temperature tabulations increases. As mentioned before, increasing the number of temperature entries in the lookup table will not increase the computational time of the forward model. It only requires more memory allocation to store these optical depths.

The optical depth tables in the microwave are structured in a similar way as in the IR, with minor differences because of the nature of the microwave spectrum. The total optical depth is computed for each layer l at nadir as

$$\tau_l^0 = \tau_{O_2+N_2}(\bar{p}_l, \Theta_l, \omega_{H_2O}) + \tau_{H_2O}(\bar{p}_l, \Theta_l, \omega_{H_2O}) \quad (0.21)$$

where the variables are defined as in the infrared equation given above. A bilinear interpolation in both temperature and moisture is performed for each pressure level to obtain optical depth at a given temperature and moisture. The microwave optical depths are computed using the model of Rosenkranz (1995) and are tabulated as functions of temperature and water vapor. Simulation studies indicate that 20 temperature and water vapor interpolation points are required for an accurate OSS representation under a wide variety of atmospheric conditions.

The optical depths along the slant path for downward and upward directions are defined as

$$\tau_l^d = \tau_l^0 \sec \theta_d \quad (0.22)$$

$$\tau_l^u = \tau_l^0 \sec \theta_{obs} \quad (0.23)$$

where θ_d and θ_{obs} are downward slant angle and scan zenith angle, respectively.

4.2.4.2 Radiance and Derivative Calculation

Figure 16 defines the numbering conventions for the layered atmosphere. T_l and T_l^* denote the transmittances from space to level l and from surface to level l , respectively. They are defined as

$$T_l = \exp\left(-\sum_{i=1}^l \tau_i^0 \sec \theta_{obs}\right) \quad (0.24)$$

$$T_l^* = \exp\left(-\sum_{i=l+1}^N \tau_i^0 \sec \theta_d\right) \quad (0.25)$$

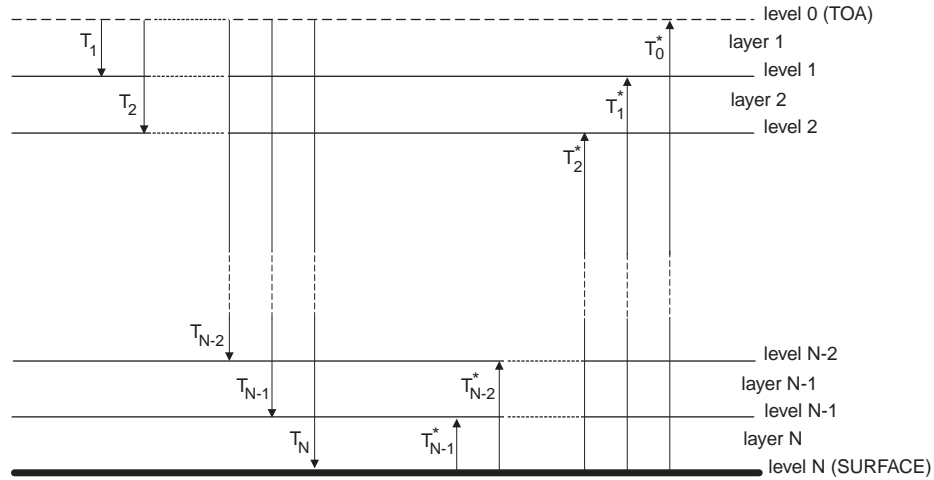


Figure 16: Numbering convention for the atmospheric layers used by OSS.

Radiances R in clear conditions are computed using the following expression derived by discretizing the radiative transfer equation [Equation (0.14) and Equation (0.16)]

$$R_{\nu} = \sum_{i=1}^N (T_{\nu,i-1} - T_{\nu,i}) B_{\nu,i}^{+} + \varepsilon_{\nu s} T_{\nu,N} B_{\nu,s}^{+} + (1 - \varepsilon_{\nu s}) T_{\nu,N} \sum_{i=1}^N (T_{\nu,i}^{*} - T_{\nu,i-1}^{*}) B_{\nu,i}^{-} \quad (0.26)$$

where B_{ν}^{\pm} represents the upward and downward Planck emission of the layer/surface and $\varepsilon_{\nu s}$ is the surface emissivity. For MW, the following term is added to (0.26)

$$R_{\cos} = (1 - \varepsilon_{\nu}) T_N^2 \Theta_c \quad (0.27)$$

where Θ_c is the cosmic background, while for daytime IR, the following term is added to (0.26)

$$R_{sol} = \rho_s T_N F_0 \cos \theta_{sun} \exp\left(-\sum_l \tau_l^0 \sec \theta_{sun}\right). \quad (0.28)$$

Derivatives of R_{ν} with respect to constituent concentrations and temperature in layer l (generally named X_l) are obtained by differentiating the previous equations using the following relations

$$\frac{\partial R}{\partial X_l} = \frac{\partial R}{\partial \tau_l^0} \frac{\partial \tau_l^0}{\partial X_l} + \frac{\partial R}{\partial B_l} \frac{\partial B_l}{\partial X_l}$$

$$\frac{\partial T_i}{\partial \tau_l^0} = \begin{cases} -T_i \sec \theta_{obs} & i \geq l \\ 0 & i < l \end{cases} \quad (0.29)$$

$$\frac{\partial T_i^*}{\partial \tau_l^0} = \begin{cases} -T_i^* \sec \theta_d & i \leq l \\ 0 & i > l \end{cases}$$

$$\begin{aligned} \frac{\partial R}{\partial X_l} = & -\frac{\partial \tau_l^0}{\partial X_l} \left\{ \left[-T_l B_l^+ + \sum_{i=l+1}^N (T_{i-1} - T_i) B_i^+ + T_N \varepsilon_s B_s^+ + (1 - \varepsilon_s) T_N \sum_{i=1}^N (T_i^* - T_{i-1}^*) B_i^- \right] \sec \theta_{obs} \right. \\ & \left. + \left[-(1 - \varepsilon_s) T_N T_{l-1}^* B_l^- + (1 - \varepsilon_s) T_N \sum_{i=1}^{l-1} (T_i^* - T_{i-1}^*) B_i^- \right] \sec \theta_d \right\} \\ & + \frac{\partial B_l^+}{\partial X_l} (T_{l-1} - T_l) + (1 - \varepsilon_s) T_N \frac{\partial B_l^-}{\partial X_l} (T_l^* - T_{l-1}^*) \end{aligned} \quad (0.30)$$

or, by introducing the two-path attenuation from level l to space, $T'_l = (1 - \varepsilon_s) T_N T_l^*$

$$\begin{aligned} \frac{\partial R}{\partial X_l} = & -\frac{\partial \tau_l^0}{\partial X_l} \left\{ \left[-T_l B_l^+ + \sum_{i=l+1}^N (T_{i-1} - T_i) B_i^+ + T_N \varepsilon_s B_s^+ + \sum_{i=1}^N (T'_i - T'_{i-1}) B_i^- \right] \sec \theta_{obs} \right. \\ & \left. + \left[-T'_{l-1} B_l^- + \sum_{i=1}^{l-1} (T'_i - T'_{i-1}) B_i^- \right] \sec \theta_d \right\} + \frac{\partial B_l^+}{\partial X_l} (T_{l-1} - T_l) + \frac{\partial B_l^-}{\partial X_l} (T'_l - T'_{l-1}) \end{aligned} \quad (0.31)$$

where X_l stands for either Θ_l or ω_l^m .

The partial derivatives of cosmic background and solar contribution should to added to the $\partial R / \partial \tau_l^0$ term

$$\frac{\partial R_{cos}}{\partial \tau_l^0} = -2 * (1 - \varepsilon_v) T_N^2 \Theta_c^* \sec \theta_{obs} \quad (0.32)$$

$$\frac{\partial R_{sol}}{\partial \tau_l^0} = -(\sec \theta_{obs} + \sec \theta_{sun}) R_{sol} \cdot \quad (0.33)$$

With the exception of the handling of the surface terms, the recursive procedure for the integration of the RTE and the calculation of derivatives over a reflective surface is similar to the one used for limb viewing. This procedure uses the fact that a perturbation in temperature or constituent concentration in any given layer of the atmosphere does not affect the emission in the atmospheric slab comprised between this layer and the observer. Therefore, derivatives can be obtained at low cost if the RTE is integrated by adding layers sequentially in the direction of the observer. The procedure is more apparent by introducing the quantities Σ_l^- and Σ_l^+ defined as the contribution to the observed radiance of the downward emission (reflected at the surface) from the atmosphere above level l and the contribution of the atmosphere below level l plus reflected downward radiation

$$\begin{aligned}\Sigma_l^- &= \sum_{i=1}^l (T'_i - T'_{i-1}) B_i^- \\ \Sigma_l^+ &= \sum_{i=l+1}^N (T_{i-1} - T_i) B_i^+ + \varepsilon_s T_N B_s + \sum_{i=1}^N (T'_i - T'_{i-1}) B_i^-\end{aligned}\quad (0.34)$$

Using these definitions, one can write

$$\begin{aligned}\frac{\partial R}{\partial X_l} &= \left[\frac{\partial R}{\partial X_l} \right]_d + \left[\frac{\partial R}{\partial X_l} \right]_u = \left[\frac{\partial \tau_l^d}{\partial X_l} (-\Sigma_{l-1}^- + B_l^- T'_{l-1}) + \frac{\partial B_l^-}{\partial X_l} (T'_l - T'_{l-1}) \right] \\ &+ \left[\frac{\partial \tau_l^u}{\partial X_l} (-\Sigma_l^+ + B_l^+ T_l) + \frac{\partial B_l^+}{\partial X_l} (T_{l-1} - T_l) \right]\end{aligned}\quad (0.35)$$

In the current version of the CrIMSS algorithm, the dependence of atmospheric transmittances on temperature is neglected in the calculations of derivatives in the infrared channels

$$\partial \tau_l^0 / \partial \Theta_l = 0 \quad . \quad (0.36)$$

This assumption is made for the sake of computational efficiency only and the code can handle the general case of $\partial \tau_l^0 / \partial \Theta_l \neq 0$ without difficulty (it should be noted that even with this extra term included, the computational cost of computing derivatives in the OSS model is always at

least an order of magnitude lower than in finite-difference methods). Another more critical approximation concerns the treatment of layer-averaged emission. In the current version of the code, the layer emission is computed using the Planck function evaluated at the density-weighted mean temperature $\bar{\Theta}$ for the layer

$$B_l^+ = B_l^- = B(\bar{\Theta}) \quad (0.37)$$

with the result that $\partial B_l / \partial \tau_l = 0$. The above approximation to the layer-mean Planck function is adequate as long as layers are not optically thick, e.g. vertical pressure grid is sufficiently fine and no cloud is present. A preliminary trade study has revealed that this approximation can produce occasional errors exceeding 0.5 K on the previously adopted 40-level grid (the errors are computed as radiance residuals relative to a reference calculation utilizing a 196-level grid). With the current 101 level grid, this number should be significantly reduces (ref the Upgrade on RTM section Figures 150 and 151).

4.2.4.3 Practical Implementation

In a first pass, at any given wavenumber, the algorithm computes the profile of transmittance from space. The recursive procedure for the computation of radiances and analytical derivatives is as follows:

1. Initialization: set $\Sigma_0^- = 0$.
2. If $(1 - \varepsilon_s)T_N > 10^{-4}$, add layers successively from TOA down to surface. Update Σ_l^- at each step and compute first part of radiance derivatives

$$\Sigma_l^- = \Sigma_{l-1}^- + (T_l' - T_{l-1}')\bar{B}_l \quad (0.38)$$

$$\left[\frac{\partial R}{\partial \tau_l} \right]_d = (-\Sigma_{l-1}^- + \bar{B}_l T_{l-1}') \sec \theta_d \quad (0.39)$$

$$\left[\frac{\partial R}{\partial \Theta_l} \right]_d = \frac{\partial \bar{B}_l}{\partial \Theta_l} (T_l' - T_{l-1}'). \quad (0.40)$$

3. Add surface term and compute derivatives with respect to skin temperature and surface emissivity

$$\Sigma_N^+ = \Sigma_N^- + T_N \varepsilon_s B_s \quad (0.41)$$

$$\frac{\partial R}{\partial \Theta_s} = T_N \varepsilon_s \frac{\partial B_s}{\partial \Theta_s} \quad (0.42)$$

$$\frac{\partial R}{\partial \varepsilon_s} = T_N B_s - \Sigma_N^- / (1 - \varepsilon_s) \quad (0.43)$$

$$\frac{\partial R}{\partial \rho_s} = T_N F_0 \cos \theta_{sun} \exp\left(-\sum_l \tau_l^0 \sec \theta_{sun}\right). \quad (0.44)$$

4. Update Σ_l^+ by adding layers from surface up to TOA and compute second part of derivatives

$$\Sigma_{l-1}^+ = \Sigma_l^+ + (T_{l-1} - T_l)\bar{B}_l \quad (0.45)$$

$$\frac{\partial R}{\partial \tau_l^0} = (-\Sigma_l^+ + \bar{B}_l T_l) \sec \theta_{obs} + \left[\frac{\partial R}{\partial \tau_l^0} \right]_d. \quad (0.46)$$

The solar and cosmic background should be added to Equation (0.46) when appropriate

$$\frac{\partial R}{\partial \Theta_l} = \frac{\partial \bar{B}_l}{\partial \Theta_l} (T_{l-1} - T_l) + \left[\frac{\partial R}{\partial \Theta_l} \right]_d. \quad (0.47)$$

5. Set $R_v = \Sigma_0^+$ and compute derivatives with respect to temperature and layer amounts for all molecular species

$$\frac{\partial R}{\partial \omega_l^m} = \frac{\partial R}{\partial \tau_l^0} \times k_l^m, \quad m = 1, \dots, M. \quad (0.48)$$

6. Background terms. In the microwave, the cosmic background is computed according to Equation (0.27). The solar contribution to the observed radiance is computed according to Equation (0.28).

4.2.4.4 Treatment of the Planck Function

The exponential calculation involved in the computation of the Planck function has an adverse effect on the computational efficiency of the OSS forward model. For apodized ILS functions, the major contributions are confined to a relatively narrow frequency range; therefore the Planck function for all the monochromatic points related to a particular channel can be approximated using a Planck function calculated at the channel-central-frequency. However, this approximation is inadequate for the unapodized ILS since the ILS extends to the edges of the

CrIS spectral bands. The Planck functions at each selected monochromatic frequencies have to be calculated. Tabulating the Planck functions is one way of saving computational time in the radiance calculation. The tabulation is performed at a set of N_T temperatures and N_F frequencies, resulting in an $N_T \times N_F$ array. The values of the Planck function at a given temperature and frequency are then obtained by a bilinear interpolation of the tabulated values. The accuracy of this approach has been tested for temperatures between 150 and 350 K and frequencies between 500 and 4000 cm^{-1} . In Figure 17, the tabulation error is plotted as a function of N_T and N_F . The error drops below 0.01 K for a 400 x 400 tabulation, which corresponds to an array with the size of 640 Kbytes. As shown in Figure 18, the maximum error occurs either at the highest or the lowest frequency, depending on temperature. Pre-computing the Planck function at the OSS frequencies and performing interpolation in temperature only could achieve a somewhat more accurate tabulation, but with several thousand spectral points. The memory requirements in this case would exceed 10 Mbytes for a similar accuracy threshold.

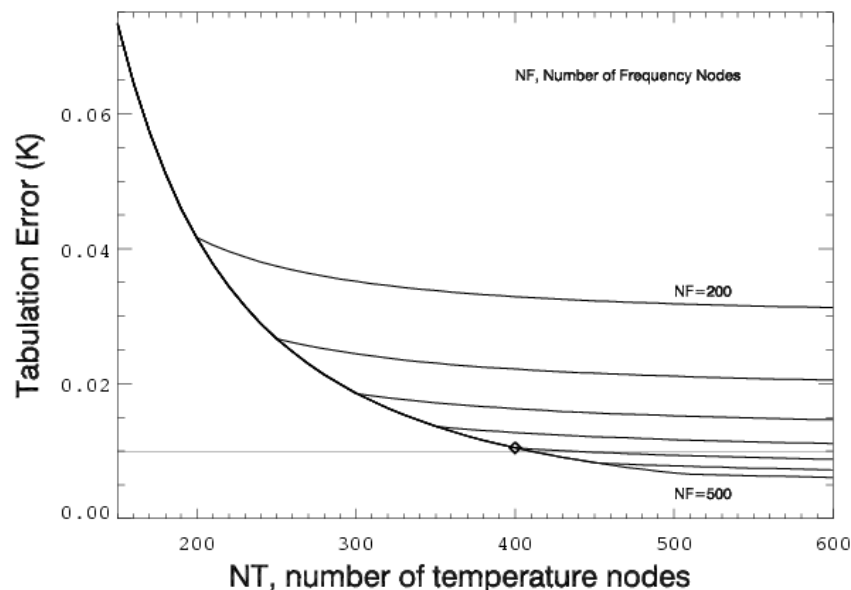


Figure 17: Planck function tabulation error as a function of the number of temperature nodes in the tabulation array. The curves are labeled by the number of frequency nodes (in intervals of 50). The diamond marks the point where the tabulation error drops below 0.01 K.

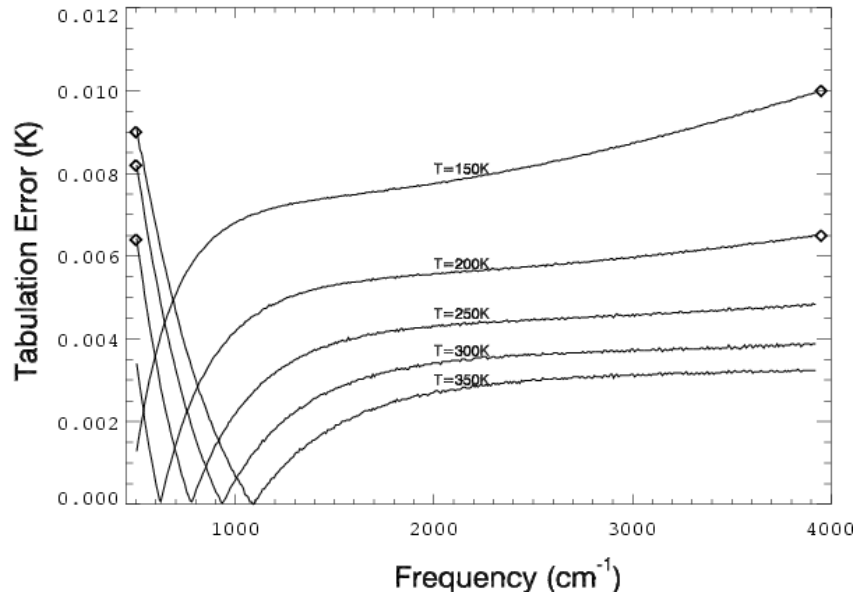


Figure 18: Absolute value of tabulation error as a function of frequency at selected temperatures between 150 and 350 K for the diamond point in Figure 17. The diamonds in this figure mark the maximum errors at each temperature.

4.2.4.5 Treatment of Clouds

4.2.4.5.1 Microwave

Cloud optical depths in the microwave are represented at the central frequency for each channel by two parameters, total liquid water Q and top pressure p_t , and they are computed as the sum of optical depths in each atmospheric layer. The cloud optical depths τ_{ij} for frequency index i and layer j are given as:

$$\tau_{ij} = Q k_{ci}(\bar{\Theta}_j^c) f \frac{\Delta_j}{\Delta} \quad (0.49)$$

where k_{ci} is the mass absorption coefficient for liquid water, $\bar{\Theta}_j^c$ is the average temperature of the cloud within layer j , and f is the cloud fraction within the FOR. The cloud proportion in layer j is equal to $\frac{\Delta_j}{\Delta}$, where Δ_j is the cloud thickness in layer j and Δ is the total cloud thickness (such that the cloud base pressure $p_b = p_t + \Delta$). If the entire cloud depth is within layer j , then $\Delta_j = \Delta$.

The absorption coefficients are computed from the model of Liebe *et al.* (1991) using an exponential formulation for the primary relaxation frequency dependence on temperature:

$$\gamma_1 = 20.1 \exp(7.88\theta), \quad \theta = 1 - \frac{300 \text{ K}}{T}. \quad (0.50)$$

Derivatives of cloud optical depth with respect to total cloud liquid and cloud-top are obtained from

$$\begin{aligned} \frac{\partial \tau_{ij}}{\partial Q} &= k_{ci}(\bar{\Theta}_j^c) f \frac{\Delta_j}{\Delta} \\ \frac{\partial \tau_{ij}}{\partial p_t} &= Q k_{ci}(\bar{\Theta}_j^c) f \frac{1}{\Delta} \frac{\partial \Delta_j}{\partial p_t}. \end{aligned} \quad (0.51)$$

Derivatives of TOA radiance with respect to total cloud liquid and cloud-top are obtained by multiplying the quantities in Equation (0.51) with $\partial R / \partial \tau_l$ in Equation (0.46) [note that τ_l in Equation (0.46) omits the frequency index i and the index l is equivalent to j in Equation (0.51)].

4.2.4.5.2 Infrared

As described in Section 5.2, the method adopted in the current code for the treatment of clouds in the IR is cloud-clearing and this does not require the modeling of cloud properties. Under overcast conditions, the CrIMSS performs clear-sky retrievals above clouds using a subset of CrIS channels determined by the CrIMSS algorithm. MW channels are included in the joint IR+MW retrieval to provide retrievals below clouds.

4.3 Inverse Model

A flowchart for the inversion is shown in Figure 19. It outlines the procedures used in an inversion process. It usually starts with some initial guess of the retrieved parameters. These parameters, along with other known information such as scan geometry, solar zenith angle, and surface pressure, are used by the forward model to generate a radiance estimate. The inversion algorithm adjusts the retrieved parameters so that the observed radiances are best fitted by the

forward model calculated radiances. If the fit is within instrument noise level, the iteration process stops, otherwise a new radiance estimate is calculated and the iteration proceeds. This section provides a theoretical basis of the inversion algorithm, while the practical implementation of MW-only and MW+IR inversions are discussed in Sections 5.3 and 5.5, respectively.

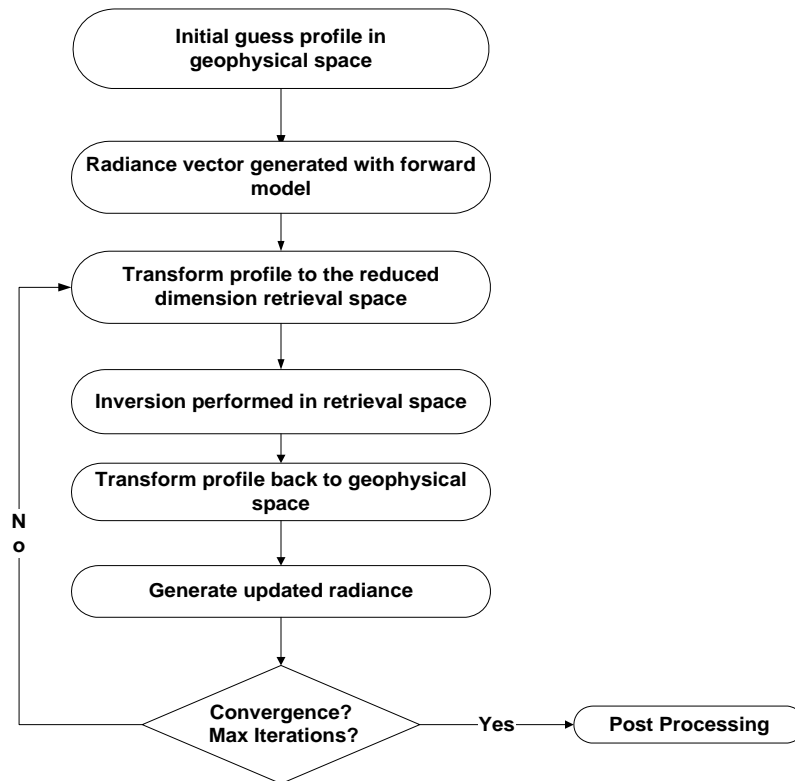


Figure 19: Inversion flowchart.

The inversion methodology adopted for both microwave and infrared is based on a constrained non-linear least squares approach (e.g., Rogers 1976). The solution to the inverse problem is found by minimizing a cost function of the form

$$\phi(x) = \|y_o - F(x) - \delta y\|^2 + g(x) \quad (0.52)$$

where the first term is the error associated with the unconstrained solution and the second term is the penalty function that is used to constrain the solution. The vectors y_o and $F(x)$ represent observed radiances and radiances calculated using the forward model, respectively. The value δy

is an empirical bias correction that is applied to the difference between observed and computed radiances – this will be discussed at the end of the section. If both the state vector and the radiances are characterized by Gaussian distributions, then the cost function has the form

$$\phi(x) = [y_o - F(x) - \partial y]^T S_y^{-1} [y_o - F(x) - \partial y] + (x - x_a)^T S_x^{-1} (x - x_a) \quad (0.53)$$

where S_y is an error covariance matrix describing the measurement and other errors and x_a and S_x are the background (*a priori*) vector and the associated error covariance matrix, respectively. An iterative solution to the inverse problem can be obtained by minimizing this cost function via a Gauss-Newton method. When the second derivative of $F(x)$ is neglected, the solution x_{i+1} at the $(i+1)^{\text{th}}$ iteration, given the solution x_i at the i^{th} iteration, is equal to

$$x_{i+1} = x_a + (K_i^T S_y^{-1} K_i + S_x^{-1})^{-1} K_i^T S_y^{-1} [y_o - y_i - \partial y + K_i (x_i - x_a)] \quad (0.54)$$

where y_i is the current value of $F(x)$ linearized about x_a and K_i is the matrix containing partial derivatives of y_i with respect to x . This form of solution for the state vector is used in the joint microwave and infrared retrieval. For the microwave-only retrieval, in which the number of retrieved variables exceeds the number of channels, an equivalent form is employed in order to accelerate the solution

$$x_{i+1} = x_a + S_x K_i^T (K_i S_x K_i^T + S_y)^{-1} [y_o - y_i - \partial y + K_i (x_i - x_a)]. \quad (0.55)$$

The need for an *a priori* constraint relates to the fact that the inversion problem is generally ill-conditioned, e.g. the existence of null-space of the observing system leads to a non-uniqueness of solution. The use of *a priori* information, when available, ensures that the derived solution is physically acceptable. This information may be used to stabilize the solution and control the step size. The background covariance constraint introduces inter-level correlation in the temperature and moisture profiles, which prevents the solution from being unstable, particularly in the microwave-only retrieval. There are some concerns that if the constraint is biased, it will introduce errors into the solution. To ensure a successful retrieval, the covariance must be derived from a large ensemble of independent measurements that describe large variability in the

state parameters. For atmospheric temperature and moisture profiles, S_x is derived from global radiosonde and rocketsonde measurements that meet the variability requirement. For parameters without complete statistical *a priori* information, no correlations are included in the S_x . For the joint MW+IR retrieval, there is more information due to the increase in the number of channels, and consequently the solution is much less dependent on the *a priori* information.\

During post-launch testing it was determined that the skin temperature constraint (departure from air temperature, $T_{air}-T_{skin}$) during daytime was too tight over land cases. The prior covariance for daytime cases over land (land fraction > 0.1) overrides the value set in the covariance LUT and is set to 5.0.

The empirical bias correction term, δy , is required for all infrared and microwave channels. For CrIS pre-launch this term was derived from proxy data derived from the Metop/IASI instrument and for ATMS this term was set to zero. Post-launch the bias correction (a.k.a. tuning) was computed from an ensemble of scenes co-located to ECMWF forecast fields. For CrIS an ensemble of clear, ocean, night, scenes within ± 60 degrees latitude were chosen for May 15, 2012 and $\delta y = \text{average}\{y_0 - F(x)\}$, where x is an estimate of the state derived from ECMWF state, trace gas climatologies, and results from un-tuned retrievals. This is the same methodology that has been done for AIRS and IASI. For CrIS a single value is derived for each channel – that is, δy is a vector of 1305 values. For ATMS a similar process is performed for all non-precipitating ocean, night, scenes within ± 60 degrees latitude for May 15, 2012. For ATMS there is a large view-angle dependence to the empirical bias correction so biases were derived for all 22 channels at each view angle, therefore, there are 22x30 values. For both ATMS and CrIS there is no evidence that this bias correction changes with time. This was determined by comparisons of May 15, 2012 and Sep. 20, 2012 focus days. The methodology is discussed in a AMS paper by Changyi Tan et al (Poster #438, 93rd AMS annual meeting, 6-10 Jan. 2013, Austin Texas) and a peer-reviewed paper is in preparation to discuss the methodology in detail.

4.3.1 Linearization Noise

A major shortcoming of the standard Gauss-Newton procedure is that it does not account for errors due to linearization. In high-resolution spectra, these errors have high frequency structures, which resemble pseudo-random noise. Ignoring these errors degrades the rate of convergence when the problem is highly non-linear or when the first-guess is far away from the solution. It is implied that the “best” solution is one that fits the observation within the model noise, i.e., it ignores the fact that the linear model cannot fit the observation better than

$$\varepsilon_{NL}(x) = F(x) - F(x_0) - K(x - x_0). \quad (0.56)$$

There are two consequences of failing to take $\varepsilon_{NL}(x)$ into account:

- For univariate problems there is a risk of overshooting, which may slow down convergence.
- For multivariate optimization problems, where conditioning is marginal, it destabilizes the solution by giving too much weight to the unconstrained solution. This tends to overfit the radiances and to introduce spurious structures in the solution vector due to amplification of non-linear noise (e.g., for cloud parameters, these spurious structures move the result further away from the actual solution and convergence may never be reached).

An acceptable solution for a certain class of multivariate optimization problems (such as atmospheric profiling) is to reduce the dimension of the state vector at the beginning of the iterative process and increase it progressively as the solution approaches the truth. This avoids the problem of noise amplification. Such a method has been successfully applied to ozone profiling (Snell *et al.* 1999). However, this procedure is not applicable for loosely correlated parameters such as cloud optical depth and cloud-top altitude. For such problems, ill-conditioning can be avoided by estimating the linearization error from the radiance residuals.

4.3.2 Non-Linear Inversion Method

The maximum likelihood method, which is essentially the inverse Hessian method, attempts to minimize the errors in the measurement space based on the assumption that the cost function is quadratic (Press *et al.* 1992, Clough *et al.* 1995). When x is far away from the solution, or $F(x)$

is very non-linear, the quadratic cost function may be a poor local approximation. In this case, the inversion may be unstable if the solution step is too large.

The standard Levenberg-Marquardt (L-M) algorithm (Levenberg 1944, Marquardt 1963) uses a control parameter λ to choose between the inverse Hessian algorithm when the error is approximately quadratic and a more conservative approach, the steepest descent method, when the error is non-linear in nature. We have implemented this technique, in combination with the maximum likelihood (ML), to test our retrieval algorithm. L-M is an improvement over the ML approach when the initial guess is far away from the solution. However, it is hard to find an optimal initial value and step size for λ which are applicable for all atmospheric conditions, since their values depend on the solution.

An *ad hoc* method has been devised based on extensive retrieval simulations. It attempts to use information about the problem (e.g. the degree of non-linearity) in combination with the radiance residual (used as a measure of the distance from the truth) to provide an estimate of $\varepsilon_{NL}(x)$. In this approach, the diagonal elements of the error covariance matrix are set to either some fraction of the error in the observed space (i.e., the difference between y_i and y_o) or to the noise variance

$$S_y(j, j) = \max \left\{ \frac{1}{\alpha} [y_i(j) - y_o(j)]^2, \sigma^2(j) \right\} \quad (0.57)$$

where α is the error control parameter and $\sigma^2(j)$ is the instrument noise variance for the j^{th} channel. The role of α is to limit the magnitude of Δx at each iteration step. The parameter α is relatively insensitive to the initial guess, with typical values ranging between 4 (for highly non-linear problems) and 100 (tends toward the ML result).

A comparison of the convergence characteristics of the above non-linear inversion algorithm (referred to as “DRAD”) with the L-M and ML methods demonstrates an overall superior performance for the DRAD method (see Section 7.1). The most noticeable improvement is achieved when the initial guess for each algorithm is based on climatology. Furthermore, cloud parameters affect the radiative transfer equation in a highly non-linear way and the DRAD

method is capable of simultaneously solving for cloud parameters and atmospheric/surface parameters. This is an important consideration in selecting an appropriate inversion technique for an operational algorithm.

4.3.3 Inversion of Apodized Spectra

As discussed in Section 4.1.3, cosine-apodized radiances and derivatives can be obtained through a linear transformation of their unapodized counterparts

$$\begin{aligned} y_{apod} &= A \cdot y_{Sinc} \\ K_{apod} &= A \cdot K_{Sinc} \\ K_{apod}^T &= K_{Sinc}^T \cdot A \end{aligned} \quad (0.58)$$

where A is symmetric matrix. The fact that the state vector x and the background covariance matrix S_x are invariant under this transformation allows us to infer the transformational properties of the measurement error covariance matrix. This can be illustrated by rewriting Equation (0.54) in the following equivalent form

$$x_{i+1} = x_a + [K_i^T A(A^{-1}S_y^{-1}A^{-1})AK_i + S_x^{-1}]^{-1} K_i^T A(A^{-1}S_y^{-1}A^{-1})[Ay_0 - Ay_i - AK_i(x_a - x_i)]. \quad (0.59)$$

From this form it is clear that for the state vector to remain invariant under the transformation from unapodized to apodized radiances, the following transformation must be applied to the error covariance matrix

$$S_y \rightarrow AS_yA. \quad (0.60)$$

Equation (0.59) indicates that the solution is left unchanged when an apodization is applied to an unapodized radiance spectrum. This conclusion is consistent with studies by Amato *et al.* (1998) and Barnet *et al.* (2000). Amato *et al.* proved analytically that the covariance matrix of the solution is left unchanged under apodization, while Barnet *et al.* derived the equivalence of solution using a regression retrieval formula.

In the unapodized case, the error covariance matrix S_y is *diagonal*, with the i^{th} channel component equal to the noise variance $\sigma^2(i)$. For the *Hamming* apodization, the only non-zero elements of A are $A(i, i) = 0.54$, $A(i \pm 1, i) = 0.23$ and under the transformation given by Equation (0.60), the only non-zero elements of S_y are

$$\begin{aligned}
S_y(i, i) &\rightarrow A(i, i) \cdot S_y(i, i) \cdot A(i, i) \\
&\quad + \sum_{k=\pm 1} A(i, i+k) \cdot S_y(i+k, i+k) \cdot A(i+k, i) \\
&= 0.2916 \cdot \sigma^2(i) + 0.0529 \cdot (\sigma^2(i-1) + \sigma^2(i+1)) \\
S_y(i, i+1) &\rightarrow A(i, i+1) \cdot S_y(i+1, i+1) \cdot A(i+1, i+1) \\
&\quad + A(i, i) \cdot S_y(i, i) \cdot A(i, i+1) \\
&= 0.1242 \cdot (\sigma^2(i) + \sigma^2(i+1)) \\
S_y(i-1, i+1) &\rightarrow A(i-1, i) \cdot S_y(i, i) \cdot A(i, i+1) \\
&= 0.0529 \cdot \sigma^2(i)
\end{aligned} \tag{0.61}$$

plus analogous expressions for the symmetrical elements. All elements beyond the main, the nearest neighbor, and the next nearest neighbor diagonals are zero. For the *Blackman* apodization, the non-zero components of A are $A(i, i) = 0.42$, $A(i \pm 1, i) = 0.25$, $A(i \pm 2, i) = 0.04$. In this case the error covariance matrix contains non-zero elements up to $S_y(i \pm 2, i \pm 2)$. We note that the formulas for the inter-channel correlation (i.e., the off-diagonal elements of S_y) obtained from Equation (0.60) are a generalization of Equation (47) in Barnett *et al.* (2000), to which they reduce when $\sigma^2(i) = \text{constant}$ (i.e., the instrument noise is the same for all channels). We further note that, in general, the diagonal elements $S_y(i, i)$ of the error covariance matrix for an apodized ILS are reduced compared with the diagonal elements $\sigma^2(i)$ in the unapodized case.

Results from a trade study on the impact of apodization on retrieval accuracy and timing are presented in Section 0.

4.3.4 Eigenvector Transformation of Retrieved Parameters

Important Note: As discussed in Appendix F, initial versions of the forward model for both the simulation and retrieval modules used a 40-level grid. In Version 4.0 this was increased to 101 levels, and accordingly, the EOFs, backgrounds and covarainces are derived for the 101 level atmospheric profiles. In addition, NGAS has compiled a large diversified training dataset to estimate these parameters. This dataset combines NWP models (including NCEP and ECMWF), in-situ data (NOAA88), and climatological databases (UARS and CIRA86), and is believed to represent the natural variability in the real world better than any of the single data source alone. Therefore, the following discussion, which is based on a 40-level pressure grid and the NOAA88 dataset, should be viewed with caution. But it is still valid in describing how this approach works and how the retrieved products may be affected.

Several methods to reduce the dimensionality of the inverse problem (and thus stabilize the solution) have been proposed in the literature (Pseudo Inverse, Single Value Decomposition). In the CrIMSS algorithm, this is achieved by projecting the state vector onto a set of pre-computed Empirical Orthogonal Functions (EOFs). The EOFs are obtained by applying principal component analysis (PCA) to a background covariance matrix derived from a large ensemble of temperature and moisture profiles representative of global climatology. The two main purposes of transforming x into the EOFs domain are: 1. Eliminating EOFs with small eigenvalues in order to stabilize the solution, and 2. Reducing the number of retrieved parameters (and thus reducing the time needed for inversion).

It should be noted that the background covariance matrix for moisture is ill-conditioned in the upper troposphere and the stratosphere, owing to the lack of measurements above 300 mb. Moreover, this problem becomes worse as the number of vertical levels increases, because inter-level correlation increases with increasing number of levels. The PCA approach avoids these complications. The number of retained EOFs is dependent on the noise and the information content of the sensor. As shown below, with the proper choice of the EOF training set,

temperature, moisture and ozone profiles can be represented accurately by 20, 10 and 7 EOFs, respectively.

The iterative equation is not changed by the EOF transformation. Before the inversion, $\Delta x = x_{i+1} - x_i$ and K_i are transformed into the EOF domain according to the following equations:

$$\begin{aligned}\Delta \tilde{x} &= U^T \Delta x \\ \tilde{K}_i &= K_i U\end{aligned}\quad (0.62)$$

where U is a matrix which contains only the significant EOFs and the vector $u^T x$ represents the projection coefficients of state vector onto the EOFs. The transformation of S_x is given by

$$\Lambda = U^T S_x U \quad (0.63)$$

where Λ is a diagonal matrix whose elements are equal to the eigenvalues of S_x . For the joint microwave and infrared retrieval, the transformed retrieval equation reads

$$\Delta \tilde{x}_{i+1} = (\tilde{K}_i^T S_y^{-1} \tilde{K}_i + \Lambda^{-1})^{-1} \tilde{K}_i^T S_y^{-1} (y_0 - y_i + \tilde{K}_i \Delta \tilde{x}_i) \quad (0.64)$$

whereas for the microwave-only retrieval it has the form

$$\Delta \tilde{x}_{i+1} = \Lambda \tilde{K}_i^T (\tilde{K}_i \Lambda \tilde{K}_i^T + S_y)^{-1} (y_0 - y_i + \tilde{K}_i \Delta \tilde{x}_i). \quad (0.65)$$

The EOFs for the temperature and moisture profiles can be obtained by performing PCA on the error covariance matrix derived from 7547 profiles in the NOAA-88 database. Figure 20 shows the first 6 EOFs for temperature. The first eigenvector represents the deviation of average coarse structure from the mean temperature profile. As the eigenvalues associated with each EOF decrease, the eigenvectors exhibit more detailed structure and their contributions to the reconstructed profiles decrease. In our implementation, the original profiles are reconstructed by adding the mean profile to the linearly combined EOFs. The accuracy of the reconstructed profiles depends on the number of selected EOFs. Figure 21 shows the mean error and standard deviation for the 7547 profiles represented using 20 EOFs. With 20 EOFs, the original profiles

can be reconstructed to better than 0.8 K at all pressure levels. Note that in Figure 21 the standard deviation is calculated at each pressure level. As shown in Figure 22, the error is smaller than 0.4 K at most altitudes when the layers are averaged according to EDR reporting requirements.

Figure 23 is a typical plot of the original and reconstructed temperature profiles. The differences appear on small vertical scales, with the result that the differences in radiances calculated using the original and reconstructed profiles are smaller than instrument noise. This indicates that at CrIS spectral resolution, the measurement is not sensitive to fine vertical structures. In order to validate the adequacy of the derived EOFs to represent independent temperature profiles, we applied twenty NOAA-88 based eigenvectors to represent 1761 temperature profiles in the TIGR database (see Figure 24). The error pattern is very similar to that in Figure 21, except above 30 mb. This is because both NOAA-88 and the TIGR data set have very limited measurements above 30 mb and they employ different extrapolation methods to generate profiles above 30 mb.

The moisture values vary by orders of magnitudes between surface and 100 mb, therefore the PCA is performed on the natural logarithm of moisture profiles. Figure 25 shows the first 6 EOFs for moisture profiles. Figure 26 shows the mean errors and standard deviation when the NOAA-88 moisture profiles are represented by 10 EOFs. The RMS error is less than 8% for most levels between 1000 to 10 mb. Figure 27 shows that for layer averaged profiles the errors are less than 3% in the region 1000 mb to 100 mb. Figure 28 again illustrates the small scale errors in the reconstruction for an individual profile, which cannot be resolved by the CrIMSS instrument. Similar to the validation discussed above for temperature, the NOAA-88 moisture EOFs have been used to reconstruct the TIGR water vapor profiles. Figure 29 shows the mean and RMS reconstruction error using 15 EOFs. At pressures greater than 400 mb, the errors are comparable to the reconstruction errors for the NOAA-88 profiles (when only 10 EOFs are used, the errors are roughly twice as large). At higher altitudes, the differences in extrapolation methods between the two databases cause large errors.

The above example of applying the EOF reconstruction to TIGR profiles using NOAA-88 based EOFs highlights the need for more accurate upper tropospheric water vapor measurements. In the

lower troposphere, both databases represent the global variability of water vapor rather well. Consequently, the NOAA-88 based EOFs can reconstruct an independent database (TIGR) quite well. On the other hand, in the upper troposphere each database uses a different extrapolation method and in this region the reconstruction errors are large. This implies that upper tropospheric moisture retrievals will improve with more data on water vapor variability in this region. It should be noted that in the above reconstruction examples, no attempt was made to decrease the reconstruction errors by optimizing the EOF coefficients. Since the retrieval algorithm solves for the EOF coefficients in an optimal way [see Equation (0.62)], we expect the errors presented above to be upper bounds.

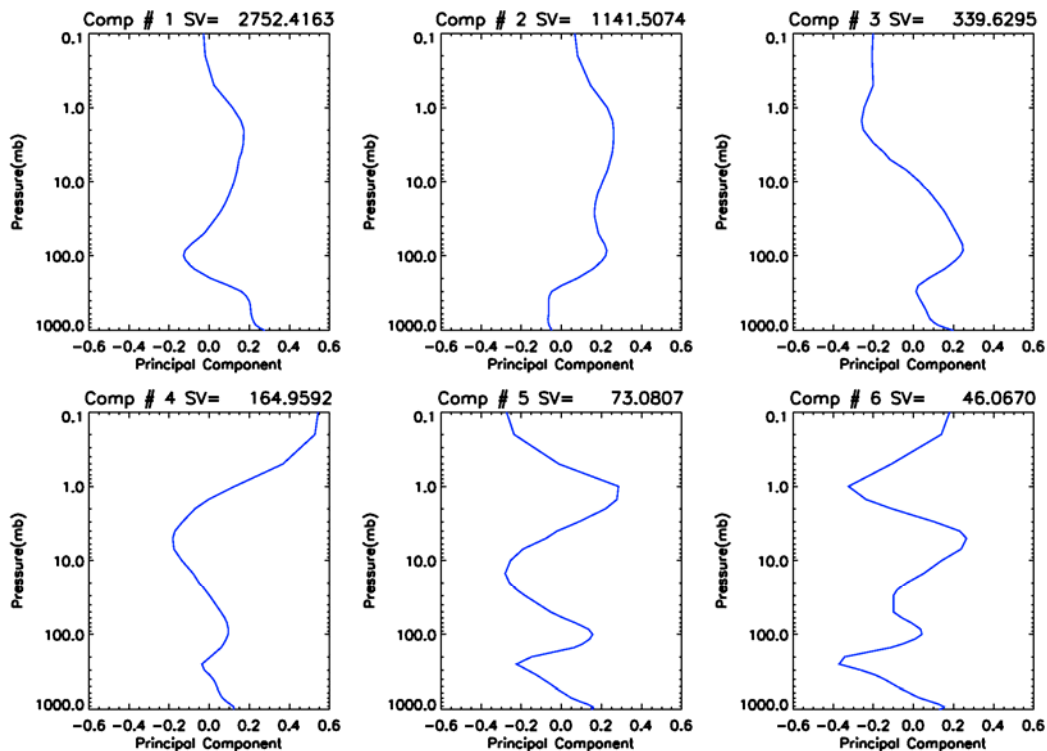


Figure 20: First 6 EOFs of the NOAA-88 temperature profiles. SV stands for “singular value” (equal to the square root of the eigenvalue).

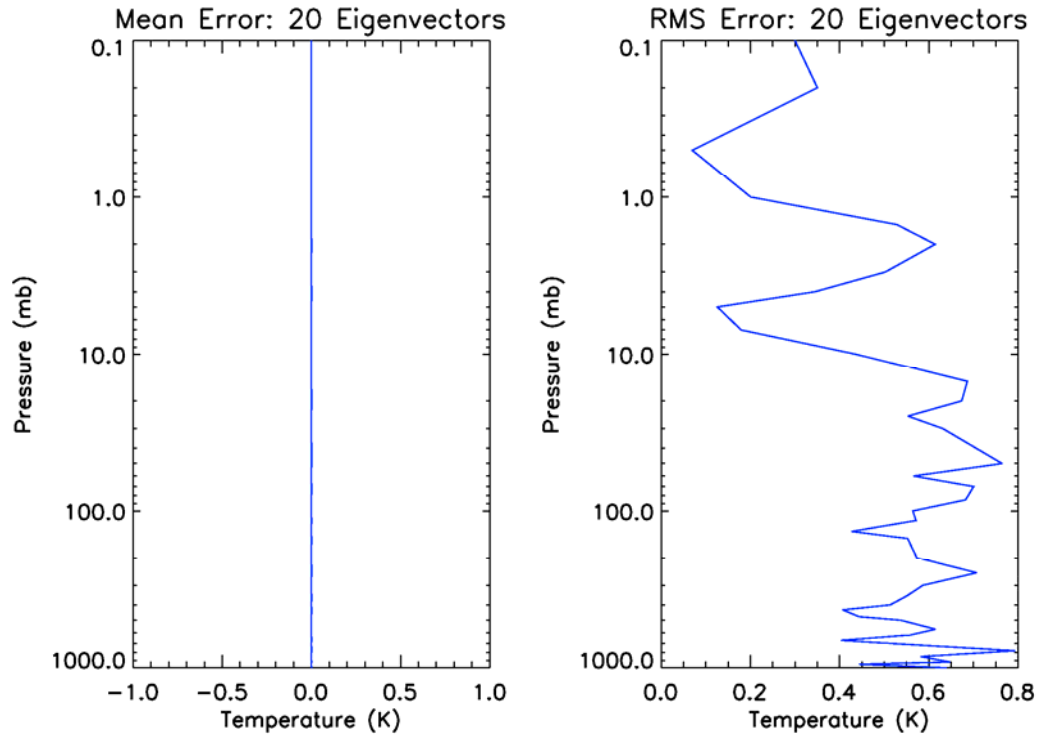


Figure 21: Bias and RMS representation errors of NOAA-88 temperature profiles using 20 EOFs.

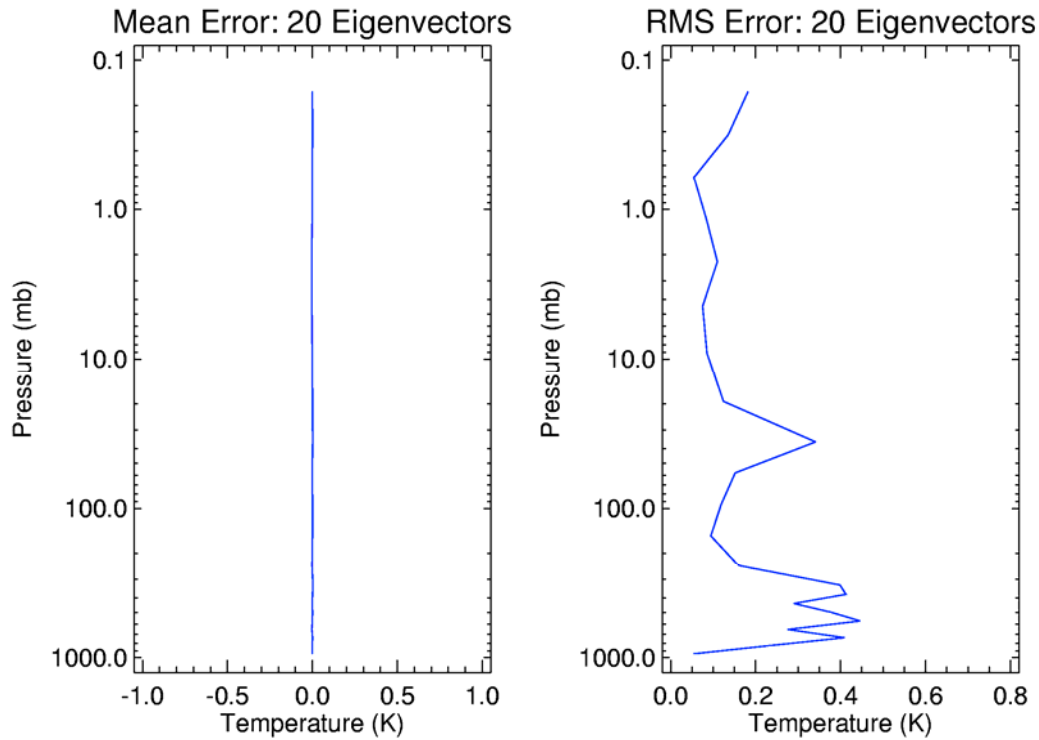


Figure 22: Layer-mean representation errors of NOAA-88 temperature profiles.

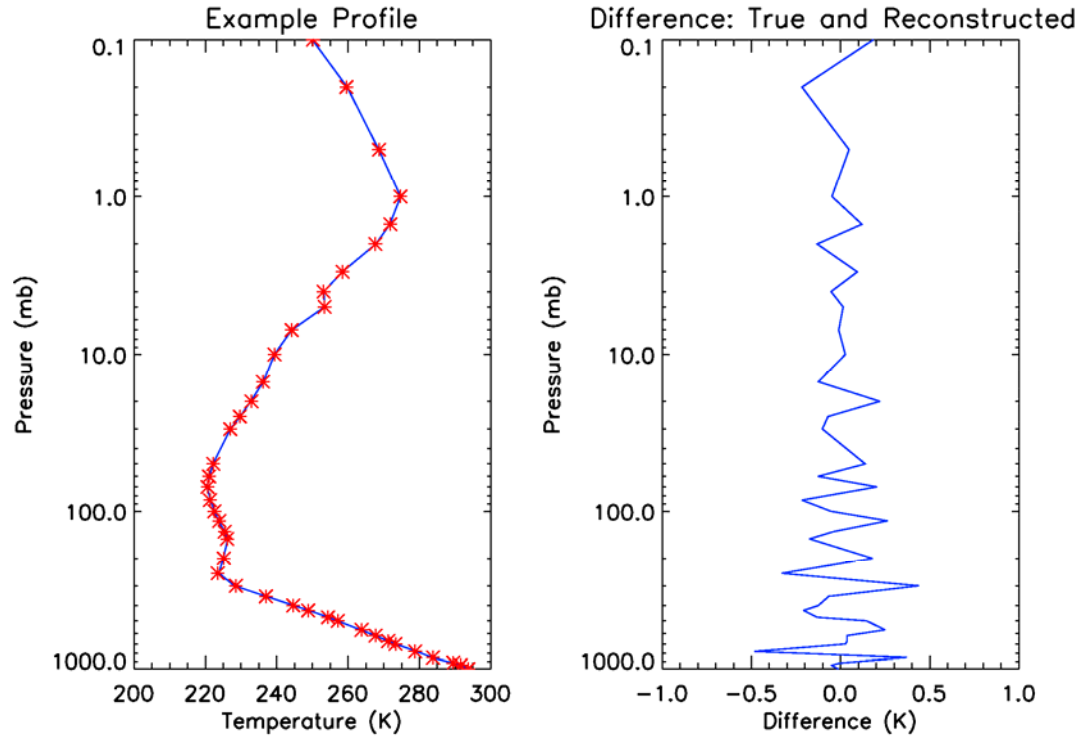


Figure 23: The original NOAA-88 temperature profile (solid line) and the profile reconstructed using 20 EOFs (stars). The plot on the right is the difference.

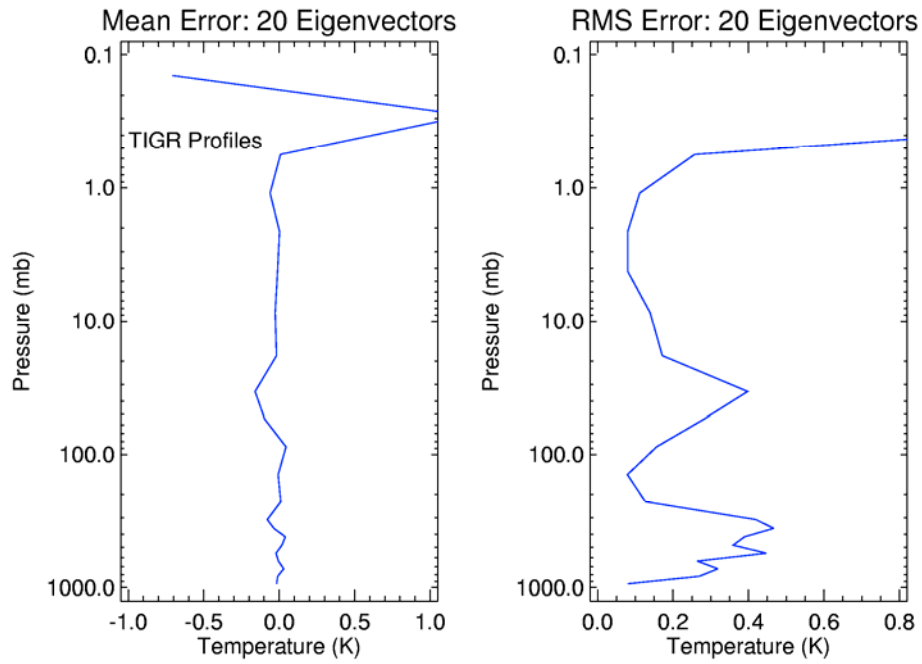


Figure 24: Mean and RMS errors when twenty NOAA-88 EOFs are used to reconstruct TIGR temperature profiles.

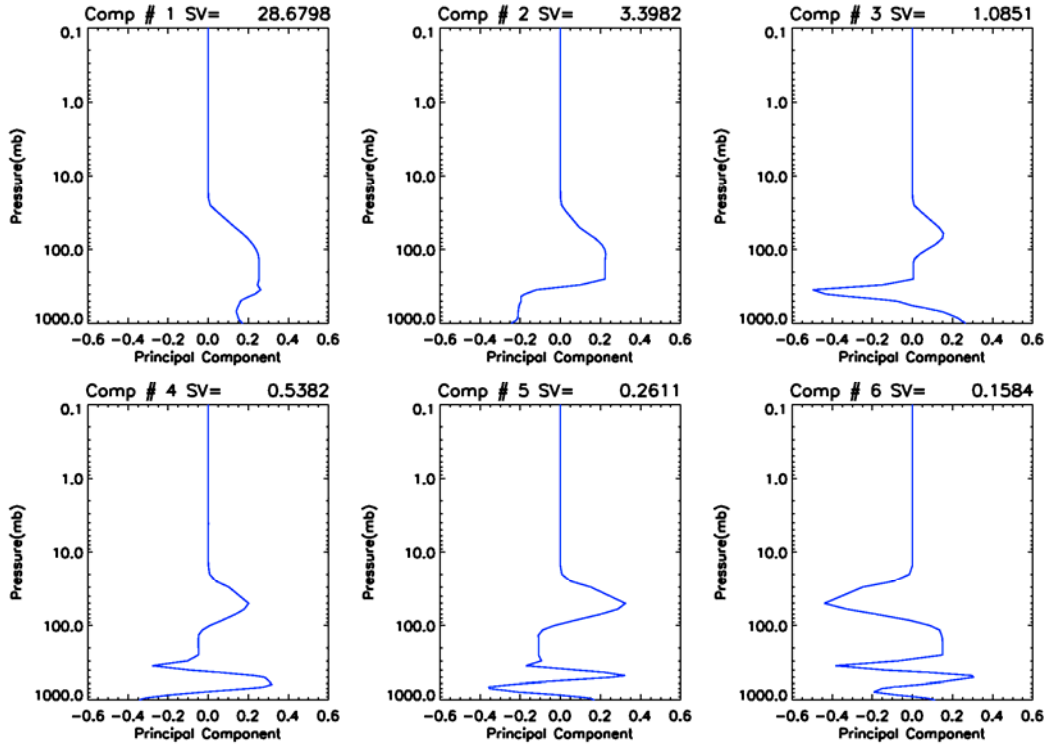


Figure 25: First 6 EOFs of the NOAA-88 moisture profiles.

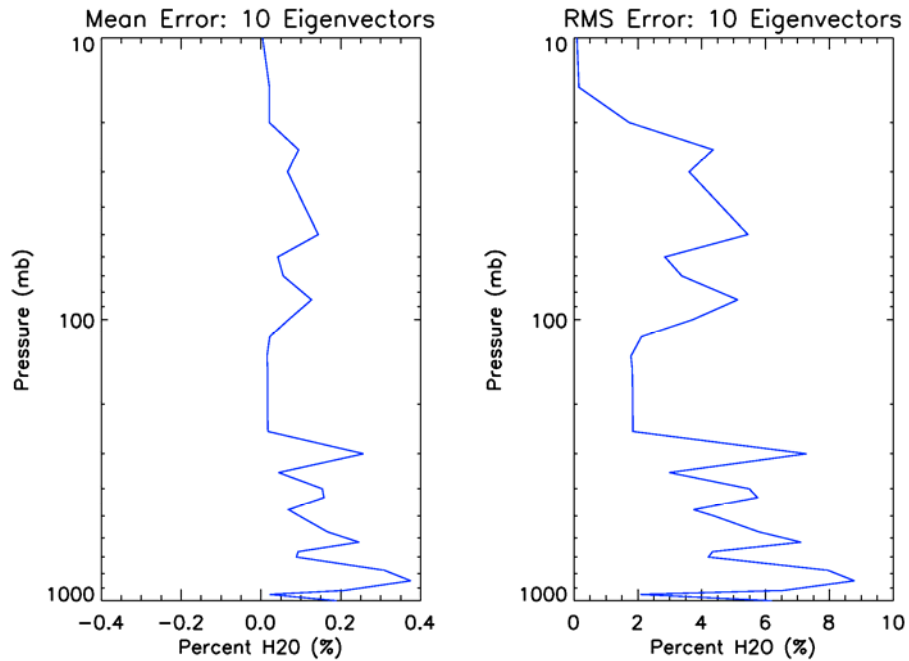


Figure 26: Bias and RMS errors of the reconstructed NOAA-88 moisture profiles using 10 eigenvectors.

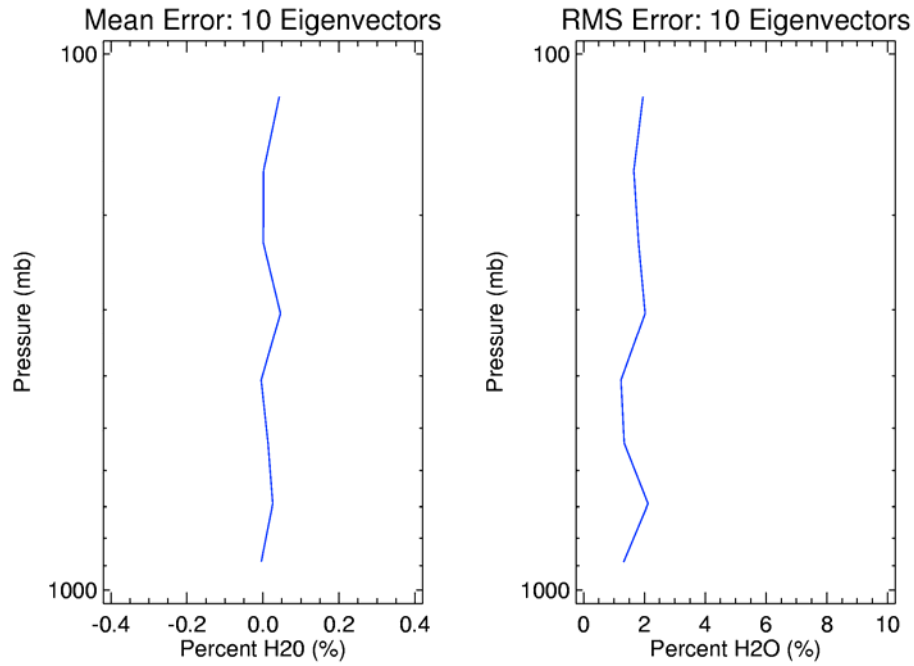


Figure 27: Layer-mean representation errors of NOAA-88 moisture profiles.

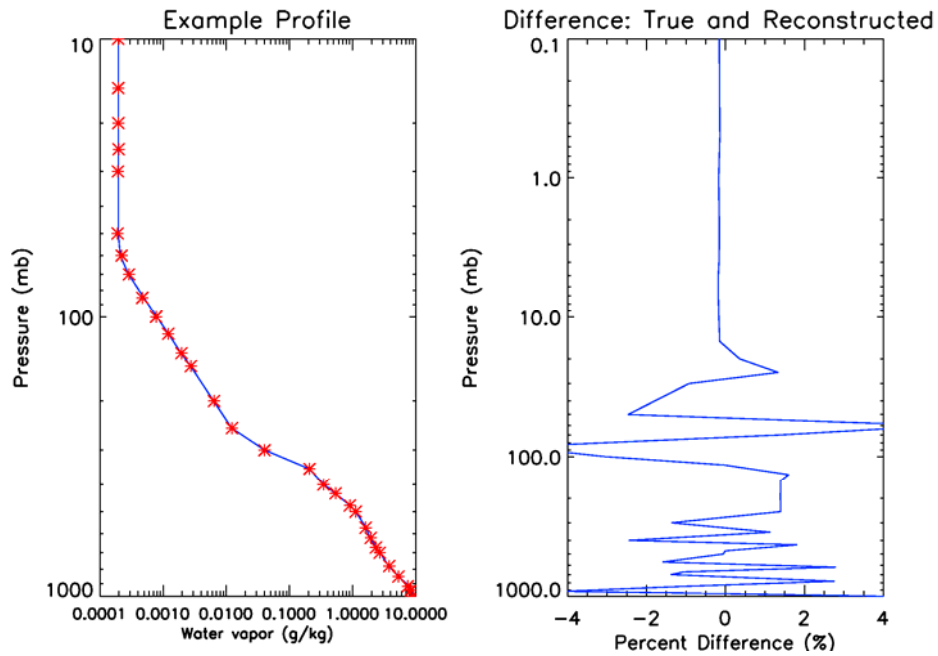


Figure 28: Example of the original and reconstructed moisture profiles and the difference between them.

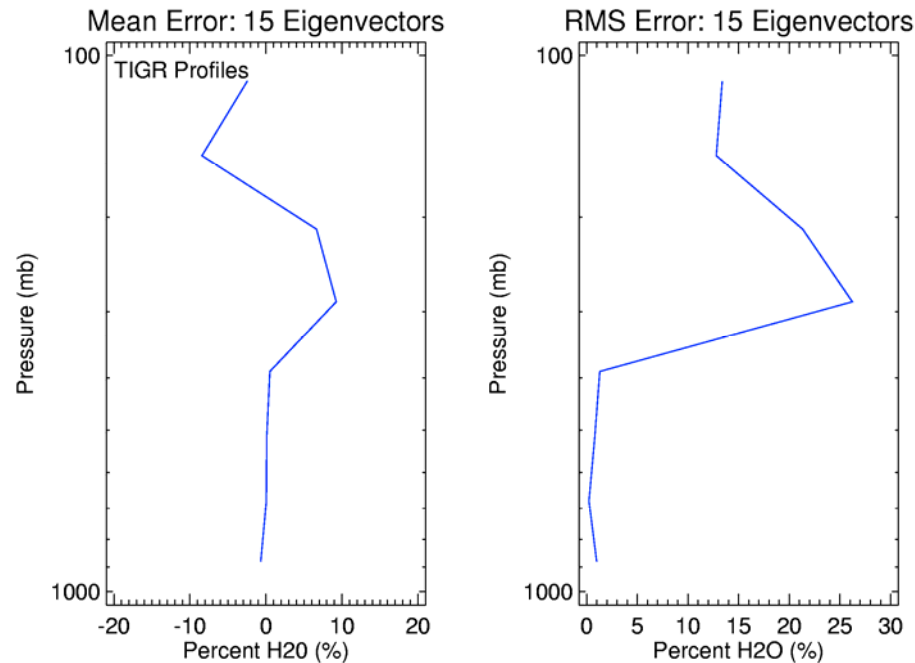


Figure 29: Bias and RMS error when eigenvectors of the NOAA-88 moisture profiles are used to reconstruct the TIGR moisture profiles.

In addition to quantifying the number of EOFs needed to accurately represent the original temperature and moisture profiles, its impact on the retrieval performance has also been studied. Figure 30 shows the RMS errors for TPW, skin temperature and average lower tropospheric temperature along with convergence rate as a function of temperature EOFs. Four hundred warm ocean profiles from the NOAA-88b database have been used in this study. Statistics for both IR/MW and MW-only retrievals are shown. When only one temperature EOF is used, none of the retrieval converges. When the number of EOFs is less than 10, the convergence rate is very low. The RMS errors shown in this figure exclude retrievals that do not converge and some of the error statistics may not be valid when the convergence rate is low. For MW-only retrieval, the retrieval performance reaches a plateau after the number of EOFs is greater than 10. For combined MW+IR retrieval, the performance is best when the number of EOFs is between 20 and 30. This trade study supports the use of 20 EOFs for temperature retrievals. It is worth mentioning that when the number of EOFs is 40 (i.e., no-EOF compression of the temperature error covariance matrix), there is instability in the temperature retrieval in the combined MW+IR retrievals but not in the MW-only retrieval. This is because for MW-only retrieval, equation (0.55) is used and the error covariance matrix is inverted after information from the measurement

is added. In the combined MW+IR retrieval, equation (0.54) is used, and the background error covariance is inverted first. Without EOFs compression, this matrix is ill-conditioned. This problem is more severe as the number of atmospheric layers increases.

The effect of varying the number of moisture EOFs on retrieval errors is shown in Figure 31. It demonstrates that 10 EOFs can be safely used and that increasing this number does not degrade the performance significantly (significant degradation only obtains when the number of EOFs is less than 5). These conclusions hold for both MW-only and MW+IR retrievals. For the reason mentioned above, the MW+IR retrieval for moisture becomes unstable when the moisture error covariance is not EOF compressed (i.e., the number of EOFs equals 40).

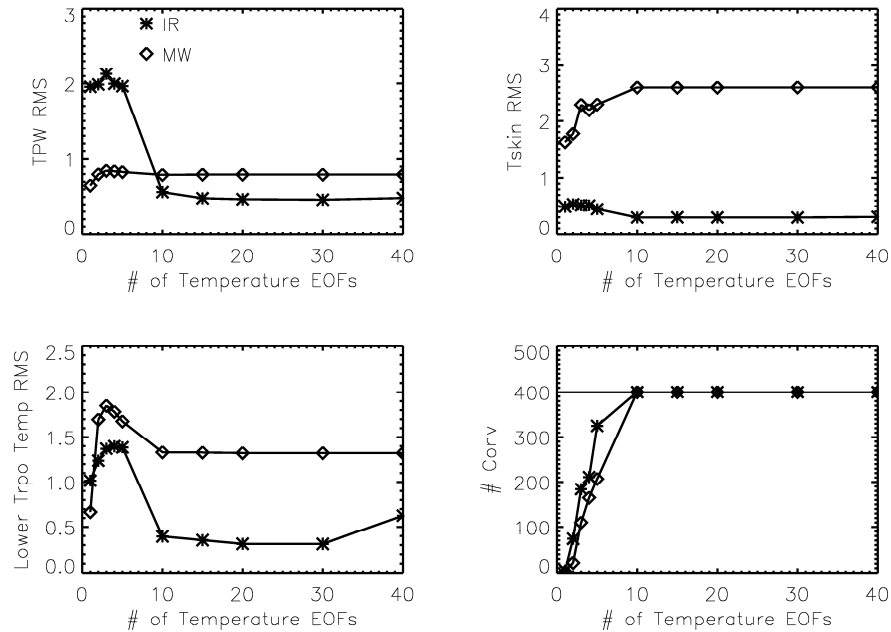


Figure 30: MW-only and MW+IR retrieval RMS statistics and convergence rate as a function of temperature EOFs.

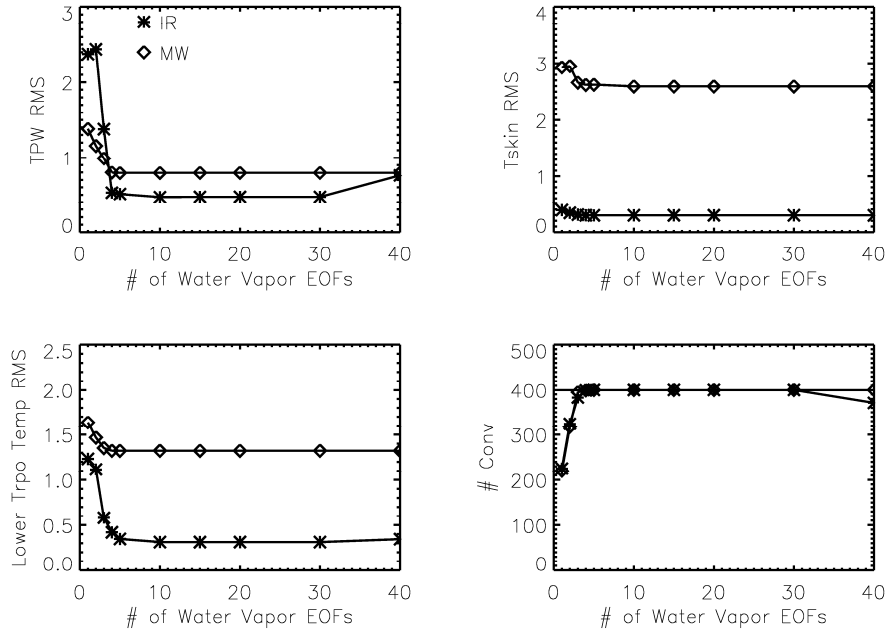


Figure 31: MW-only and MW+IR retrieval RMS statistics and convergence rate as a function of moisture EOFs.

4.4 Retrieval Strategies Under Cloudy Conditions

A critical consideration in the design of an infrared retrieval process is the treatment of clouds. The likelihood of cloud contamination within a CrIS FOR is high. For example, the probability of one clear FOV is only 45%, whereas the probability of two clear FOVs is only 35% (Smith *et al.* 1996). Clouds are difficult to model in the IR because of multiple scattering effects, complex cloud geometry, multiple cloud layers with multiple reflection and scattering, etc. A brief overview on the strategy employed in the current EDR algorithm is given here, and the detailed implementation is discussed in section 5.5.2

4.4.1 Cloud-clearing (CC)

The CC approach (Smith 1968; Chahine 1974, 1977) exploits the radiance contrasts between adjacent FOVs without modeling the cloud effects and performs a clear retrieval on “cloud-cleared” radiances computed for each FOV cluster within a FOR. This approach has been used in the analysis of HIRS2/MSU data (Susskind *et al.* 1984; Susskind and Reuter 1985; Chahine and Susskind 1989) and in the operational HIRS2/MSU retrievals (McMillin and Dean 1982). Chahine and Susskind (1989) showed that with the CC approach, the retrieval accuracy does not degrade appreciably for cloud fractions of up to 80%. A potential shortcoming of the CC method is its underlying assumption that the only source of spatial inhomogeneities in the retrievals are clouds and that other atmospheric/surface constituents are spatially homogeneous. The CC method is the primary cloud-treatment strategy available in the current CrIMSS algorithm, with implementation similar to that adopted in the AIRS code (see Section 5.5.2).

5.0 DETAILED DESCRIPTION OF CrIMSS EDR ALGORITHM

As mentioned in Section 4.0, there are 7 modules in the CrIMSS EDR algorithm. This section provides a detailed description of each of the 7 modules.

5.1 Initialization

The initialization process provides “static” data (i.e., data that do not change with time) required by the retrieval algorithm.

5.1.1 Instrument Specifications and Related Parameters

For the microwave sensor, the instrument specifications include ATMS frequencies, channel NEdT values, ATMS SDR remapping noise amplification/reduction factors. For the infrared sensor, they include CrIS channel frequencies, instrument noise, and a channel selection file.

5.1.2 Forward Model Parameters

For both IR and MW, the forward model parameters consist of two parts. The first part includes the location and weights of selected monochromatic points, i.e., OSS parameters. The second part includes optical depth (or absorption coefficient) lookup table files. The monochromatic radiative transfer calculation uses these lookup tables to generate optical depths of each atmospheric layer for given temperature, moisture and trace gases profiles. In the infrared forward model, a solar spectrum is also needed to calculate solar contributions to the observed radiances. In the current version of the code, the solar spectrum of Kurucz (1992) is used. Since the current CrIMSS code is capable of simulating three ILS functions, 3 solar spectra degraded to the CrIS spectral resolution have been provided.

The EDR algorithm has added functions to properly handle the errors in the forward models. The uncertainty (random error) of both MW and IR forward models are pre-characterized and combined with the sensor radiance errors before it is used to evaluate the residuals between the

observed and the retrieved radiances. In addition, the algorithm will remove the IR RTM bias from the computed IR radiances before it is compared to the measured (or cloud cleared) radiances.

5.1.3 Topography and Land/Ocean Mask

Topography and land/ocean masks are obtained from a digital elevation map (DEM). The elevation information is used to calculate the surface pressure and convert the latitude and longitude from sea level to the CrIS footprint elevation. The land/ocean mask is used to select appropriate surface background and associated error covariance matrices. It is also used to identify coastal lines and aid the scene classification module to group appropriate FOVs together for the cloud-clearing.

The current algorithm relies on the USGS GTOPO30 map for both purposes (more information about the map can be found in <http://edcwww.cr.usgs.gov/landdaac/gtopo30/gtopo30.html>). It should be noted that since other NPOESS and NPP sensors also need a DEM, it would be beneficial for all sensor algorithms to use a consistent DEM for data processing.

5.1.4 Atmospheric/Surface Mean Profiles and Background Covariance

The inverse model uses atmospheric/surface mean profiles and background covariance matrices as an *a priori* constraint on the CrIMSS physical retrievals.

The atmospheric portions of the *a priori* fields have been derived using a large diversified database composed of NCEP, ECMWF, and NOAA88b atmospheric profiles. For each set, global ocean and land fields have been generated, as well as fields stratified according to the method described in Section 5.3.2. The design of the code allows for an upgrade of this stratification scheme in the future.

In addition to the atmospheric covariance and background, *a priori* constraints on both MW and IR surface emissivities are required. For MW surface emissivity over the ocean background, the

Wilheit (1979) model was used to compute MW emissivities at ATMS scan angles and channel center frequencies using input from NCEP wind speed and surface temperature data. Changes in the polarization of the channels as a function of scan angle are included. For land, emissivities are obtained using English's semi-empirical model. In the IR, the surface emissivity is obtained from the ASTER and MODIS spectral emissivity databases.

It is important to point out that these means and covariances will be updated once new data of high quality become available, and the algorithm design allows for such quick and easy updates.

5.2 Input and Pre-Processing

The main inputs to the CrIMSS retrieval algorithm are the calibrated microwave and infrared radiances and NWP surface pressure or profiles.

5.2.1 Microwave SDR

Initial development of the CrIMSS algorithm assumes that the microwave SDR data are the AMSU and MHS radiances as specified at the Goddard Space Flight Center in December 1995 for AMSU and by Matra Marconi in 1995 for MHS. Latitude and longitude for each AMSU and MHS FOV are provided with a 5 km mapping error, with the MHS data interpolated to AMSU footprints. NEdN and radiometric bias errors due to calibration and interpolation are associated with microwave SDRs.

Since version 3.0, the code has been updated to reflect the actual CrIMSS sensor-suite, in which the ATMS sensor is the microwave component. Two key differences between AMSU/MHS and ATMS are the sensor noise and the sensor field-of-view (FOV). It is important that the sensor noise is included properly in the retrieval algorithm, taking into account the impact on the noise level of the mapping of the ATMS FOVs to the CrIS FOR. The current version of the CrIMSS science code reads in both the ATMS sensor noise and a noise reduction factor (due to remapping) for each of the CrIS FOR. The noise reduction factors are obtained from the NGES SDR algorithm description documents (see Appendix D).

5.2.2 Infrared SDR

The infrared SDRs consist of spectra apodized with a specified Instrument Line Shape (ILS) function and corrected for the off-optical axis effects (e.g., spectral shift, self-apodization, and phase distortion), with associated quality control flags. Information about NEdN, radiometric uncertainties, spectral shift errors, band-to-band co-registration errors, and line-of-sight (LOS) jitter errors are used to define the error covariance matrix for the infrared retrieval. Additional information in the infrared SDRs includes the scan angle, latitude and longitude for each CrIS FOV (5 km mapping error), and channel centers interpolated to the CrIS frequency grid defined in Table 7.

5.2.2.1 Local Angle Adjustment of Infrared SDRs

The CrIS cloud-clearing algorithm uses observations collected in a 3×3 FOV array to correct the observed radiances for the presence of cloud. This method assumes that the observations collected at the 9 FOVs are equivalent except for the cloud amount. In fact, the observations are viewed along slightly differing paths through the atmosphere. This difference in atmospheric path modifies the weighting functions for each of CrIS channels. The resulting radiance differences are a source of error in the retrieval if they are incorrectly attributed to cloud. However, the problem can be addressed by adjusting the observations to a common, central zenith angle. The radiance adjustment for a given observation (i.e., at each FOV) is computed for each CrIS channel as a linear function of the observed radiances for all channels. The coefficients used in the correction are determined through a regression analysis based on a representative set of radiances generated for the appropriate geometry. The correction process is referred to as the Local Angle Adjustment (LAA) and is performed in the preprocessing module prior to the retrievals. The CrIS LAA approach is similar to that outlined in the AIRS ATBD.

5.2.2.1.1 Local Angle Adjustment Methodology

The scan angle-adjusted radiance is calculated from the observed radiance for each of the 9 FOVs using the following equation,

$$R_{adj}(p_i, \nu_j, \varphi_k) = R_{obs}(p_i, \nu_j, \varphi_k) + A(p_i, \nu_j, \varphi_k) \quad (0.66)$$

where p_i indicates the atmospheric condition, ν_j is the wavenumber, and φ_k is the scan angle corresponding to the center FOV. For the central FOV, $R_{obs} = R_{ctr}$ and $A = 0$. For all other FOVs, the value of $A(p_i, \nu_j, \varphi_k)$ is computed as a linear function of the observed radiance $R_{obs}(p_i, \nu, \varphi_k)$ at all wavenumbers. The coefficients of the function are determined via a regression analysis on $R_{ctr} - R_{obs}$ based on a representative sample of spectra R_{obs} . In practice, the regression against R_{obs} leads to singularities. To prevent this, a set of eigenvectors is computed from R_{obs} to use as the predictors. Also, to increase sensitivity at long wavenumbers (i.e., CrIS SWIR band), the observed radiances are normalized by the Planck function given by

$$P(\nu, T) = c_1 \nu^3 / (e^{(c_2 \nu / T)} - 1) \quad (0.67)$$

where c_1 and c_2 are the first and second radiation constants and T is a temperature which results in approximately equal weighting across the three bands (e.g., $T=300K$).

The singular value decomposition of the observed radiances is then written as

$$\mathbf{R}_{obs}(p, \nu, \varphi_k) / P(\nu) = \mathbf{U} \mathbf{w} \mathbf{V}^T \quad (0.68)$$

where \mathbf{R}_{obs} is matrix of observed radiances with N_p by N_ν elements, \mathbf{V}^T is a matrix of eigenvectors with N_ν by N_ν elements and \mathbf{w} is a diagonal matrix of N_ν eigenvalues sorted from largest to smallest. The product $\mathbf{U} \mathbf{w}$ is a N_p by N_ν matrix of projection coefficients onto the set of eigenvectors. Setting $\mathbf{X} = \mathbf{U} \mathbf{w}$, we compute the predictors using

$$\mathbf{X}(p, \nu, \varphi_k) = [\mathbf{R}_{obs}(p, \nu, \varphi_k) / P(\nu)] \times \mathbf{V} \quad (0.69)$$

In practice, we find that $N_{eof} = 20$ eigenvectors are sufficient for the regression analysis. Therefore \mathbf{V}^T is truncated to N_v by N_{eof} elements and \mathbf{X} has N_p by N_{eof} elements.

The regression equation for wavenumber ν_j and scan angle φ_k is written as

$$A(p, \nu_j, \varphi_k) = C_0(\nu_j, \varphi_k) + \bar{C}(\nu_j, \varphi_k) \mathbf{X}(p, \nu, \varphi_k) \quad (0.70)$$

where C_0 is a constant and \bar{C} is an array with N_{eof} elements. The regression is applied to each wavenumber, FOV, and scan angle. Therefore the total number of coefficients generated is $(N_{eof} + 1) \times (N_v) \times (N_{FOV} - 1) \times (N_{FOR} / 2)$.

5.2.2.1.2 Regression Based on AIRS-Simulated Scanline and NOAA-88 Datasets

The LAA algorithm has been developed for a scan geometry that is modeled after the CrIS design. The CrIS scan geometry assumptions are described in Appendix C.

The training dataset for the LAA algorithm should provide good representation of the radiance differences that result from the difference in scan angle over all geophysical conditions. The AIRS-simulated scanline dataset and the NOAA-88b dataset have been used to compute the LAA eigenvectors and regression coefficients. This section describes the procedures used to generate the model parameters. The resulting algorithm has been applied to simulated CrIS radiances generated from both the scanline and NOAA-88b datasets with good results (i.e., the performance degradation introduced in the retrievals by the differences in scan angle is largely eliminated when the LAA is applied).

The scanline dataset consists of 240 scanlines with 15 FORs on each side of nadir. The atmospheric profiles represent a variety of conditions. The NOAA-88b dataset has been added to extend the variability. IR clouds provided with the scanline dataset were included in the simulations and the variety of the cloud heights and fractions was important for proper training of the regression.

In order to generate the radiance training set from the scanline simulations, all geophysical properties for the 9 FOVs within a FOR were fixed to a common value except for the scan angle and latitude/longitude. The scan angles were recomputed to be consistent with the CrIS design. Variations in solar zenith angle between FOVs (which is based on latitude/longitude) are an additional source of error introduced for daytime observations. For these simulations, the solar variations were approximated using the coordinates provided in the original AIRS dataset. Noise was excluded from the simulated radiances but written out as a separate file to facilitate testing. It is important for the purpose of generating the regression coefficients that the noise pattern introduced at each FOV be the same as that introduced in the central, reference FOV, otherwise the difference owing to noise will dominate and the regression will not be successful.

Separate eigenvectors and regression coefficients were computed for night ($SZA > 85$) and day ($SZA \leq 85$). Because the CrIS scan pattern is symmetrical across the satellite subpoint, the regression analysis was performed based on data from the first half of the scan only. At each of the 15 FORs, 16 radiance spectra were selected at random and used to compute the nighttime V_{night} and daytime V_{day} eigenvectors. For each FOR, and at each FOV within these FORs, the regression coefficients were computed from all nighttime or daytime radiances. Twenty EOFs were used in the regression. Figure 32 shows the relative amplitude of the first 100 eigenvalues. The uncertainty (i.e., RMS difference) in the regression was computed in brightness temperature units, and compared against the uncertainty in the uncorrected brightness temperatures and with the noise amplitude as a function of wavenumber. This is illustrated for the first FOR in Figure 33 and Figure 34 shows the band-average uncertainties as a function of scan angle for CrIS band 1. The results demonstrate that the brightness temperature errors can be reduced by way of the local angle adjustment to an insignificant level relative to the noise amplitude. This is true also for daytime conditions, though in that case residual uncertainties in the SWIR band are somewhat elevated compared to nighttime.

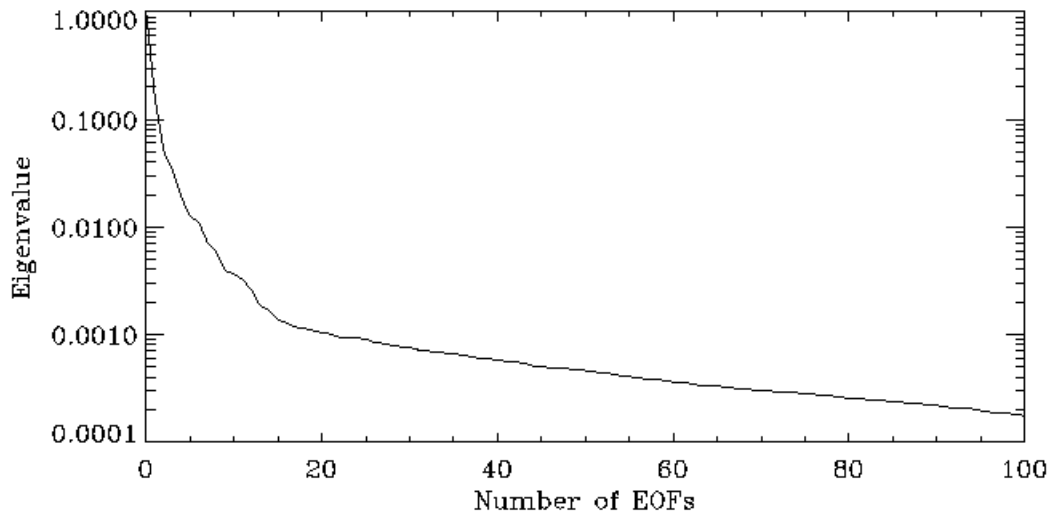


Figure 32: Eigenvalues based on nighttime simulations sorted by decreasing amplitude. The first 20 EOFs were used in the regression analysis.

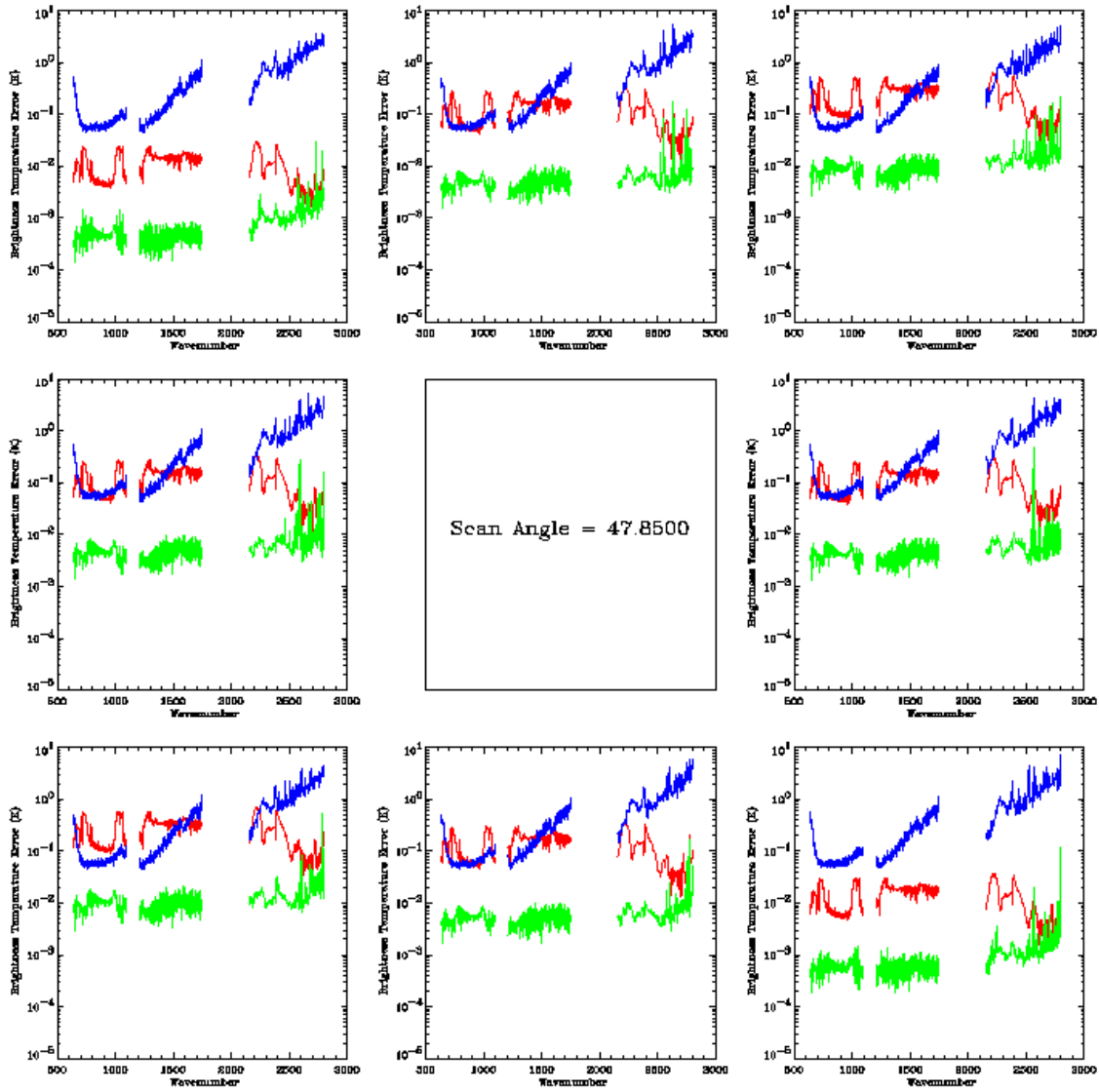


Figure 33: Uncertainty versus wavenumber for maximum scan angle. The largest radiance errors resulting from scan angle differences will occur at the edge-of-scan. Here, the brightness temperature uncertainty under nighttime conditions (computed based on the full set of 240 scanlines) is illustrated before (red) and after (green) the radiance adjustment and in comparison to the noise (blue).

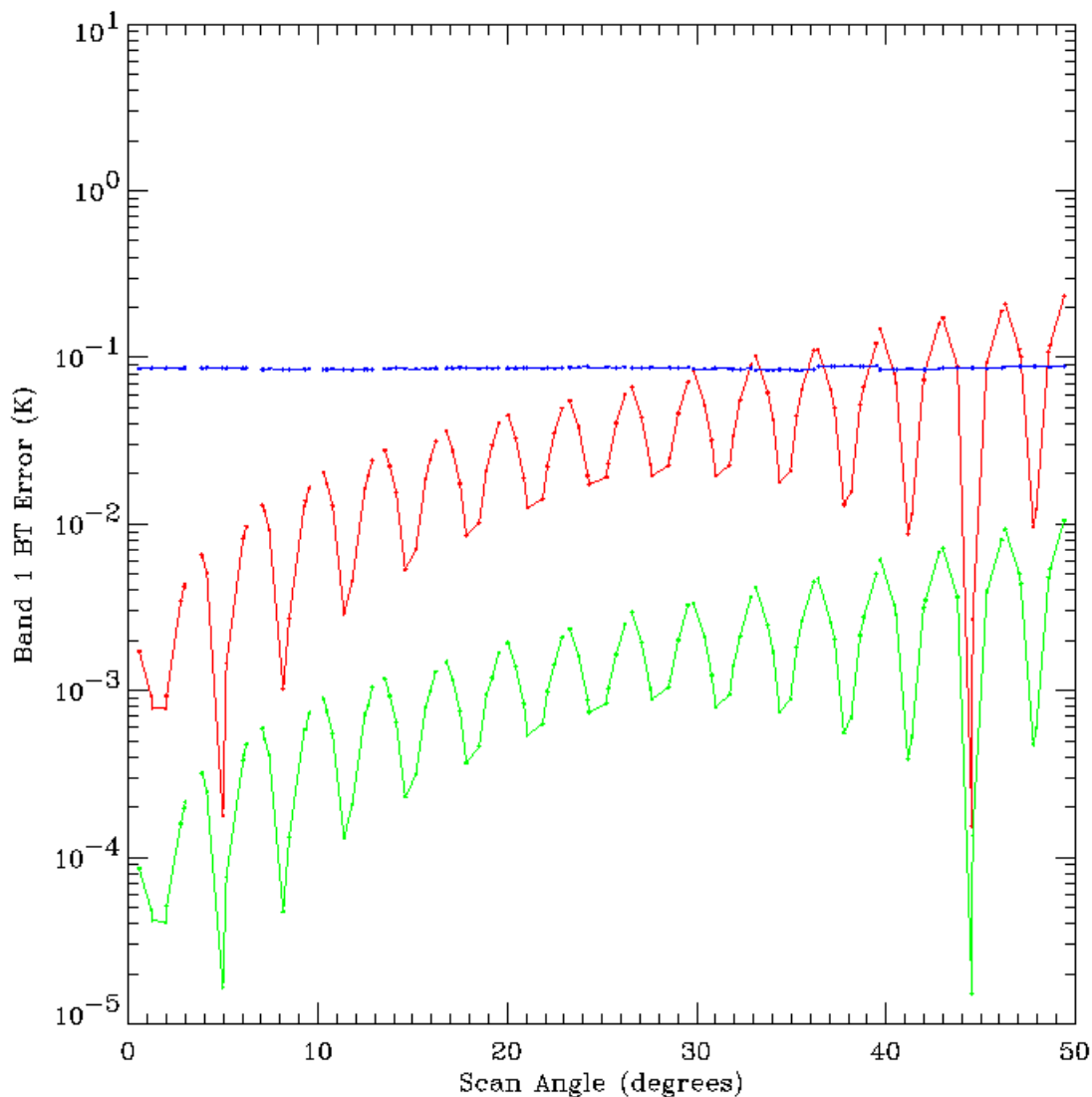


Figure 34: Band 1 averaged uncertainty as a function of scan angle. Brightness temperature errors are shown before LAA (red) and after LAA (green) for 15 FORs and 8 off-center FOVs. These errors impact the retrievals when equal to or greater than the noise amplitude (i.e., scan angles greater than 20 degrees). Applying LAA reduces errors to a level below the noise.

5.2.3 Terrain-height Correction for Longitude and Latitude

The sea-level longitude and latitude of each FOV are corrected for topography by determining the point of intersection of the instrument line-of-sight (LOS) with topography. This is accomplished via a search method (the implementation follows that described in the MODIS

ATBD). A critical input to this method is the LOS unit vector in Earth-centered reference (ECR) system. This vector is determined by the instrument orbital and viewing geometry and it is assumed that it will be available as part of the SDR input [e.g., Equation (104) in the CrIMSS SDR ATBD].

5.2.4 External Data Inputs

The external data required for the retrieval are of the “static” and “dynamic” type. The “static” database (i.e., information that is only occasionally updated) is read in during initialization. The “dynamic” database is updated on a regular basis. It includes surface pressure and virtual temperature fields from an NWP model (to determine surface pressure at the CrIS footprint). Additional external data will be required if the microwave sensor is lost.

5.2.4.1 Required Data in Case of Failure of the Microwave Instruments

- NWP fields are needed to provide an initial guess for the IR retrieval.

5.2.5 Precipitation Check

In the CrIMSS algorithm, scenes with precipitating clouds are detected using the NOAA/NESDIS day 1 algorithm (<http://orbit-net.nesdis.noaa.gov/arad2/MSPPS/>). Over land, the algorithm applies a scattering index test using the 23 and 89 GHz channels. Over ocean the algorithm relies on both a scattering index test and an emission based test. The emission test uses the cloud liquid water information obtained from the 23, 31, and 50 GHz channels. For both land and ocean, thresholds are applied to determine if precipitation is present or not. Further analysis of the scene is performed to differentiate precipitation from snow cover, sea ice and deserts. Figure 34A shows the flow of the NESDIS precipitation testing. The NESDIS algorithm currently implemented only applies to AMSU channels. The coefficients/thresholds will have to be updated when ATMS is on orbit. In the CrIMSS algorithm, precipitation detection is used as one of the quality indicators on the final retrieval.

The CrIMSS algorithm incorporates a radiance residual test, which is applied after each iteration in the retrieval process (see section 4.3). Precipitating clouds will typically cause inconsistencies between the calculated SDR and the observation. Since scattering clouds are not modeled in the forward model (see Section 4.2.4.5), the residual will not converge to an acceptable value. Thus, the radiance residual test is another indicator of when precipitating clouds are present within the scene.

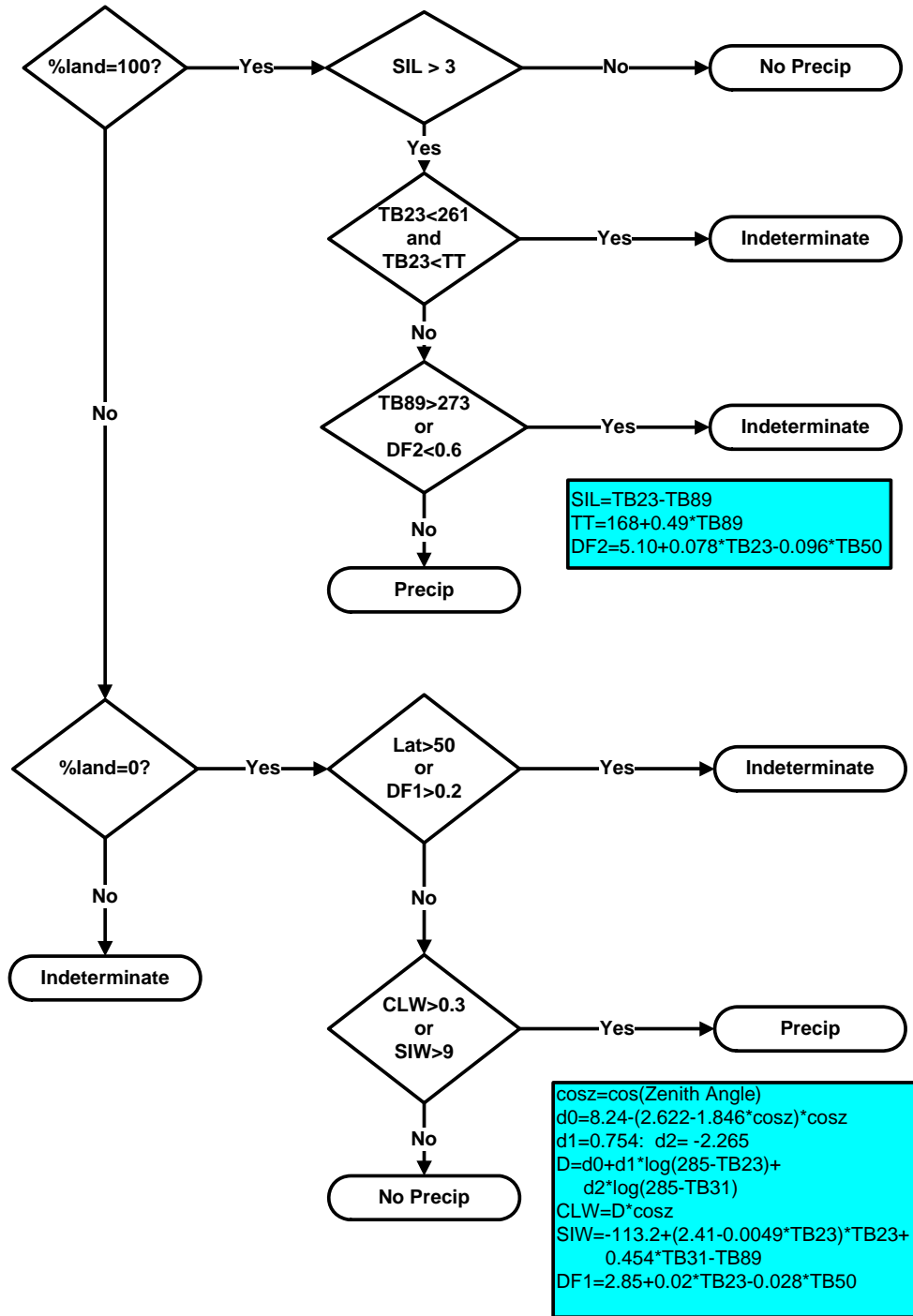


Figure 35: NOAA/NESDIS Day-1 precipitation detection algorithm (for AMSU)

5.2.6 Surface Type Determination

The retrieval performance can be improved by adopting the appropriate mean profile and background fields. This is sometimes referred to as air-mass classification or surface type determination. There are different methods which may be used to identify surface type. Current CrIMSS algorithm uses a method based on the land fraction and skin temperature determined from a preliminary MW-only retrieval (see Section 5.3.2). Given land fraction, the MW brightness temperatures are used to classify the surface into one of 8 types [(ocean_global_w_ice, ocean_ice, ocean_warm, land_global, land_200_240, land_240_260, land_260_280, land_warm)] (see Section 5.3.2 and Figure 38 for detailed description). This surface type classification was successfully applied to the scanline scenes provided by IPO (see section 7.6). Once the surface type is determined, the corresponding covariance matrix, which is trained with emissivities in that category, will be used in the retrieval.

5.2.7 Surface Pressure Computation

The CrIMSS retrieval algorithm requires an accurate estimate of the average surface pressure within an FOV/FOR. To meet this need globally, a method has been developed which starts with NWP surface pressures, available on a coarse grid, and adjusts them for local surface features within the observation FOV (the same method can be applied to the entire FOR).

5.2.7.1 Input Data

The following data are required:

- From an NWP model
 - Surface pressure field
 - Temperature and water vapor mixing ratio profiles
 - Surface elevations at NWP grid-points (from NWP source)

- From a digital elevation map (DEM)
 - Average elevation within FOV

Since the CrIMSS measurements are continuous in time, the NWP data required at each observation time should be an interpolation of an analysis (past) and a forecast (future). If an analysis is not available, then two forecasts could be used, and if NWP data are not available, then climatology fields could be used. For testing purposes, the CrIMSS algorithm currently only reads in template fields. The elevation correction algorithm uses the hydrostatic equation for moist atmospheres which requires the virtual temperature profile T_v . T_v is computed from temperature T and water vapor mixing ratio q as follows

$$T_v = (1 + 0.61\sigma)T$$

$$\sigma \equiv \frac{q}{q+1} \quad (0.71)$$

The USGS GTOPO30 30-second DEM should be adequate for the determination of the average elevation at the CrIMSS observation point. The current CrIMSS algorithm uses a version of GTOPO30 degraded to 1/20 degree.

5.2.7.2 Method

The simplest method to approximate the surface pressure at an observation point is to perform a linear interpolation using gridded NWP surface pressures. For oceans and land areas for which there is little variability in the elevation within an NWP grid box, this approximation is optimal. The method we propose attempts to correct the above first order approximation for local surface features. At each NWP grid point, the hydrostatic equation is used to calculate the pressure at the elevation of the CrIMSS observation point. The elevation at a CrIMSS observation point is determined using the DEM.

The first step in the process is a time interpolation of the NWP data to the observation time. A simple linear interpolation method is used. Using the DEM, the average elevation h within the CrIMSS FOV is calculated by averaging all the DEM pixels that fall within the FOV footprint.

We next use the hydrostatic equation for an isothermal layer along with the NWP data to calculate pressure P_h at height h . This is performed at each NWP grid point. The form of the hydrostatic equation used is as follows:

$$P_h = P_{ref} \exp \left[\frac{g(H_m)}{R_d T_v(H_m)} (H_{ref} - h) \right] \quad (0.72)$$

where $R_d = 287.04 \text{ J K}^{-1} \text{ kg}^{-1}$. This form of the hydrostatic equation is derived assuming an isothermal layer with the integration extending from H_{ref} to h . The variables needed for the calculation are defined as follows.

- h : Average elevation at the CrIMSS observation point.
- P_{ref} : Either NWP surface pressure P_{Surf} or NWP level pressure P_{Lev} .
- H_{ref} : Either the NWP surface height H_{Surf} or the height of an NWP pressure level H_{Lev} .
- H_m : Mid-point between H_{ref} and h .
- $T_v(H_m)$: Virtual temperature at H_m interpolated/extrapolated from NWP levels.

If for a particular NWP grid point $h > H_{Surf}$, then the integration of the hydrostatic equation will either proceed from $H_{Surf}(H_{ref}=H_{Surf}, P_{ref}=P_{Surf})$ or from one of the NWP pressure levels ($H_{ref}=H_{Lev}, P_{ref}=P_{Lev}$) depending upon which interval h falls within. If on the other hand $h < H_{Surf}$, then the integration will proceed from $H_{Surf}(H_{ref}=H_{Surf}, P_{ref}=P_{Surf})$. Once H_{ref} is defined, T_v is calculated using a simple linear interpolation/extrapolation from the closest NWP levels. The variation with altitude of the acceleration due to gravity is also accounted for in the P_h calculation.

Once P_h has been calculated for each of the four NWP grid points surrounding the CrIMSS observation point, a bi-linear interpolation is performed to generate the surface pressure which is used in the CrIMSS retrieval algorithm.

The steps are listed again below:

1. Interpolate NWP fields to observation time.
2. Using DEM, calculate average surface elevation within the observation footprint.
3. At each NWP grid point surrounding the observation, use the hydrostatic equation and the NWP data to calculate P_{hi} , the pressure at the observation point elevation.
4. Perform bi-linear interpolation of P_{hi} to the observation point, $\sum \alpha_i * P_{hi}$, where α_i depends on the distance of the observation point from the surrounding NWP grid points.

It should be pointed out that in the current code implementation, the CrIS FOV size is fixed and assumed to be a 15km box. The actual shape, size, and orientation of a CrIS FOV have not been used in determining its average terrain height. The EDR impacts caused by the uncertainty in such computed terrain heights have not been fully evaluated, but are not expected to be substantial for AVTP and AVMP because these two EDRs are not very sensitive to surface pressure errors. However, the quality of the retrieved atmospheric pressure profiles will be more affected.

5.2.7.3 Example

Using the above method, surface pressure has been determined for the Tibetan Plateau/India region (latitude 0-35°N, longitude 65-95°E) at 0.1°-resolution in latitude and longitude. The DEM points falling within 15 km sized regions corresponding to the size of CrIS footprints at nadir are included in the determination of average elevation. Figure 36a shows the surface pressure field determined using the above technique, while Figure 36b shows the result of interpolating the NWP surface pressures with no elevation correction applied. As can be seen, a

straightforward interpolation of the NWP surface pressure captures the general shape and boundaries of elevated terrain, but misses the localized variations.

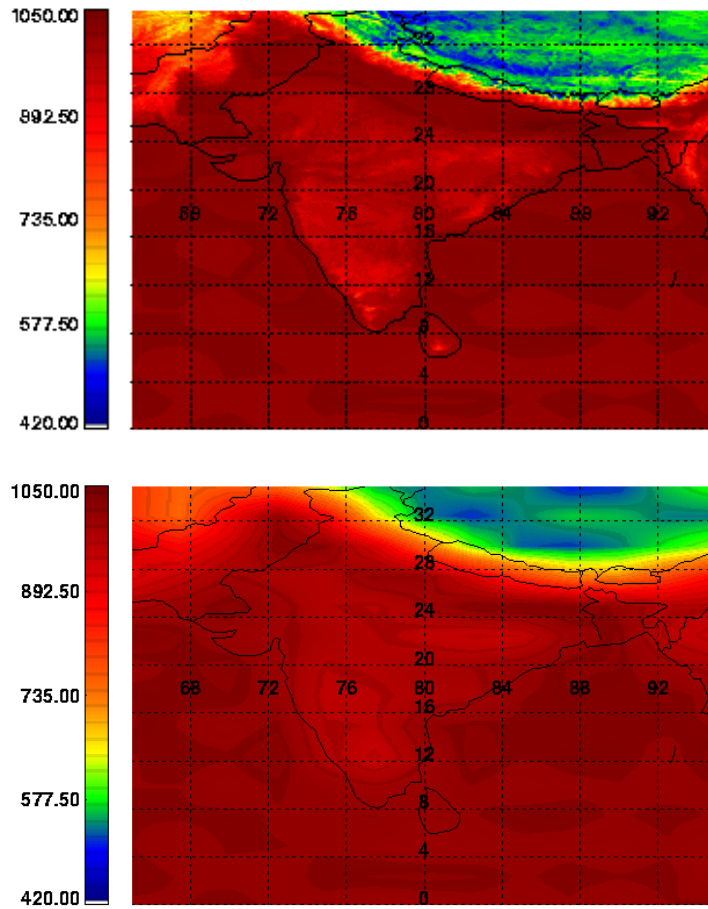


Figure 36: Surface pressure for the Tibetan Plateau/India region at 0.1° -resolution. Top: Calculated using the method described in this section. Bottom: Obtained from a direct interpolation of NWP data.

5.2.8 NWP Initial Guess

If there is a failure of the microwave instrumentation, the initial guess profiles for the IR retrievals will be obtained from NWP fields. We have implemented methods to ingest, interpolate and reformat NWP temperature and water vapor fields to CrIMSS observation points.

The NWP fields are typically on a standard grid and available at specific forecast/analysis times. The profiles are first interpolated in time and space to the CrIMSS FOR latitude/longitude. Since the NWP fields will typically not be on the CrIMSS leveling grid, the NWP profiles are mapped from their native grid to that required by the CrIMSS algorithm.

5.2.8.1 Method

As is the case for the surface pressure calculation, the NWP data used at each observation time should be an interpolation of an analysis and a forecast. The requirement of having NWP data close to the observation time is much more stringent in this situation than for the surface pressure. The interpolation in time is a simple linear method. The same bilinear interpolation used in the final step of the surface pressure calculation is used to generate profiles at the CrIMSS observation point.

Several factors need to be considered when using NWP data in the retrieval algorithms:

- NWP data may be on a different pressure grid than those used in the retrieval algorithms.
- Appropriate covariances need to be incorporated.

To deal with the pressure level mismatch, we apply a regression matrix to map from the NWP levels to the levels required by the CrIMSS algorithm. This method can be used to either interpolate between levels, extrapolate to lower pressure levels, or both. Exactly which levels are involved in the mapping depends on the source of the NWP fields. The regression matrix can be built from either NOAA-88 profiles, TIGR profiles, or any profile set which has levels that are in both the NWP data and those required for CrIMSS.

Given a set of profiles containing both the NWP levels and the levels required by the CrIMSS algorithm, a linear least-square method is used to generate a regression matrix which will map a profile vector from dimension n_{NWP} to dimension n_{CrIMSS} (Eyre 1989a). The profile transformation takes the form

$$x_{CrIMSS} = Dx_{NWP} . \quad (0.73)$$

where D is the regression matrix. It should be noted that D does not need to be based completely on the regression analysis. If a simple linear interpolation between levels is desired, the appropriate matrix elements could be changed. Another example is for the case of water vapor, where the data set from which the regression matrix is being built may only have reliable data up to a certain level and is then extrapolated from there. A different extrapolation scheme can be implemented by again replacing the appropriate matrix elements.

Without microwave-only retrieval, the implemented surface type determination module as discussed in Sec 5.2.6 will not be exercised. As a result, there will be only two surface types used by the algorithm in case of microwave instrumentation failure: global ocean and global land.

The algorithm's performance when NWP is used as initial guess has not been fully evaluated. The performance is expected to be somewhat impacted by the quality of the NWP initial guess, particularly when clouds are present in the scene. Again, the graceful degradation option is in preparation for unlikely events when ATMS fails to produce quality SDRs, and will not be exercised in normal operating conditions.

5.3 Microwave-Only Retrieval

5.3.1 General Description

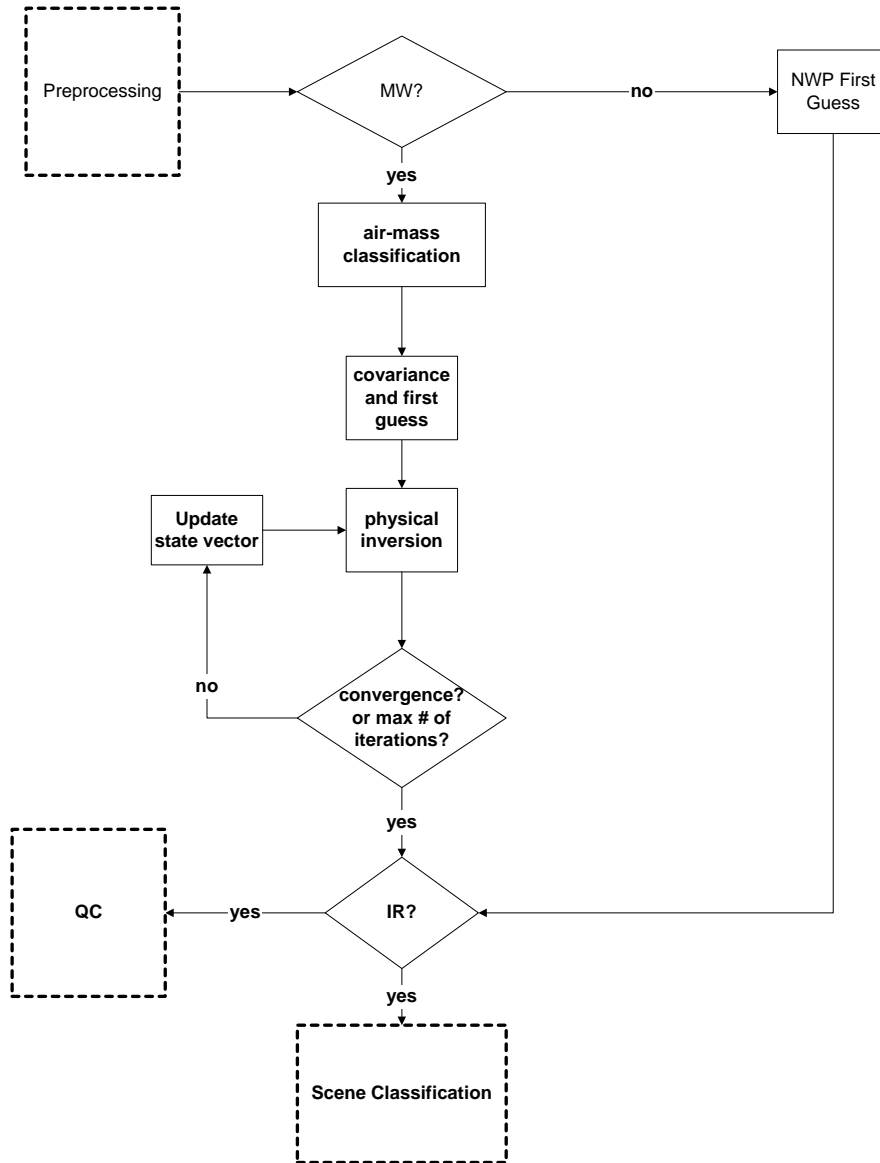


Figure 37: Functional Flow Diagram for MW Retrieval.

The functional flow diagram for microwave retrieval is shown in Figure 37. The microwave retrieval algorithm uses radiances measured by the ATMS sensor and performs a physical

inversion using a climatology background and the associated covariance as a constraint. The climatology background is also used as the first guess for the physical retrieval. Trade studies have been performed using regression generated first guess. It only resulted in a slight improvement in the speed of convergence and does not change the retrieval performance. A simultaneous retrieval of temperature, moisture, skin temperature, surface emissivity, cloud liquid water path, and cloud-top pressure is accomplished using all the ATMS channels. For those ATMS channels with higher spatial resolution than CrIS FOR, they are remapped into CrIS FOR via MW SDR algorithm. For channels 1 and 2, the re-mapped ATMS footprints (5.5 degree) are larger than the 3.3 degree CrIS FOR size. Spatial scene inhomogeneity due to surface and atmospheric profiles (or clouds) may introduce errors for these two channels relative to the CrIS FOR. The algorithm makes an estimate of this error and relaxes the radiance error covariance matrix for these two channels to account for it. For ATMS a total of 22 channel radiances are used in the inversion. Each MW channel has an on-off flag and any channel can be excluded from the retrieval if the SDR quality is bad. Since the inversion process is highly non-linear in the presence of cloud, the DRAD modification to the maximum likelihood method is employed (see Section 4.3.2). The *a priori* information for the retrieval is described in Sections 5.1 and 5.2. The convergence criterion for the microwave retrieval is based on normalized χ^2_{MW}

$$\chi^2_{MW} = \frac{1}{nchanmw} \sum_{i=1}^{nchanmw} \frac{(\Theta_i^{retr} - \Theta_i^{obs})^2}{N_i^{MW}} \quad (0.74)$$

where $nchanmw$ is the number of microwave channels, Θ_i^{retr} and Θ_i^{obs} are the retrieved and observed brightness temperatures, and N_i^{MW} is the noise variance for the i^{th} MW channel. Currently the convergence criterion is for χ^2_{MW} to be less than 1.0 and the maximum number of iterations is set to 7.

The parameters retrieved in the microwave are listed in Table 15. In the current algorithm, the surface pressure is obtained from an NWP model output combined with knowledge of local topography (see Section 5.2.7). Uncertainties in surface pressure produced by current NWP models vary seasonally and are estimated at 2.5 mb globally (e.g., Devenyi and Schlatter 1994;

Goerss and Phoebus 1993). These errors do not include errors in the interpolation performed as part of pre-processing. The errors can be much larger locally in instances of rapid cyclogenesis. Comparisons between mesoscale models and actual measurements performed in the context of North Atlantic Storm Experiment indicated errors as large as 13 mb. Since both MW and IR have limited sensitivity to surface pressure, the error from NWP first guess does not impact the retrieval accuracy of atmospheric temperature and moisture profiles.

Table 15: Parameters Retrieved in the Microwave.

Parameter	# of elements
Temperature	20 EOFs
Water vapor	10 EOFs
Skin Temperature	1
Surface Emissivity	5 EOFs
Cloud Liquid Water	1
Cloud-top Pressure	1

Note that variable surface pressure causes specific difficulties in the microwave, because the retrieval relies heavily on the natural correlation between surface skin temperature (T_{skin}) and surface air temperature (T_{sfc}). In order to avoid the additional complexity of having to modify background error covariance to accommodate variations in surface terrain height, the algorithm is set to retrieve T_{sfc} and $\Delta T = T_{skin} - T_{sfc}$ instead of T_{sfc} and T_{skin} . In this scheme the surface air temperature also drives the surface skin temperature and the correction term ΔT represents the departure of actual surface skin temperature from T_{sfc} . It should be noted that the retrieval is unaffected by this change of variables. However, because ΔT is statistically uncorrelated with T_{sfc} , the background and background error covariance matrix for ΔT remain independent of terrain height (i.e., the covariance need not be modified over elevated terrain). The derivatives of MW radiances with respect to T_{skin} and ΔT are calculated as follow:

$$\frac{dR}{dT_{sfc}^{new}} = \frac{dR}{dT_{sfc}} + \frac{dR}{dT_{skin}} \quad (0.75)$$

$$\frac{dR}{d\Delta T} = \frac{dR}{dT_{skin}} . \quad (0.76)$$

Equations (0.75) and (0.76) are derived after the transformation of variables.

The microwave algorithm is configured to retrieve surface emissivity in the EOF representation (currently, 5 EOFs are used). This approach captures correlation between different MW channels. The emissivity retrieval is constrained using appropriate covariances described in Sections 5.1 and 5.2 (see also Section 5.3.2 below), with the matrices stabilized by the use of the EOF transformation.

The treatment of clouds in the microwave is described in Section 4.2.4.5.1. The retrieved cloud parameters are total liquid water and cloud-top pressure. ATMS has very limited retrieval skill for the cloud thickness. Currently, clouds are modeled assuming a fixed thickness and a uniform vertical distribution of droplets within the cloud and variations in cloud effective temperature are accounted for by adjusting cloud-top pressure. The algorithm considers Rayleigh absorption by cloud droplets, but ignores scattering by ice crystals and precipitation size particles. The clouds are treated in the linear regime of absorption, e.g. it is assumed that the impact of the vertical and horizontal distribution of clouds is negligible. This may not hold for clouds with high density of water droplets near the cloud-top.

5.3.2 Covariance Stratification

In situations when the retrieval converges within the instrument noise but with poor performance (i.e., lack of information content), improvements can only be achieved by providing a more accurate specification of the *a priori* field (first guess, background mean and covariance). Stratification of atmospheric and surface background and associated covariances is one way of achieving performance improvement. This specification should be based on the physical information about the profile to be retrieved, either contained in the radiances or determined during the retrieval. Such a procedure is sometimes referred to as air-mass classification. We have employed a simple classification scheme based on the land fraction and the skin

temperature and surface emissivities determined during the MW-only retrieval. The flowchart for this scheme is shown in Figure 38. Following an initial MW-only retrieval in which global *a priori* fields (separately for ocean and land) are employed, the scheme selects an appropriate stratified covariance field based on the land fraction (ocean or land), the skin temperature and surface emissivity determined during this initial retrieval. The MW-only retrieval is then repeated with the updated *a priori* field, followed by the MW+IR retrieval with the same field. In total, 8 covariance fields are employed (2 global fields, 4 T_{skin} -stratified fields for land, and 2 T_{skin} -stratified fields for ocean). This simple air-mass classification scheme leads to a noticeable improvement in both the algorithm performance and the convergence rate, especially for cold profiles (i.e., in the polar regions). Moreover, stratifying the covariance fields improves the convergence rate of the algorithm.

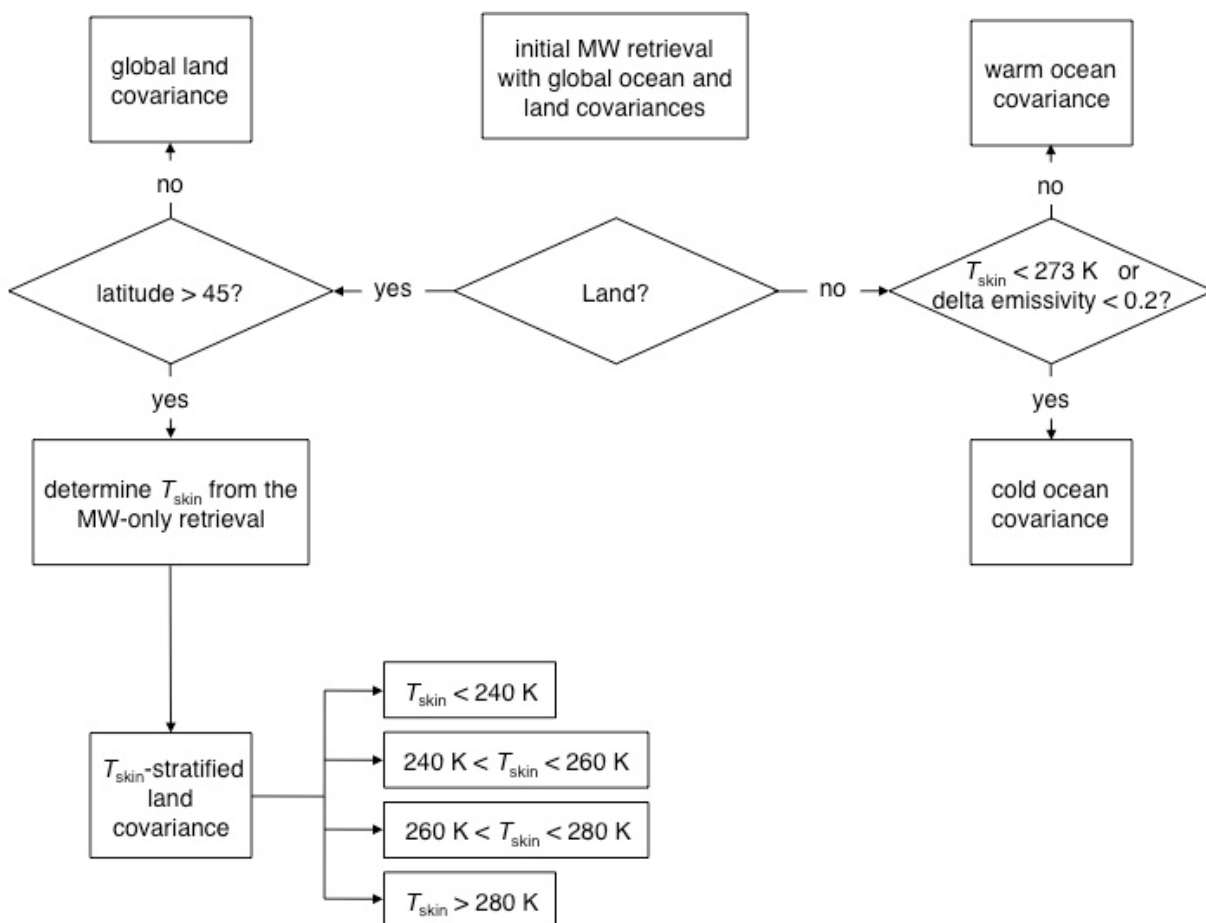


Figure 38: Flowchart for the covariance stratification scheme employed in the retrieval. Delta emissivity is defined as the difference between the retrieved emissivity for ATMS

channels 1 and 22.

5.4 Scene Classification

5.4.1 Overview

The purpose of the scene classification module is to identify the cloud conditions within a FOR. This information is used to determine the appropriate retrieval strategy. A scene classification is essential for optimizing the retrieval quality and interpretation. It is anticipated that the majority of scenes are partly cloudy, to which the cloud-clearing method will be applicable. However, it is also beneficial to have the flexibility to perform clear retrievals and, on the other extreme, to deal with overcast conditions. A scene classification strategy depends on the instrument configuration and the number of FOVs per FOR, with the current scheme designed for a 3×3 FOV configuration. Appendix G addresses scene classification strategies in the event of a detector failure in the CrIS instrument.

Several tests are applied to extract cloud information from the observations. As a first step, each FOV is designated as clear or cloudy by comparing simulated IR clear radiances, generated using the MW-retrieved state vector, with the measured IR radiances. Next, the information content in the measurements is used to estimate the number of “cloud formations” within the FOR following the method of Chahine (1977). This information is used to group the FOVs in a way designed to optimize the retrieval quality and maximize the number of reports per FOR. Each group, or cluster, will have a cloud condition classification assigned to it. This designation will be used to determine the retrieval strategy. The flow diagram of the scene classification module is shown in Figure 39.

5.4.2 Clear FOV Identification

Before determining the number of cloud formations, the FOVs within one FOR are tested for cloudiness. This is done by comparing the observed radiance spectrum with an estimated clear

CrIS spectrum calculated using the atmospheric parameters and surface skin temperature obtained from the MW first stage retrieval. If the RMS difference is smaller than a certain threshold, the FOV is declared “clear”. Since the MW retrieval does not provide IR emissivities and reflectivities, they are fixed to the climatology background. The sensitivity of this method for identifying clear FOVs is limited by the errors in the MW retrieved parameters and errors in the assumed IR surface properties. More accurate estimates of IR emissivity and reflectivity may become possible when external information from other sensors is used. The threshold used is generated from the instrument noise, amplified to account for MW retrieval errors and surface parameter uncertainty. In the current CrIMSS EDR algorithm, the scene classification module only uses clear-FOV test to distinguish between overcast and clear-sky conditions when there is no thermal contrast between adjacent FOVs.

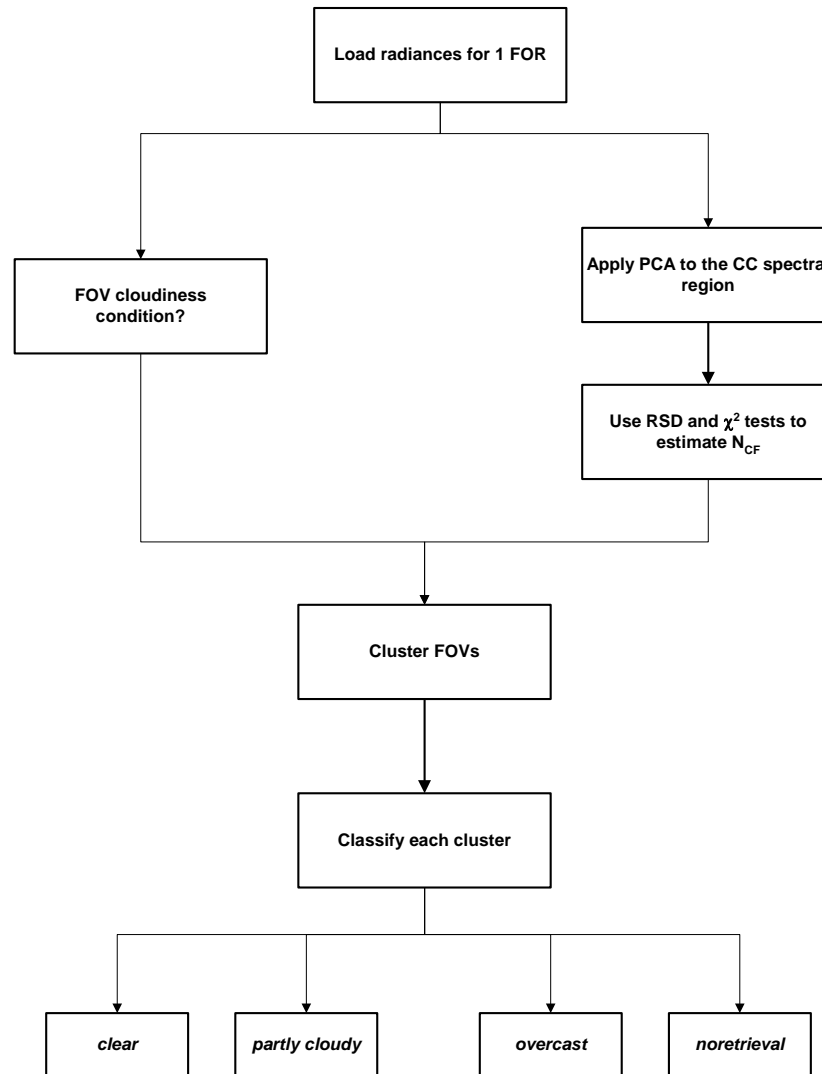


Figure 39: Flow Diagram of the Scene Classification Module.

5.4.3 Estimating the Number of Cloud Formations

Within one FOR, all 9 radiance spectra in the cloud-clearing spectral region between 709.5 and 746 cm^{-1} are used to form a data matrix. The above spectral region is the same region used in the cloud-clearing method (Section 0), thus it is referred to as the CC spectral region. A Principal

Component Analysis (PCA) is performed on this data matrix. In practical implementation, PCA is performed using a Singular Value Decomposition (SVD), with the eigenvalues λ_n equal to the square of singular values. PCA expands the data matrix into 9 orthonormal principal components. The principal components with large eigenvalues are considered significant and are associated with cloud signatures, while the remaining components are associated with measurement noise.

The number of FOVs needed to perform successful cloud-clearing within a FOR is one more than the number of cloud formations, N_{CF} , within the FOR. This number is approximately the number of significant principal components N_{PC} characterizing the scene, $N_{PC} \cong N_{CF} + 1$. Thus, determining N_{PC} allows an estimation of the number of cloud formations.

Two tests are used to determine N_{PC} . The first test determines N_{PC} as the smallest value of n for which the Residual Standard Deviation (RSD), defined as

$$RSD = \left[\frac{1}{nchan * (nfov - n)} \sum_{j=n+1}^{nfov} \lambda_j \right]^{1/2} \quad (0.77)$$

is smaller than the estimated measurement noise ($nchan$ is the total number of channels in the CC spectral region and $nfov$ is 9 for the CrIS configuration). The second test relies on the evaluation of χ_n^2 defined as

$$\chi_n^2 \equiv \sum_{i=1}^{nchan} \sum_{k=1}^{nfov} \frac{[R_{ik} - \hat{R}_{ik}(n)]^2}{\sigma_{ik}^2} \quad (0.78)$$

where R_{ik} is the measured radiance in FOV k and channel i , $\hat{R}_{ik}(n)$ is the radiance reconstructed using the first n components, and σ_{ik} is the noise standard deviation associated with R_{ik} . N_{PC} is defined in this case as the value of n for which $\chi_n^2 < (nchan - n)(nfov - n)$. Since each test could give a different number, the larger of the two is used.

Figure 40 shows an example of Principal Components derived from simulated CrIS radiances for a FOR with 2 cloud layers with cloud-tops at 300 and 400 mb and randomly assigned cloud fractions for each FOV. The associated eigenvalues, λ_n ; $n=1, \dots, N_{FOV}$ ($=9$), are shown in Figure 41. The first component, associated with the largest eigenvalue, represents the average radiance spectrum for the 9 FOVs. As shown in Figure 41, the magnitude of λ_n decreases rapidly as n increases, with the higher components displaying random structure caused by the instrument noise. From Figure 41 it appears that the first three components explain most of the variability of the scene, consistent with the fact that the radiances in each FOV are computed as a linear combination of the clear radiance and two cloudy radiances. From Figure 42 we see that the RSD and $\chi^2(n)$ tests would both return $N_{PC} = 3$, which translates into $N_{CF} = 2$. We also see from Figure 42 the need for the two tests, each line crossing is between $n=2,3$ but not the same distance from these termination points.

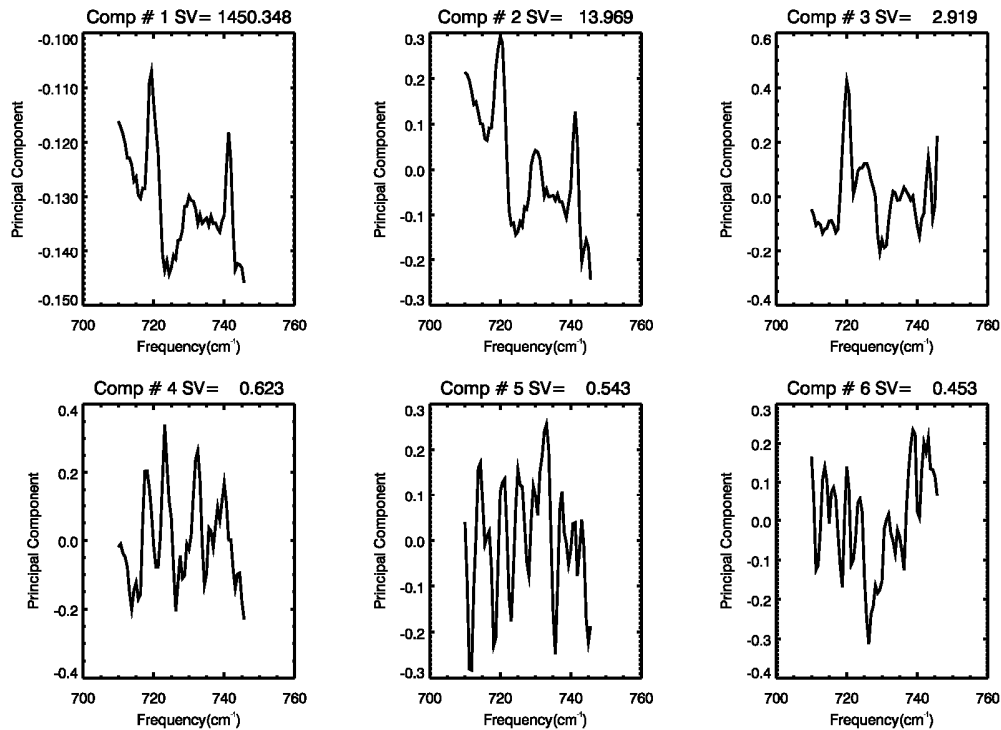


Figure 40: First 6 EOFs resulting from PCA.

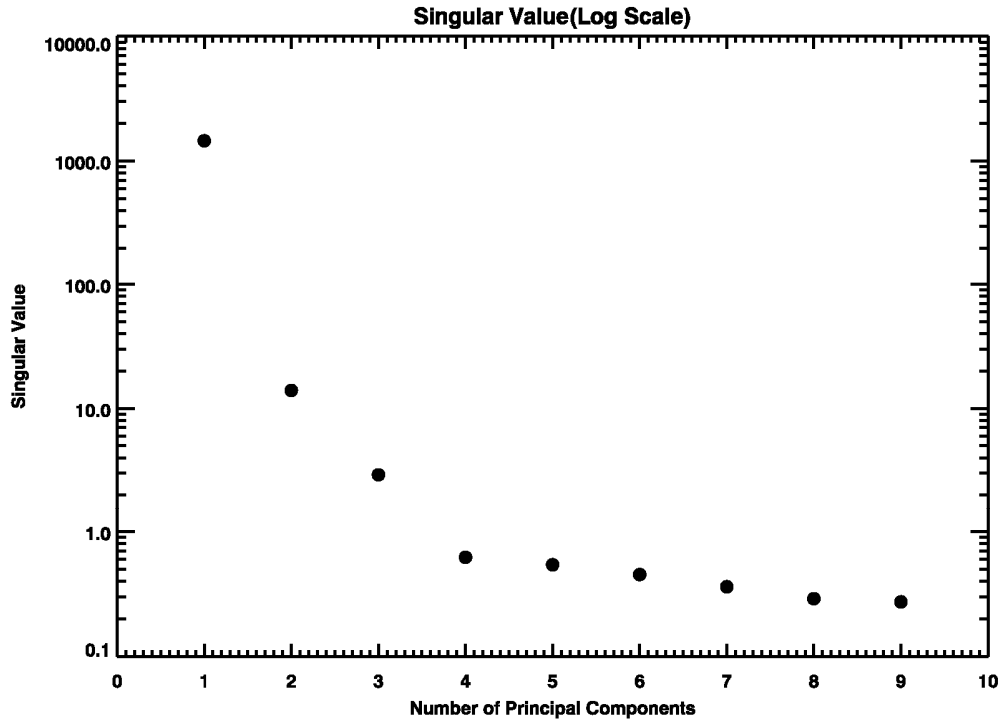


Figure 41: Magnitudes of singular values (equal to the square root of eigenvalues λ).

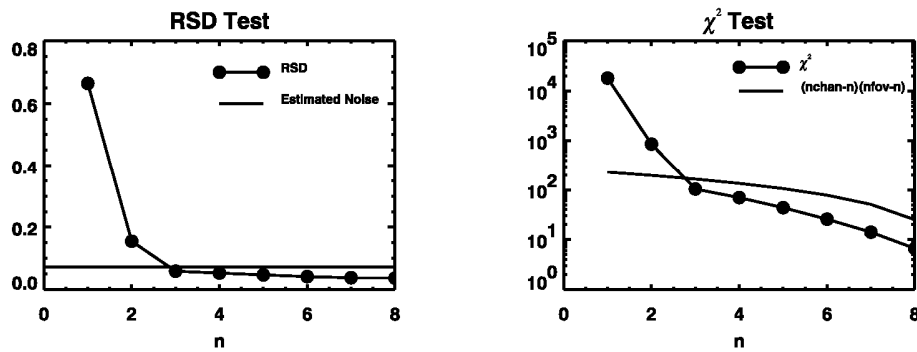


Figure 42: Left: The RSD test as a function of n for the scene described in the text. Right: The χ^2 test for the scene described in the text.

As is the case for the CC method (Section 0), the above technique is more accurate for scenes that are homogeneous except for the cloud structure. Other scene inhomogeneities, such as

surface variability and moisture fields, could cause the number of cloud formations to be overestimated. For scenes that are indeed cloudy this is not necessarily a problem. As we will show in the next section, more sensitivity tests will be performed to check the validity of the cloud formation algorithm. If the scene is in fact clear, yet the inhomogeneities are large enough to still cause a misclassification after all the tests are performed, a reasonable retrieval will still be produced but it will not be optimized for the conditions.

In implementation we have defined tuning parameters to optimize the identification. Results from a detailed trade study of the tuning parameters used in determining the number of cloud formations are presented in Section 7.2. We should also point out that the estimated number of cloud formations, N_{CF} , is used in the cloud-clearing algorithm to ensure that only cloud variability information and not instrument noise is incorporated into the estimated clear sky radiance (see Section 5.5.2).

5.4.4 Formation of FOV Clusters

The most important component of the classification module is the attempt to determine the cloud conditions within the FOR. From there the clustering can be modified to group any combination of FOVs. The implementation of the algorithm can be easily modified to handle any clustering scheme desired. Identifying what is in the scene gives more flexibility in deciding the best retrieval procedure and allows for a better understanding as to what the final retrieval quality should be. We incorporated a classification scheme into the algorithm in order to maximize the amount of information extracted from the measurements.

Once both the FOVs are tested for cloudiness and N_{CF} is determined, the next step consists of the grouping of FOVs within the FOR to form clusters, on which appropriate retrievals will be performed. There are obviously many different groupings that can be implemented, but we will discuss only two which have proven to be most useful in both testing the algorithm and maximizing both the retrieval quality and the number of reports per FOR. Each cluster formed will be labeled either *clear*, *partly cloudy*, *overcast* or *no retrieval*. The appropriate retrieval strategy for each category will be discussed in Section 5.5.1.

The first scheme uses the predetermined estimate of the number of cloud formations, N_{CF} , and chooses from three clustering schemes. The general flow diagram for this scheme is shown in Figure 43. When $N_{CF} = 0$, the second test above has determined that there is no contrast within the FOR. The next step is to determine whether this is a case of a completely cloud-free FOR or an overcast scene. To do this we rely on the FOV-based cloudiness test. If the majority of the FOVs have been determined to be cloud-free, each individual FOV is considered to be a cluster labeled as *clear*. If this is not the case a single 9 FOV cluster is formed labeled as *overcast*.

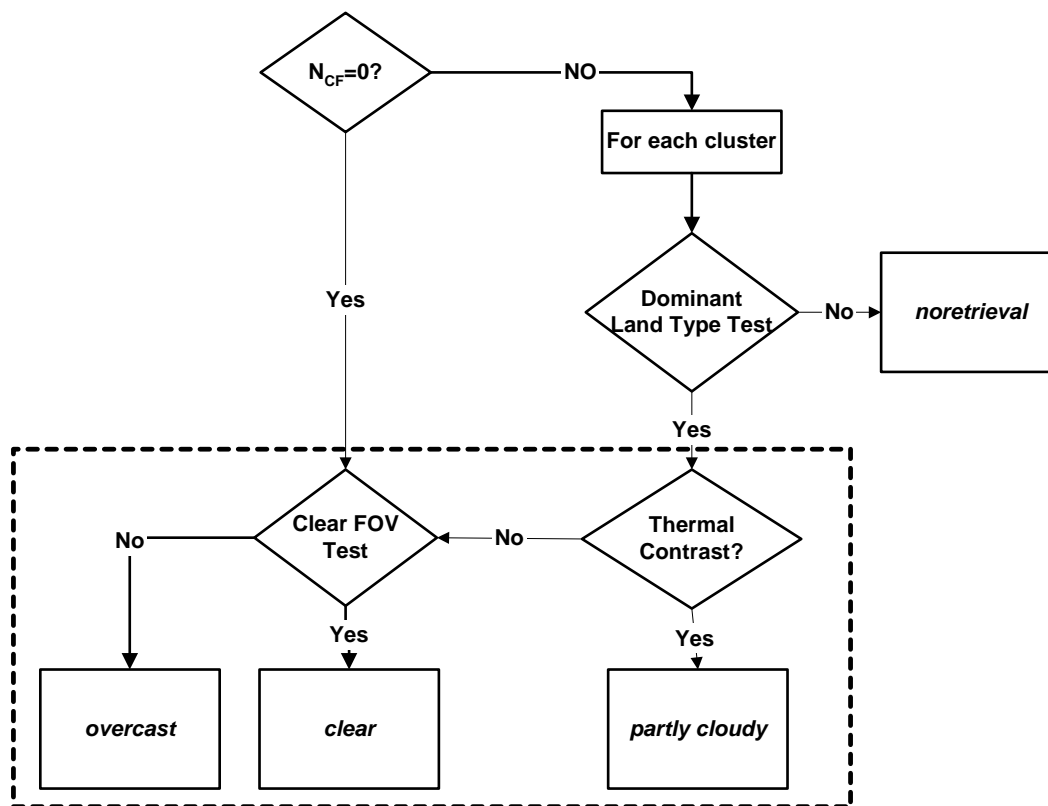


Figure 43: Flow diagram for the surface classification scheme.

When $N_{CF} = 0$, if the FOR is identified as clear by the clear-sky test, each individual FOV is considered to be a cluster and 9 clear-sky retrievals will be performed to provide maximum

horizontal reports, otherwise the one 9-FOV cluster is formed and the cluster is considered overcast. When $1 < N_{CF} < 3$, four clusters consisting of 4 adjacent FOVs in the four corner locations within the FOR are formed. An example of an FOV cluster formed in this case is shown in Figure 44. Similar clusters are formed in the three other corner locations (FOVs # 1, 2, 4, 5, # 2, 3, 5, 6, and # 5, 6, 8, 9). As we discussed above, the cloud-clearing method requires at least $(N_{CF} + 1)$ FOVs per cluster. An additional requirement for this scheme that may reduce the number of FOVs within the cluster to less than 4 is that the grouped FOVs have the same predominant surface type (ocean or land). If the number of FOVs with the same predominant surface type is less than $N_{CF} + 1$, this cluster will be labeled as *no retrieval*. If the cluster fails the thermal contrast test and the FOVs within the cluster are not identified as clear via the clear FOV test, then the scene is assumed to be overcast. When $N_{CF} \geq 3$, all 9 FOVs are combined into a single cluster.

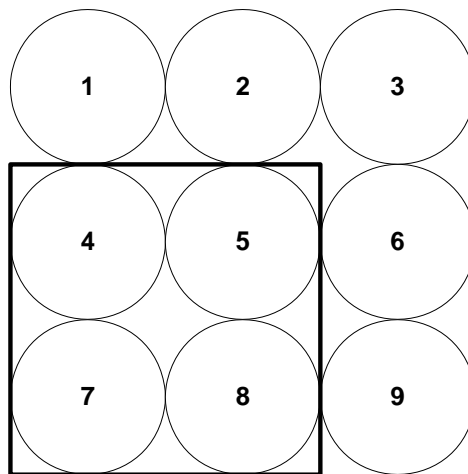


Figure 44: Clustering pattern when the number of estimated cloud formations is between 1 and 3. The four FOVs enclosed in the box are grouped into a cluster. Similar clusters are formed in the three other corner locations within the FOR. This clustering scheme is used when $iclsmode = 1$. See text for details.

For the scenes with $N_{CF} \geq 1$ the clusters are stratified by surface type (ocean or land). FOVs with land fraction $\geq 30\%$ are classified as land, all others are classified as ocean. A sub-cluster is formed from the FOVs with the dominant surface type. If the number of FOVs within the sub-cluster with the dominant surface type is less than $N_{CF} + 1$, the cluster is labeled *no retrieval*, there

is insufficient information to perform CC. If there are enough FOVs within the sub-cluster, a thermal contrast test between the FOVs is performed. Even though the FOR has been determined to be partly cloudy, the clusters need to be tested to determine their conditions. The thermal contrast test consists of calculating the average contrast between the warmest and coldest FOVs within the sub-cluster for channels within the CC spectral range. The determination of which FOV is the warmest/coldest is done by averaging the brightness temperature in the CC spectral region for each FOV and sorting. The contrast is compared with the corresponding average instrument noise for this same spectral region. If the contrast is greater than the noise the cluster is labeled *partly cloudy*. If the contrast is less than the noise we again look at the FOV-based clear/cloudy classification (see Section 5.4.2). This is the same procedure we used for the $N_{CF} = 0$ branch except this time it is applied to the sub-clusters. As we did in that case, we need to determine if the lack of contrast is because the sub-cluster is cloud-free or overcast. If the sub-cluster has been determined to be cloud-free, we label the cluster *clear*. Otherwise the cluster is labeled *overcast*.

The other scheme, for which most of the development and testing of the algorithm has been performed, is to have one cluster with 9 FOVs. This is the method used by the AIRS team and historically operationally. The thermal contrast test is performed on the cluster. If contrast is found and $N_{CF} \geq 0$, the cluster is labeled *partly cloudy*. If not, we look at the FOV-based cloudiness test. As before, if the majority of the FOVs have been determined to be cloud-free, the cluster is labeled *clear*. If not, the cluster is labeled *overcast*. The boxed-in region in Figure 43 illustrates the flow for this scheme. In this scheme, the CC can handle up to 8 cloud formations. In this scheme, the number of cloud formations determined in the scene classification module will only be used in the cloud-clearing algorithm to perform a stable CC parameter retrieval.

It should be noted that the CC algorithm relies on its own thermal contrast test in addition to the information provided by the scene classification module. Depending upon the outcome of this test, the CC algorithm has the ability to switch between a genuine cloud-cleared retrieval and a clear-sky retrieval based on the cluster-mean radiance.

As was pointed out earlier, non-cloud inhomogeneities within the scene could cause misclassification and in fact induce large errors into the cloud-cleared retrieval.

5.5 Joint Microwave and Infrared Retrieval

5.5.1 General Description

The joint microwave and infrared retrieval begins with the FOV selection described in Section 0. Each cluster has been classified by the scene classification scheme. Depending upon the designation, *clear*, *partly cloudy*, *overcast* or *no retrieval*, an appropriate retrieval strategy is implemented. Table 16 lists the four possible outcomes from the scene classification and the corresponding retrieval strategies. When the cluster has been classified as *clear*, a retrieval is performed assuming cloud-free conditions using the MW and IR radiances (i.e., no cloud-clearing is performed). When the cluster is classified as *partly cloudy*, CC is performed on this cluster. When the cluster is classified *no retrieval*, the cluster contains inhomogeneous surface type (i.e., the number of FOVs with the dominant surface type is less than the number of cloud formations estimated during scene classification). No retrieval is performed on this cluster. Finally, when the scene is classified *overcast*, the cluster is assumed to be overcast and no IR retrieval is performed. Instead, the MW only retrieval is reported.

Table 16: Retrieval Flags and Associated Retrieval Strategies

Classification	Retrieval Strategy
<i>clear</i>	Clear retrievals
<i>partly cloudy</i>	Cloud-clearing
<i>overcast</i>	Skip retrieval for this cluster
<i>no retrieval</i>	Skip retrieval for this cluster

As in the microwave-only retrieval, the physical inversion at this stage is based on the modified maximum likelihood method, with the EOF representation used to reduce the dimension of the state vector and accelerate the retrieval. As described in Section 4.3.2, channel weights are dynamically adjusted to account for linearization errors and to improve the convergence rate of the retrieval. An optimization of the IR channel selection also improves the execution time of the algorithm (see Sections 5.5.3 and 0).

The flowchart for the joint microwave and infrared retrieval is shown in Figure 45. For each FOR, the retrieval consists of the following steps

1. Microwave-only retrieval provides first guess estimates of temperature and moisture profiles, skin temperature, surface emissivity, and cloud parameters.
2. The scene classification module uses microwave results to identify clear FOVs.
3. The scene classification module groups FOVs into clusters and sets retrieval flags for each cluster. These flags determine the appropriate retrieval strategy.
4. If the cluster has no thermal contrast between CrIS FOVs, radiances within that cluster are averaged.
5. If the scene is partly cloudy, an estimate of clear infrared radiances R_{clr} is obtained by applying the forward model to the current estimate of the state vector. Cloud-clearing is performed using R_{clr} and radiances from pre-selected FOVs (see Section 0). Only one iteration is performed at this step. Uncertainties in the state vector are accounted for in the error covariance matrix and are assumed to decrease with each iteration. The cloud-clearing parameter η is used to calculate cloud-cleared radiances for all channels used in the retrieval. The implementation of the CC algorithm is described in more detail in Section 0.
6. If the cluster is overcast, IR retrieval is skipped and the MW only retrieval results from step 1 are reported.
7. If the cluster is inhomogeneous (i.e., the number of FOVs with predominant surface type is less than the number of cloud formations), the scheme will skip this cluster and provide no EDRs.

8. A physical retrieval is performed using the radiances obtained from step 4 or 5 and the MW radiances. Temperature and moisture profiles, MW and IR emissivities, IR solar reflectivities, MW cloud parameters, and skin temperature are retrieved simultaneously.
9. If the solution has converged (see below) or the maximum number of iterations is reached, the process stops (the maximum number of iterations is currently set to 4). Otherwise, steps 8-9 are repeated.
10. Quality control is performed and EDRs are reported with appropriate quality flags.

A normalized χ^2 is used to check the convergence of the retrieval

$$\chi^2 = \sum_{i=1}^{nchan} \frac{(R_i^{retr} - R_i^{cc})^2}{N_i} / nchan \quad (0.79)$$

where $nchan$ is the number of channels used in the retrieval, R^{retr} and R^{cc} are the retrieved and cloud-cleared radiances, respectively, and N_i is the noise variance for the i^{th} channel, which includes the noise amplification factor due to cloud-clearing (see Section 0). Currently the convergence criteria are for χ^2 to be less than 0.7 and for the relative change of χ^2 between two consecutive iterations to be less than 10%.

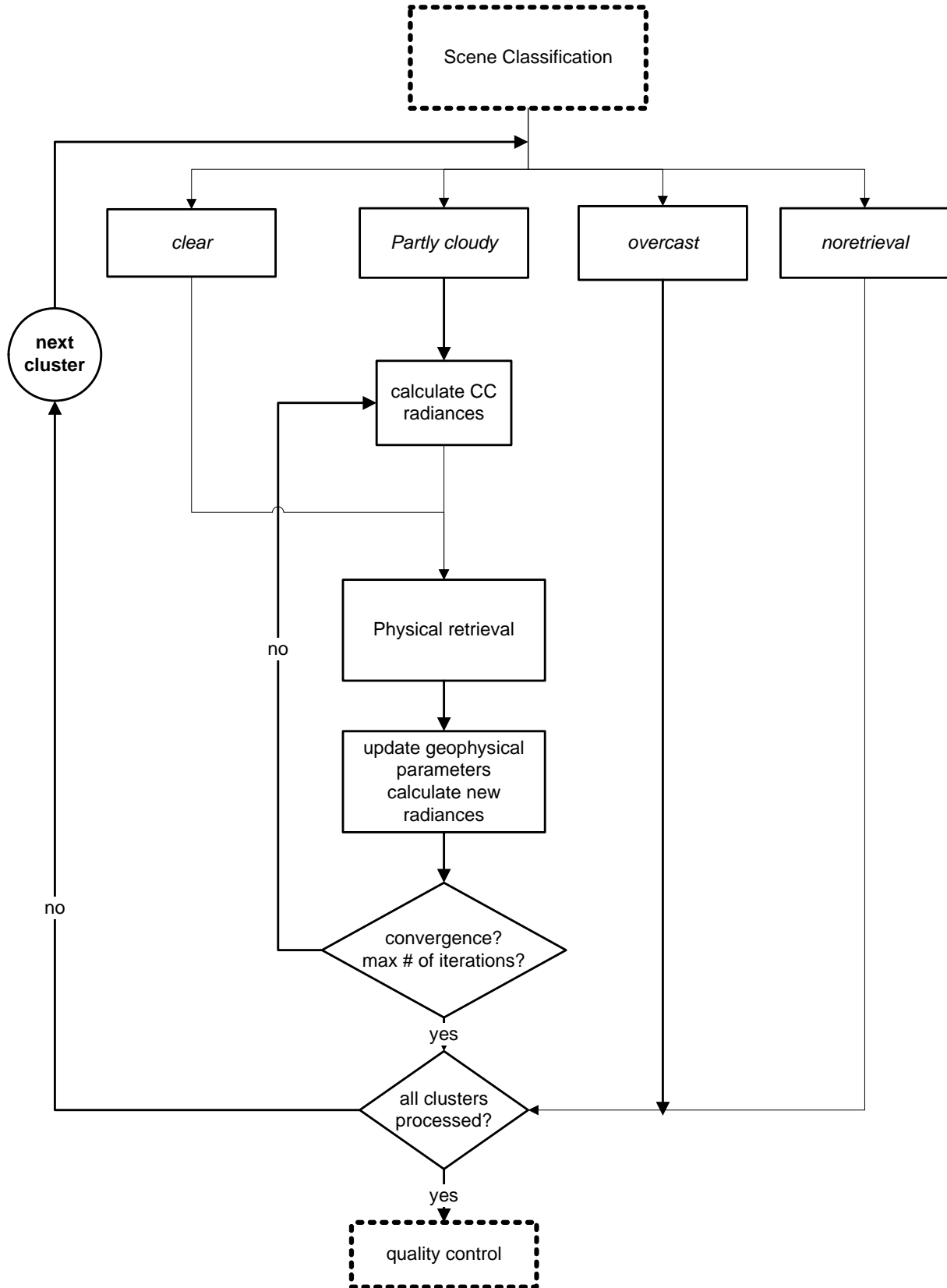


Figure 45: Flowchart for the Joint Microwave and Infrared Retrieval.

5.5.2 Implementation of the Cloud-clearing Method

In the cloud-clearing approach, the measured radiances are used to estimate clear radiances for each FOV cluster (i.e., radiances that would be observed if the entire cluster was cloud-free) and performing the retrieval on these clear radiances. In this approach, there is no need to model the radiative and reflective properties of clouds. The underlying assumption is that the FOVs within each cluster are homogeneous, except for the amount of cloud cover in each FOV. The cloud cover is assigned to different cloud formations, whose number is estimated during scene classification. The clear radiances and the radiances that would be observed if the entire cluster was covered by a particular cloud formation are therefore assumed to have the same values in each FOV. Consequently, differences in the measured FOV radiances within the cluster are attributed to differences in the fractional cloudiness between FOVs.

Based on the above assumptions, the clear radiance $\hat{R}_{i,clr}$ for channel i can be expressed as a linear combination of the measured radiances (Chahine 1977)

$$\hat{R}_{i,clr} = \bar{R}_{i,1} + \eta_1 [\bar{R}_{i,1} - \bar{R}_{i,K+1}] + \dots + \eta_k [\bar{R}_{i,1} - \bar{R}_{i,(K+2)-k}] + \dots + \eta_K [\bar{R}_{i,1} - \bar{R}_{i,2}] \quad (0.80)$$

where $\eta_1 \dots \eta_K$ are unknown channel-independent constants, $\bar{R}_{i,1} \dots \bar{R}_{i,K+1}$ are the measured radiances and at least $K+1$ FOVs are needed to solve for K cloud formations. As discussed in Section 0, in the current implementation of the scene classification module, the number of FOVs within each cluster can only have values of 1 (which corresponds to a clear FOR), 4, or 9. Within each cluster, the FOVs are ordered from the clearest to cloudiest (such that the FOV with the highest $11 \mu\text{m}$ radiances is assumed to be FOV #1). Thus η_1 multiplies the largest radiance differences and η_K the smallest. Once $\eta_1 \dots \eta_K$ are determined, Equation (0.80) is used to reconstruct clear radiances for all channels used in the retrieval process and the reconstructed clear radiances are used in the EDR retrieval.

Applying Equation (0.80) to different infrared channels generally results in different estimates of $\eta_1 \dots \eta_K$. The parameters $\eta_1 \dots \eta_K$ are determined in a least-square sense by assuming that Equation (0.80) holds for a set of N so-called “cloud-clearing channels,” giving rise to the following set of equations

$$\begin{pmatrix} R_{1,clr} - \bar{R}_{1,1} \\ R_{2,clr} - \bar{R}_{2,1} \\ \dots \\ R_{N,clr} - \bar{R}_{N,1} \end{pmatrix} = \begin{pmatrix} \bar{R}_{1,1} - \bar{R}_{1,K+1} & \bar{R}_{1,1} - \bar{R}_{1,K} & \dots & \bar{R}_{1,1} - \bar{R}_{1,2} \\ \bar{R}_{2,1} - \bar{R}_{2,K+1} & \bar{R}_{2,1} - \bar{R}_{2,K} & \dots & \bar{R}_{2,1} - \bar{R}_{2,2} \\ \dots & \dots & \dots & \dots \\ \bar{R}_{N,1} - \bar{R}_{N,K+1} & \bar{R}_{N,1} - \bar{R}_{N,K} & \dots & \bar{R}_{N,1} - \bar{R}_{N,2} \end{pmatrix} R \begin{pmatrix} \eta_1 \\ \eta_2 \\ \dots \\ \eta_K \end{pmatrix} \quad (0.81)$$

or in matrix form

$$C = D\eta \quad (0.82)$$

The weighted least-square solution to Equation (0.82) is given by

$$\eta = (D^T N^{-1} D)^{-1} D^T N^{-1} C \quad (0.83)$$

where N is an error covariance matrix (see below). Equation (0.83) is applied at each step of the iterative solution to the joint microwave and infrared retrieval, with D computed based on the current estimate of clear radiances. At the first iterative step, D is computed by applying the infrared forward model to the geophysical state vector determined by the microwave-only retrieval. Once η is computed from Equation (0.83), the clear radiances in all channels are updated using Equation (0.80), except for channels that are insensitive to clouds, for which a better estimate of clear radiances can usually be obtained by averaging measured radiances

$$R_{i,clr} = \frac{1}{K+1} \sum_{k=1}^{K+1} \bar{R}_{i,k} \quad (0.84)$$

This is equivalent to defining separate values of η for channels that do not see clouds as $\eta = -1/(K + 1)$ and using them to produce clear-radiance estimates for these channels. Currently, a channel is considered to be insensitive to clouds if $|\bar{R}_{i,1} - \bar{R}_{i,K+1}| \leq 3\sqrt{2NE\Delta N_i}$ for the channel.

Two issues of particular importance for the cloud-clearing algorithm are the selection of cloud-clearing channels and the definition of the error covariance matrix N in Equation (0.83). Following Chahine (1974), Susskind *et al.* (1993), and the AIRS ATBD, we include channels in both the 15 μm and the 4.3 μm spectral regions in determining η . The selected channels lie between absorption lines to produce weighting functions with minimal stratospheric contributions and maximum sensitivity to clouds. In addition, channels with strong water vapor and ozone absorption are avoided. Specifically, we define the cloud-clearing region as the intervals 709.5-746 cm^{-1} and 2190-2250 cm^{-1} , excluding cloud-insensitive channels with small thermal contrast (i.e., $|\bar{R}_{i,1} - \bar{R}_{i,K+1}| \leq 3\sqrt{2NE\Delta N_i}$). In situations where the number of cloud-insensitive channels is less than 4, the algorithm sets $\eta = -1/(K + 1)$ and performs a clear-retrieval for the cluster. A potential complication with this approach is that a small thermal contrast between FOVs can exist not only under cloud-free conditions, but can also be caused by identical cloud cover in all FOVs (e.g., full overcast). However, in the latter case, a “clear” retrieval (which is cloud-contaminated) is likely to generate a mismatch with the MW-only retrieval (which is unaffected by clouds) and the profile will be rejected during quality control (see Section 5.6.2). The scene classification module also identifies the overcast clusters so the joint microwave and infrared retrieval can handle the clusters differently.

The definition of N takes into account both the effects of instrumental noise and the uncertainties in the estimates of the geophysical parameters at each step of the iterative process. Thus, channels with either large instrumental noise or which are affected significantly by errors in the estimated profile, which is used to build R_{clr} , should be de-weighted. By applying the theory of the propagation of errors to Equation (0.82) we obtain an estimate of N ,

$$N_{kl} = \sum_{ij} \frac{\partial R_{clr}^k}{\partial X_i} \frac{\partial R_{clr}^l}{\partial X_j} S(X_i, X_j) + \left[\left(1 + \sum_{i=1}^{nfov-1} \eta_i\right)^2 + \sum_{i=1}^{nfov-1} \eta_i^2 \right] NE\Delta N^2 \quad (0.85)$$

Where X_i are state vector elements, R^k are radiances for channel k , $NE\Delta N$ is the instrument noise matrix, $nfov$ is the number of FOVs within the cluster and S is the estimated retrieval error covariance matrix. The first term accounts for the impact of errors in the state vector on the estimated clear sky radiance while the second term accounts for instrument noise. The summation is over all elements of the state vector. The state vector retrieval error covariance is calculated during the inversion procedure and is given by (Rodgers 1976),

$$S = \left(K_i^T S_y^{-1} K_i + S_x^{-1} \right)^{-1} . \quad (0.86)$$

A by-product of the cloud-clearing method is the appearance of the noise amplification factor A caused by the extrapolation of the measured cloud-contaminated radiances to cloud-clear radiances. This factor multiplies the instrument noise variance $\sigma^2(j)$ used to define the error covariance matrix in the full retrieval [Equation (0.57)]. It is equal to $\left[\overline{\delta R} \overline{\delta R}^T \right]_{ii} / NE\Delta N_i^2$, which from Equation (0.80) gives

$$A = \left(1 + \sum_k \eta_k \right)^2 + \sum_k \eta_k^2 . \quad (0.87)$$

When solving for η in the cloud-clearing process, the matrix $D^T N^{-1} D$ contains information about the number of cloud formations. If we perform a singular value decomposition of the matrix (i.e. $D^T N^{-1} D = U W U^T$), the number of significant eigenvectors (U) should be equal to the number of cloud formations plus one. This number has been determined in the scene classification module using the PCA method and two statistical tests based on the sensor noises. Other eigenvectors with small singular values (W) represent the variations due to the noise in the measured spectra. The current EDR algorithm uses the cloud formation information determined in the scene classification module and performs the matrix inversion of $D^T N^{-1} D$ using the truncated SVD method. In the truncated SVD inversion, the eigenvectors associated with

instrument noise are not used in the inversion. The number of significant eigenvectors retained in the inversion equals the number of cloud formations plus one. Thus $(D^T N^{-1} D)^{-1} = U^T W^{-1} U'$, where U' and S' are truncated eigenvectors and singular values. This way the solution for η is much less susceptible to instrument noise. This is very important when the cloud contrasts between FOVs are very small. One such example is a field-of-regard with very small cloud fractions in each FOV such as thin cirrus clouds.

5.5.3 Channel Selection

The CrIS design provides over a thousand channels (see Table 7). However, not all of these channels need to be used in order to meet the CrIS accuracy requirements. An inspection of Equation (0.54) indicates that channels with small values of the partial derivatives K contribute little to the retrieved state vector. Eliminating those channels from the retrieval would therefore have little impact on the retrieval accuracy, but it would help in speeding up the retrieval process. In order to select an optimal subset of channels meeting CrIS accuracy and timing requirements, we have employed a modified version of the entropy-based method described by Rodgers (1996). This section provides a description of our channel selection method. The results from a trade study into the impact of channel selection on the temperature and water vapor retrievals are presented in Section 0.

Channel selection is performed sequentially by ranking channels according to their information content. The entropy (or information content) gained by adding the i^{th} channel to the retrieval can be expressed as

$$\delta S_i = \frac{1}{2} \ln(1 + \hat{k}_i^T \hat{S}_{i-1} \hat{k}_i) \quad (0.88)$$

where \hat{S}_{i-1} is the normalized covariance matrix given $i-1$ previously selected channels and \hat{k}_i is the vector containing the normalized derivatives for the i^{th} channel. The normalization is done according to the formula

$$\hat{k} = S_y^{-1/2} K S_x^{-1/2} \quad (0.89)$$

in which multiplication by $S_y^{-1/2}$ normalizes K with respect to its measurement errors and taking the product $K S_x^{-1/2}$ removes the intra-channel dependencies. At the beginning of the selection process (i.e., for $i = 0$), \hat{S}_i is equal to the identity matrix

$$\hat{S}_0 = I = S_x^{-1} S_x \quad (0.90)$$

The change in entropy is then calculated for each channel using Equation (0.88). After locating the channel with the largest δS , \hat{S}_i is updated using the formula:

$$\hat{S}_i = \frac{\hat{S}_{i-1} \left\{ I - \hat{k}_i \left(\hat{S}_{i-1} \hat{k}_i \right)^T \right\}}{1 + \hat{k}_i^T \hat{S}_{i-1} \hat{k}_i} \quad (0.91)$$

and the process (i.e., Equation (0.88) and Equation (0.91)) is repeated until all channels have been ranked or $\delta S \approx 0$.

The following modifications to the original algorithm described by Rogers have been adopted:

1. In order to meet EDR accuracy requirements, the channels are selected separately for temperature, water vapor, and surface parameters (i.e., the appropriate S_x and K matrices are constructed for each EDR) and then combined into a single set. The combined channel set contains prescribed fractions of channels from the sets computed for each EDR (subject to constraints on the maximum number of channels from each EDR set).
2. Some channels are eliminated prior to the selection process based on their water vapor and trace gas derivatives. This pre-selection technique is designed to eliminate channels sensitive to water vapor from the temperature channel set and those that are affected by trace from the temperature, water vapor, and surface parameter retrieval. Only channels with derivatives falling below a set threshold are incorporated into the entropy-based selection process.

3. *A priori* information can be used to eliminate certain channels and/or bands. This is done by modifying elements of the measurement covariance matrix S_y when calculating δS from Equation (0.88). In particular, setting a diagonal element in S_y to a large positive value reduces $k_i S_y^{-1}$ and the corresponding δS_i for the channel.
4. Entropies are computed using K and δS calculated for N different atmospheric profiles, selected by latitude (e.g., polar, mid-latitude, tropics) and/or terrain type (e.g. ocean, land), with the total entropy for the i^{th} channel equal to the sum of entropies for each profile:

$$\delta S_i^{total} = \sum_{j=0}^N \delta S_{ij} . \quad (0.92)$$

In the baseline algorithm, the retrieval is performed using all channels. However, the algorithm can also perform retrieval using only a subset of channels. While using all infrared channels maximizes the information content of CrIS radiances, it requires significantly more computational resources than the method based on a subset of channels selected in order to satisfy the timing requirements discussed in Section 2.6. In fact, as described in Section 0, a subset of 300-400 channels can be selected to achieve significant time and memory savings with only a small degradation in the retrieval performance. The gain in computation between the two approaches is approximately a factor of 3 (see Section 0). It should be emphasized that the benefits of channel selection are only significant when the ILS is spectrally localized. Channel selection does not improve the computational efficiency when the ILS is unapodized and a broad portion of the spectrum is needed to compute the radiance for a given channel.

5.5.4 Trace Gas Variability

The radiances measured by CrIS depend on the distribution of absorbing species, primarily H₂O, O₃, CO₂, N₂O, CO, and CH₄. In the current CrIS algorithm, only the variations in the vertical profiles of H₂O and O₃ are accounted for, with CO₂, N₂O, CO, and CH₄ treated as “fixed” gases for which standard distributions are assumed (e.g., 360 parts per million per volume for CO₂). However, trace gases exhibit large spatial and temporal variability caused by natural and

anthropogenic sources. This variability may need to be accounted for in order to meet the accuracy requirements for CrIS EDRs.

The focus of the algorithm development work with regard to trace gases has been on devising a correction scheme that would minimize the impact variable trace gas distributions on the EDR retrievals, rather than on retrieving the trace gas abundances themselves. It has been determined that the retrieval of nondimensional column scaling factors (relative to the reference profiles used in generating the OSS optical depth tables) is adequate for this purpose. For N₂O and CH₄ which are well-mixed in the troposphere, a slightly modified column retrieval is also available as an option. The modification consists of adjusting the optical depths for N₂O and CH₄ in such a way that they correspond to a profile in which the mixing ratio of the gas is set to the surface value in the reference profile up to the tropopause level and is left unchanged at the reference value above that level. Following the modification of the optical depths, a standard column scaling factor retrieval is performed. In the current implementation, the tropopause level is determined as the level of minimum temperature in the temperature profile obtained in the MW-only retrieval. To avoid unrealistic tropopause locations (e.g., boundary layer inversions), the minimum is constrained to lie between 400 and 90 mbar and if no such minimum is found, the tropopause level is set to 100 and 250 mbar for tropical and extratropical latitudes, respectively. This retrieval strategy for N₂O and CH₄ (rather than a direct column retrieval) leads to a slight but consistent improvement (1-2%) in the moisture retrieval, especially under cloudy conditions.

Section 7.5 describes a trade study into the impact of trace gas variability on the algorithm performance.

5.5.5 Retrieved Parameters

The parameters retrieved during the joint microwave and infrared retrieval include temperature and water vapor profiles, surface parameters, and column amounts of trace gases. The retrieved parameters are listed in Table 17.

Table 17: Parameters Retrieved in the Joint MW+IR Retrieval.

Parameter	# of elements
Temperature	20 EOFs
Water Vapor	10 EOFs
Ozone	7 EOFs
Other Trace Gases	
Skin Temperature	1**
MW Surface Emissivity	5 EOFs
MW Cloud Liquid Water	1
MW Cloud-top Pressure	1
IR Surface Emissivity	12 hinge points
IR Surface Reflectivity	12 hinge points

** Currently a single skin temperature is retrieved for the microwave and IR bands.

Temperature, Ozone and water vapor profiles are retrieved as the projection coefficients of the pre-determined EOFs. Twenty EOFs for temperature profiles, 7 EOFs for Ozone profiles and ten EOFs for water profiles are adequate for representing the atmospheric variability and stabilizing the inversion algorithm. Owing to the high information content of the CrIS instrument, the correlation between surface air temperature and skin temperature is removed from the background covariance matrix.

The retrieved microwave cloud and surface emissivity parameters are the same as in the MW-only retrieval. The treatment of surface emissivity in the infrared is more complicated than in the microwave due to the hyperspectral nature of the measurement. The infrared surface emissivity can display complex spectral structure and depart significantly from unity in non-vegetated areas in the 10 and 3.7 μm windows. Estimates of this complexity can be determined based on the ASTER database. The ASTER emissivity database indicates that approximately one hinge point every 10 cm^{-1} is required in order to accurately represent the emissivity of rock formations and evaporation present in arid and semi-arid regions. Note, however, that the ASTER database relies on laboratory measurements, and significant smoothing may occur in nature due to mixing of materials within a FOV.

A good retrieval of surface emissivity is needed to maintain retrieval performance for lower troposphere temperature and water vapor. The cloud-clearing algorithm also relies on a good retrieval in the presence of low clouds, since channels used for cloud-clearing are sensitive to surface parameters. However, retrieval simulations have shown that *a priori* knowledge of the

surface emissivity is not required for clear-sky retrievals. Currently, based on limited NOAA-88 database and AIRS-simulated scanline scenes, 12 IR emissivity and solar reflectivity hinge points are retrieved (at 680, 780, 815, 850, 900, 925, 950, 1214, 1245, 1300, 2200, 2550 cm^{-1}). It is expected that retrievals using real data will need a larger number of hinge points in order to represent highly variable surface emissivities in some land areas.

5.6 Quality Control

Assessing the quality of the retrieved atmospheric and surface parameters will be critical for the assimilation of these data into NWP models. We have identified three possible quality control tests that will estimate the accuracy, and hence the usability, of the retrievals. The tests determine the final output profile, either second stage MW and IR retrieval, first stage MW-only retrieval or background. For instance, if the retrieval using only microwave SDR provided an accurate product and the combined microwave and infrared SDR retrieval appeared inaccurate, the microwave retrieval would be the final output. A quality control flag is also returned to indicate which profile is reported.

5.6.1 Normalized χ^2

This test is performed at the end of the joint MW+IR retrieval. The normalized χ^2 used in the test is defined in Equation (0.79) and if its value is larger than 1.0, the retrieval is not reported.

5.6.2 Deviation Between MW-Only and Joint MW+IR Retrievals

Since the retrieval is less sensitive to cloud in the MW compared with IR, the RMS of the retrieved temperature profiles between the MW-only retrieval and the joint MW+IR retrieval can be used to assess the quality of the retrievals. The quantity used in this test is defined as

$$\sigma = \sqrt{\frac{\sum_{i=1}^{nlev} (T_i(MW) - T_i(MW / IR))^2}{nlev}} \quad (0.93)$$

where the sum is over the lowest 3 km of the atmosphere, $nlev$ is the number of pressure levels in that region and T is the retrieved temperature at each pressure level. If σ is larger than 3.0 K, the retrieval is not reported. This test is only performed if the first stage MW retrieval passes the quality control test described below. It should also be noted that this test is only useful if the

MW-only retrieval is close to the truth. If this is not the case, the joint MW+IR retrieval that varies little from the MW-only retrieval, but is far away from the truth, will pass the test. It is also possible that the joint retrieval makes significant improvement over the MW-only first guess, but is nevertheless rejected. Since the MW retrieval performs better over oceans, this test is most reliable for these environments. This test is implemented but not applied in the current algorithm for reasons described in 5.6.3.

5.6.3 MW Quality Control Test

If the MW radiances generated during the joint MW+IR retrieval are very different from the observed radiances, this indicates that there is cloud signature in the cloud-cleared radiances and the normalized χ^2_{MW} for the MW channels, defined in Equation (0.74), is large. In the current code, if χ^2_{MW} is larger than 4, the retrieval is rejected.

Extensive tests at NGST indicate that the IR&MW combined retrievals, if passing the MW quality control test, are far more accurate than the MW-only retrievals. Because this test verifies if the MW radiances can be produced from the IR&MW combined retrieval, and if it is passed, that means the IR&MW combined retrieval results should be one of the solutions to the MW-only inversion, and it is not necessarily less accurate than the output from the MW-only retrieval. In other words, it is impossible to differentiate the quality of these two solutions. However, since the IR data is also used in deriving the IR&MW combined retrieval results, it is more likely this solution is improved rather than degraded over the MW-only results. Our tests have confirmed this.

5.6.4 Flow Diagram

Figure 46 represents an overview of the quality control procedure.

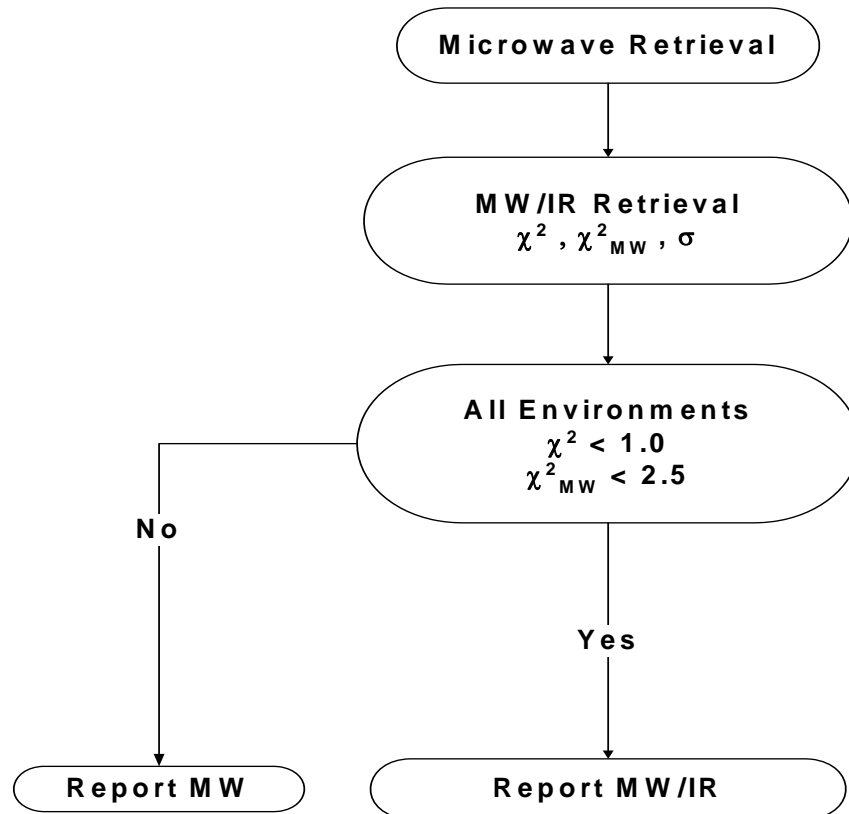


Figure 46: Quality Control Flow Diagram.

5.6.5 Alternative QC Methods

Some of the current QC tests have been ineffective in detecting erroneous retrievals for scenes with low-level clouds in the FOR. Surface properties and atmospheric profiles can compensate for the cloud leading to a residual that is below the threshold.

Several other quality control methods are possible. For ocean scenes, the second stage MW and IR retrieved SST should have little variability for adjacent FORs across a single scan. Large differences in the retrieved SST for adjacent FORs could indicate errors in the cloud-cleared radiances. The cloud-clearing method is more effective for scenes with high clouds. Thus, a test on the variability of the retrieved SST could be used to detect low cloud.

Another approach to QC could involve a comparison between cloud-cleared radiances and co-located VIIRS radiances in cloud-free regions. The minimum cloud optical depth specified for VIIRS is 0.03, which is close to the threshold that affects CrIMSS retrievals. If the difference between the cloud-cleared CrIMSS radiances and cloud-free VIIRS radiances is greater than 2 K, the retrieval may be biased.

5.7 Output and Post-Processing

Important Note: Starting with Version 4.0 of the CrIMSS EDR code, the radiative transfer is performed on a 101-level grid, instead of a 40-level grid. This change is discussed in Appendix F.

5.7.1 Required Outputs

The primary EDRs for CrIMSS are the profiles of pressure, temperature, and moisture, with the pressure profile reported on an altitude grid and the temperature and moisture profiles reported on pressure grids. These reporting grids differ from the internal pressure grid used in the retrieval and RT calculations. The internal grid is determined through a trade-off between computational efficiency and numerical accuracy of the forward model. The internal pressure levels are defined in a slant sensor coordinate system, i.e., along the view angle of the sensor, but to comply with IPO requirements, the EDRs are also reported in a local vertical coordinate system (see Section 5.7.3.4). The choice of slant (rather than vertical) grid for reporting atmospheric profiles provides a product that is not degraded by post-processing. The output in this coordinate system can be expected to be representative of the vertical structure of the atmosphere, as long as the atmosphere is horizontally homogeneous or the scale of the features of interest is greater than 20 km at edge-of-scan. The best approach for making use of the CrIS data in this context is to directly assimilate the product in the satellite coordinate. A complete set of auxiliary data output with the EDRs allows for the precise determination of the location of the temperature or water vapor product at any pressure level.

5.7.2 Optional Outputs

Besides pressure, temperature, and moisture profiles, additional outputs provided by the CrIMSS algorithm include ozone profile, cloud-top height, cloud fraction, cloud emissivity (ice water path for thin cirrus clouds), T_{skin} , and surface emissivity.

5.7.3 Post-Processing

This section describes the post-processing that is performed in the current version of the code.

5.7.3.1 Pressure Profile Computation

As mentioned above, the retrieval of temperature and moisture profiles is performed on a set of internal pressure levels. However, the EDR pressures are required at a set of reporting altitudes (every 1 km between 0 and 30 km) and they are calculated using the following procedure:

1. Specific humidity σ and virtual temperature T_v are calculated for each retrieval level given temperature T and humidity q for the level

$$\sigma = \frac{q}{q+1}$$

$$T_v = (1 + 0.61\sigma)T$$

2. Altitude is computed for each retrieval level using the hydrostatic equation

$$z_i = \sum_{j=2}^i \frac{R_d}{g} \frac{T_{vj} + T_{vj-1}}{2} \ln \left(\frac{p_{j-1}}{p_j} \right)$$

The above summation extends from the surface ($j=1$). p_j are the internal pressure levels (p_1 is the surface pressure), R_d is the gas constant for dry air, and g is the gravity acceleration, which varies with geographical location and height.

3. With surface pressure as the boundary term, the hydrostatic equation is integrated to obtain pressures at the reporting altitudes. In the code this is implemented by an interpolation from the retrieval grid of pressures and corresponding altitudes to a grid defined by the reporting altitudes.

Figure 47 shows the results from 60 pressure profile calculations distributed globally with a surface pressure RMS error of 2.0 mb.

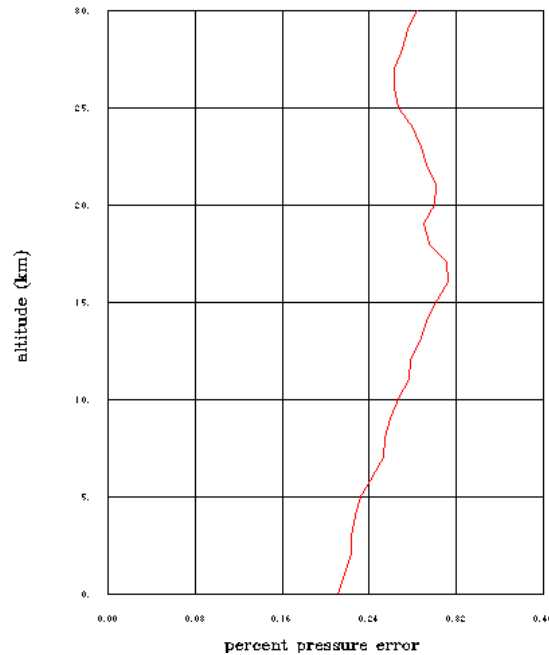


Figure 47: Pressure Profile Uncertainty.

5.7.3.2 Temperature and Water Vapor Profile Interpolation

In order to produce temperature and moisture profiles on the reporting grids, an interpolation from the internal grid (currently 101 levels) to the reporting grids is required. For temperature, the interpolation involves the assumption that the logarithm of temperature varies linearly with the logarithm of pressure. This assumption is rigorously valid if potential temperature is conserved (i.e., under isentropic conditions) and is equivalent to the assumption that temperature varies linearly with altitude if the difference between temperature and virtual temperature is neglected. This is consistent with the approach for calculating pressures at the reporting altitudes. For moisture, a linear interpolation of the mixing ratios is performed between the logarithm of the mixing ratio and the logarithm of the pressure.

5.7.3.3 Vertical Averaging of Temperature and Water Vapor Profiles

According to the CrIMSS EDR vertical reporting specification, the atmospheric temperature and moisture profiles have to be averaged around the vertical reporting pressure with a specific layer thickness. The center of the temperature vertical reporting pressures and the vertical cell sizes are listed in **Error! Reference source not found.**. The center of the moisture vertical reporting pressures and the vertical cell sizes are listed in **Error! Reference source not found.**. According to the reporting requirements, there are 25 levels for moisture and 43 levels for temperature (Table 18).

Table 18: Vertical grids employed in the CrIMSS algorithm.

Level index	Temperature reporting grid (mb)	Temperature reporting cell size (km)	Moisture reporting grid (mb)	Moisture reporting cell size (km)
1	0.5	5	100	2
2	0.7	5	150	2
3	0.9	5	200	2
4	1	5	250	2
5	3	5	300	2
6	5	5	350	2
7	7	5	400	2
8	9	5	450	2
9	10	5	500	2
10	30	3	550	2
11	50	3	600	2
12	70	3	650	2
13	90	3	700	2
14	100	3	750	2
15	125	3	800	2
16	150	3	850	2
17	175	3	870	2
18	200	3	890	2
19	225	3	910	2

20	250	3	930	2
21	275	3	950	2
22	300	3	970	2
23	350	3	990	2
24	400	3	1010	2
25	450	3	1030	2
26	500	1		
27	550	1		
28	600	1		
29	650	1		
30	700	1		
31	750	1		
32	800	1		
33	850	1		
34	870	1		
35	890	1		
36	900	1		
37	920	1		
38	940	1		
39	960	1		
40	980	1		
41	1000	1		
42	1020	1		
43	1040	1		

The following steps are done to perform vertical averaging:

- Logarithmically interpolate temperature and moisture from the OSS radiative transfer pressure grid to the CrIMSS-specified reporting pressure grids.
- Calculate altitudes at reporting grids from the interpolated temperature, moisture, and pressure according to the hydrostatic formula

$$\Delta z = z_2 - z_1 = \frac{RT}{g_0} \ln(p_1 / p_2)$$

where R is the dry gas constant ($= 287 \text{ J K}^{-1} \text{ kg}^{-1}$), \bar{T}_v is the averaged virtual potential temperature between the two levels, and g_0 is the gravitational acceleration at the sea level ($= 9.802 \text{ m s}^{-2}$). The virtual potential temperature is given as $T_v = T(1 + 0.61r)$, where T is the in situ temperature, and r is the mixing ratio (in kg kg^{-1}). The mixing ratio is approximated by the specific humidity, i.e., $r = m_v / m_d \approx m_v / (m_v + m_d) = q$, where m_v and m_d are the mass of the water vapor and dry air, respectively.

- Define cell boundary altitudes from the reporting heights and the thresholds specified by the requirement document for each profile.
- Calculate pressure values at the cell boundaries by interpolation from the cell boundary altitudes, the reporting pressure, and the reporting altitudes.
- Interpolate temperature and moisture from the reporting and the OSS radiative transfer grids to those at cell boundaries.
- Perform arithmetic averaging over all points that fall into each cell.

5.7.3.4 Slant-to-Vertical Conversion

The CrIMSS EDRs are retrieved along the sensor slant path. In order to conform to the CrIS reporting requirements, a slant-to-vertical conversion is performed as part of post-processing. However, since CrIS measurements are not Nyquist-sampled and the retrieval product is provided on a sparse set of locations (reporting interval varies with cloudiness), this conversion is likely to degrade the EDR performance. An error budget allocation for this conversion is based on the EDR requirements listed in Section 2.0, which apply to the quantities defined along the local vertical path (in other words, the conversion errors should be less than the difference between the EDR requirements and the slant path RMS errors). Among several possible approaches to the conversion, a recursive filter method appears to offer the best combination of accuracy and speed. This section offers general information on different approaches to the problem of regridding and describes the recursive filter. An error analysis for the slant-to-vertical conversion based on the recursive filter approach is presented in Section 0.

5.7.3.4.1 General Remarks on Regridding and Interpolation Algorithms

The problem of interpolation of data present either on a grid or at irregularly spaced locations to a set of gridpoints has been the subject of study for a long time in meteorology. Typically, fields are undersampled in meteorology and diverse methods have been devised to spread information to all gridpoints in the neighborhood of observations (Daley 1991; Thiebaut and Pedder 1987). Among possible approaches are: surface fitting (in which functional forms are fitted to available observations), distance weighting schemes (which compute analyzed values from a weighted average of surrounding observations), and statistical interpolation/variational techniques (which take into account the error statistics of observations and background field). The surface fitting method often encounters problems of underfitting (fewer degrees of freedom in the functional form than in the data, leading to a poor fit) or overfitting (more degrees of freedom in the functional form than in the data, leading to a poor analysis in data-sparse areas). Standard distance-weighting schemes perform poorly with an anisotropic distribution of observations (e.g., near the edge-of-scan), since the weights given to observations do not take the relative locations of observations into account. The statistical approaches avoid many of these problems. However, some of them (e.g., those based on 3dvar and 4dvar techniques) are computationally expensive. Lorenc (1992) compared the theoretical basis and performance of statistical interpolation with those of iterative schemes (e.g., the successive correction method) and showed that under certain conditions iterative schemes can approximate the results of statistical interpolation methods. He also demonstrated the near-equivalence of employing a recursive filter on the analysis increments to explicitly take into account the error covariance of the background field.

Based on the above considerations, we have adopted the recursive filter approach for the problem of interpolating a set of CrIS observations located along the slant paths to the set defined by the positions of the local vertical for each FOV. Our approach is based on the methodology of Hayden and Purser (1988, 1995) and is described below.

5.7.3.4.2 Recursive Filter

The recursive filter provides a computationally efficient interpolation method capable of producing realistic results for datasets with spatial inhomogeneities of coverage. This latter feature is especially relevant in the present application, where data gaps may develop under cloudy conditions and near the edge-of-scan. The basic computational steps for the n^{th} pass of the analysis include the following:

1. Background values are bi-linearly interpolated to observation locations (i.e., the slant-path locations) at each pressure level. In the present application, the background field is set to the average value of the meteorological field (temperature or moisture) in the domain.
2. The observation increments (observed value – interpolated background) are spread to the 4 surrounding grid points using the adjoint of the linear interpolation operator

$$\begin{aligned} X_i &= \sum_{k:|dx_k|<\delta}^K \left(1 - \frac{|dx_k|}{\delta}\right) \hat{X}_k \\ \hat{X}_k &= \hat{W}_k (\hat{O}_k - \hat{A}_k) \end{aligned} \quad (0.94)$$

where dx_k is the distance between observation (center of the retrieval cluster) and the gridpoint, δ is the grid spacing, \hat{A}_k is the gridded background interpolated to the observation location during step 1, \hat{O}_k is the retrieved geophysical parameter, and \hat{W}_k is a quality weight.

3. The resulting field of gridded increments is then smoothed through repeated application of the filter, resulting in an updated gridded field for the $(n+1)^{\text{st}}$ pass

$$A(n+1) = A(n) + \frac{G * [W(O - A(n))] + W_b [A_b - A(n)]}{G * W + W_b}. \quad (0.95)$$

This formula is a generalization of Equation (13) in Hayden and Purser (1995), accounting for the deviations of the analysis field from the background field with the weights W_b . The filter operator G^* indicates the distribution and smoothing of values from the observation points to the grid points. It is applied quasi-horizontally (on each pressure level), one or more times, both to the weights W and the weighted residuals $W(O-A)$. The filter consists of a forward and a reverse operator applied in both horizontal dimensions. The fundamental

equation for the forward filter in one dimension is given by equation (1) of Hayden and Purser (1995)

$$A_i' = \alpha A_{i-1}' + (1 - \alpha) A_i, \quad 0 < \alpha < 1 \quad (0.96)$$

where A and A' are the input and output fields, respectively, and $1 - \alpha \equiv \beta$ is a smoothing parameter that controls the spatial scale of the filter. The corresponding equation for the reverse filter is

$$A_i'' = \alpha A_{i+1}'' + (1 - \alpha) A_i' . \quad (0.97)$$

Both the forward and reverse filter expressions are modified at the boundaries to account for the finite size of the computational domain. The result of L iterations of the combined forward and reverse filter asymptotically approaches that of a single application of a Gaussian filter (Barnes 1964)

$$G_j \approx G_o \exp \left[-\frac{|j|^2}{2L(\lambda\delta)^2} \right] \quad (0.98)$$

$$G_o \approx \frac{1}{\sqrt{2\pi(L\lambda^2)}} .$$

with the length scale R defined as

$$R^2 = 2L(\lambda\delta)^2 \quad (0.99)$$

or, equivalently,

$$R^2 = \frac{2L\alpha\delta^2}{(1 - \alpha)^2} . \quad (0.100)$$

In the application of the filter, L and δ are constants, R is prescribed for the analysis pass using the formulation of Hayden and Purser (1995), and α is obtained by inverting Equation (0.100).

4. The updated gridded field is bi-linearly interpolated to the analysis points (i.e., local-vertical locations).

In our implementation, the filter is applied at each pressure level over a quasi-square domain encompassing 40 adjacent scan lines. Available slant-path retrievals (temperature and logarithm of water vapor mixing ratio) in this domain are treated as observations. The resolution of the intermediate grid δ and the filter parameters (L , R , W , W_b , number of analysis passes) are tuned by extensive experimentation with meteorological fields obtained from NWP models (see Section 0).

5.8 Computational Timing

Important Note: These results refer to the 40-level radiative transfer grid. Starting with Version 4.0, the radiative transfer and geophysical parameter retrieval are performed on a 101-level grid (see Appendix F).

Table 19 presents timing results for RT and derivatives calculations and a single MW+IR inversion performed on an SGI workstation with a single 195MHz RS10000 processor. Results for three channel sets are shown, including the full CrIS spectrum (1305 channels), the CrIS spectrum excluding the O₃ main band (937 channels), and a subset of 346 channels selected using the entropy ranking method. The timing results shown in Table 19 refer to the *Blackman* apodization (the results for other apodizations are presented in Section 7.3).

Table 19: Timing (in seconds) for the RT Model and the Joint MW+IR Retrieval.

	Full Channel Set	Channel Set w/o O ₃ Main Band	346 Channels
<i>osstran</i>	0.112	0.072	0.035
<i>ossrad</i>	0.143	0.100	0.043
<i>set_irmw_invert</i>	0.057	0.043	0.016
<i>InvertI</i>	0.099	0.072	0.031
Total	0.310	0.287	0.125

The timing requirements allow for 20 minutes to process 1.25 orbits. The internal processing requirements are 18 minutes, which correspond to 38 ms per FOR. The current CrIMSS algorithm, running on an SGI workstation, is approximately 30 times slower than the requirement. This estimate was calculated using the values given in Table 19 and based on the assumptions that, on average, 3 MW/IR iterations are needed per report, and 3 reports are generated per FOR. It should be noted that the CrIMSS algorithm retrieves temperature and water vapor profiles simultaneously, rather than sequentially. A trade study has shown that this choice results in 14-18% degradation in computational performance.

6.0 ALGORITHM VALIDATION

In addition to testing the CrIMSS EDR algorithms using simulated scenes, it is clearly essential to apply the retrieval method to actual instrument data. To this end we have applied the CrIMSS retrieval algorithm to both satellite-based AMSU and aircraft-based NAST-I observations. This section presents initial results from this study. It should be emphasized that the validation work described here is very limited. It is crucial to have extensive pre-launch tuning and validations to ensure that the algorithm performs to the specifications. Generally, the radiative transfer forward models need to be tested and improved with most up-to-date spectroscopy and co-located truth data. The cloud treatment strategies and methodology and the treatment of surface properties need to be fully tested with real data. The background and covariance information will undoubtedly be improved by using current or future satellite sensors such as AIRS/AMSU and IASI. After the launch of CrIMSS on NPP, the validation of the CrIMSS algorithm will be coordinated with planned field validation activities.

6.1 Validating CrIMSS Algorithm using AMSU Data

6.1.1 Brief Description of the AER Testbed

To validate various algorithms, AER has set up a testbed that collects co-located radiosondes and NWP fields. The NWP (typically NCEP-MRF) field is used for bias tuning and for comparison with CrIMSS retrievals. The sondes have been compiled over 10000 matches with criteria of 6 hours temporal difference and 200 km spatial difference with AMSU measurements. Figure 48 show a flow diagram of the AMSU testbed.

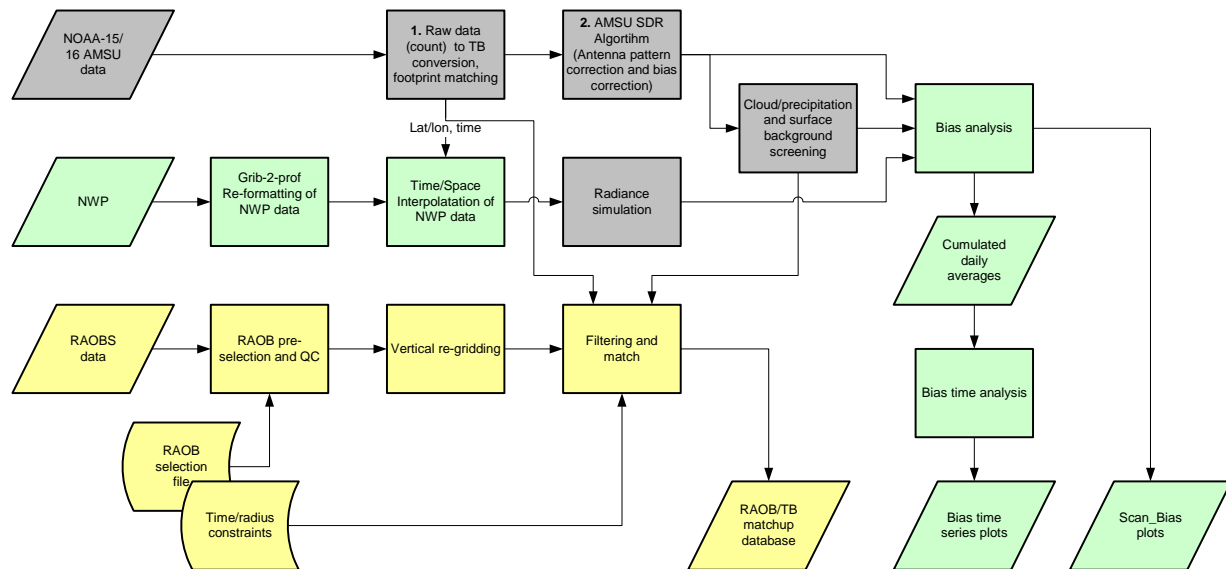


Figure 48: Flow diagram of the AMSU testbed.

6.1.2 CrIMSS MW Retrieval Performance on Real AMSU Data

Figure 49 illustrates the CrIMSS MW retrieval performance (represented as RMS errors in temperature and moisture). The red curves represent retrievals performed on AMSU radiances simulated using raob profiles. The performance is very similar to what is obtained when either the NOAA-88 dataset or scanline dataset are used in simulation/retrieval performance evaluation. The blue curves represent retrieval performance on real AMSU (onboard the NOAA-16 satellite) measurements. The temperature performance is close to the simulated retrieval, but moisture retrieval deviates from the simulated retrieval significantly. This is because moisture is highly variable and the sondes are not exactly co-located with AMSU measurements. The degradation in performance above 300 mb is due to the poor quality of the raobs in the upper troposphere. In the future, using co-located AIRS data should provide a much better moisture truth for comparisons.

Figure 50 and Figure 51 show the total precipitable water (TPW) retrieval from the real AMSU measurements and from the MFR model, respectively. Their difference is shown in Figure 52. The agreement between the NWP model forecast and the AMSU retrieval is very good. The large residuals correlate well with large retrieved cloud liquid water amounts and with large

radiance residual errors. This indicates that the precipitable cloud is the cause of the degraded moisture retrievals.

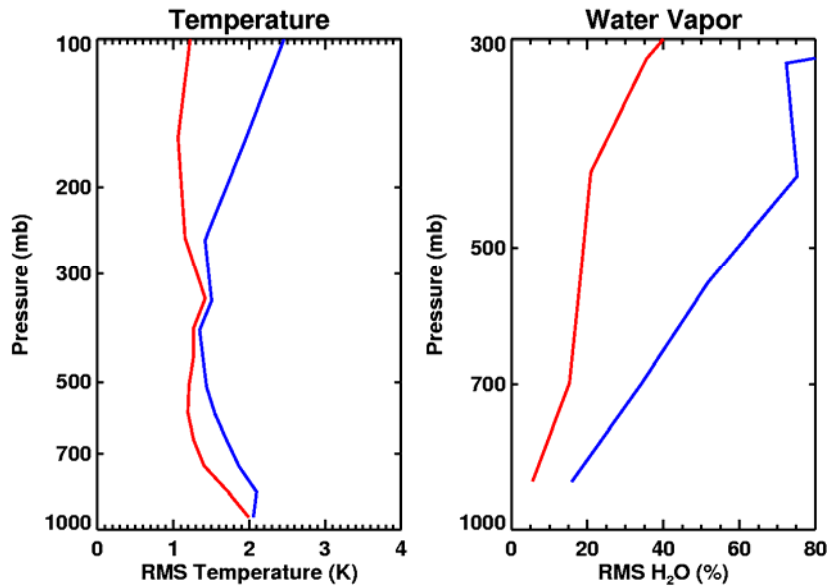


Figure 49: Performance of the CrIMSS MW retrieval algorithm.

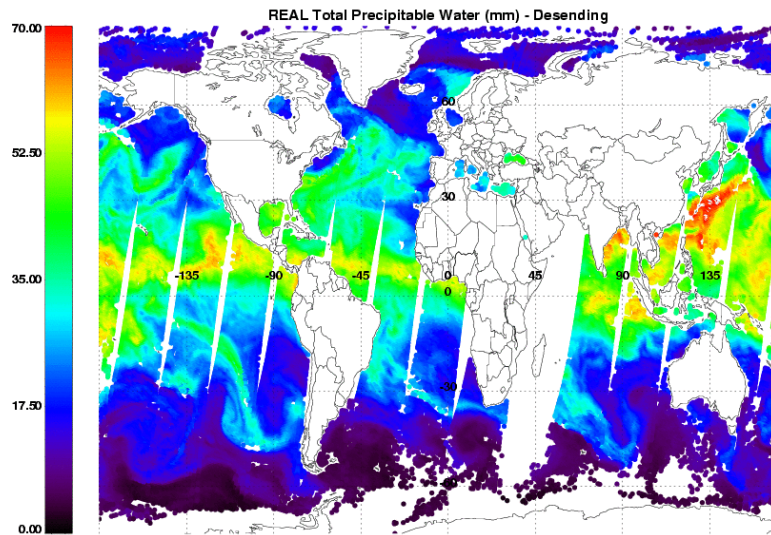


Figure 50: Total precipitable water retrieval from AMSU.

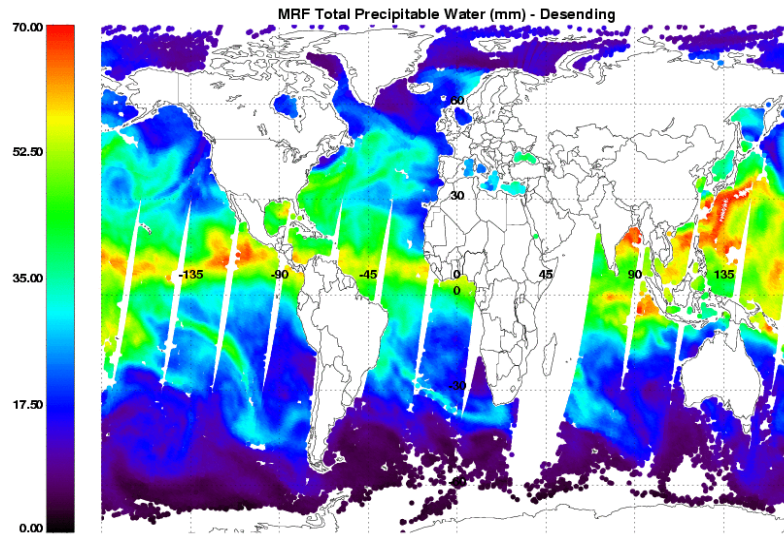


Figure 51: Total precipitable water retrieval from the MRF model.

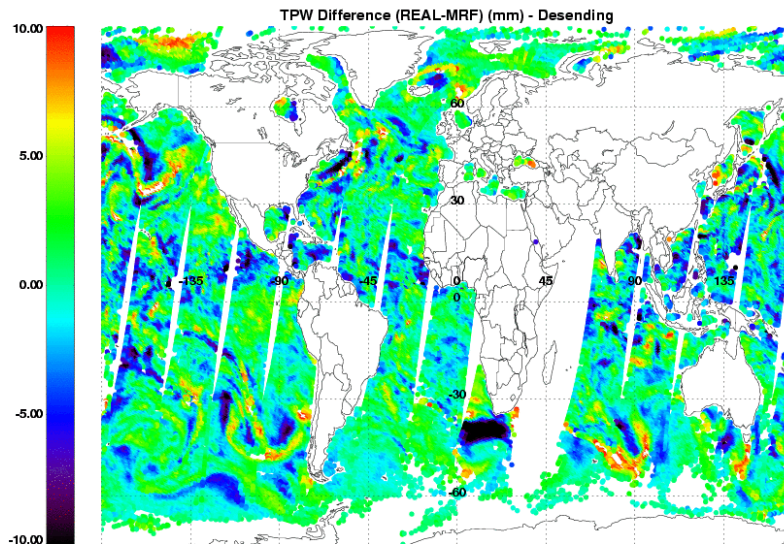


Figure 52: Difference in TPW between AMSU retrieval and MRF model.

Figure 53 shows CrIMSS AMSU retrieval for April 8, 2003 using AMSU-A and AMSU-B measurements from the NOAA-16 satellite while Figure 54 shows retrievals from the NOAA website.

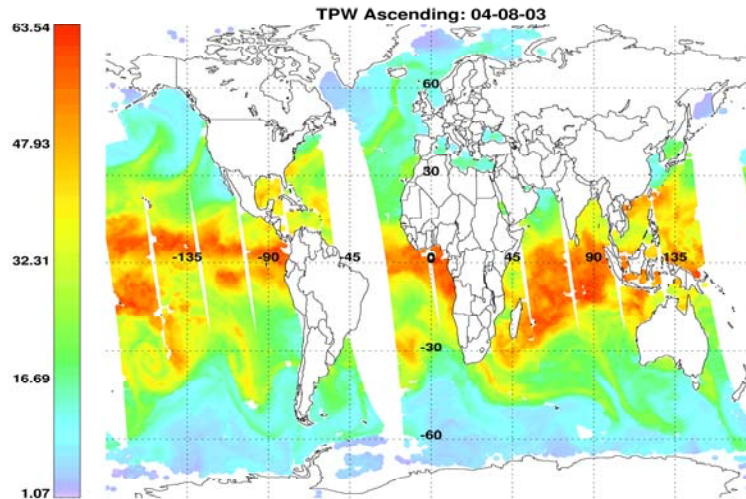


Figure 53: CrIMSS-retrieved TPW from AMSU data.

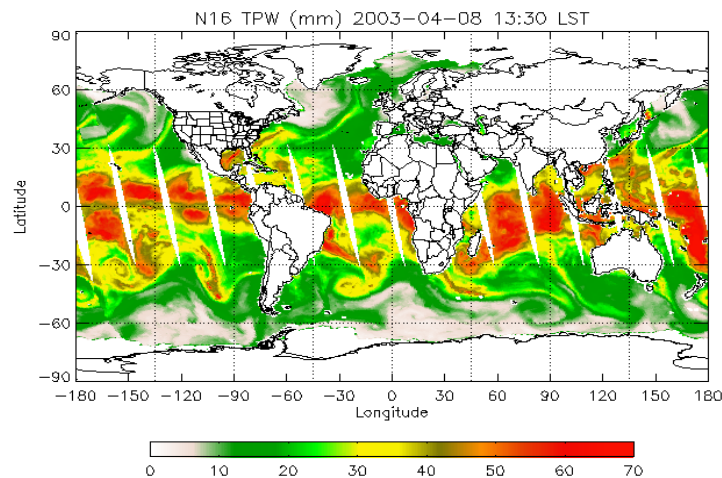


Figure 54: AMSU TPW retrieval from the NOAA website.

6.1.3 Future Work

The above results represent a preliminary validation of the CrIMSS algorithm using real AMSU data. More work is needed to achieve a comprehensive validation and tuning of the CrIMSS algorithm, including more extensive comparisons with NOAA and NASA (EOS AMSU) algorithms, improving retrievals over land and coastlines, and improving the knowledge of MW surface emissivities (the AIRS/AMSU data should provide good data for this purpose). In

addition, an effort should be made to isolate errors from forward model and from measurements in the bias spectra.

6.2 Validation of CrIMSS Algorithm Using NAST-I Data

NAST-I is an interferometer similar to CrIS, but with different spectral resolution and band limits. This section discusses the transformation of the NAST-I measurements to the CrIS spectral grid, followed by an evaluation of the performance of the CrIS OSS model when applied to NAST-I spectra. This evaluation offers a very preliminary validation of the CrIS forward model. Also described are retrieval results obtained using the NAST-I observations during the CAMEX-3 field campaign and their comparisons with ancillary and correlative data.

6.2.1 Degrading NAST-I Observations to the CrIS Spectral Grid

Table 20: NAST-I Instrument Specifications

Spectral Resolution	0.25 cm ⁻¹
Spectral Range: LW	645-1300 cm ⁻¹
Spectral Range: MW	1290-2000 cm ⁻¹
Spectral Range: SW	1980-2700 cm ⁻¹
Spatial Resolution	2.6km @ 20km
Scan Width	=/- 48°
FOR/Scan	13
NEDT	<0.1-0.25 @ 260 K

Table 20 lists the NAST-I specifications relevant for this study. Since NAST-I has a uniform frequency-sampling grid, it is relatively straightforward to transform the measurements from the resolution and coverage given in Table 20 to that of CrIS. The steps are as follows: 1) Transform the measurements from spectral space to optical path difference (OPD) space by FFT methods. This will generate an interferogram. 2) Apply a *Blackman* apodization to the interferogram. 3) Transform the resulting interferogram back to spectral space, again using FFT. 4) Resample the apodized spectra to the CrIS spectral grid. Figure 1 shows a measurement on both the NAST-I grid and CrIS grid.

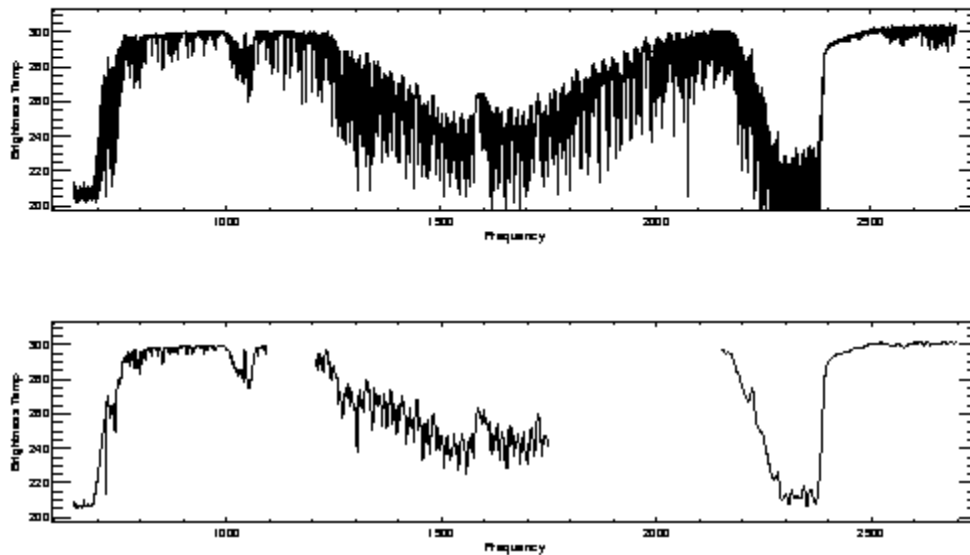


Figure 55: Top: NAST-I measurement Bottom: NAST-I degraded to CrIS resolution and with a Blackman apodization applied.

6.2.2 Preliminary Evaluation of the CrIS Forward Model

It should be emphasized that this study was carried out with an early version (V2.0) of the CrIMSS code and should be repeated with the latest version of the CrIMSS code after finishing the update of the radiative transfer model. There are several issues that make this CrIS version of OSS inadequate for retrievals on NAST-I measurements. The two issues preliminarily addressed here are: 1. Neglect of important atmospheric absorbers, such as nitric acid and chlorofluorocarbons, and 2. Relatively coarse atmospheric layering. An initial attempt to perform retrievals with version 2.0 of the CrIS forward model failed, with the radiance residuals showing apparent signatures of molecules not included in the radiative transfer model. To compensate for these missing absorbers and potential layering issues, a comparison was made between the latest CrIS model and an NAST-I specific OSS forward model that included the missing absorbers and had more layers. Fifty random NOAA-88 profiles were used to generate radiances with each

model. A simple bias curve was generated from the radiance residuals. Figure 56 shows the bias in brightness temperature.

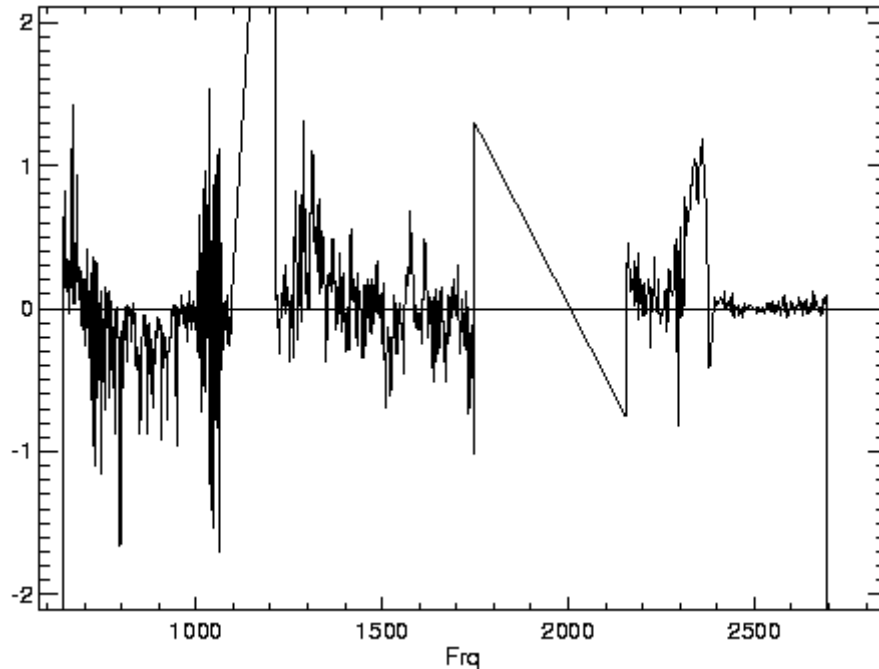


Figure 56: Bias correction, in brightness temperature, applied to NAST-I observations before retrievals are performed. This correction has been obtained by comparing CrIS OSS with a model that includes more layers and more absorbers.

The two RT models are very similar, the only difference being that the NAST-I model includes more layers and more atmospheric absorbers than the CrIS model. Figure 57 shows the difference between two runs of LBLRTM, one with the trace gases indicated, the other with these excluded. By comparing Figure 56 and Figure 57, it is evident that the signatures of F11, F12 and HNO₃ are missing from the CrIS version of the OSS forward model. The rest of the residual in Figure 56 is due to layering, which accounts for the bulk of the bias in MWIR and in the CO₂ region in LWIR. Thus as a first order attempt to correct for the deficiencies in the CrIS model, the bias curve in Figure 56 was added to the NAST-I observations before retrievals were performed (results are shown below).

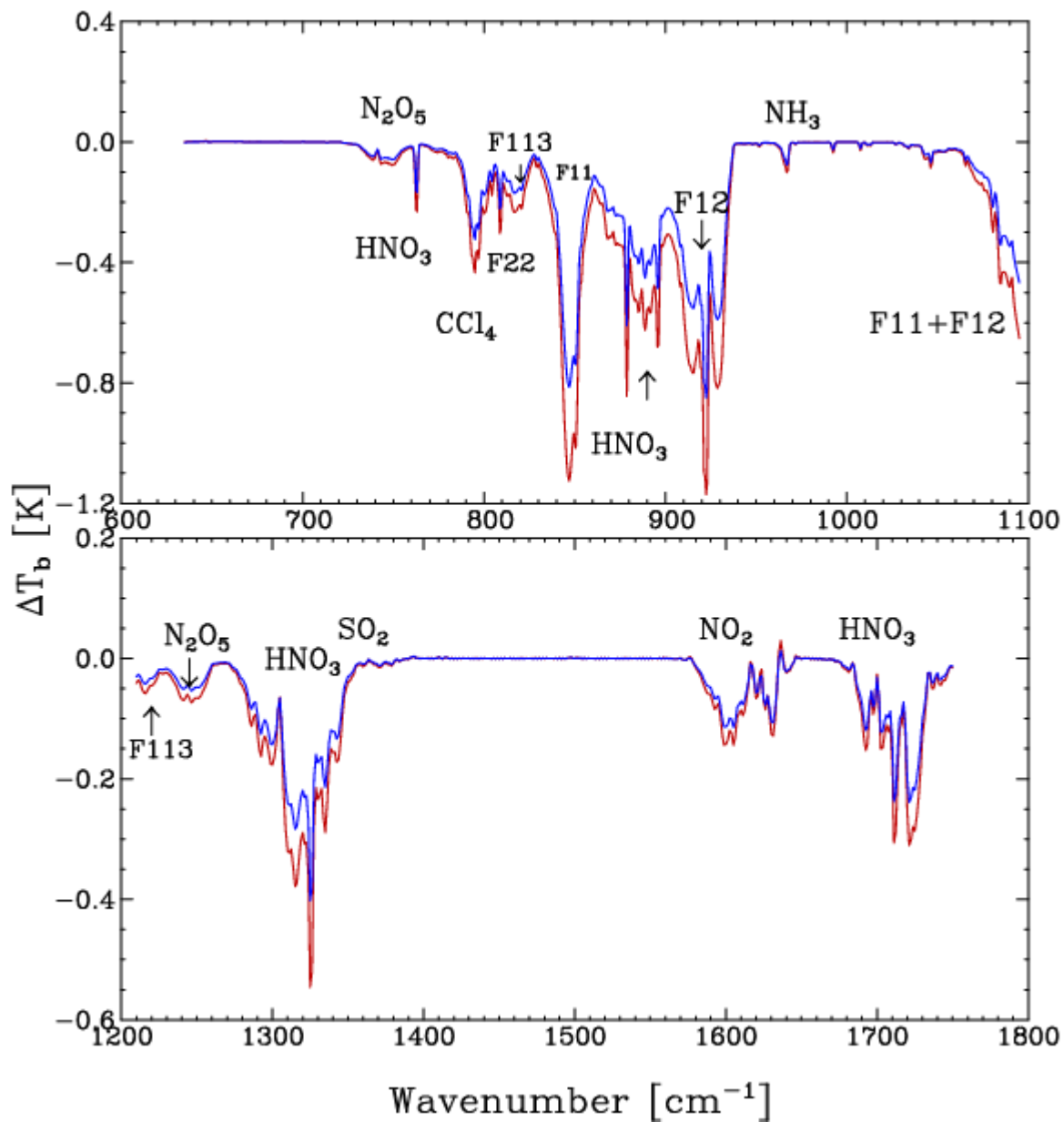


Figure 57: Difference between LBLRTM-generated radiances with and without certain trace gases included. The gases are indicated in the region where they have significant spectral features. The blue curve is for nadir calculations while the red curve is for calculations performed assuming a 45° observation angle.

6.2.3 CAMEX-3 Retrievals

The CAMEX-3 field campaign took place in August and September 1998. NAST-I data were collected during this campaign. On September 13-14, NAST-I was mounted on the ER-2 which flew in loops off the coast of Andros Island in the Bahamas. Several other airborne and ground based instruments collected data during this time period. The most relevant for this study were radiosondes launched from the Island and dropsondes dropped from a DC-8 which flew in unison, but at different altitudes, for a period of time. Figure 58 shows the flight path and locations of the radiosonde launch points and where the dropsondes were employed.

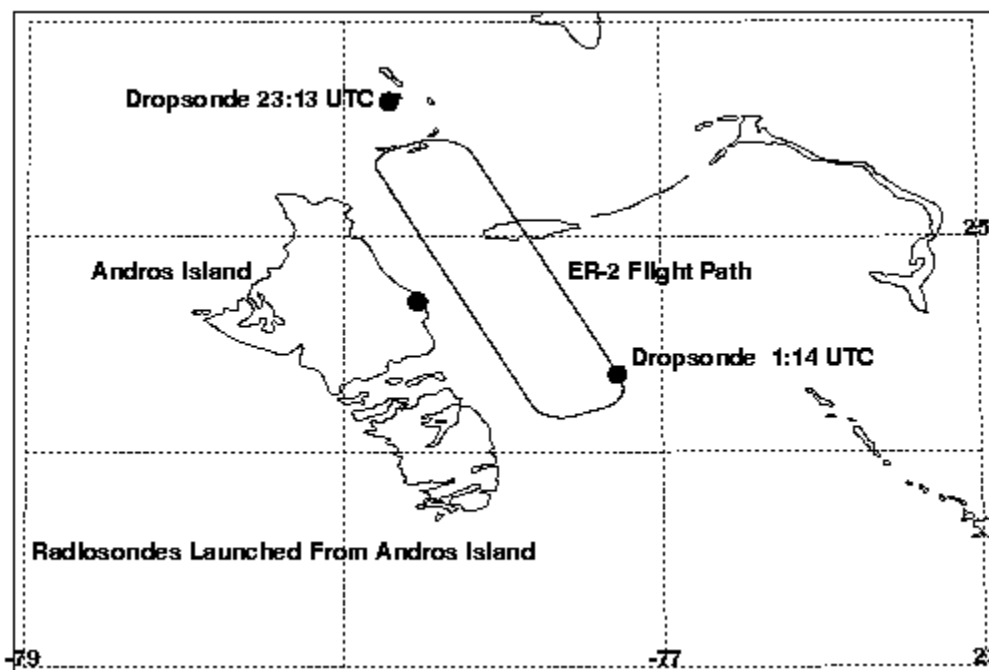


Figure 58: Flight path of ER-2, location of radiosonde launch and locations of dropsondes for CAMEX-3 on September 13-14.

NAST-I is a cross-track scanning instrument but we have only performed retrievals on the nadir looking measurements. The ER-2 performed the loop pattern illustrated in Figure 58 about five times during this observation period. We performed retrievals for all measurements for which the ER-2 was not in a turn. Figure 59 shows a comparison between the radiosonde collected at 23:47 and a close in space and time observation. Even though there are co-location issues with the radiosonde, the retrieval captures the general features, in particular the increase in moisture

above 400 mb. The radiosonde is compared with the single retrieval which optimizes “how good” the retrieval appears since we can choose from several retrievals that are reasonably close in space and time; we do not have a direct fly-over for this pass. All retrievals in the general area close to the launch point have the same general shape as the moisture profile, increase in moisture around 400 mb, but there is variability for adjacent measurements. We feel that for the most part we are capturing true variability since independent retrievals performed upon LASE observations (http://asd-www.larc.nasa.gov/lidar/cm3/cm3_15.html) also indicate large local variations in the moisture content.

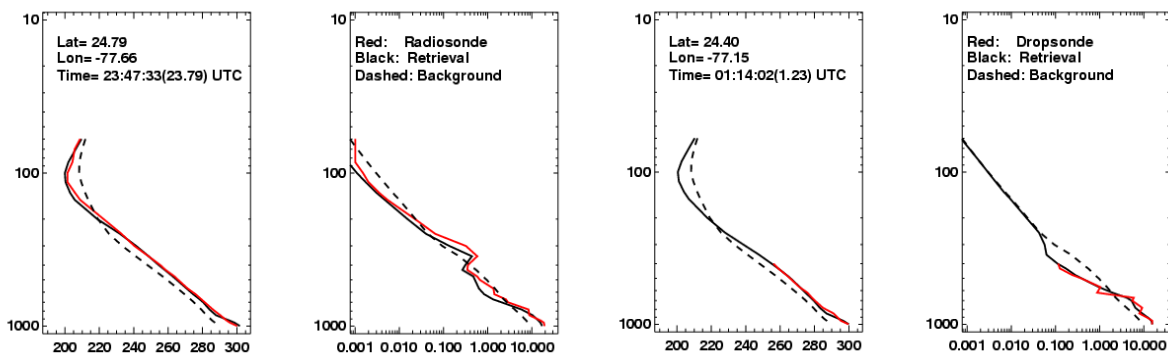


Figure 59: Comparison of NAST-I retrievals with radiosonde launched from Andros Island (left) and dropsonde dropped from the DC-8 (right).

Also shown in Figure 59 is a comparison between the measurement closest in time and space to the time and location of the drop point for the dropsonde. This case is basically co-located, but the dropsonde was on the DC-8 which only flew at about 8 km (400 mb). The comparison is quite good below 400 mb. Above 400 mb, the retrieved moisture is very different from measurements taken closer to the island. As shown in Figure 60, the retrieved upper tropospheric moisture exhibits significant large-scale variability, with a large decrease between the island-side pass and the pass further from the island. This feature is also retrieved independently from LASE observations. Figure 61 demonstrates that this moisture structure is real and part of a large-scale moisture variation. It should be pointed out that only two passes, one close to the island and one further from the island, are shown in Figure 60. The pattern of low to high upper tropospheric moisture when moving away from the island repeats itself for all the passes. It should also be

noted that the ER-2 headed back for Florida after performing the looping pattern and there were NAST-I observations for this time period. Figure 61 indicates even larger moisture content on the west side of the island and indeed we retrieve increased moisture amounts in the upper troposphere in this region.

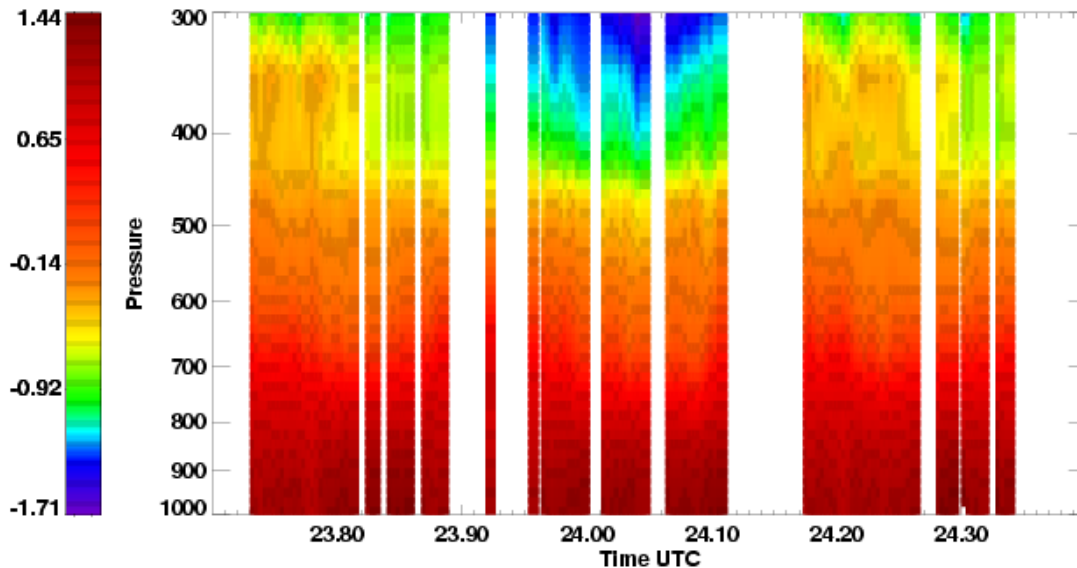


Figure 60: Moisture retrieval pattern, on a log scale, as the ER-2 flies on a pass close to the island, far from the island and then back close to the island. The wide gaps in the retrievals represent flight turns while the narrow gaps are caused by clouds and a small island (see Figure 58). CrIS retrievals, performed on a sparse pressure grid, have been interpolated to generate a continuous plot.

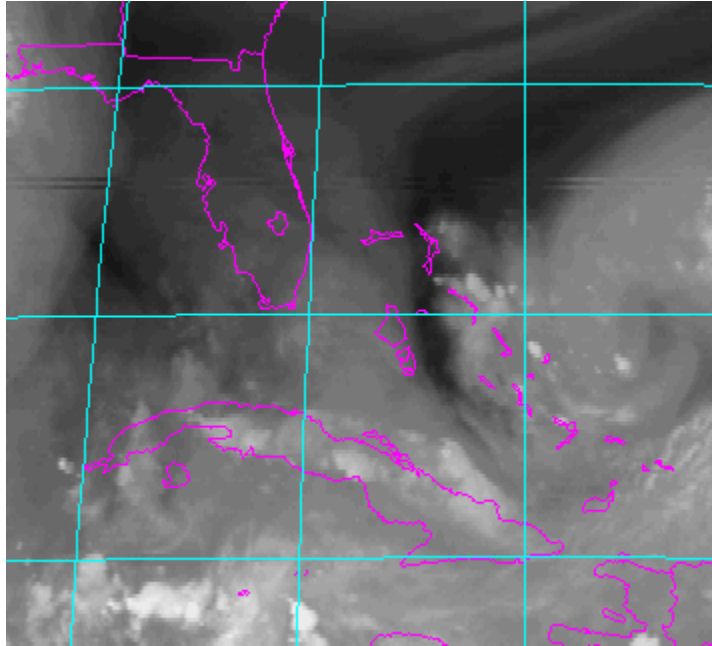


Figure 61: GOES water vapor channel image of the Andros Island region taken on September 13 and 23:45 UTC.

6.2.4 Future Work

The most pressing issue is the update of the radiative transfer model, incorporating the latest spectroscopy and all known absorbers in the spectral regions covered by CrIMSS. Several campaigns have been run since CAMEX-3 for which NAST-I has flown and co-located radiosondes have been collected. These data should be analyzed with the most up-to-date OSS model and CrIMSS retrieval algorithm. Once the radiative transfer model and clear retrievals are satisfactory, retrievals under partially cloudy conditions will be performed.

7.0 TRADE STUDIES

7.1 Impact of Inversion Method

In this study, the maximum-likelihood (ML) method for solving Equation (0.54) was compared with the Levenberg-Marquardt (L-M) method and the DRAD method. The three methods (described in Section 4.3.2) have been evaluated with regard to their convergence properties and the resulting retrieval errors using sets of simulated data to mimic different environmental and initial conditions.

In the first set of test cases, 200 profiles were retrieved using simulated radiances to mimic clear and cloudy land/ocean conditions. In all cases, a simulated AMSU/MHS microwave retrieval was used to provide an initial guess for the IR-based CrIS retrievals. The profiles, in the clear-sky cases, were obtained using simulated radiances for one CrIS instantaneous field-of-view (FOV), and the cloudy profiles were estimated using the radiances for 3 FOVs and the cloud-clearing algorithm. The radiances for the cloudy cases were simulated using a 2-layer cloud model. This simulated cloud structure had cloud-tops at 396 and 618 mb, and cloud fractions of (0.13, 0.12), (0.23, 0.22) and (0.32, 0.33) in each of the 3 FOVs. This cloud formation is equivalent to the hard cloud case described in Susskind *et al.* (1998).

The temperature and water vapor profiles were obtained carrying out 8 iterations with each of the three inversion algorithms. At each iteration, the resulting profiles as well the χ^2 errors were recorded. The χ^2 at each iteration was divided by the number of CrIS channels to form "normalized" χ^2 values. These values were then used to establish a simple convergence criterion. The criterion was met if the χ^2 was less than a fixed threshold. Finally, a retrieval rate was calculated based on the number of cases that meet this criterion at each iterative step. The resulting retrieval rates for each of the three algorithms and their average errors are shown in Figure 62 and Figure 63. These plots illustrate that the DRAD and the L-M algorithms have comparable retrieval rates. They also show that the ML algorithm's performance lags behind the other two in both clear and cloudy cases. These plots also show that the average χ^2 does not

decrease asymptotically for all cases. This indicates that the ML method does not converge for all of the test cases.

Figure 64 through Figure 66 show the root mean square (RMS) errors for the first 4 iterations of DRAD, L-M, and ML algorithms (these results were obtained for the same 200 clear-sky land scenes as above). The DRAD and the L-M algorithms have similar RMS values, but the DRAD method requires 2 iterations to obtain a stable solution, whereas the L-M reaches it after a minimum of 3-4 iterations. In this case, the ML algorithm actually diverges from its minimum water vapor error as the number of iterations increases. This indicates that the ML method tends to overfit the data, which is in part due to the fact that S_ϵ does not represent the errors associated with the forward model (mapping from profile to radiance space).

Similar comparisons have been performed using a first guess based on climatology. These experiments were designed to assess the robustness of the inversion approaches with respect to the quality of the first guess, which is an important consideration in operational environments. The clear-sky cases described above were rerun under these conditions. The resulting retrieval rates and average errors are plotted in Figure 67 and their average temperature and water vapor RMS errors for the first 4 iterations are shown in Figure 68 through Figure 70. These plots illustrate the importance of a good initial guess and demonstrate that the performance of all 3 algorithms is affected by the initial conditions. The L-M and ML algorithms are most affected by the lack of a good initial guess. Under these conditions the ML algorithm has an unacceptable retrieval rate of $< 50\%$.

Overall, this study has shown that the ad-hoc DRAD algorithm has better performance than either the Levenberg-Marquardt or the maximum likelihood methods. The most noticeable improvement in performance is obtained when the initial guess is based on climatology rather than the microwave retrieval. These results illustrate that the performance of the DRAD, L-M and ML is tightly coupled to the initial guess, with the DRAD method showing superior convergence characteristics when the first guess is far away from the true solution. This is an important consideration in selecting an appropriate inversion technique for an operational algorithm. The DRAD algorithm has the added advantage in that its control parameter α is easy

to tune. Numerous trials have shown that varying α between 2 and 10 has only an impact on the retrieval process. The control parameter λ in the L-M algorithm, on the other hand, can have a significant impact on the retrieval process. Assigning λ a large initial value degrades the convergence rate, whereas setting λ to a small initial value may force the algorithm to spend several iterations searching for the appropriate step size.

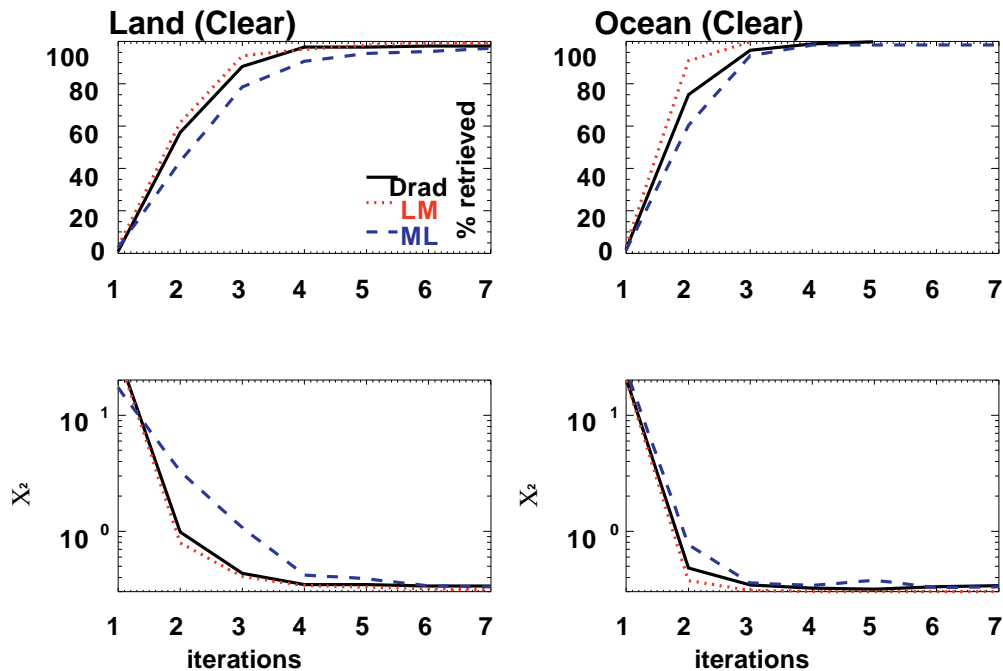


Figure 62: Algorithm retrieval rates and χ^2 values versus iteration number for clear-sky land and ocean cases (microwave first guess). Results obtained using the DRAD, Levenberg-Marquardt, and Maximum Likelihood methods are shown. The upper plots describe the number of retrievals that meet the radiance convergence criterion ($\chi^2 < 2$). The lower plots show average χ^2 values for profiles that converged in 8 iterations.

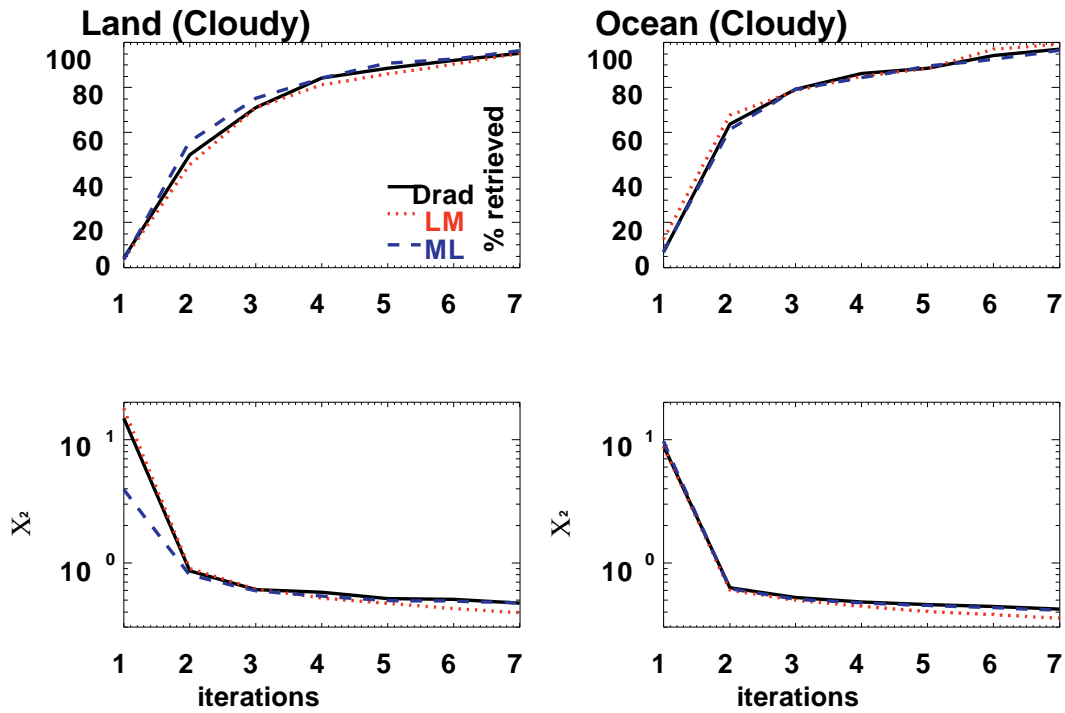


Figure 63: Algorithm retrieval rates and χ^2 values versus iteration number for clear-sky land and ocean cases (microwave first guess). Refer to Figure 62

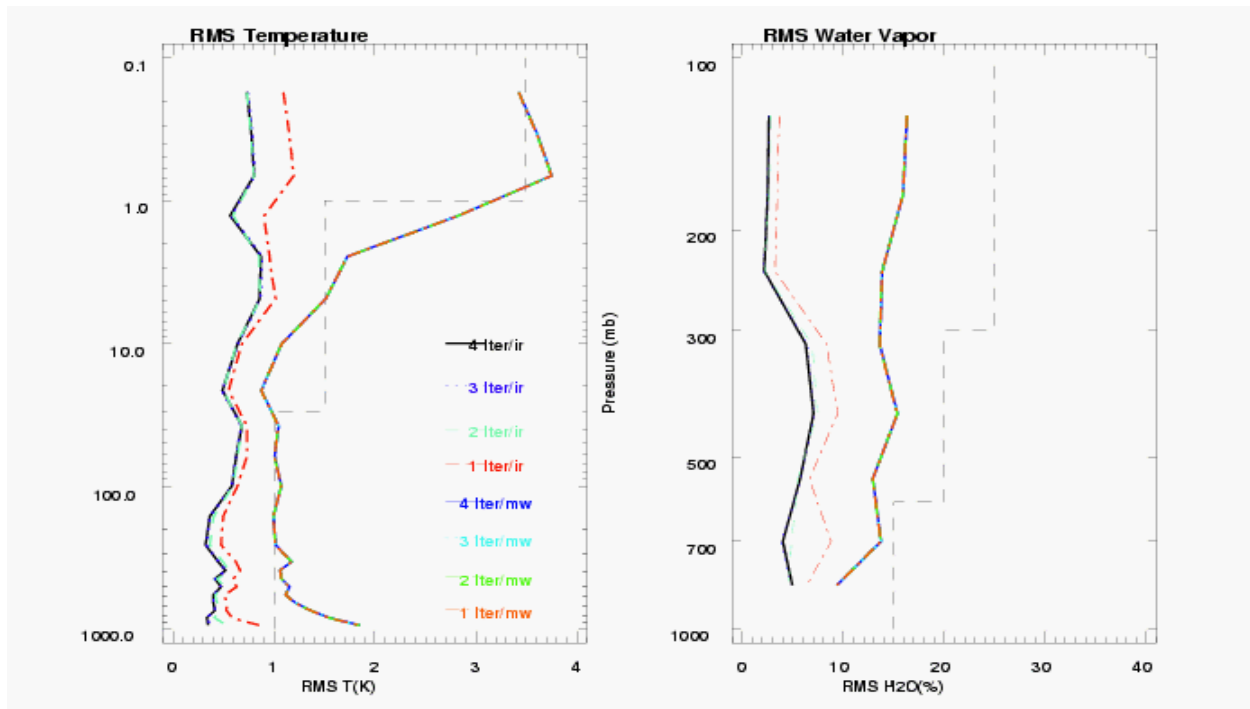


Figure 64: Temperature and water vapor RMS errors for 200 clear-sky land profiles retrieved using the DRAD algorithm.

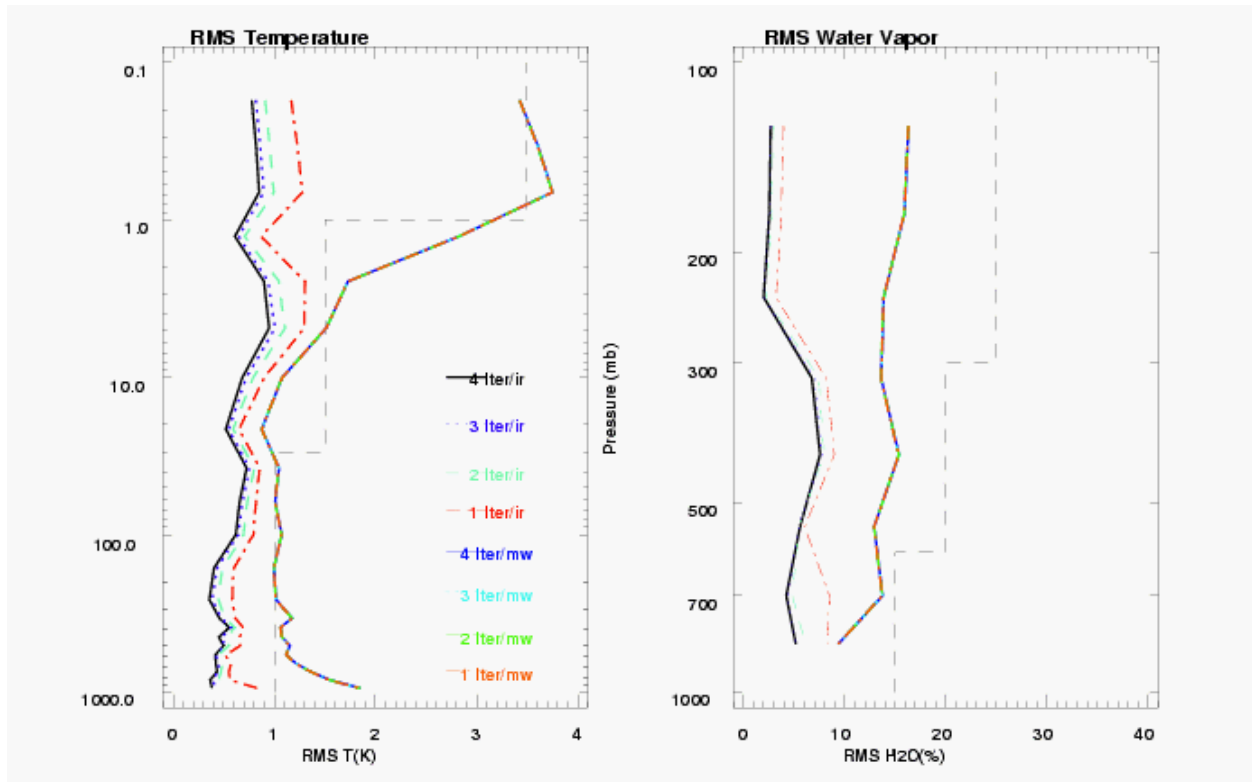


Figure 65: Similar to Figure 64, but for the Levenberg-Marquadt algorithm.

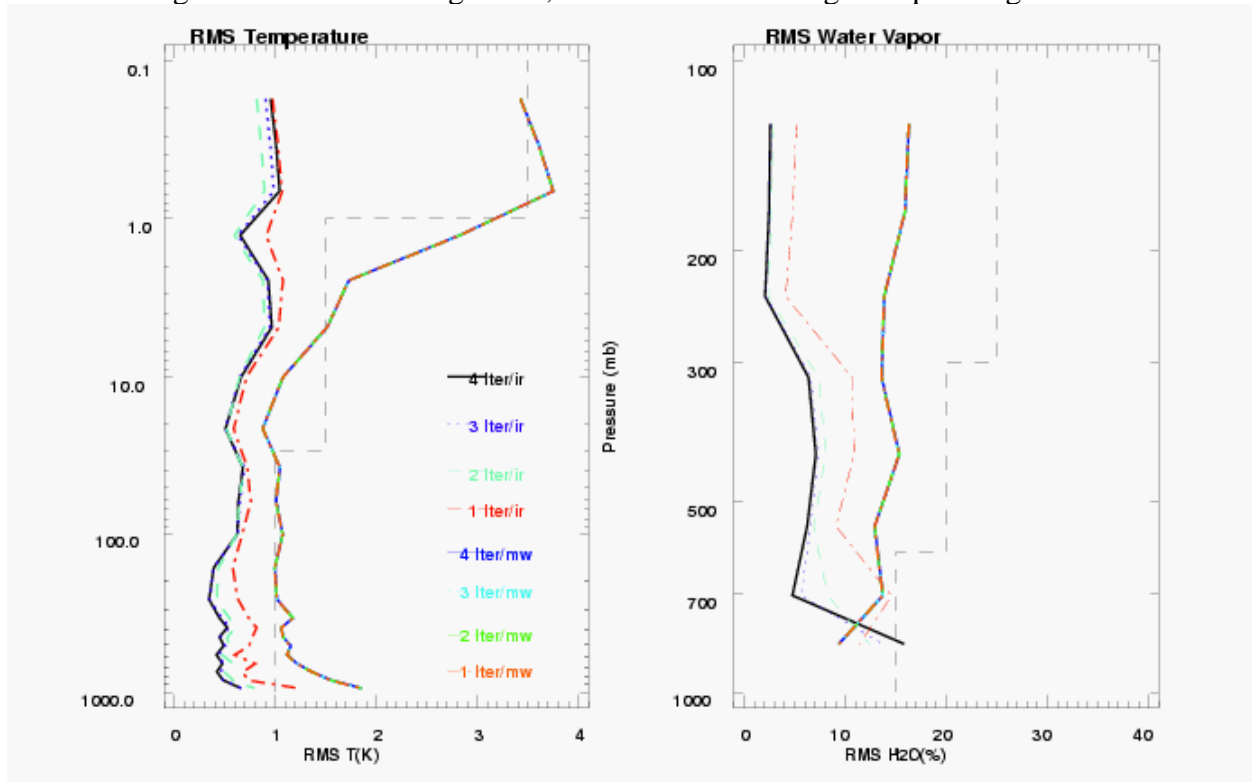


Figure 66: Similar to Figure 64, but for the Maximum Likelihood algorithm.

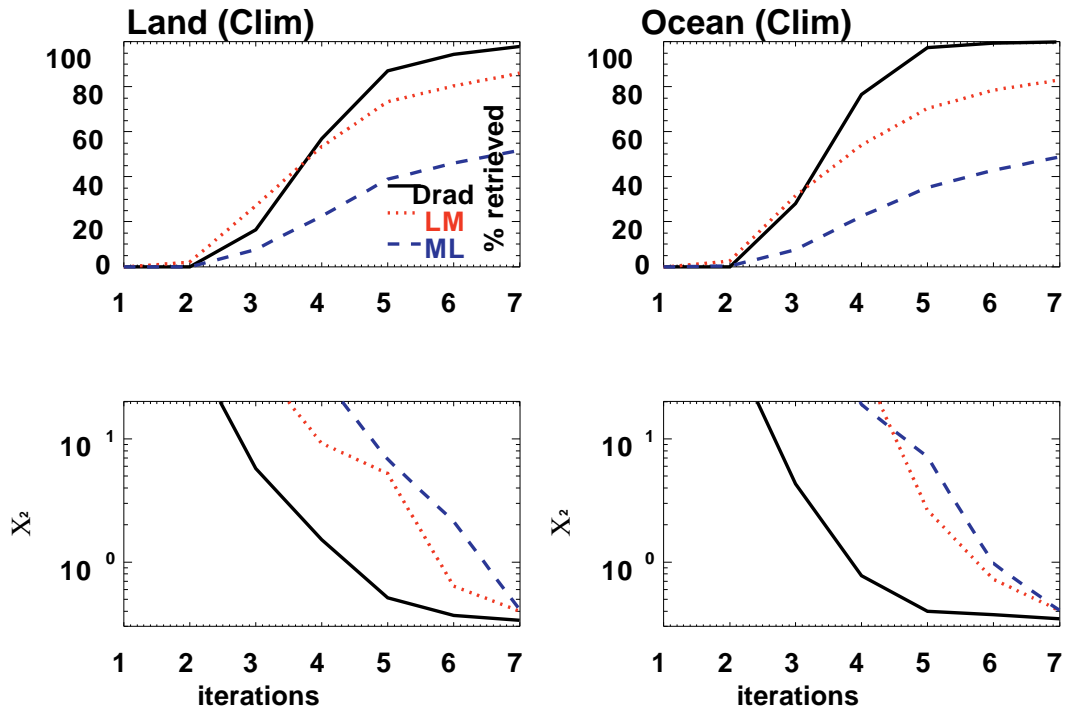


Figure 67: Similar to Figure 62, but for climatology first guess.

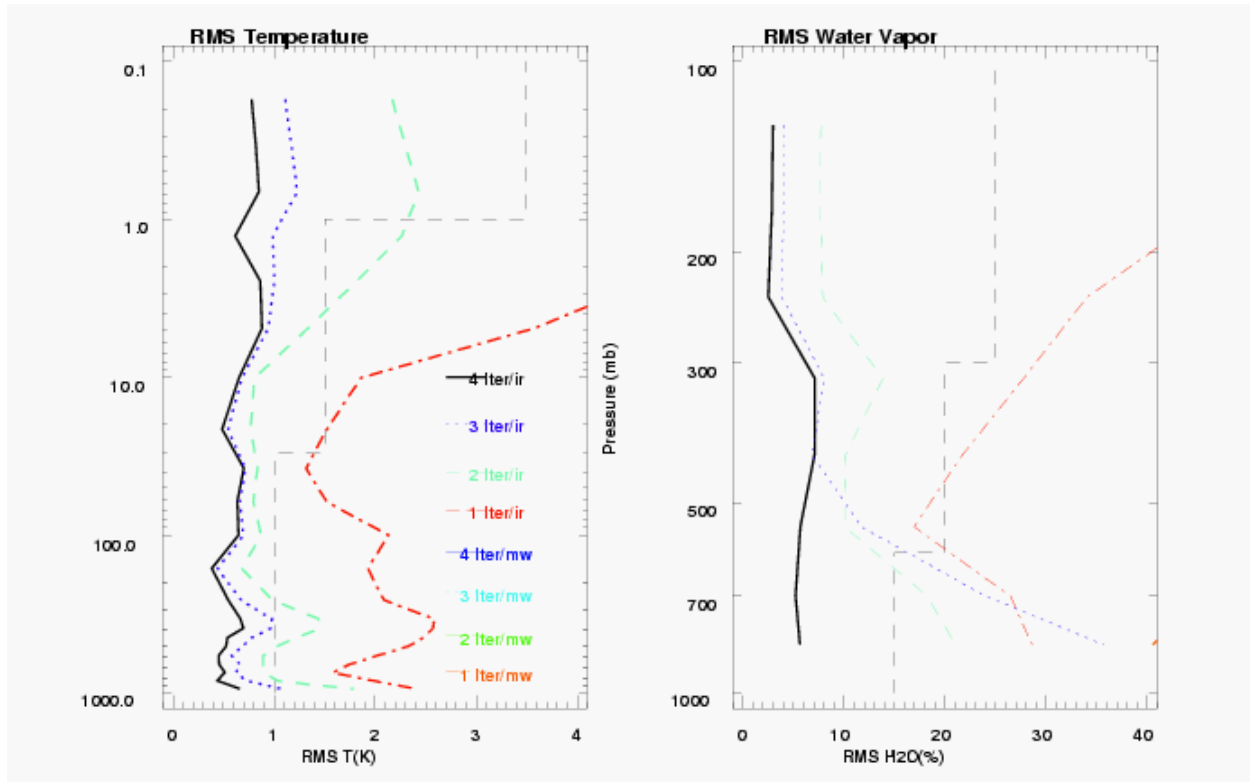


Figure 68: Temperature and water vapor RMS errors for 200 clear-sky land profiles retrieved using the DRAD algorithm and a climatology first guess.

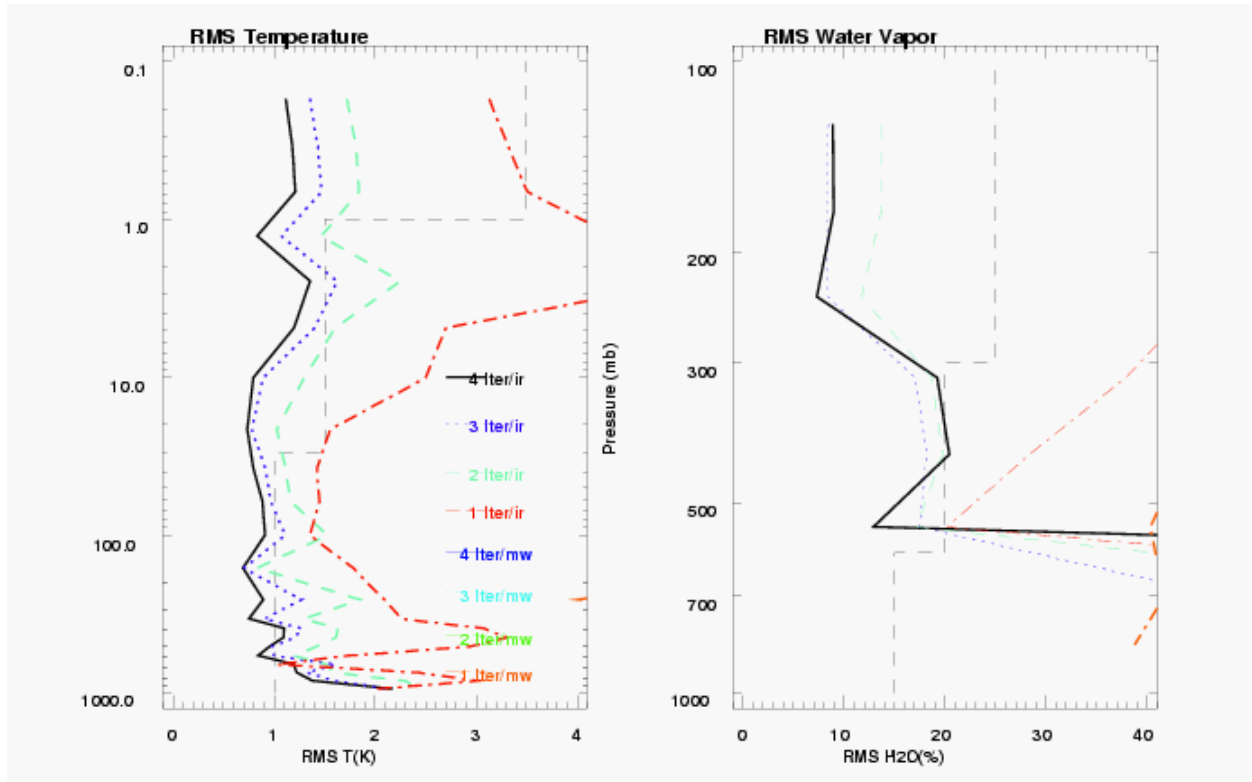


Figure 69: Similar to Figure 68, but for the Levenberg-Marquardt algorithm.

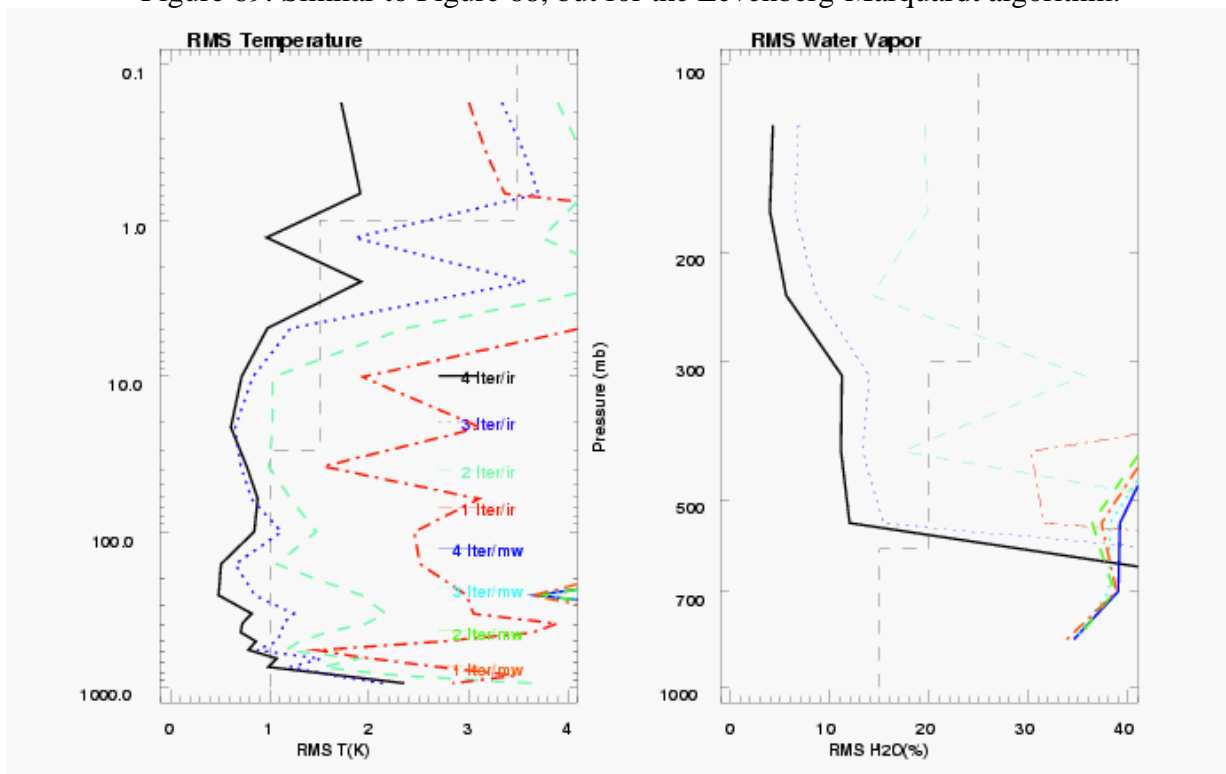


Figure 70: Similar to Figure 68, but for the Maximum Likelihood algorithm.

7.2 Determination of the Number of Cloud Formations

As discussed in Section 5.4.3, the number of cloud formations N_{CF} within a FOR is estimated using two parameters, the Residual Standard Deviation $RSD(n)$ and a normalized $\chi^2(n)$. In the practical implementation, N_{CF} is set equal to the largest number $n-1$ for which $RSD < \sigma/\gamma_1$ or $\chi^2 < [(nchan - n)(nfov - n)]/\gamma_2$, where σ is the instrument noise averaged over the spectral region 709.5-746 cm^{-1} and γ_1 and γ_2 are tuning parameters set in the main program. The tuning parameters have been tuned by comparing N_{CF} determined by the scene classification module with the true N_{CF} . The AIRS-simulated scanline dataset was used in the tuning. For this study, $N_{CF} = 2$ has been assigned to FORs in which the average cloudiness for each of the two cloud formations exceeds 20% and the cloud-top pressure is less than 400 and 600 hPa for the 1st and 2nd cloud formation, respectively. On the other hand, $N_{CF} \leq 1$ has been assigned to scenes in which the average cloudiness is less than 10% and the cloud-top pressure is greater than 700 mbar for each cloud formation. In Figure 71, we plot the percentage of scenes for which N_{CF} determined by the scene classification module is equal to the “true” N_{CF} as a function of the tuning parameters γ_1 and γ_2 . For $N_{CF} \leq 1$ (red lines in Figure 71), small values of γ_1 and γ_2 are necessary to achieve a correct identification of N_{CF} , whereas for $N_{CF} = 2$, the curves of success rate in determining N_{CF} versus γ_1 and γ_2 are bell-shaped. It should also be noted that the optimal values of γ_1 and γ_2 depend strongly on the noise. Consequently, they depend strongly on the apodization, with the values for *sinc* much smaller than for *Blackman* (the values for *Hamming*, not shown, are intermediate between *sinc* and *Blackman*). The parameters adopted in the current version of the algorithm ($\gamma_1 = 1.5$ and $\gamma_2 = 2.0$ for *Blackman*, $\gamma_1 = 1.2$ and $\gamma_2 = 1.4$ for *Hamming*, and $\gamma_1 = 0.7$ and $\gamma_2 = 0.7$ for *sinc*) are a compromise in achieving a high success rate (70-80%) for both $N_{CF} \leq 1$ and $N_{CF} = 2$.

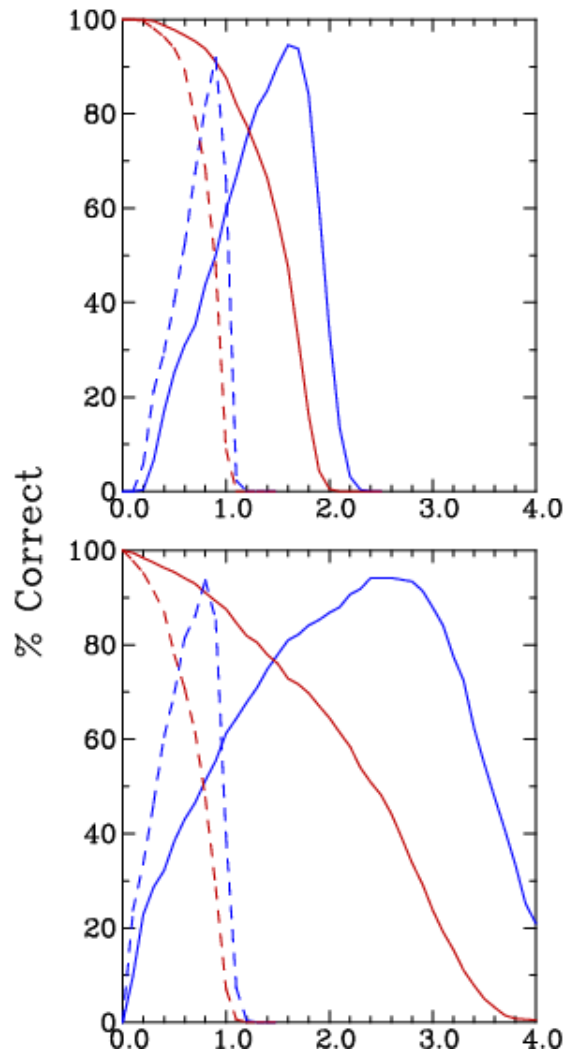


Figure 71: Frequency of correct determination of the number of cloud formations N_{CF} as a function of the tuning parameters γ_1 and γ_2 (upper and lower panel, respectively). The red curves are for scenes in which the true $N_{CF} \leq 1$, while the blue lines are for scenes in which the true $N_{CF} = 2$ (see text for the definition of true N_{CF}). The solid and dashed lines are for *Blackman* and *sinc*, respectively.

Another example of the application of the PCA to the estimation of the number of cloud formations is shown in Figure 72. In this figure, the number of cloud formations is estimated for the 16 weather product testbed scanlines, each with 30 FORs and 9 FOVs per FOR (see Section 0 for more information about the weather product testbed scanlines). For each FOR we show the average cloud fraction for each cloud formation; the scanlines have a maximum of two cloud formations. We also show the cloud-top pressures for each cloud formation. The PCA has been performed on radiances generated for these scenes. As can be seen, the estimated number of

cloud formations is overestimated only for a few FORs and in most cases matches the true number. In some cases the estimated number of cloud formations is smaller than the true number, indicating that two cloud formations are radiatively indistinguishable (within the noise level) from each other. As is illustrated in the figure, most of these cases are scenes where the clouds are close together or there is a very low cloud in the scene. On the other hand, an overestimate of the number of cloud formations causes no problem for the CC algorithm, in fact it may lead to better temperature retrievals above the cloud due to FOV averaging.

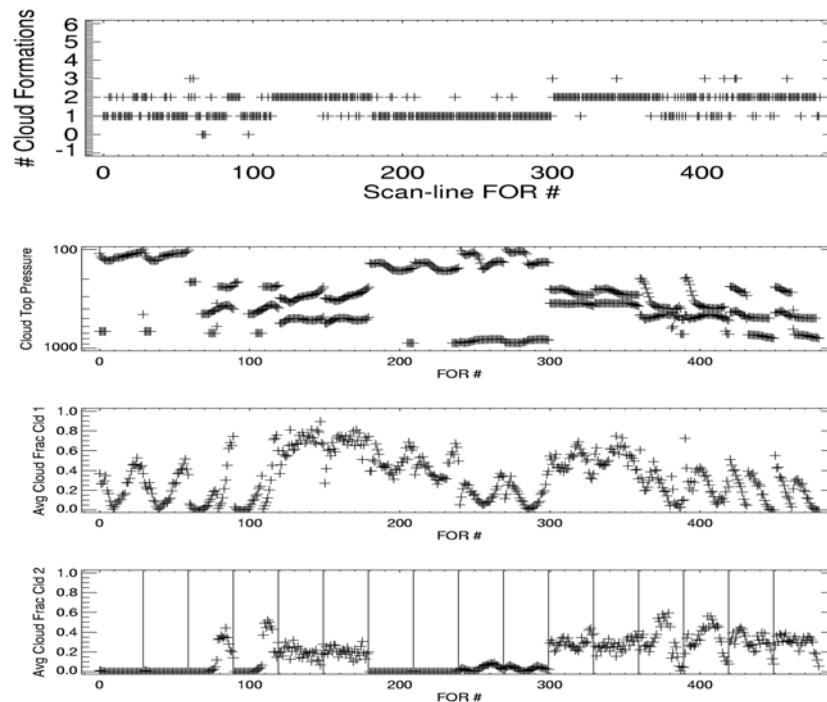


Figure 72: Application of PCA to estimate the number of cloud formations for the weather product testbed scanlines. Sixteen scans with 30 FORs per scan with 9 FOVs. From top to bottom: Number of estimated cloud formations, cloud-top pressures, average cloud fraction for cloud 1 and average cloud fraction for cloud 2.

7.3 Impact of Apodization

As discussed in Section 4.3, when an unapodized spectrum is transformed into an apodized spectrum, the noise in adjacent channels becomes correlated. The measurement error covariance matrix, which has a diagonal form for an unapodized spectrum, now contains off-diagonal elements. When the proper noise correlation is included in the error covariance matrix, the EDR retrieval performance should be the same regardless of whether the spectrum is apodized or not. This is illustrated in Figure 73 for 400 ocean profiles. All three apodization functions give similar performance. Minor differences between the three ILSs seen in Figure 73 result from the application of the DRAD algorithm, in which the diagonal terms of S_y contain a quadratic dependence on channel radiances. This non-linear term is not invariant under the transformation of S_y given by Equation (0.60), i.e., $A \cdot (\delta y)^2 A \neq (A \cdot \delta y)^T \cdot (A \cdot \delta y)$. However, the impact of this non-linearity appears to be fairly small.

It should be mentioned that inverting a full noise covariance matrix, which includes inter-channel correlations, is computationally very expensive. As the number of channels $nchan$ increases, the computational time associated with inverting this matrix is proportional to $nchan^3/2$. In this trade study, special treatments have been applied to invert this sparse matrix, but the computational cost of inverting the full error covariance matrix remains high. The timings related to the matrix inversion are listed in Table 21 through Table 23. The third and fourth columns in these tables list the times associated with inverting Equation (0.54). When S_y is diagonal, the total time needed for inverting Equation (0.54) is much less. As the number of channels decreases, the difference in computational time between including diagonal and off-diagonal matrix elements becomes smaller.

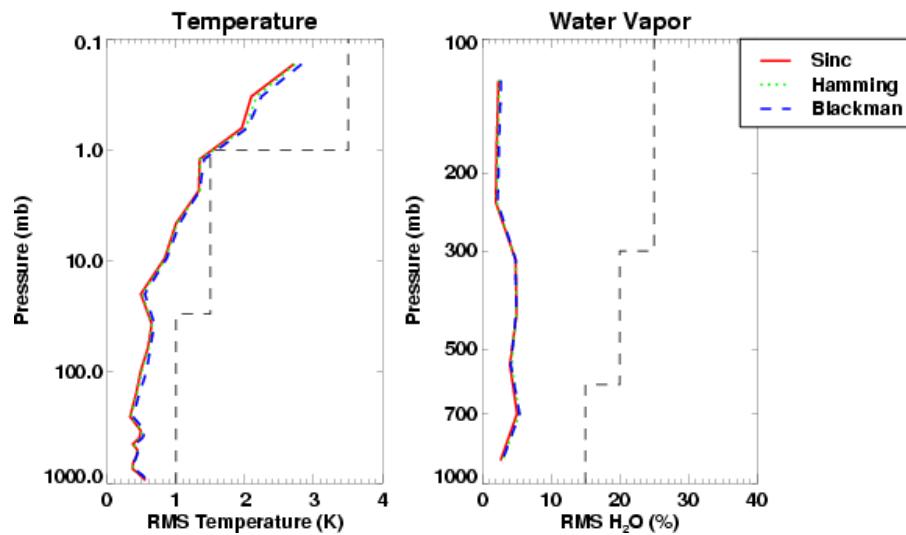


Figure 73: EDR performance using error covariance matrices for *Hamming* and *Blackman* apodizations computed self-consistently using Equation (0.60).

In order to meet timing requirements, trade studies have been performed to find ways to decrease the computational time associated with the inversion of apodized spectra. Results show that ignoring the off-diagonal elements of S_y , while keeping the diagonal elements at their correct values given by Equation (0.60), degrades the EDR performance significantly. On the other hand, when the off-diagonal elements are ignored, but the diagonal elements are set to those of *sinc* (i.e., with no A -matrix transformation and hence no reduction of the noise variance), the EDR algorithm produces acceptable results for a wide variety of clear and cloudy scenes. This method has been adopted for the current code. Figure 74 shows the EDR performance for 400 clear ocean scenes with three different apodization functions and a modified error covariance for *Hamming* and *Blackman*. In producing Figure 74, the correlated noise for the apodized spectra (*Hamming* and *Blackman*) has been approximated by setting $S_y(i,i) = \sigma^2(i)$ and setting the off-diagonal elements to zero [instead of retaining the off-diagonal elements, while keeping the diagonal elements $S_y(i,i)$ smaller than $\sigma^2(i)$]. *Blackman* ILS is the strongest apodization function among the three ILSs studied and it provides the largest degradation relative to the *sinc*

ILS. However, even in this case the results are better than when the off-diagonal elements are ignored and the diagonal elements are set to their proper A -matrix transformed values.

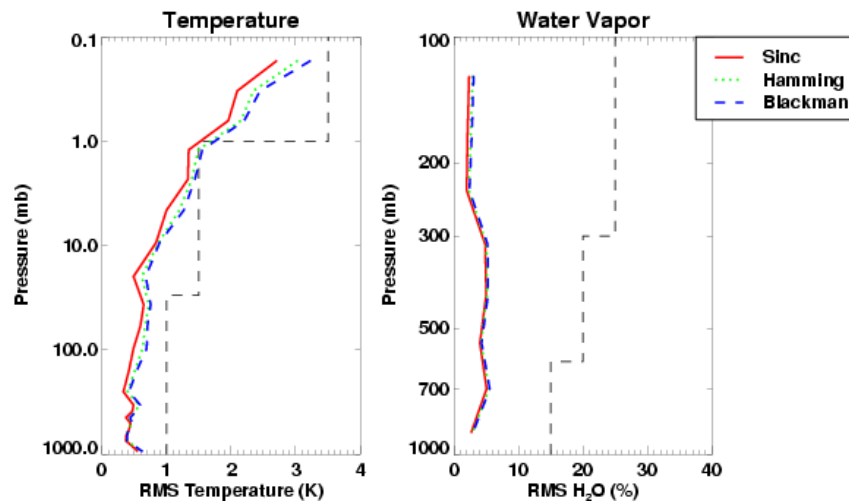


Figure 74: Impact of ignoring off-diagonal elements, while relaxing the noise variance, on the EDR retrieval accuracy for *Hamming* and *Blackman*. Results for *sinc* are shown for reference.

Apparently, there is a trade-off between accuracy and computational burden. The results shown in Figure 73 indicate that a consistent treatment of measurement noise is necessary for achieving good retrieval performance when an apodized ILS is used. However, retaining the off-diagonal elements of S_y requires a computationally expensive matrix inversion, which can significantly slow down the inversion. We have measured timing for different apodizations, noise treatment, and retrieval channel sets, and the results are summarized in Table 21 through Table 23 for the most time-consuming subroutines in the infrared retrieval. The three tables present timing results obtained with the full channel set, the channel set excluding the O_3 main band, and an optimal channel set selected based on the criteria described in Section 5.5.3. Two of the time-consuming subroutines, *osstran* and *ossrad*, are parts of the forward model. The first calculates the total optical depths at the *OSS*-selected spectral points, while the second computes the radiances and their derivatives. The other two time-consuming subroutines, *Invert* and *SetIRMWInvert*, are used in the inverse model. It should be noted that in calculating radiances, a monochromatic treatment of the Planck function is used for *sinc*, while for *Blackman* and

Hamming the central frequency approach is employed. This difference makes the timing of *ossrad* approximately two times longer for *sinc* compared with the apodized case.

Several conclusions can be drawn from the timing results. When a diagonal form of the error covariance matrix is used (the first three rows in each timing table), the timing for each of the four subroutines is approximately linear in the number of channels. In contrast, when the non-diagonal elements are retained, the timing of *Invert* and *SetIRMWInvert* grows with the number of channels faster than linearly. For a large number of channels (Table 21 and Table 22), the off-diagonal treatment of the error covariance matrix in *Invert* and *SetIRMWInvert* is very time-consuming, nullifying the timing advantage of the central frequency Planck function treatment for *Hamming* and *Blackman* compared with the monochromatic treatment for *sinc*. In this case, *sinc* appears to offer an optimal combination of accuracy and speed. One concern with using *sinc* ILS is that the contribution of cloud to the radiance is not localized spectrally and this may not be suitable for the cloud-clearing algorithm. On the other hand, for a small number of channels (Table 23), the *Invert* and *SetIRMWInvert* subroutines are much less time-consuming, even with an off-diagonal treatment of S_y , and consequently in this case *Hamming* or *Blackman* might be acceptable.

Table 21: Timing Results for 1305 Channels.

	Planck	<i>Invert</i>	<i>SetIrMw</i>	<i>Ossrad</i>	<i>Osstran</i>	Total of Four
<i>sinc</i> , diag. noise	Mono Freq	0.097	0.057	0.296	0.123	0.473
<i>Hamming</i> , diag. noise	Center Freq	0.097	0.057	0.142	0.110	0.306
<i>Blackman</i> , diag. noise	Center Freq	0.099	0.057	0.143	0.112	0.310
<i>Hamming</i> , off-diag. noise	Center Freq	0.592	0.958	0.141	0.108	1.799
<i>Blackman</i> , off-diag. noise	Center Freq	0.596	1.185	0.144	0.112	2.037

Table 22: Timing Results for 937 Channels.

	Planck	<i>Invert</i>	<i>SetIrMw</i>	<i>Ossrad</i>	<i>Osstran</i>	Total of Four
<i>sinc</i> , diag. noise	Mono Freq	0.072	0.045	0.211	0.084	0.412
<i>Hamming</i> , diag. noise	Center Freq	0.073	0.044	0.100	0.077	0.294
<i>Blackman</i> , diag. noise	Center Freq	0.072	0.043	0.100	0.072	0.287
<i>Hamming</i> , off-diag. noise	Center Freq	0.330	0.472	0.100	0.079	0.981
<i>Blackman</i> , off-diag. noise	Center Freq	0.328	0.543	0.101	0.074	1.046

Table 23: Timing Results for 346 Channels.

	Planck	<i>Invert</i>	<i>SetIrMw</i>	<i>Ossrad</i>	<i>Osstran</i>	Total of Four
<i>sinc</i> , diag.noise	Mono Freq	0.032	0.016	0.091	0.042	0.181
<i>Hamming</i> , diag.noise	Center Freq	0.032	0.016	0.043	0.036	0.127
<i>Blackman</i> , diag.noise	Center Freq	0.031	0.016	0.043	0.035	0.125
<i>Hamming</i> , off-diag. noise	Center Freq	0.063	0.054	0.043	0.036	0.196
<i>Blackman</i> , off-diag. noise	Center Freq	0.062	0.058	0.043	0.035	0.198

7.4 Impact of Channel Selection

The channel selection in the CrIMSS algorithm has been implemented using the entropy method described in Section 5.5.3. The channel entropies have been sequentially ranked for 5 parameters (temperature with and without MWIR, water vapor, skin temperature, surface emissivity, and solar reflectivity), with several atmospheric profiles (polar, mid-latitude, and tropical, ocean/land) used to calculate the derivatives. Trade studies involving subsets of these profiles have produced different channel sets, but they had small impact on the retrieval performance. As noted above, spectral regions where trace gas derivatives exceed a certain threshold are excluded from the channel selection in order to minimize trace gas interference with the retrievals. The trace gases considered are O₃ (LWIR), CH₄/N₂O (MWIR) and CO/ N₂O (SWIR). In addition, for temperature channel selection we also excluded channels sensitive to water vapor. The water vapor and trace gas derivatives and their threshold values are shown in Figure 75 and Figure 76. These figures also illustrate a typical selected set containing 350 channels. As shown in Figure 76, the threshold value adopted for the N₂O derivatives results in most SWIR channels being retained by the selection process. This choice minimizes errors in the retrieved skin temperatures. Figure 77 shows a typical plot of temperature entropy as a function of wavenumber. This plot illustrates that MWIR contains a significant portion of the temperature information. However, since these channels are also sensitive to water vapor, they were not used in selecting channels for temperature retrievals.

The results from the entropy ranking process for each EDR were used to construct a single channel set for simultaneously retrieving temperature, water vapor, and the surface parameters. This combined channel set is constructed as follows: 30% of channels are the top-ranked channels selected for temperature without MWIR, 14% are from the channels for temperature with MWIR (maximum of 40 channels), 14% for water vapor (maximum of 40 channels), 14% skin temperature (maximum of 50 channels), 14% emissivity (maximum of 30 channels) and 14% for reflectivity (maximum of 30 channels). The combined sets totaling between 25 and 500 channels are illustrated in Figure 78. A channel selection of 350 elements is also illustrated in Figure 75 and Figure 76, with the channels for that selection listed in Table 24.

The channel sets from Figure 78 were used to simultaneously retrieve temperature, water vapor, and surface parameters from a diverse set of simulated data and the resulting errors were compared to those obtained using all CrIS channels. The profiles of RMS errors for temperature and water vapor obtained using sets of 150, 300, and 400 channels are shown in Figure 79 for the case of 200 clear-sky ocean simulations. As can be seen, the retrievals based on 300-400 channels are nearly identical, in the RMS sense, to those obtained using the full complement of CrIS channels. Consequently, the current version of the CrIS employs a set containing 400 channels. This reduction in the number of channels relative to the full set of channels leads to a ~2.5-fold increase in the computational speed for the retrieval algorithm. Most of these gains result from the reduction in the number of forward model calculations and of matrix inversions.

Table 24: Selected Channels for CrIS.

EDR	Wavenumber (cm ⁻¹)	Number of Channels Selected
Temperature	662.5-908.75	144
	1231.25-1535.0	23
	2160.0-2400.0	63
Water Vapor	1337.5-1652.5	40
Skin Temperature	1095.0-1246.25	29
Surface Emissivity and Reflectivity	2160.0-2492.5	21

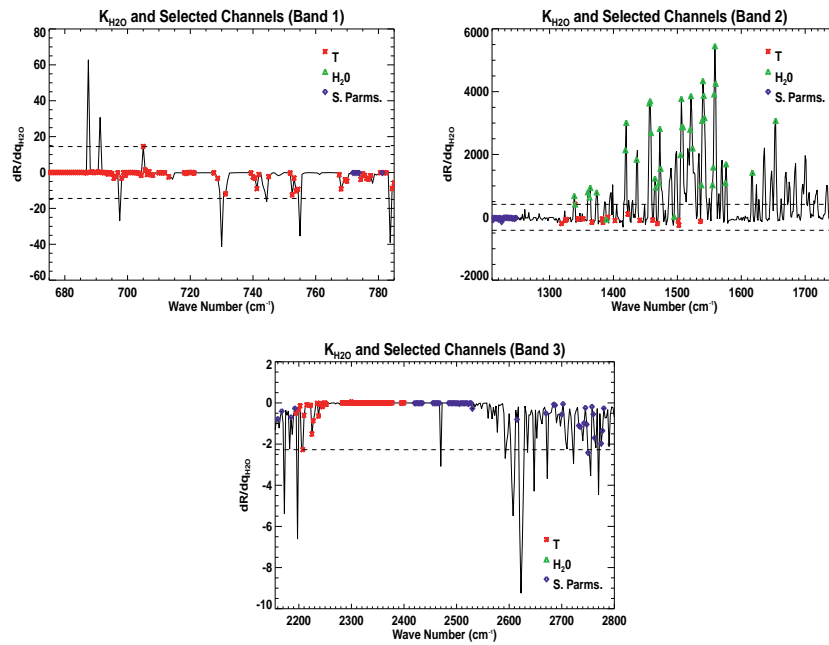


Figure 75: Water vapor derivatives and selection thresholds. Channels for which the absolute values of water vapor derivatives exceed the threshold are excluded from the entropy-based channel selection for temperature.

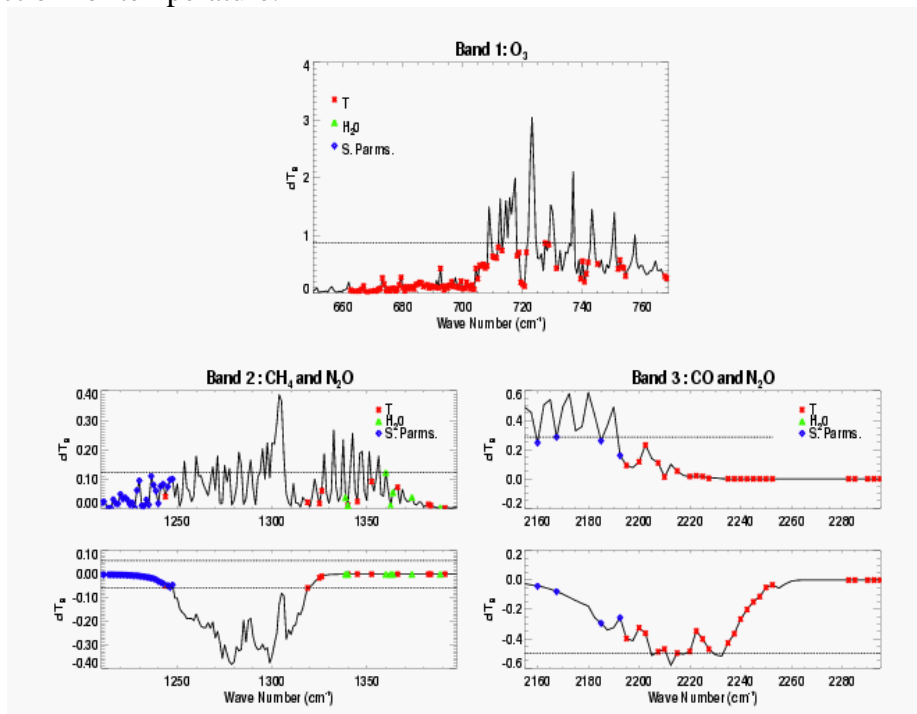


Figure 76: Trace gas derivatives and selection thresholds. Channels for which the absolute values of trace gas derivatives exceed the threshold are excluded from the channel selection for temperature, water vapor, and surface parameters.

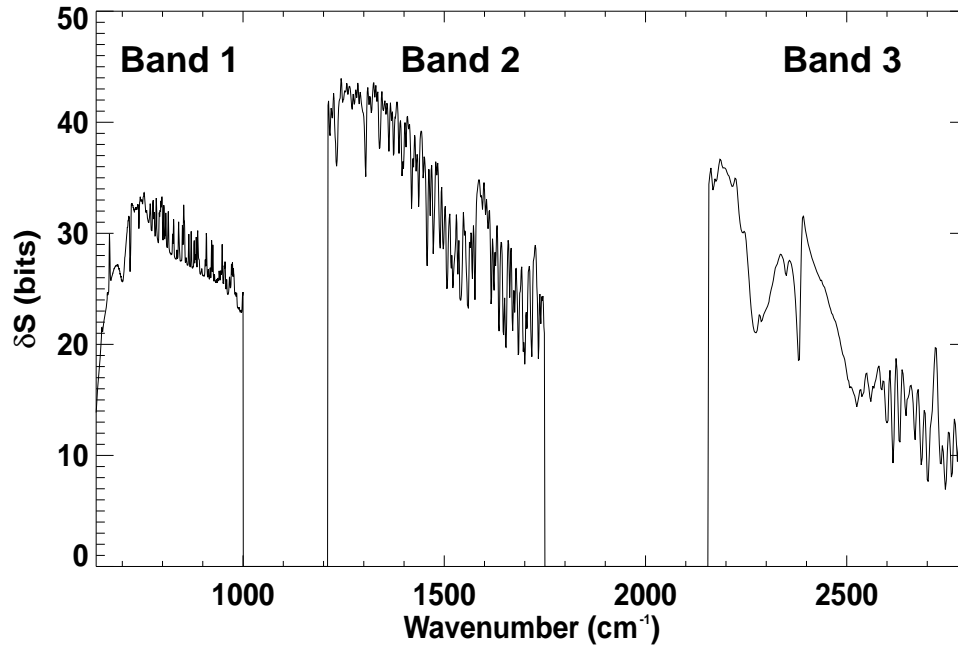


Figure 77: Typical Temperature Entropy (δS) per Channel.

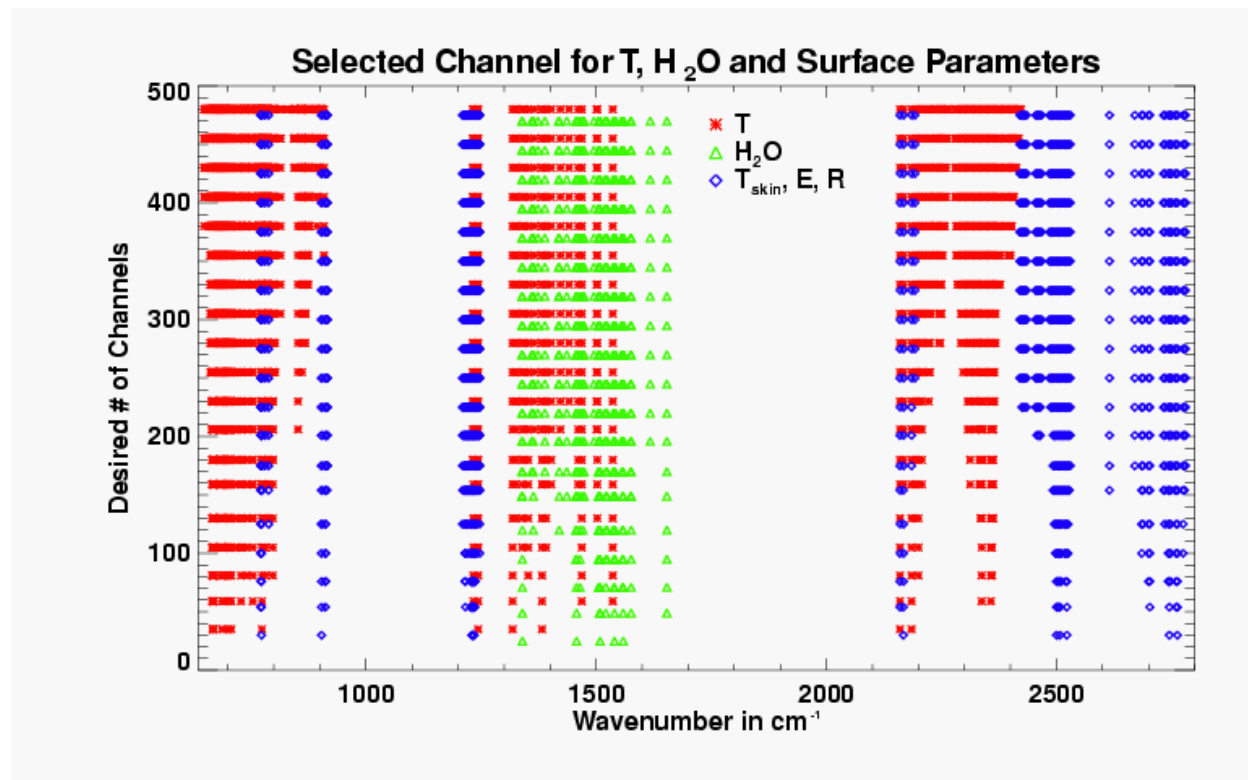


Figure 78: Selected channels for temperature T (with and without MWIR), water vapor, and the surface parameters as a function of the total number of channels. The temperature channels selected in MWIR are based on information in all three bands (non-weighted S_e).

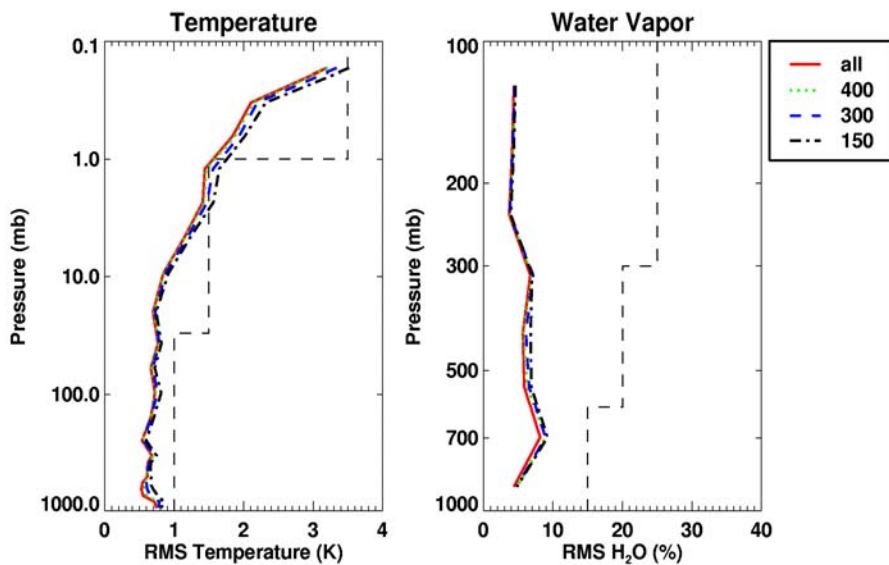


Figure 79: RMS errors for temperature and water vapor for 200 clear-sky ocean scenes. Results from second stage retrievals performed using all IR channels and subsets of 150, 300, and 400 channels are shown.

7.5 Impact of Trace Gas Variability

Note: In the current version, the algorithm has been modified to retrieve Ozone profile simultaneously with other atmospheric and surface parameters.

In this trade study, the impact of spatial and temporal variability in O₃, N₂O, CO, and CH₄ on CrIS retrievals has been investigated. A climatological database for ozone is contained within the NOAA-88b dataset and has been adopted for this study. Future studies will assess the effect of variable ozone under more stressing conditions, e.g., those characteristic of a stratospheric ozone hole. The distributions of other trace gases are less well known than for ozone, as they are routinely measured only at a limited number of surface stations. In the absence of global tropospheric measurements, the impact of variable non-O₃ trace gas concentrations has been evaluated using profiles the NCAR MOZART model (Brasseur *et al.* 1998). MOZART (Model for OZone And Related chemical Tracers) is a three-dimensional chemical transport model developed for studies of the global budget of ozone and its precursors. The output from the MOZART model has also been utilized in the validation of remote sensors of the chemical composition of the troposphere (e.g, from the MOPITT instrument). The model simulates the distribution of 56 chemical species from the surface to about 3 mbar using a state-of-the-art chemistry module and accounting for transport by both large-scale winds and subgrid-scale mixing processes. In the version of MOZART used for the present study, the grid-scale winds have been obtained from the NCAR CCM3 model. A complete set of trace gas profiles used in this study is shown in Figure 80. Although the MOZART model does include contributions from anthropogenic sources, it does not represent periods of high pollution (in other words, its trace gas distributions reflect “climatological” conditions). To assess the impact of industrial pollution, we have also conducted experiments with the mixing ratios of N₂O and CH₄ enhanced in the boundary layer by 50-100% relative to the profiles shown in Figure 80.

Perhaps the most straightforward method of assessing the radiative impact of a variable trace gas is by considering the radiative deviation from the radiance calculated assuming a “fixed” profile. The envelope of deviations for a set of 200 land profiles is shown in Figure 81 through Figure 84 for O₃, N₂O, CO, and CH₄, respectively. Variable ozone has the largest radiative impact, followed by N₂O. In this study, the main ozone band near 1000 cm⁻¹ has been excluded.

Consistent with its large effect on simulated radiances, variable ozone has by far the largest impact on the retrieved EDRs and it is essential that the column retrieval of O₃ be performed each time the algorithm is applied. With column retrieval, the impact of variable O₃ is about 0.2 K in temperature and up to 5% in moisture. The other gases have a much smaller effect under “climatological” conditions (as represented by the MOZART model), although variable N₂O can have a 0.1 K and 2% effect. The impact of variable N₂O and CH₄ is much larger when their concentrations are enhanced in the boundary layer, in some cases leading to non-compliance with the EDR accuracy requirements (especially when N₂O concentrations are enhanced). The best algorithm performance under these conditions is achieved with the modified column retrieval described in Section 5.5.4. However, the greatest advantage of the modified column retrieval is obtained when considering retrieving the trace gas abundances themselves. As shown in Figure 85, the modified retrieval improves the accuracy of column retrieval for N₂O by almost a factor of 2 (0.5 vs. 1% RMS error), with a smaller but consistent improvement for CH₄ as well. The results in Figure 85 have been obtained for clear-sky warm land profiles, but the modified retrieval consistently improves column retrieval of N₂O and CH₄ for a wide variety of other scenes (including warm/cold, clear/cloudy, and land/ocean).

Several factors need to be considered if the trace gas variability is to be properly accounted for. The choice of apodization plays a significant role, with the *sinc* function producing generally the best results. An example is shown in Figure 86. As in the baseline retrieval, an important role is also played by the choice of covariance matrix. For the warm profiles considered in this study, the best results have been obtained using a warm covariance matrix. Under cloudy conditions, the uncertainties in the unknown trace gas profiles can cause errors in the estimates of cloud-clear radiances. In the current algorithm, this has been ameliorated by introducing empirical error

terms involving the derivatives of radiance with respect to column amounts of O_3 and N_2O , with the parameters tuned to yield an overall optimal performance under a variety of cloud conditions.

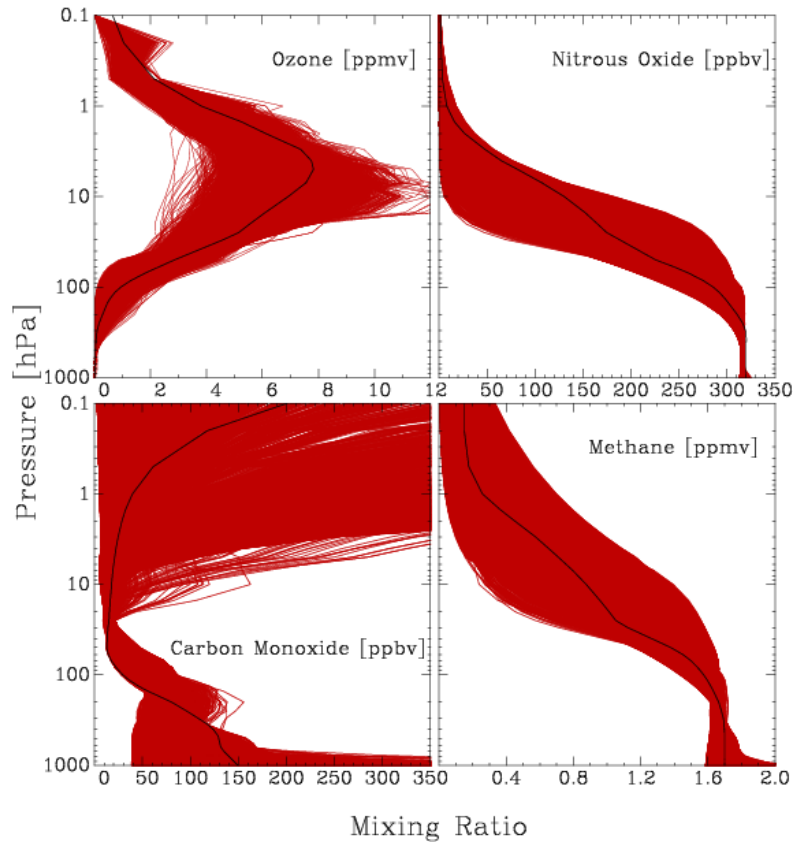


Figure 80: Trace gas profiles used in evaluating the sensitivity of the CrIS retrieval to trace gas variability. The ozone profiles are from the NOAA-88 database, while the profiles of N_2O , CO, and CH_4 are from the MOZART model. The black lines represent reference profiles from the U.S. Standard Atmosphere.

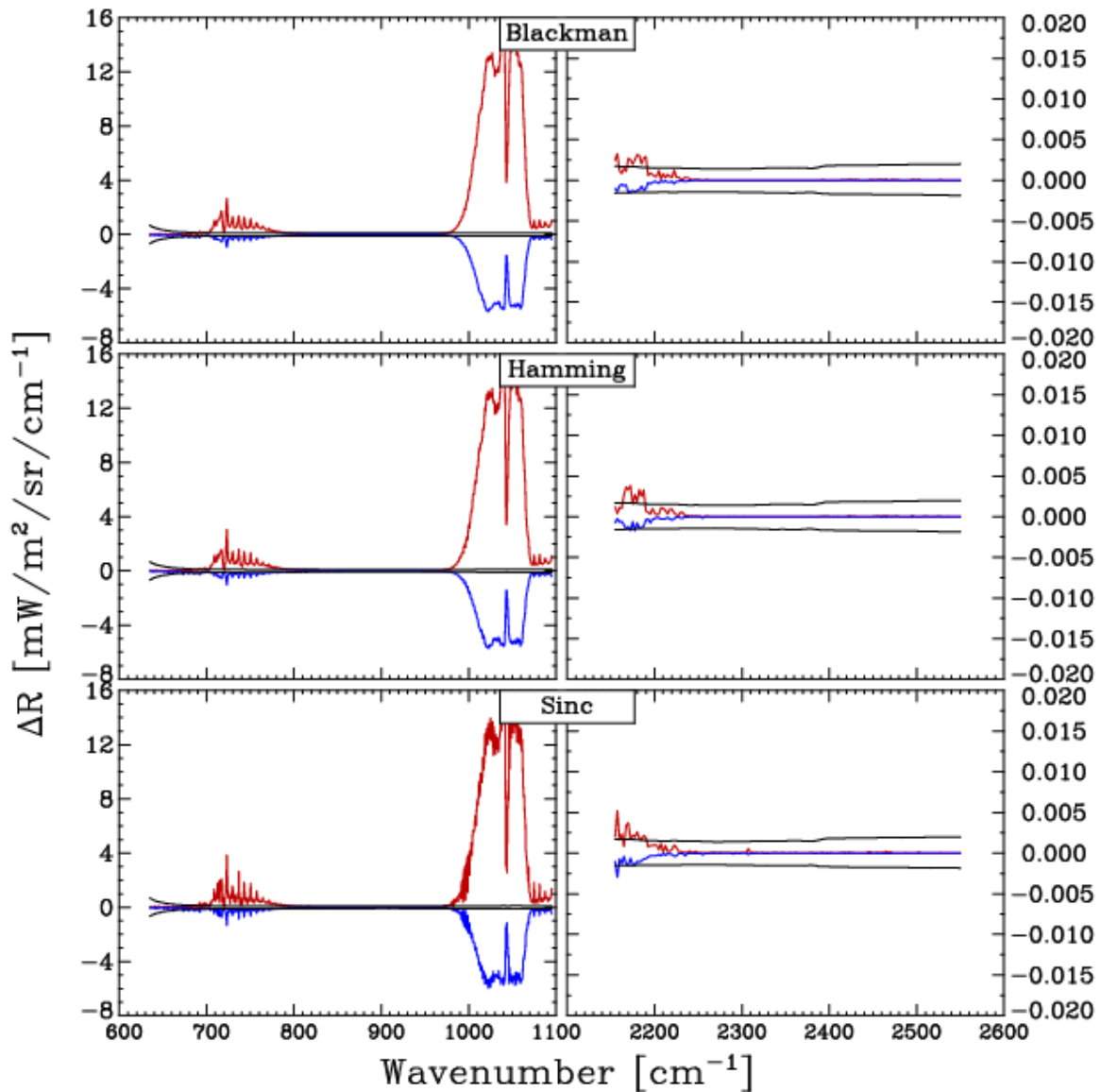


Figure 81: Radiative effects of variable ozone. The red and blue lines show the maximum positive and maximum negative radiance differences (relative to the standard profile) in each CrIS channel for a set of 200 land profiles under clear-sky conditions. Black lines represent CrIS instrument noise. Only results for the LWIR and SWIR bands are shown (note the very different vertical scales for the two bands), as the impact of variable ozone is below the noise level in MWIR.

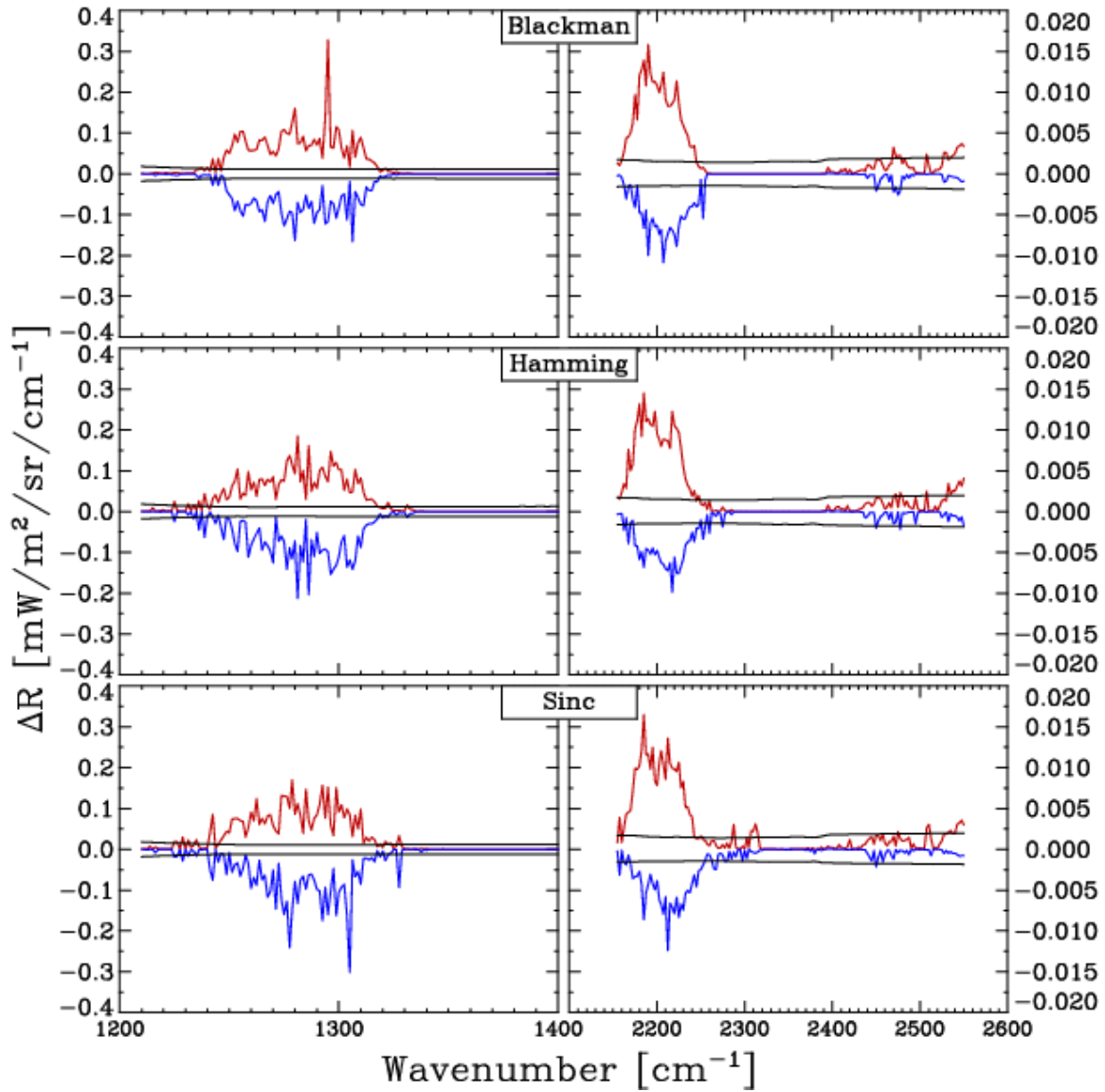


Figure 82: Radiative effects of variable N_2O . The impact of variable N_2O is near-zero in LWIR.

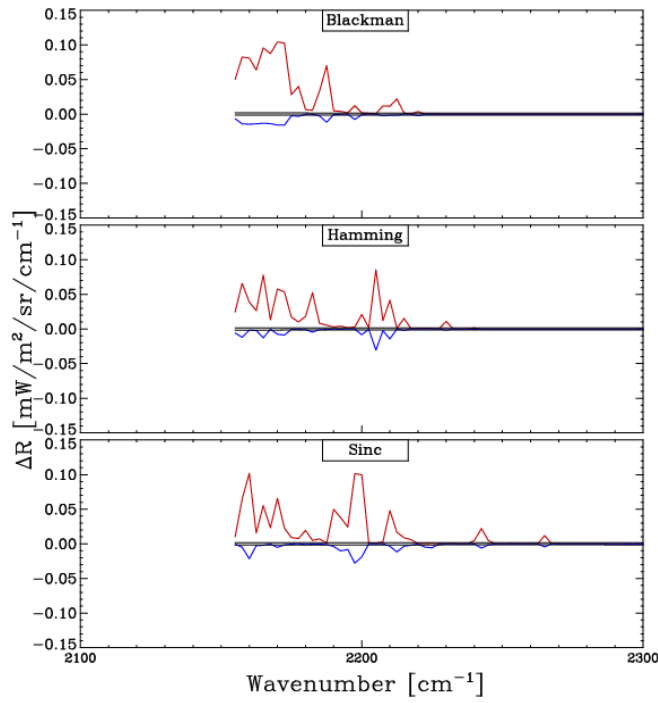


Figure 83: Radiative effect of variable CO. For CrIS, the radiative impact of variable CO is only significant in the portion of the SWIR band shown here.

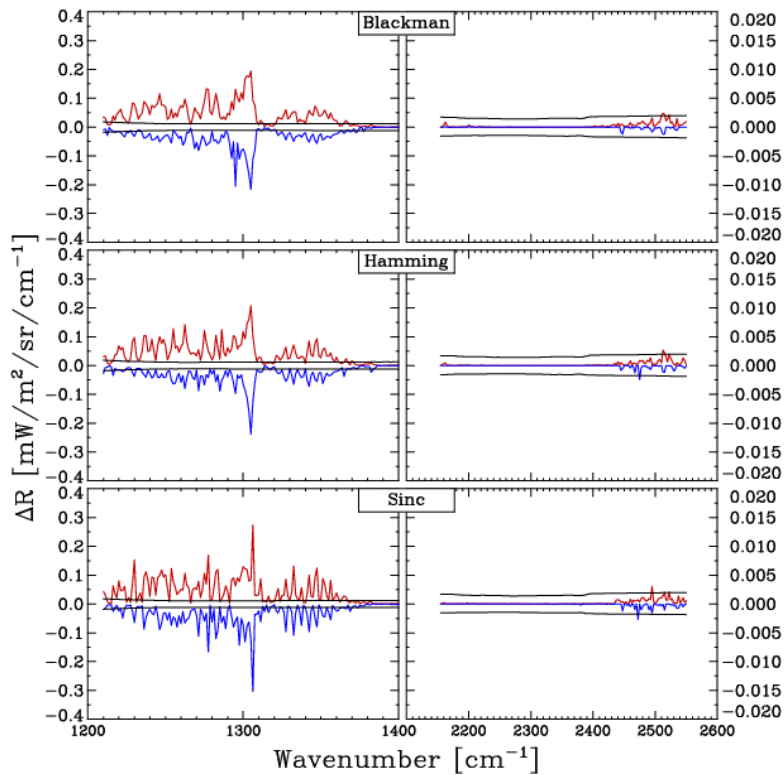


Figure 84: Radiative effect of variable CH₄.

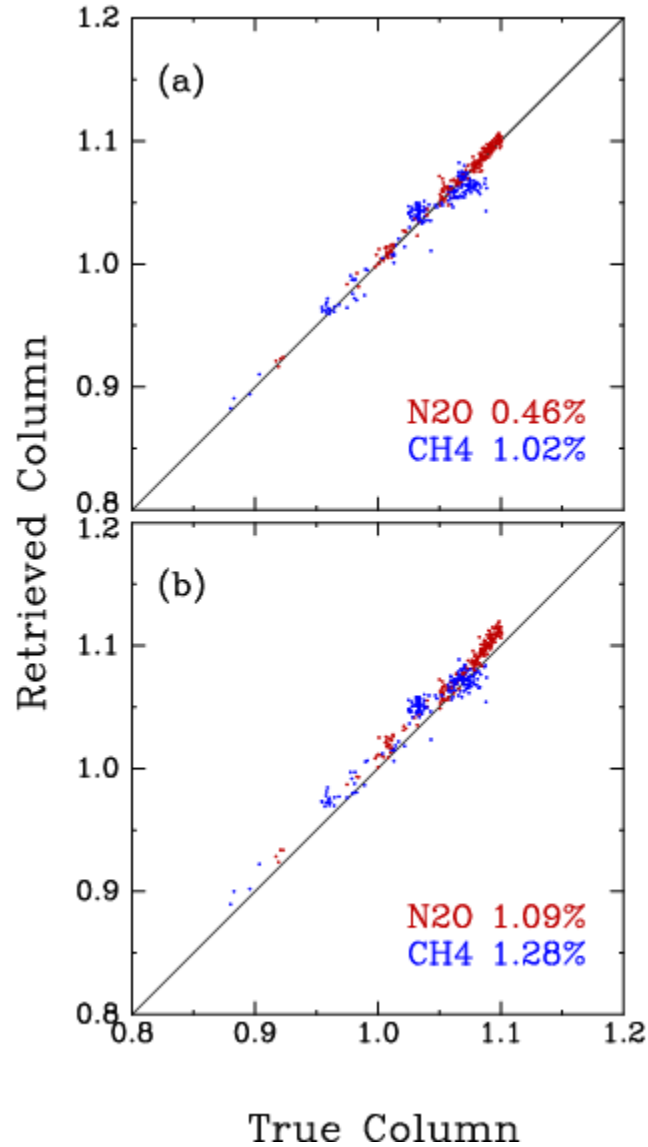


Figure 85: Scatter plots of retrieved vs. true column amounts (in non-dimensional units) for N₂O and CH₄ (red and blue dots, respectively). The results in this figure have been obtained for warm clear-sky land profiles using (a) modified column retrieval for N₂O and CH₄ and (b) standard column retrieval for N₂O and CH₄. The numbers in each panel give the RMS error for each species.

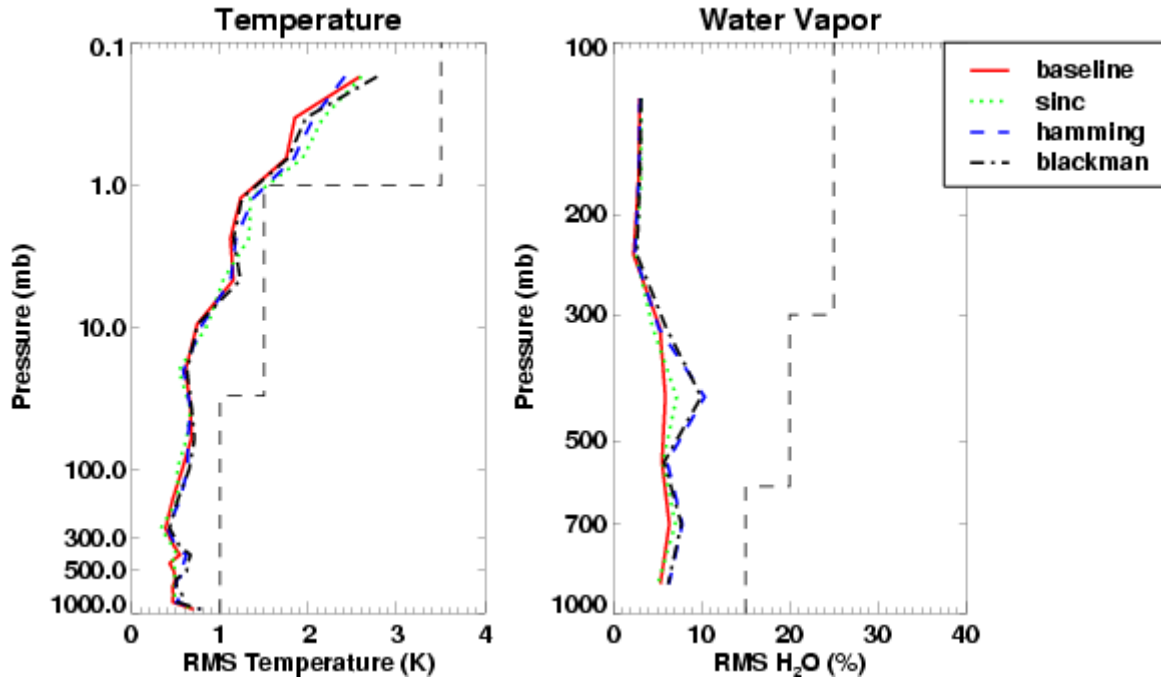


Figure 86: Effect of trace gas variability and apodization on EDR retrievals. The results shown in this figure have been obtained for 200 land profiles under clear-sky conditions, with the trace gas profiles from the NOAA-88 and MOZART databases (see Figure 80). The solid lines show the retrieval results in the baseline case of no trace gas variability.

7.6 Application of QC to Scanline Retrievals

The CrIS weather product testbed developed by the IPO consists of sets of profiles designed and grouped to represent the proposed CrIS and AMSU/MHS footprint configuration. The locations of the scanlines are shown in Figure 87. The set simulates CrIMSS scans, with sixteen scans sampled over the globe. Each scanline has 30 FORs and each FOR has 9 CrIS/MHS FOVs. This scanline dataset should be distinguished from the global set of AIRS-simulated scanlines used in the testing of retrieval performance.

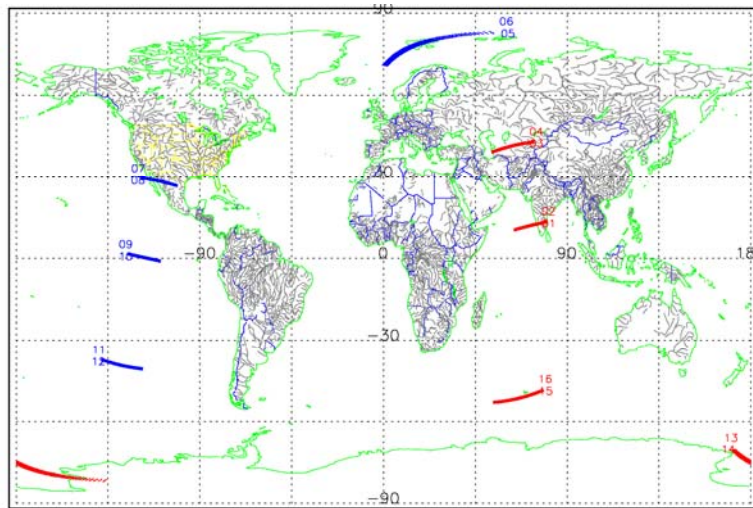


Figure 87: Location of scanlines.

There is a variety of cloud and surface conditions for each scanline. Figure 88 shows the average cloud-top pressure, average cloud fraction, and maximum contrast within a FOR. These are the three most important factors affecting a successful application of the cloud-clearing method. The algorithm is least effective for low clouds and low contrast. Figure 89 shows the error in the retrieved lower tropospheric temperature for each FOR (270 in all). A comparison of Figure 88 with Figure 89a reveals correlation between large cloud fraction, low contrast, low cloud-top pressure, and the goodness of the retrieval. In Figure 89b, the application of each QC test is illustrated. The first level below the zero line represents profiles rejected by the MW+IR χ^2 test, the second level are the profiles rejected by the MW-only χ^2_{MW} test, and the third level are

profiles rejected by the RMS between the first and second stage temperature profile retrievals. There is much overlap between the second and third test, suggesting that one of them might be eliminated.

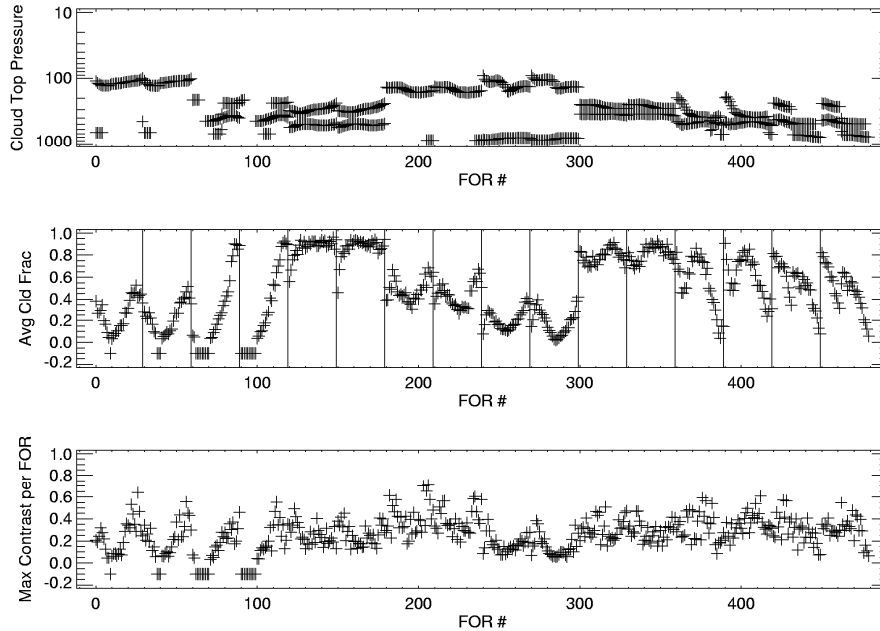


Figure 88: From top to bottom: average cloud-top pressure, average cloud fraction (the vertical lines divide the 16 scanlines), and maximum cloud contrast for each FOR.

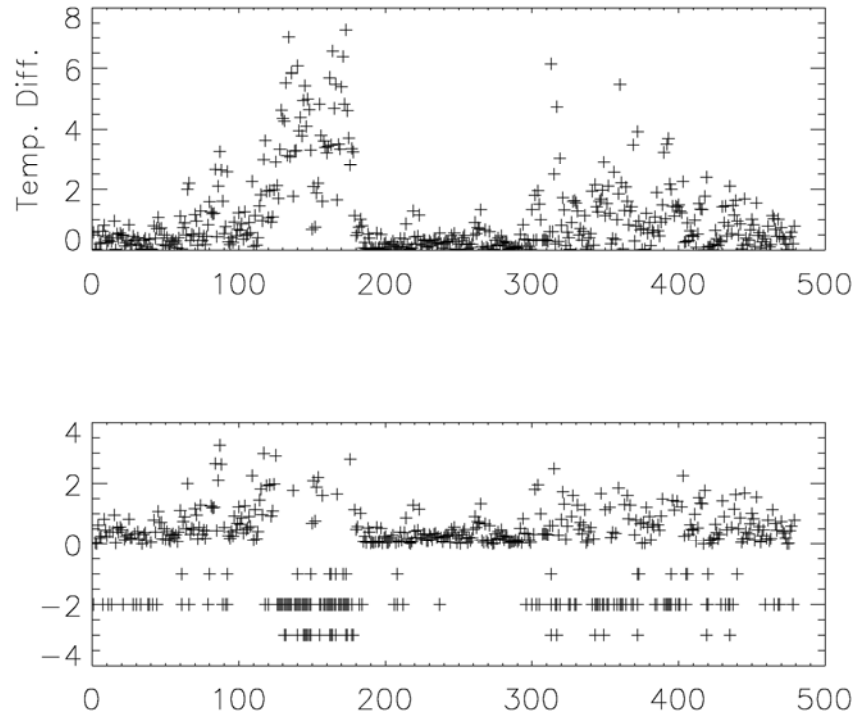


Figure 89: Top: Absolute value of the difference in the average lower tropospheric temperature for each FOR. Bottom: Same, but with the rejection criterion applied - negative numbers refer to applicable rejection criteria (see text).

To determine the thresholds for the various QC tests, the retrievals were ordered according to their error in lower tropospheric temperatures. The results are illustrated in Figure 90. All three tests diverge as the temperature error gets large, indicating that for the extreme cases each test will work and a more varied and extensive data set will be needed to finalize the thresholds. Figure 91 shows the RMS error for temperature and moisture retrievals with and without rejection. It should be pointed out that the variability of the profiles across each scan is small. Since the MW-only retrieval is minimally affected by clouds, the MW retrievals also vary little across a scan and the MW-only retrievals are fairly good for these scanlines. This is again an indication that more scanline type datasets will be needed to ensure that the QC thresholds are optimal.

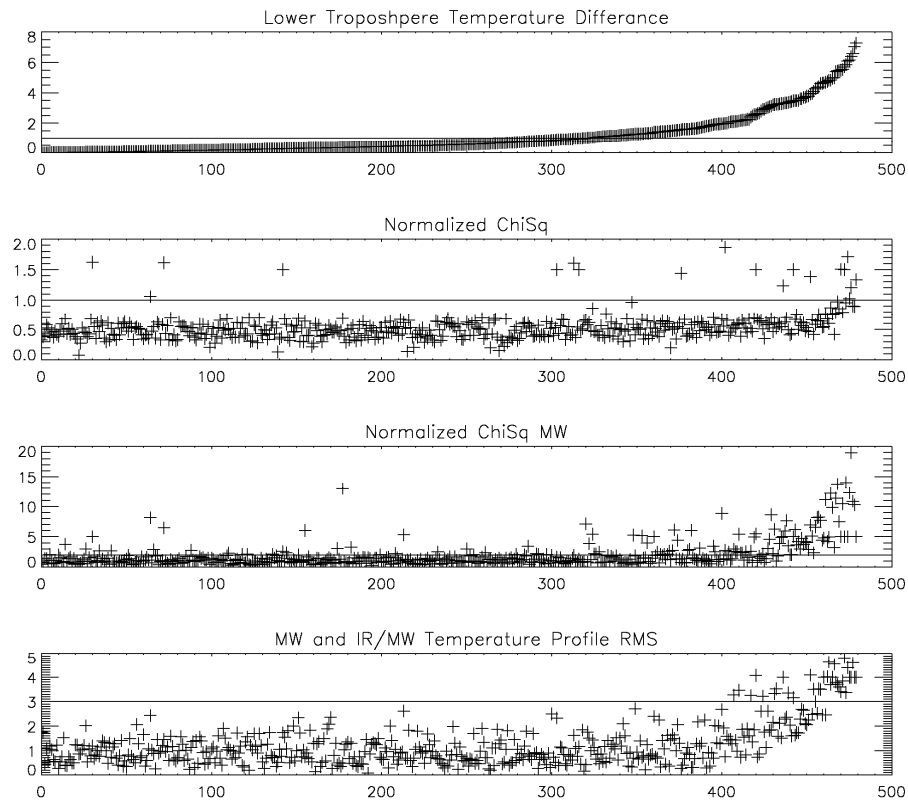


Figure 90: (a) Error in the lower tropospheric temperature for each FOR (sequenced from small to large), (b) χ^2 plotted in the same sequence as (a), (c) χ^2 MW plotted in the same sequence as (a), (d) σ plotted in the same sequence as (a).

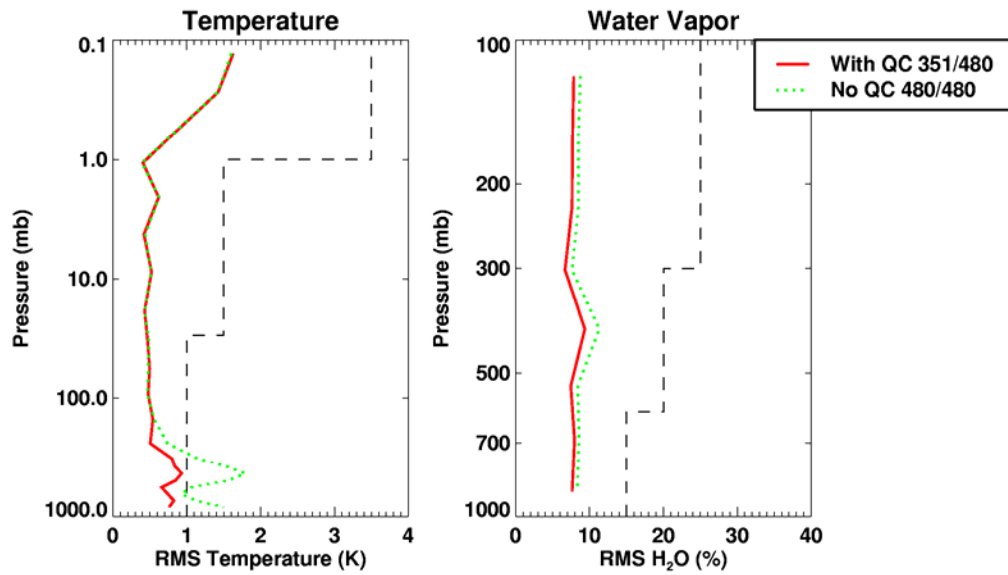


Figure 91: RMS error for temperature and moisture. Results with and without QC are presented. With QC implemented, 129 profiles out of 480 were rejected (27%).

7.7 Error Analysis for the Slant-to-Vertical Conversion

As described in Section 5.7.3.4, the temperature and moisture profiles retrieved along the slant paths are transformed to the local vertical paths by means of a recursive filter. The errors associated with this transformation have been estimated using meteorological fields simulated by the NCEP ETA model (Mesinger *et al.* 1988; Black 1994) and the Penn State/NCAR MM5 model. Examples of temperature and moisture fields adopted for the error analysis are shown in Figure 92. The ETA model simulation was performed on a 40 km grid, whereas the MM5 simulation was performed on a 15 km grid (with the MM5 simulation especially designed to mimic the ETA-model simulation in a domain covering the Great Lake Region). There is a qualitative similarity between the models, with the higher resolution MM5 fields exhibiting more small-scale variability. For the ETA model, a somewhat wider range of scenes (in addition to that shown in Figure 92) has been considered, but the MM5 error analysis is based on the fields shown in Figure 92. However, as the meteorological conditions shown in Figure 92 represent a rather stressing frontal situation, we expect the errors computed under these conditions to be on the upper end of a possible error budget.

The meteorological fields from the ETA and MM5 models have been Fourier-decomposed in order to obtain expressions from which the “true” values at the local vertical locations could be calculated analytically. The RMS differences between these true values and the values obtained at the same locations by applying the recursive filter are taken as the error budget of the slant-to-vertical conversion based on the recursive filter. In a similar way, the RMS differences between the true values and the slant profile values represent the error in the slant-to-vertical conversion based on equating the slant profile with the local vertical profile.

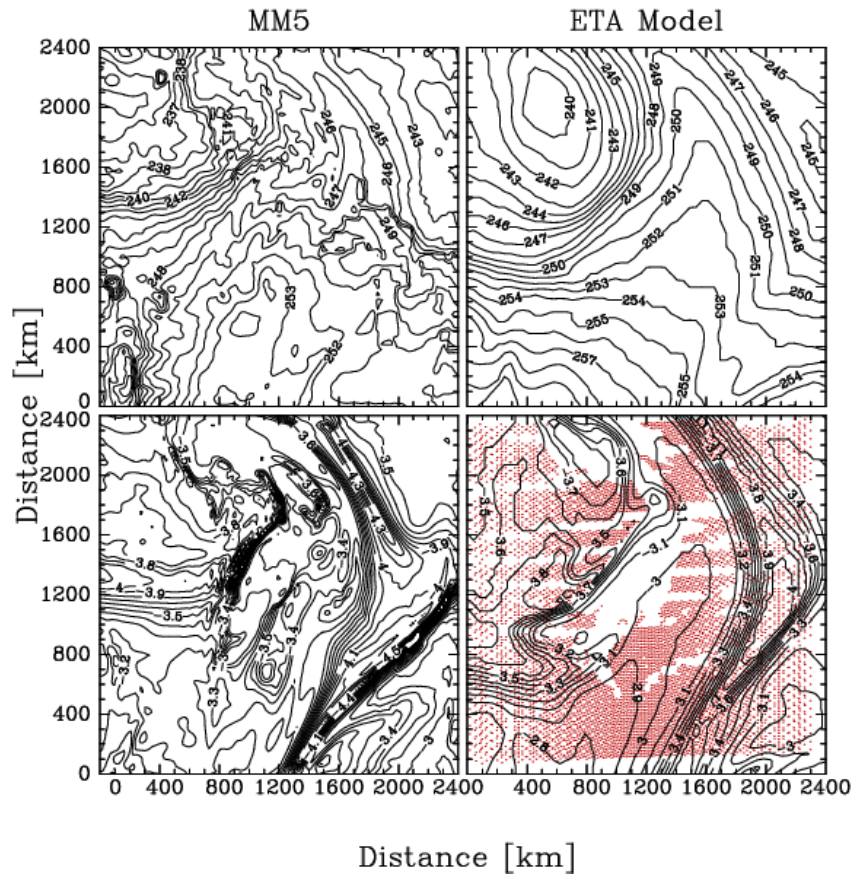


Figure 92: Temperature (upper panels, contour interval 1 K) and moisture (lower panels, contour interval 0.1 in the \log_{10} of water vapor mass mixing ratio in g/kg) for March 20th, 2001 over the Great Lake Region. On the left are the fields simulated by the MM5 model, with the corresponding fields from the ETA model shown on the right. The red dots in the lower right panel represent locations of CrIS footprints at the surface (excluding cloudy FOVs).

In order to illustrate the dependence of the conversion error on the spatial variability of the simulated field, the RMS errors for the two conversion methods are plotted in Figure 93 as a function of the number of Fourier components used to represent the field. The errors in Figure 93 have been computed for the MM5-simulated moisture field and they have been calculated in a layer-mean sense for a 2 km thick layer centered at 450 mb. The errors increase as more Fourier components are retained. For a small number of components (less than 1000), the recursive filter produces small errors ($\leq 1\%$) that are comparable to those computed for the smoothly varying ETA model moisture field (see below). Asymptotically, these errors grow to almost 2.5%, but are about 0.2% smaller than for the slant = local vertical approximation. The errors shown in

Figure 93 have been computed assuming 1 report per FOR, which maximizes the error budget (on the other hand, it diminishes the difference between the two approaches to the conversion). It should also be noted that the relatively large errors in Figure 93 are caused by a numerical aspect of the moisture simulation in the MM5. The moisture field is advected using a low-order finite-difference scheme, which produces numerical grid-cell scale oscillations known as over- and under-shots. The under-shots occasionally produce negative mixing ratios, which are eliminated by an ad-hoc numerical procedure called filling. This procedure creates very small moisture mixing ratios locally (several orders of magnitude smaller than “physical” values at neighboring gridpoints). Although these very small values are sporadic, they lead to very large RMS errors when these errors are expressed as percent of the true values. The moisture fields used to produce the RMS error budget in Figure 93 have been artificially modified by setting the very small moisture values to the average of the not-very-small values over the computational domain (without this modification, the RMS errors expressed in percent would be very large). This procedure reduces the numerical artifact to a large extent, but apparently is unable to eliminate it completely.

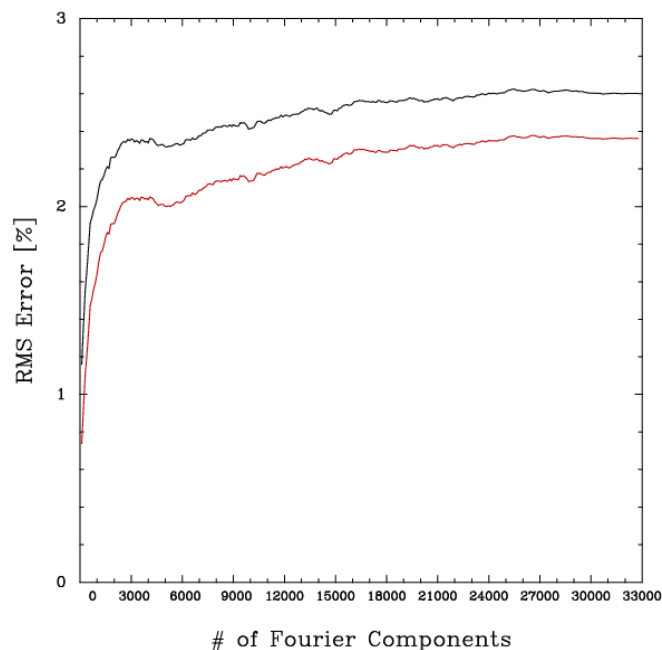


Figure 93: RMS error for the slant-to-vertical conversion in a 2 km thick layer centered at 450 hPa for the moisture field simulated by the MM5 model as a function of the number of Fourier components used to represent the field. Lower curve: recursive filter; upper curve: slant = local vertical approximation.

Layer-mean RMS errors for the two methods applied to ETA model fields are shown in Figure 94. Equating the slant and local vertical profiles produces errors of less than 0.1 K in temperature and less than 1% in moisture. The largest errors in temperature occur at 100 hPa, indicating that they are mainly due to the increasing distance between the slant and local vertical profiles with altitude. The errors in the highest layer are smaller than at 100 hPa, but this is most likely due to the degraded quality of the simulation at the top model level. In contrast, the moisture errors maximize around 400 hPa, reflecting maximum spatial variability in the mid-troposphere.

Application of the recursive filter reduces the conversion errors at all levels (except, of course, at the surface, where the slant and local vertical values are identical). The improvement appears to be a function of the number of reports, with the greatest improvement achieved for 9 reports per FOR (the RMS error of less than 0.02 K for temperature and less than 0.3% for moisture with the application of the recursive filter). The improvement is only marginal with 1 report per FOR, but even in this case it is consistent over the vertical range considered.

Layer-mean RMS conversion errors for the MM5-simulated fields are plotted in Figure 95. As in the case of ETA model fields, the recursive filter produces consistently smaller errors than the slant = local vertical approximation, with the greatest improvement for 9 reports per FOR (and only marginal improvement for 1 report per FOR). The largest contrast to the ETA model results is provided by the large errors for moisture, about 2.5% at 450 hPa with either method when 1 report per FOR is available. These large errors are partially due to the higher spatial resolution of the MM5 model (and thus a larger amount of small-scale variability), but the numerical artifact mentioned above is also suspected to play a role. It should be noted that that even in this case the recursive filter performs consistently better than the slant = local vertical approximation, especially in the upper troposphere where it reduces the moisture errors to less than 1% when 9 reports are available per FOR.

In conclusion, the slant-to-vertical conversion produces errors that are a strong function of the spatial variability in the meteorological fields. For temperature, these errors can be reduced to less than 0.1 K by the application of the recursive filter, both in the 40 km fields simulated by the

ETA model and in the 15 km fields simulated by the MM5 (for the MM5 temperature field, the RMS errors can be as large as 0.2 K if only 1 report is available per FOR). Layer-mean RMS errors in moisture are less than 1% when the recursive filter is applied to the ETA model field (it can be less than 0.3% if all 9 reports are available for each FOR). Regardless of the number of reports, in the case of ETA-simulated fields the errors caused by the slant-to-vertical conversion appear smaller than the error budget allocation defined by the EDR requirements for both temperature and moisture. However, when the moisture field is simulated at the higher resolution of the MM5 run, these errors can be as large as 2.5% in the mid-troposphere. These large errors are a function of the spatial variability in the simulated field and some portion of this variability at the smaller scales appears to be caused by numerical artifacts in the MM5 simulation. Nevertheless, these results indicate that the slant-to-vertical conversion errors can be significant if the meteorological field exhibits significant variability at spatial scales comparable to or smaller than the size of a CrIS FOV. In view of the stressing situation represented by the MM5 field, we regard the error profiles as representative of the error budget for the slant-to-vertical conversion under general conditions.

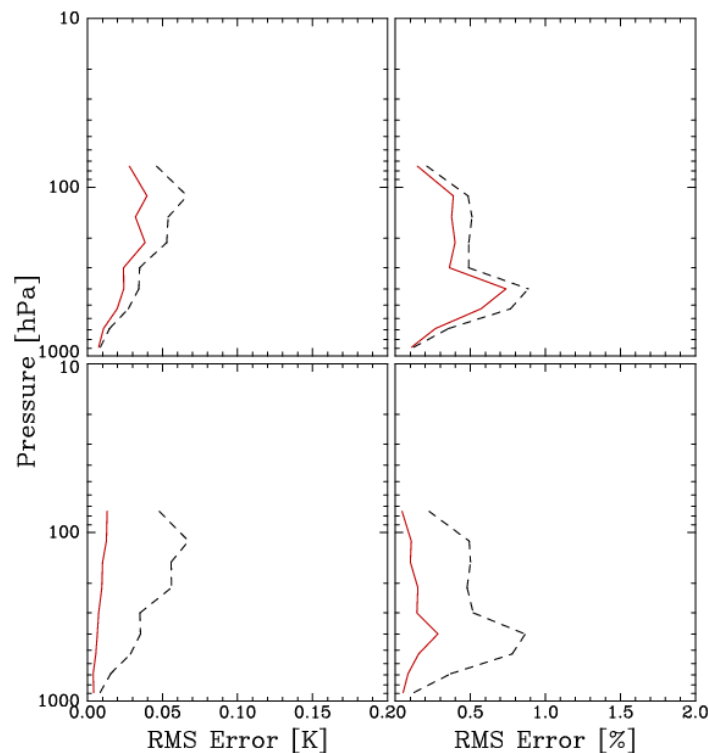


Figure 94: Layer-mean RMS errors for temperature and moisture simulated by the ETA model. Dashed lines: local vertical = slant; solid lines: local vertical obtained from the application of the recursive filter. The upper and lower panels are for 1 and 9 reports per FOR, respectively.

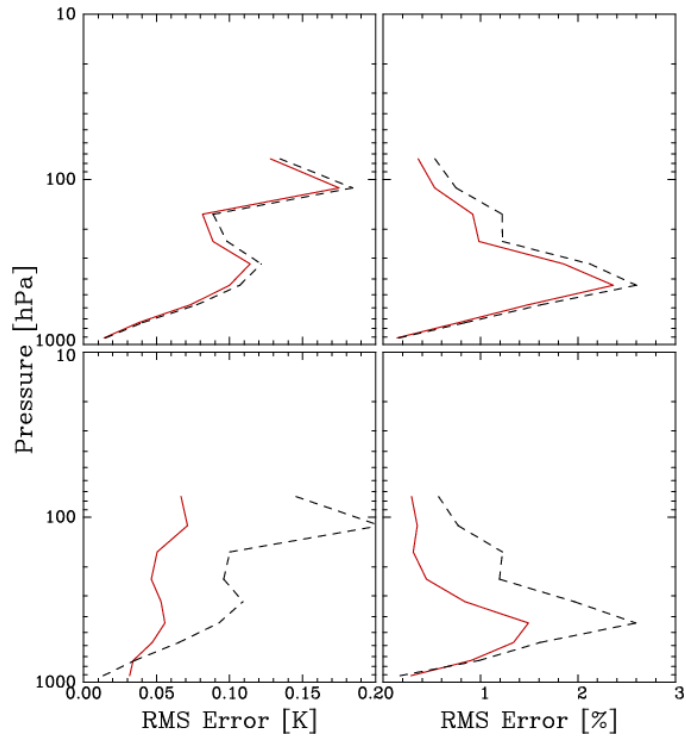


Figure 95: Analogous to Figure 94, but for the MM5 model. The RMS error profiles in this figure are taken as representative of the error budget in the slant-to-vertical conversion.

7.8 Impact of Switching from AMSU/MHS to ATMS

There are two main purposes for the microwave component of the CrIMSS EDR retrieval algorithm. First, it provides a first guess estimate of the temperature and moisture profiles and the constraint for the cloud-clearing algorithm. Second, it provides EDR retrievals below clouds for overcast conditions. Therefore the quality of microwave retrievals is tightly connected with the CrIMSS EDR performance.

Prior to version 3.0, the retrieval algorithm has assumed that the microwave sounder has the characteristics of AMSU and MHS (although the ATMS was included as an option in version 2.3). However, the actual sounder to fly as part of CrIMSS will be ATMS. In addition to the differences in the number of channels and quasi-polarizations, the footprint sizes are different between AMSU/MHS and ATMS. The sensor characteristics of microwave sounders are given in Section 3.2. The objective of the ATMS trade studies is to assess the impact on the CrIMSS EDR performance when AMSU/MHS is replaced with ATMS.

This section is divided into two parts. The first part discusses the impact of the noise factor for the re-sampled ATMS radiance on the CrIMSS EDR performance under clear (no cloud) and cloudy conditions. It should be noted that the noise amplification (reduction) factor provides an adequate representation of the noise characteristics only under homogeneous scene conditions. When the scenes are inhomogeneous, the retrieval performance degradation due to the footprint-matching error may dominate. The second part of the trade study examines the impact of inhomogeneous scenes on the EDR retrieval.

7.8.1 Impact of ATMS Noise Amplification on Homogeneous Scenes

This section describes a trade study of microwave retrieval performance based on the ATMS noise amplification factor for homogeneous scenes. The ATMS noise characteristics are summarized in Table 25. Both NGES (Northrop Grumman Electronic Systems, the supplier of ATMS) and AER-computed noise amplification factors independently using the Backus-Gilbert

footprint matching method. The results from these two studies are not in agreement, with the AER calculations predicting smaller noise factors and, consequently, better retrievals.

Table 25: ATMS Noise Characteristics

#	Freq (GHz)	NEAT (K)	#	Freq (GHz)	NEAT (K)
1	23.8	0.50	12	$57.290344 \pm 0.3222 \pm 0.048$	1.00
2	31.4	0.60	13	$57.290344 \pm 0.3222 \pm 0.022$	1.50
3	50.3	0.70	14	$57.290344 \pm 0.3222 \pm 0.010$	2.20
4	51.76	0.50	15	$57.290344 \pm 0.3222 \pm 0.0045$	3.60
5	52.8	0.50	16	88.2	0.30
6	53.596 ± 0.115	0.50	17	165.5	0.60
7	54.40	0.50	18	183.31 ± 7	0.80
8	54.94	0.50	19	183.31 ± 4.5	0.80
9	55.50	0.50	20	183.31 ± 3	0.80
10	57.290344	0.75	21	183.31 ± 1.8	0.80
11	57.290344 ± 0.217	1.00	22	183.31 ± 1	0.90

To determine the impact on homogeneous scenes, a scene consisting of 400 FORs was selected at random from the NOAA-88b dataset. Nine FOVs were simulated and the scan angles were chosen at random from the set of 30 values.

7.8.1.1 Performance Based on NGES Noise Amplification Factors (Cloud-Free)

The baseline noise model assumes a one-over-square-root-of-nine reduction in the noise amplitude for all 22 channels. Figure 96 shows the noise amplification factors as a function of scan angle computed by NGES using the Backus-Gilbert method. Figure 97 shows a comparison of the mean noise amplitude for the baseline noise model with the noise amplitudes based on the Backus-Gilbert calculations. These results have been averaged over all 400 FORs of the simulation profiles. For channels 1 and 2 there is a large increase in the predicted noise, while there is a decrease for channels 16 to 22. There is little effect in channels 3-15, which is to be

expected since the NGES calculation for these channels is essentially equivalent to one-over-square-root-of-nine.

Figure 98 compares the MW retrieval performance for simulations based on the baseline noise model and for those based on the Backus-Gilbert noise estimates (BG-1-22). Only the water vapor shows any significant difference. At high altitudes, the retrieval is improved. Lower in the atmosphere the retrieval is worse. Figure 99 shows the results of simulations using baseline noise for channels 3-22 and Backus-Gilbert for 1 and 2 (BG1-2) and of simulations using baseline noise for channels 1-15 and Backus-Gilbert for 16-22. The figure illustrates how the increased noise in channels 1-2 leads to increased errors in water vapor and the decreased noise in channels 16-22 leads to decreased errors in water vapor.

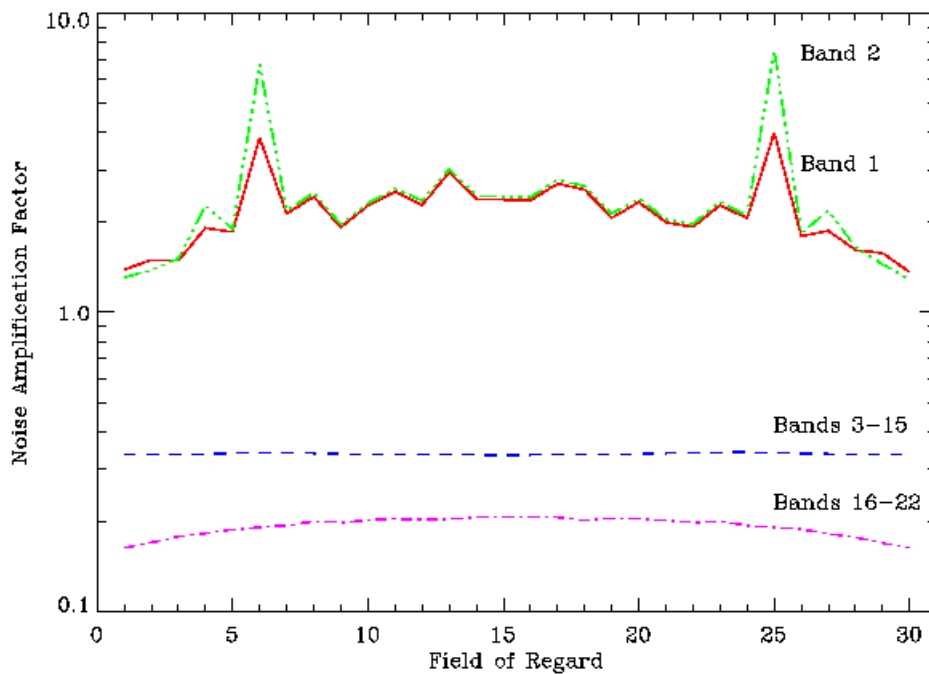


Figure 96: ATMS noise amplification factors based on NGES Backus-Gilbert calculations.

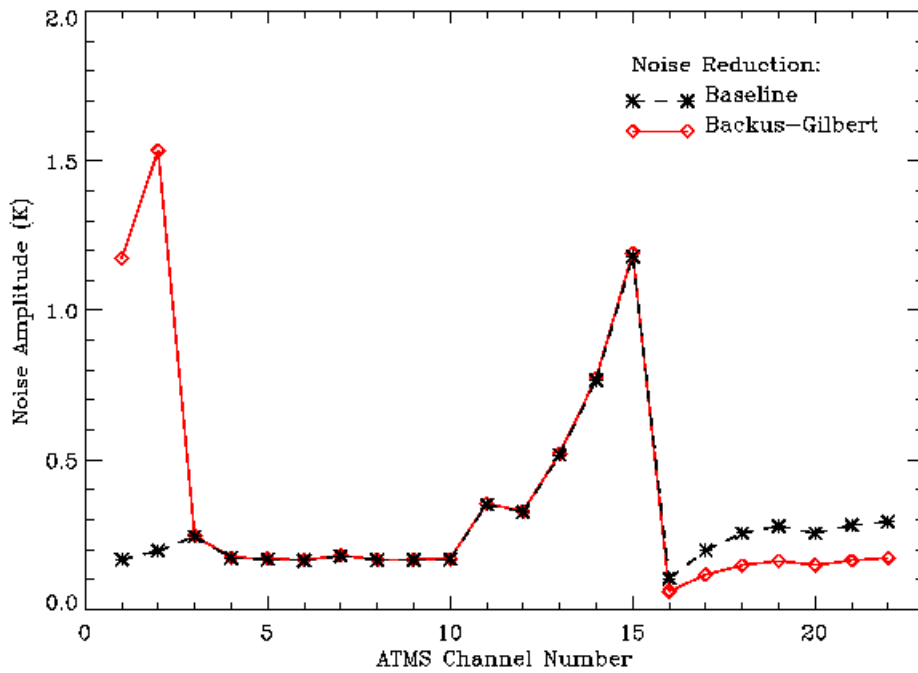


Figure 97: Noise amplitude for ATMS simulations computed from simulations of 400 random FORs. The baseline noise model assumes a noise reduction of one-over-root-nine.

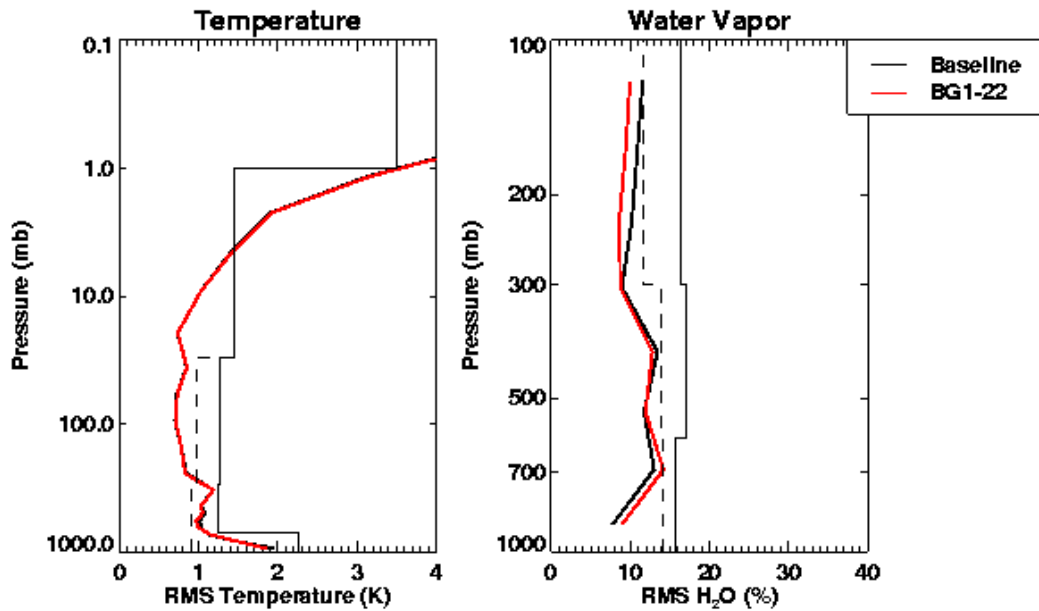


Figure 98: MW retrieval performance for the baseline (one-over-root-nine) noise model and based on the NGES Backus-Gilbert noise amplification estimates.

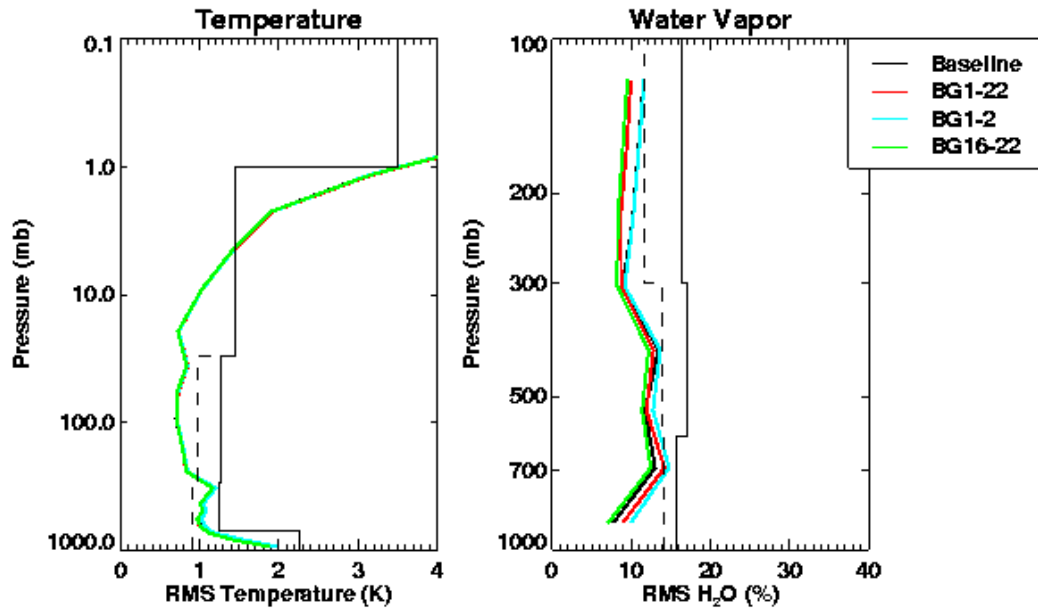


Figure 99: MW retrieval performance based on four noise models. BG-1-22 used Backus-Gilbert noise estimates for channels 1 to 22. BG1-2 and BG16-22 used Backus-Gilbert noise estimates for channels 1 to 2 and 16 to 22, respectively, and used baseline noise estimates for the other channels.

The simulations were repeated for fixed scan angles for both the Backus-Gilbert and baseline noise models. Figure 100 shows the difference in RMS water vapor performance for Backus-Gilbert with respect to the baseline as a function of FOR. The impact of the noise amplification is less than 2% and there is little variation with scan angle.

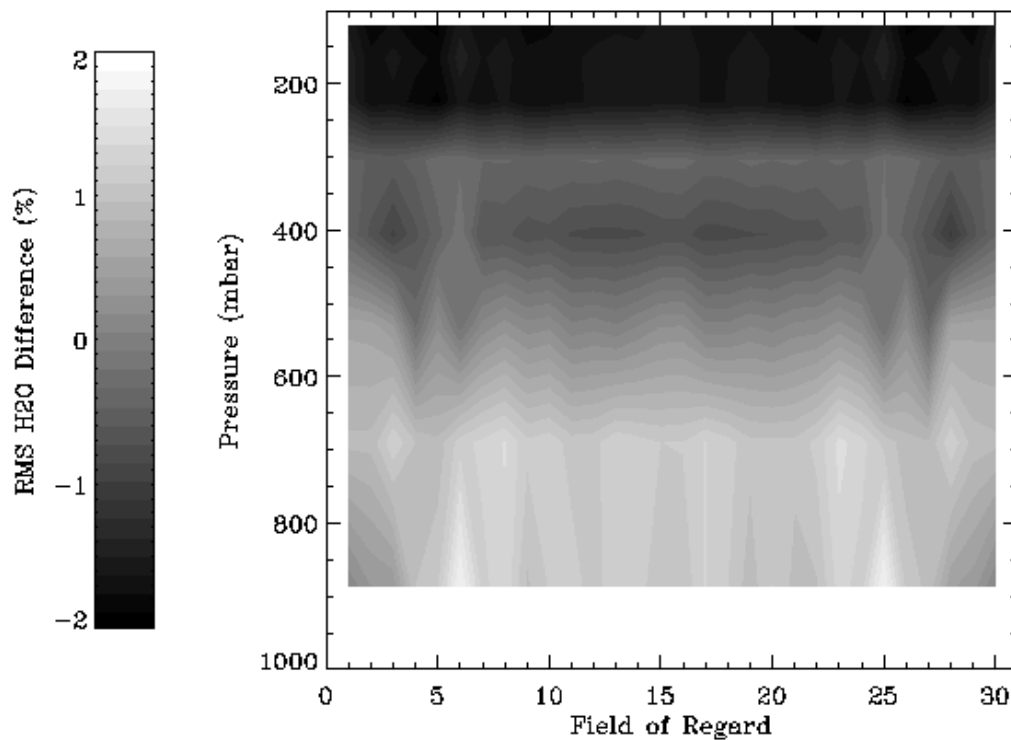


Figure 100: Difference in water vapor performance with respect the baseline noise model as a function of FOR (i.e., scan angle). The difference is less than 2% and there is little variation with scan angle.

7.8.1.2 Performance Under Cloudy Conditions

The effect on performance of the ATMS-contractor noise predictions has also been investigated under cloudy conditions. This section examines the impact of the increased noise in ATMS channels 1 and 2 on the MW and MW/IR retrievals. Additional inputs for these simulations (which are a departure from the clear-sky study) were as follows.

- ATMS noise adopted from a recommended NASA specification (see Table 26).
- Prigent emissivities were used in place of Grody model.
- Random profiles from NOAA88b selected over land only.
- 2 FOV simulated.

- Cloud located at 700 mbar with fractions 0.35 and 0.65.

Table 26: Recommended ATMS Noise Characteristics

#	Freq (GHz)	NE Δ T (K)	#	Freq (GHz)	NE Δ T (K)
1	23.8	0.90	12	57.290344 \pm 0.3222 \pm 0.048	1.20
2	31.4	0.90	13	57.290344 \pm 0.3222 \pm 0.022	1.50
3	50.3	1.20	14	57.290344 \pm 0.3222 \pm 0.010	2.40
4	51.76	0.75	15	57.290344 \pm 0.3222 \pm 0.0045	3.60
5	52.8	0.75	16	88.2	0.50
6	53.596 \pm 0.115	0.75	17	165.5	0.60
7	54.40	0.75	18	183.31 \pm 7	0.80
8	54.94	0.75	19	183.31 \pm 4.5	0.80
9	55.50	0.75	20	183.31 \pm 3	0.80
10	57.290344	0.75	21	183.31 \pm 1.8	0.80
11	57.290344 \pm 0.217	1.20	22	183.31 \pm 1	0.90

Figure 101 illustrates the noise amplitude derived from simulations of 400 FORs at random scan angles for the 22 ATMS channels and with 2 FOVs per FOR. Values are computed using the baseline noise and including the NGES noise amplification factors. NGES factors predict an increase in noise in channels 1 and 2 and a reduction in noise for channels 16 to 22. The baseline calculations represent a one-over-square-root-of-nine noise reduction for channels 1 to 15 and a one-over-square-root-of-two noise reduction for channels 16 to 22. These resulting amplitudes, which are measured from the data, are compared with the expected values in order to verify the modifications made to the simulation code.

Figure 102 shows the results of the MW and MW/IR retrievals based on simulations generated with the baseline noise amplification (1) and with the NGES noise amplification (2). The results were compared with retrievals produced using the repository (baseline) version of the simulation and retrieval codes (not shown) in order to verify the code modifications made to the retrieval code. The results show that the MW water vapor retrieval based on the NGES noise is improved relative to the baseline. This is largely due to the decreased noise in channels 16 to 22, which

seems to compensate for the increased noise in channels 1 and 2. The MW temperature retrievals show very little difference in performance with respect to the baseline. This is due to the fact that the noise amplitude in channels 3 to 15 is the same for both simulations. The MW/IR retrievals of temperature and water vapor exhibit very little difference in performance with and without the noise amplification. In other words, the MW/IR retrieval is not sensitive to small differences in the first guess provided by the MW retrieval.

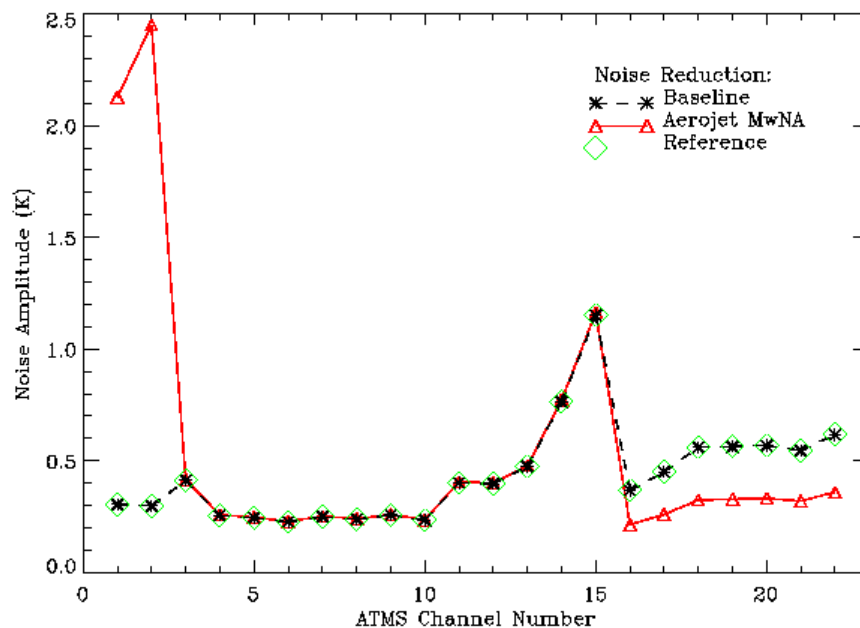


Figure 101: Noise amplitude for simulations based on the baseline ATMS noise and including the ATMS noise amplification factors computed by NGES.

To further investigate the influence of channels 1 and 2 in the MW and MW/IR retrievals, simulations were conducted using the baseline noise and omitting channels 1 and 2 in the retrievals. In this case, the simulations were generated for FOR #1 only (which, at edge-of-scan, demonstrated the largest effect on the MW retrievals). The results are illustrated in Figure 103. The MW retrieval of water vapor is degraded near the surface in the absence of the two bands but the MW/IR retrieval is affected very little.

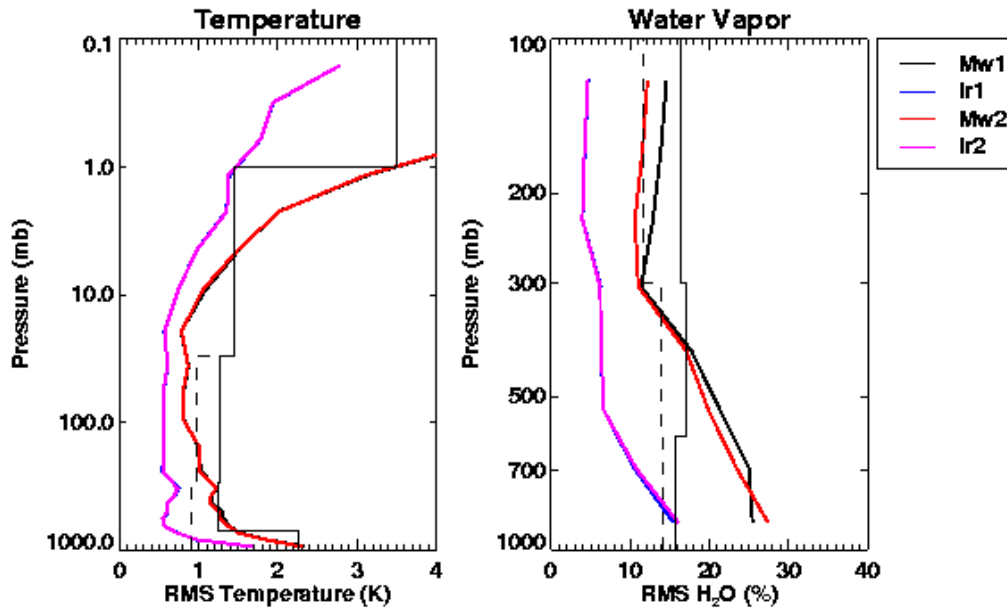


Figure 102: MW and MW/IR retrieval performance statistics based on simulations with the baseline ATMS noise (1) and with ATMS noise amplification factors computed by NGES (2).

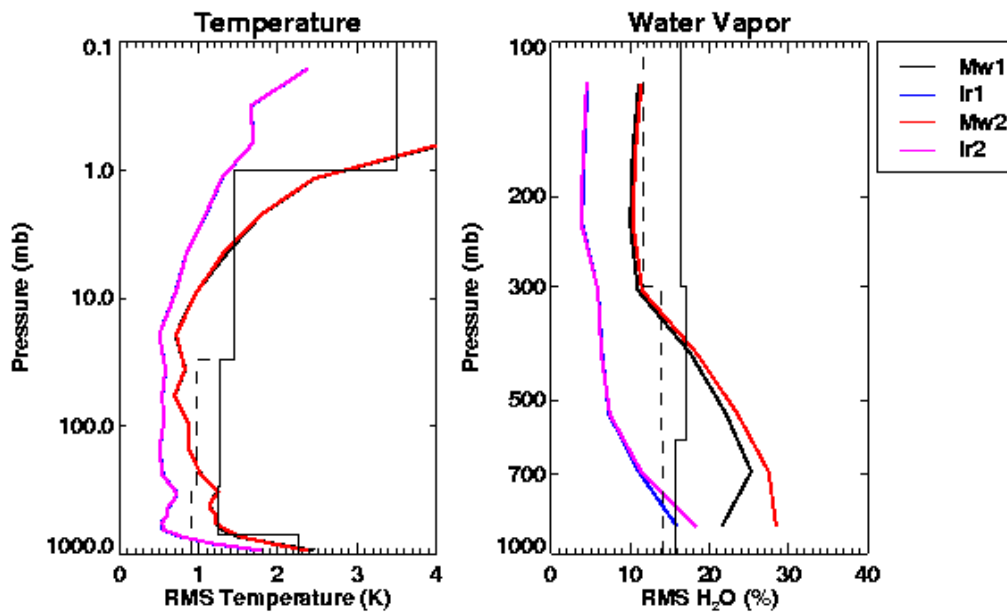


Figure 103: MW and MW/IR retrieval performance statistics based on simulations with the baseline ATMS noise including channels 1 and 2 (1) and excluding channels 1 and 2 (2).

Finally, the impact on MW and MW/IR retrievals was investigated using the noise amplification factors computed by AER. In this case, simulations were conducted at edge-of-scan only (FOR #1). The noise amplitude computed based on the AER noise amplification predictions are

illustrated in Figure 104. The performance results are presented in Figure 105. The results show that both the temperature and water vapor MW retrievals are improved relative to the baseline. The improvement in temperature is to the decreased noise predicted for channels 3 to 15. In addition, the MW/IR retrievals exhibit some improvement in both temperature and water vapor relative to the baseline.

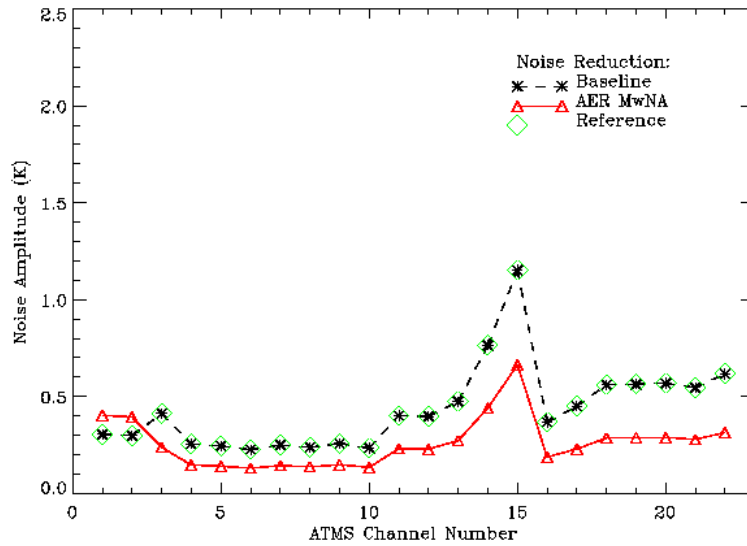


Figure 104: Noise amplitude for simulations based on the baseline ATMS noise and including the ATMS noise amplification factors computed by AER (for FOR #1).

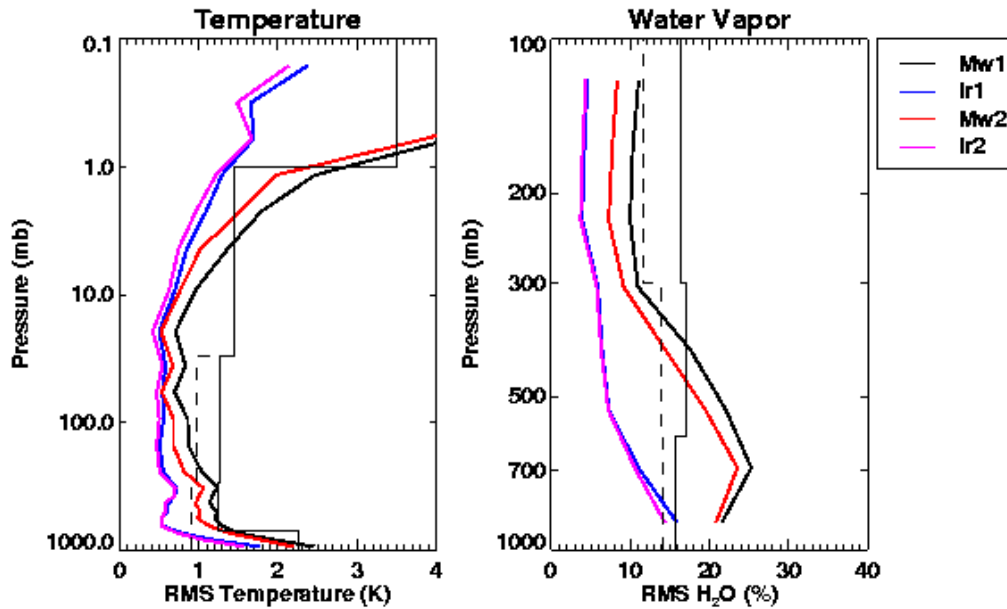


Figure 105: MW and MW/IR retrieval performance statistics based on simulations with the baseline ATMS noise (1) and with ATMS noise amplification factors computed by AER (2). The simulations are at edge-of-scan (FOR #1).

The following figures provide updated results based on footprint matching to the 3.3 degree CrIS FOR. The noise levels for AER and NGES are plotted in Figure 106, although we have assumed that NGES’s noise for channel 16 is really for the 2.2 degree FOV (not 1.1 degrees as indicated in their memo).

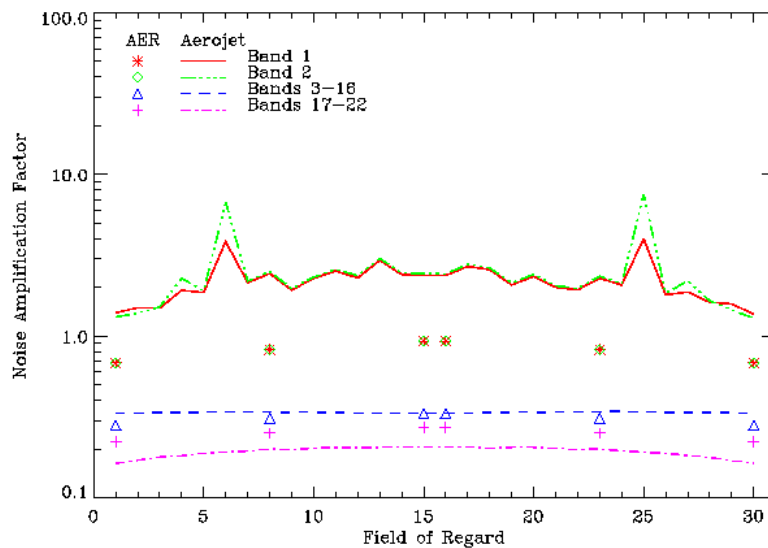


Figure 106: NGES and AER noise amplification factors comparison.

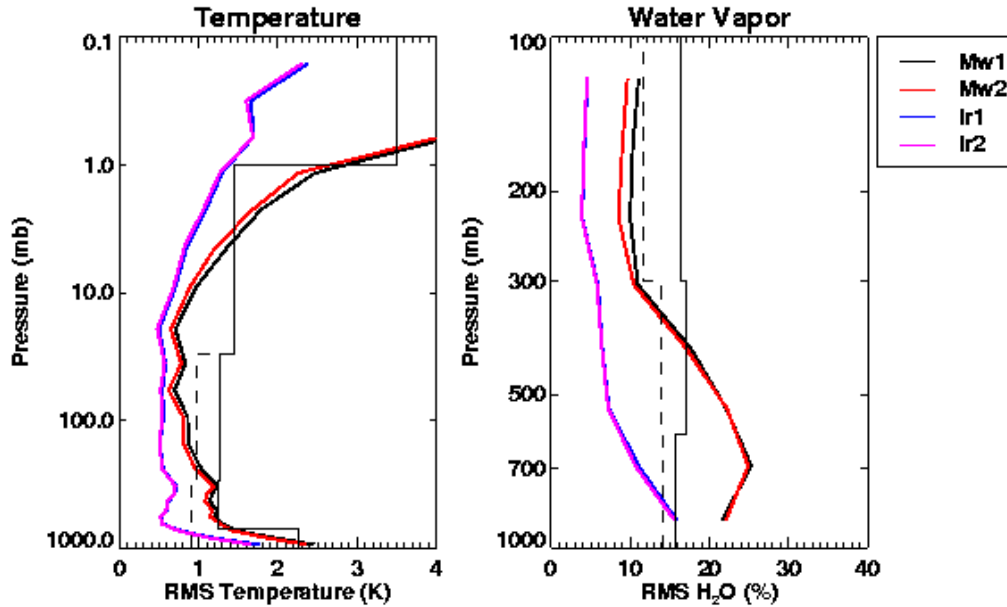


Figure 107: Performance based on AER noise amplification estimates (2) compared to baseline (1) for 700 mbar cloud and for FOR #1.

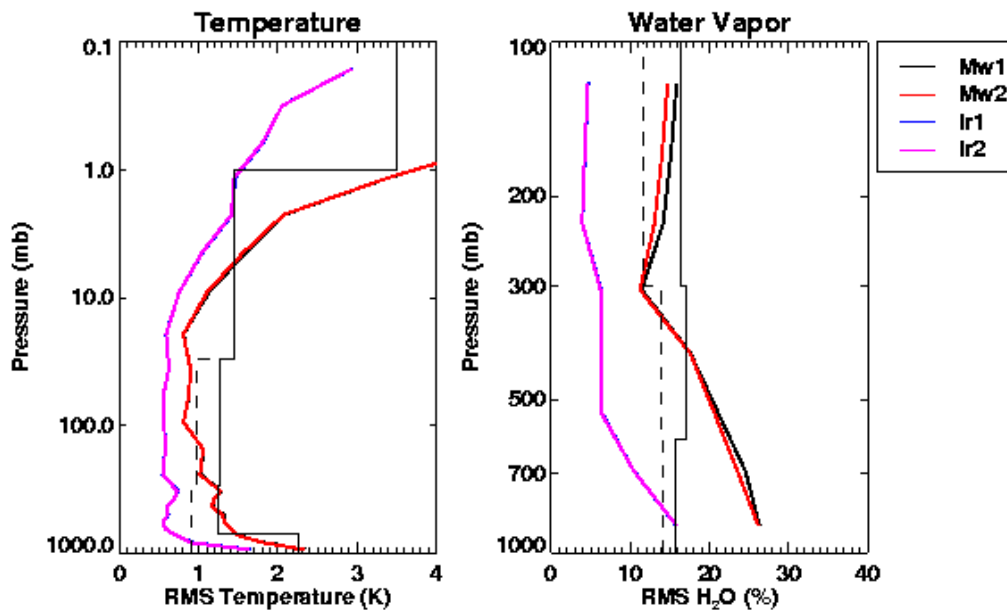


Figure 108: Performance based on AER noise amplification estimates (2) compared to baseline (1) for 700 mbar cloud and for FOR #14.

7.8.2 Impact of ATMS Remapping Under Inhomogeneous Conditions

The impact of remapping of the ATMS footprint to that of CrIS under inhomogeneous scene conditions has also been investigated. In this section we describe the construction of the inhomogeneous scene, the application to the microwave and infrared simulations, and the EDR algorithm performance results.

7.8.2.1 Overview of Inhomogeneity Studies using MM5 Scenes

The purpose of this study is to evaluate the performance of the CrIMSS temperature and water vapor retrievals for scenes with realistic spatial variability. To accomplish this we have used high spatial resolution (2 km) scenes constructed using the MM5 model (see Appendix B) to simulate the ATMS and CrIS observations and explored the relationship between spatial resolution and noise when matching the ATMS data to CrIS. Two trade studies were performed:

1. 50 GHz channels spatial resolution/noise trade study

ATMS channels 3 through 15 have a spatial resolution of 2.2 degrees compared to the CrIS FOR of 3.3 degrees. These channels measure temperature. The high spatial resolution of these channels is a potential advantage over AMSU for which the spatial resolution in comparable channels is 3.3 degrees. The purpose of this study is to investigate possible advantages to improved spatial resolution in these bands for a scene with realistic spatial variability at the cost of increased sensor noise.

2. 23/31 GHz channels spatial resolution/noise trade study

ATMS channels 1 and 2 have a much larger footprint (5.2 degrees) compared to CrIS (3.3 degrees). These channels provide information about both the column water vapor amount and surface characteristics. This size mismatch is a source of noise for the retrievals in the case of inhomogeneous scenes. The purpose of this study is to investigate the relationship between averaging ATMS data in order to decrease sensor noise and to maintain the highest resolution possible in order to reduce errors resulting from inhomogeneities within the scene.

7.8.2.2 MM5 Scene and ATMS/CrIS Simulations

The 2 km MM5 scene was used to evaluate performance under inhomogeneous conditions and to determine the impact of total noise due to spatial inhomogeneities. To simplify the analysis, the entire scene was treated as if it was observed at a single scan angle (i.e., nadir or edge-of-scan). In this way, noise statistics and performance were computed at a given angle using the information from the entire scene. The high spatial resolution of the input scene (2 km) compared to the actual CrIS footprint (16 km at nadir) was required to ensure that the spatial variability of the input scene had not been reduced by smoothing. Clouds were excluded from the initial simulations.

The spatial extent of the 2 km and 15 km MM5 scenes are shown in Figure 109. The 2 km scene was used to derive noise statistics and to evaluate performance. The 15 km scene was used (with profiles from NOAA-88) to define the covariance for the retrievals.

The degree of variability in temperature and water vapor over the extent of the 2 km MM5 scene is illustrated in Figure 110 and Figure 111. Temperature varies slowly, but strong gradients in water vapor are possible.

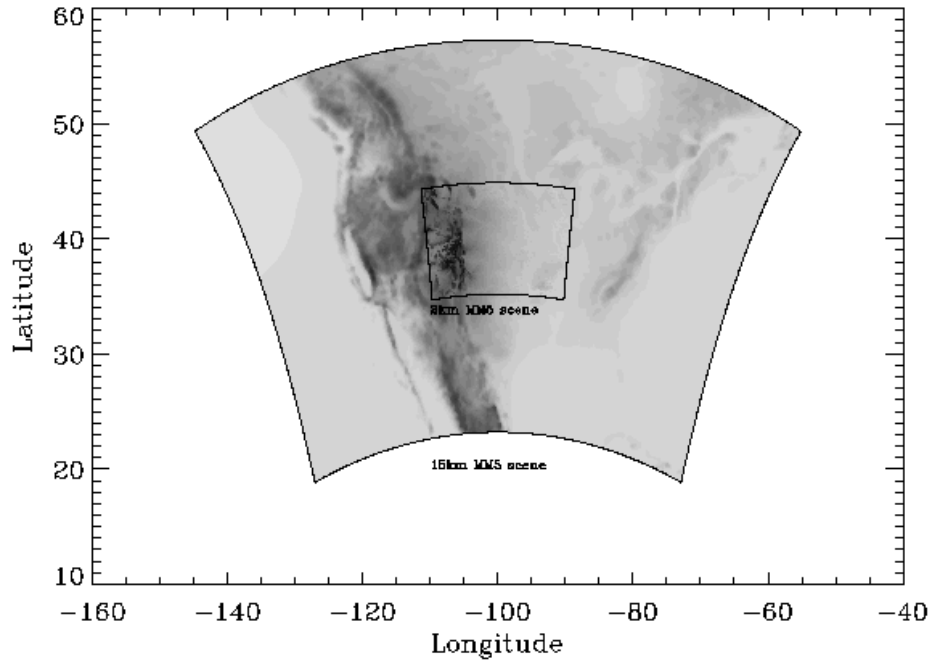


Figure 109: Surface pressure as a function of latitude and longitude showing the extent of the 2 km and 15 km resolution MM5 scenes. Simulations and retrievals were based on the 2 km scene. The covariance was computed based on data from the 15 km scene merged with data from the NOAA-88 profile database.

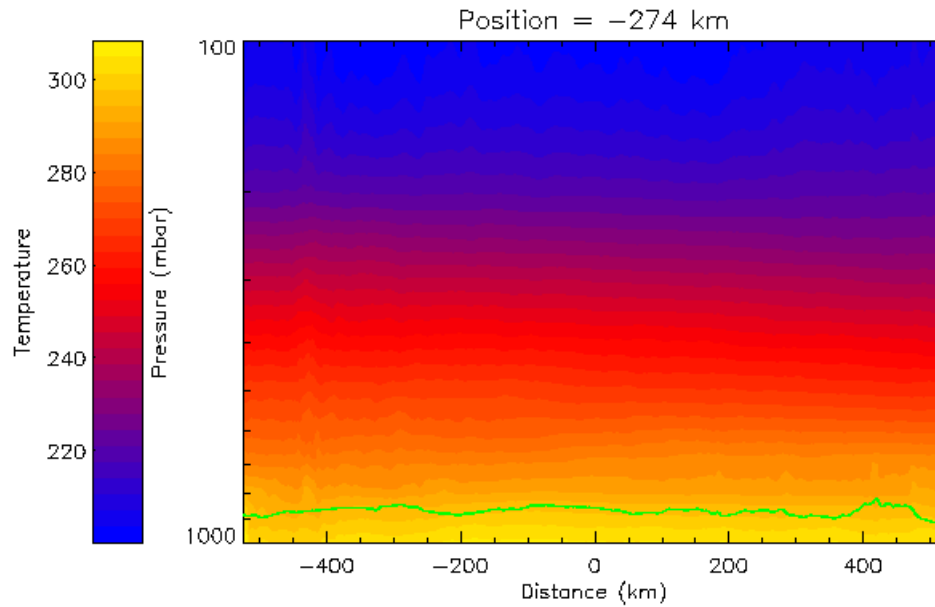


Figure 110: Air temperature below 100 mbar for a slice through the MM5 scene. The green line indicates surface pressure.

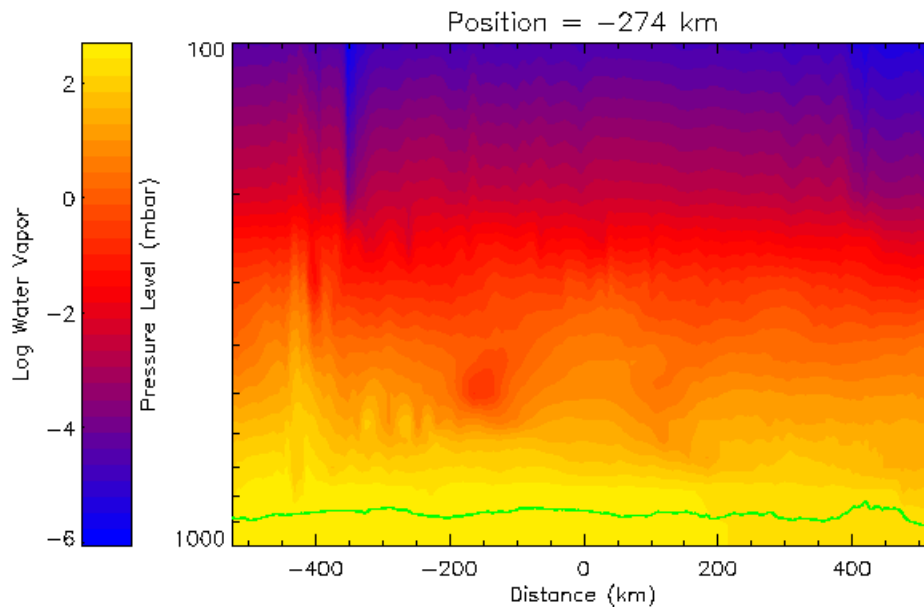


Figure 111: Water vapor for one slice through the MM5 scene. The green line indicates surface pressure.

The simulation of ATMS and CrIS data at nadir proceeded as follows. The MM5 scene was used as input to generate noise-free MW SDRs at 2 km resolution. These data were mapped to the ATMS channels by averaging all MM5 data points within the ATMS footprints (5.2, 2.2, and 1.1

degree resolution). The high-resolution of the MM5 data guarantees that the ATMS data are well represented by this approach. Noise was added to the ATMS SDRs at this point. The ATMS data were matched to the CrIS FOR by averaging all ATMS data points within each CrIS footprint. This simplistic approach to footprint matching does not attempt to minimize differences in ATMS/CrIS point spread functions. Cases with decreased resolution were represented by matching the ATMS to the area contained within the CrIS FOR plus 1.1 degrees and to the CrIS FOR plus 2.2 degrees. For reference, the 2 km MW SDRs were also mapped directly to the CrIS FOR footprint (15 km).

Figure 112 illustrates how the MM5 scene was sampled. Shown are the locations and sizes of the ATMS and CrIS footprints.

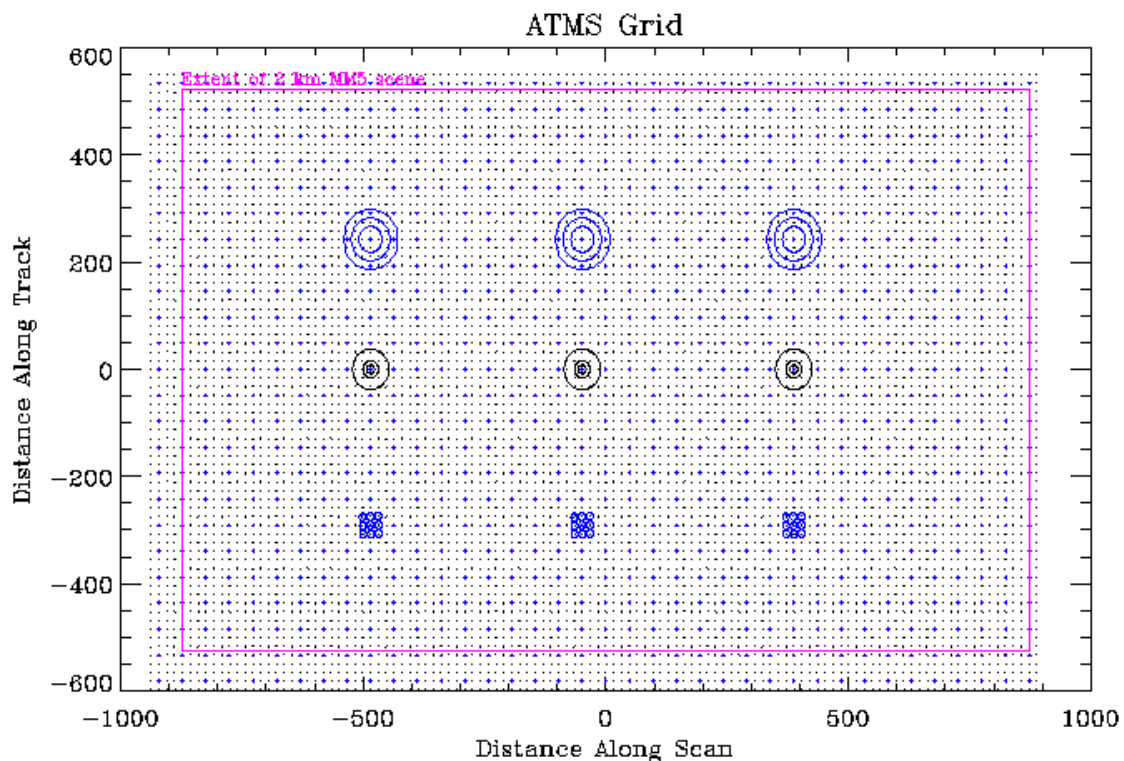


Figure 112: Selected ATMS and CrIS gridpoints and footprints used in the simulations. Black dots represent ATMS sampling at nadir. Blue dots represent CrIS sampling at nadir. The 3 ATMS footprint sizes at nadir are shown as concentric black circles. The small blue circle (top) represents CrIS field-of-regard (FOR) size at nadir. The larger blue circles represent the CrIS FOR plus 1.1 degrees and CrIS FOR plus 2.2 degrees. The set of nine blue circles (bottom) represent the CrIS FOVs at nadir. The extent of the MM5 scene is shown as a pink rectangle.

Figure 113 through Figure 115 show the signal in selected ATMS channels at the original 2 km scale. Channels 1 and 2 vary considerably due to variations in surface altitude/temperature. There is little variability in the channels sensitive to air temperature above the surface, while channels sensitive to water vapor exhibit moderate variations.

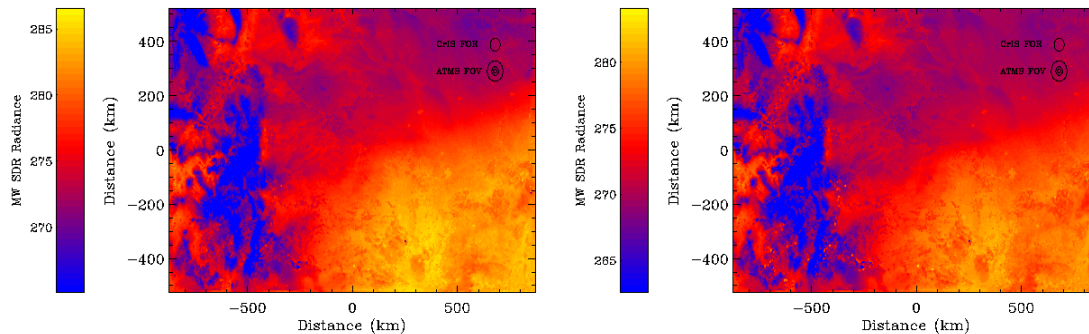


Figure 113: Simulated radiances in ATMS channels 1 (left) and 2 (right) based on the 2 km MM5 scene (at nadir). The sizes of the CrIS and ATMS footprints are indicated.

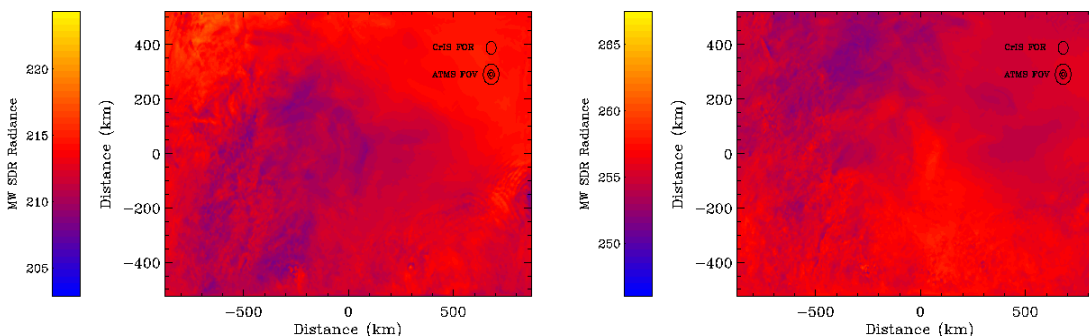


Figure 114: Simulated radiances in ATMS channels 10 (left) and 15 (right) based on the 2 km MM5 scene (at nadir). The sizes of the CrIS and ATMS footprints are indicated.

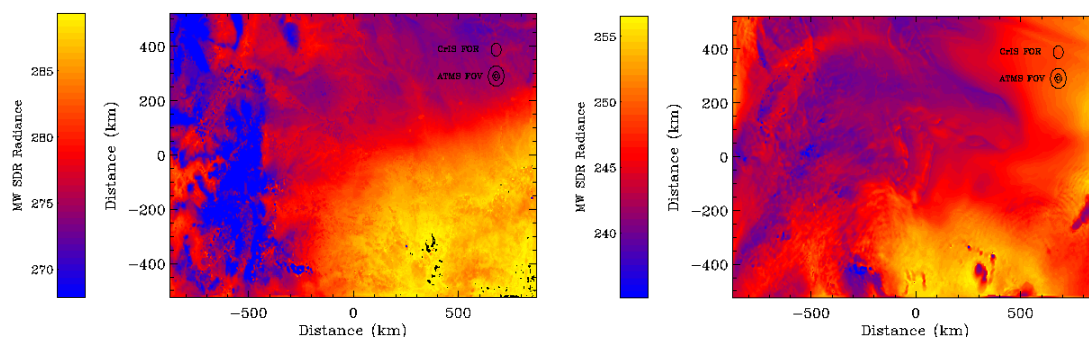


Figure 115: Simulated radiances in ATMS channel 16 (left) and 22 (right) based on the 2 km MM5 scene (at nadir). The sizes of the CrIS and ATMS footprints are indicated.

The total noise contribution in the simulations was evaluated by comparing the footprint matched SDRs (i.e., to CrIS FOR, CrIS FOR + 1.1 degrees, and CrIS FOR + 2.2 degrees) to the SDRs mapped directly to the CrIS FOR. The sensor, scene, and total noise contributions normalized by the noise amplitude for each ATMS channel is given in Table 27. ATMS SDRs matched to the CrIS FOR result in a sensor noise reduction of approximately one-over-square-root-of nine in all channels. However, the scene noise dominates, particularly for those ATMS channels that see the surface. For those ATMS channels that measure air temperature, the scene noise is a small contribution. The sensor and total noise contributions are plotted in Figure 116 for the full MM5 scene, while Figure 117 shows the total noise contributions for the left and right halves of the MM5 scene. Clearly, much larger errors are possible due to the mountainous terrain in the western portion of the scene.

Table 27: Noise Amplification Factors (NAFs) for ATMS Matched to CrIS.

ATMS Properties				NAF (FOR)			NAF (FOR+1.1)			NAF (FOR+2.2)		
Bands (Frequency, Resolution, NEdT)				Snr	Scn	Tot	Snr	Scn	Tot	Snr	Scn	Tot
1	23.8	5.2	0.90	0.33	0.54	0.63	0.22	0.69	0.73	0.16	0.85	0.86
2	31.4	5.2	0.90	0.34	0.52	0.63	0.22	0.67	0.72	0.16	0.82	0.84
3	50.3	2.2	1.20	0.34	0.15	0.36	0.21	0.39	0.43	0.16	0.56	0.58
4	51.76	2.2	0.75	0.33	0.22	0.39	0.21	0.58	0.62	0.16	0.83	0.85
5	52.8	2.2	0.75	0.33	0.18	0.39	0.21	0.47	0.52	0.16	0.67	0.69
6	53.596 ± 0.115	2.2	0.75	0.33	0.11	0.35	0.22	0.27	0.34	0.17	0.39	0.41
7	54.40	2.2	0.75	0.33	0.05	0.34	0.22	0.11	0.25	0.17	0.14	0.22
8	54.94	2.2	0.75	0.31	0.04	0.31	0.22	0.08	0.23	0.17	0.12	0.20
9	55.50	2.2	0.75	0.32	0.05	0.32	0.20	0.12	0.24	0.15	0.18	0.23
10	57.290	2.2	0.75	0.34	0.08	0.35	0.22	0.20	0.29	0.16	0.28	0.33
11	57.290 ± 0.217	2.2	1.20	0.33	0.04	0.33	0.21	0.11	0.24	0.15	0.16	0.22
12	57.290 ± 0.322 ± 0.048	2.2	1.20	0.35	0.04	0.35	0.23	0.11	0.25	0.17	0.15	0.23
13	57.290 ± 0.322 ± 0.022	2.2	1.50	0.32	0.04	0.32	0.21	0.09	0.22	0.15	0.13	0.20
14	57.290 ± 0.322 ± 0.010	2.2	2.40	0.33	0.03	0.33	0.21	0.06	0.22	0.17	0.08	0.19
15	57.290 ± 0.322 ± 0.005	2.2	3.60	0.32	0.02	0.32	0.22	0.03	0.22	0.17	0.05	0.18
16	88.2	1.1	0.50	0.33	0.43	0.55	0.21	1.09	1.12	0.16	1.55	1.56
17	165.5	1.1	0.60	0.35	0.29	0.46	0.23	0.89	0.93	0.17	1.32	1.33
18	183.31 ± 7	1.1	0.80	0.34	0.16	0.38	0.21	0.48	0.55	0.16	0.72	0.76
19	183.31 ± 4.5	1.1	0.80	0.32	0.13	0.34	0.20	0.39	0.44	0.15	0.60	0.62
20	183.31 ± 3	1.1	0.80	0.34	0.13	0.37	0.22	0.35	0.41	0.16	0.53	0.55
21	183.31 ± 1.8	1.1	0.80	0.34	0.19	0.40	0.22	0.35	0.42	0.16	0.51	0.54
22	183.31 ± 1	1.1	0.90	0.31	0.32	0.46	0.21	0.39	0.46	0.15	0.50	0.54

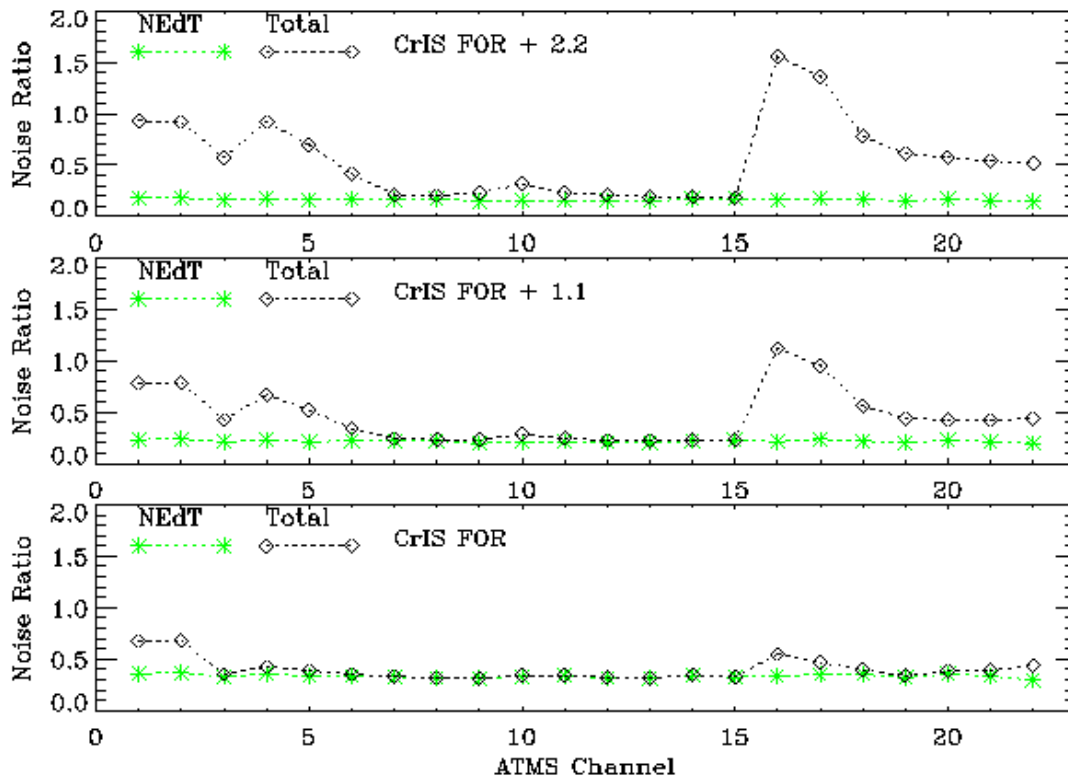


Figure 116: Sensor and total noise for entire MM5 scene based on nadir geometry.

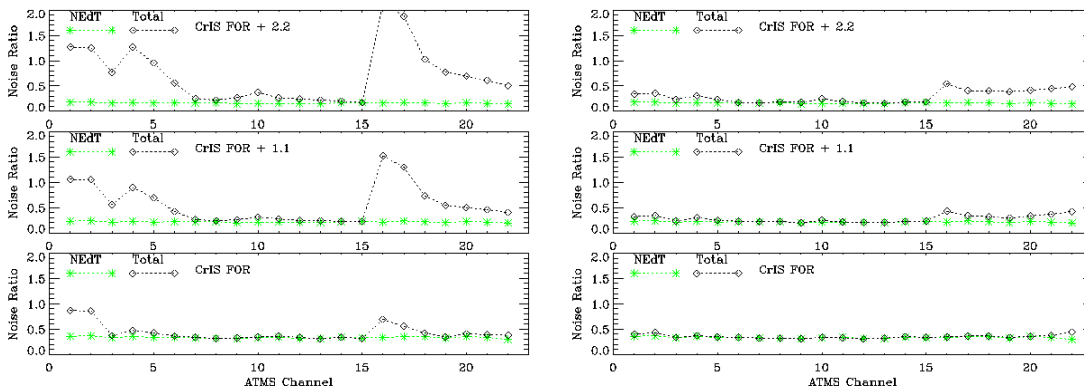


Figure 117: Sensor and total noise for left and right halves of MM5 scene based on nadir geometry.

The noise contribution resulting from a match to footprints larger than the CrIS FOR is given in Table 28. In this case, the noise-free MW SDRs were mapped directly to the indicated footprint sizes and differenced with the SDRs derived by mapping the MM5 data to the CrIS FOR. In Table 29 the scene noise is evaluated for the left and right portions of the 2 km MM5 scene.

Again, the mountainous region on the left leads to noise contributions, much larger than that from the plains region on the right. The magnitude of the scene errors is similar to that computed via matching ATMS footprints to CrIS presented in Table 27.

Table 28: Scene Noise Amplification Factors Relative to CrIS FOR.

ATMS Properties				Scene Noise Amplification Factors					
Bands (Frequencies, Resolution, NedT)				FOR +1.1	FOR+2.2	FOR+3.3	FOR+4.4	FOR+5.5	FOR+6.6
1	23.8	5.2	0.90	0.48	0.79	1.00	1.14	1.26	1.35
2	31.4	5.2	0.90	0.47	0.76	0.96	1.09	1.20	1.28
3	50.3	2.2	1.20	0.35	0.55	0.69	0.79	0.86	0.83
4	51.76	2.2	0.75	0.52	0.83	1.03	1.18	1.30	1.40
5	52.8	2.2	0.75	0.42	0.67	0.83	0.95	1.05	1.13
6	53.596 ± 0.115	2.2	0.75	0.26	0.40	0.49	0.56	0.63	0.68
7	54.40	2.2	0.75	0.11	0.15	0.19	0.21	0.24	0.26
8	54.94	2.2	0.75	0.08	0.12	0.15	0.17	0.19	0.21
9	55.50	2.2	0.75	0.11	0.18	0.23	0.26	0.29	0.31
10	57.290	2.2	0.75	0.17	0.28	0.35	0.41	0.45	0.49
11	57.290 ± 0.217	2.2	1.20	0.10	0.16	0.20	0.23	0.26	0.28
12	57.290 ± 0.322 ± 0.048	2.2	1.20	0.10	0.15	0.19	0.22	0.24	0.26
13	57.290 ± 0.322 ± 0.022	2.2	1.50	0.08	0.13	0.16	0.18	0.21	0.23
14	57.290 ± 0.322 ± 0.010	2.2	2.40	0.05	0.08	0.10	0.12	0.13	0.15
15	57.290 ± 0.322 ± 0.005	2.2	3.60	0.03	0.05	0.06	0.07	0.08	0.09
16	88.2	1.1	0.50	1.03	1.56	1.91	2.16	2.37	2.53
17	165.5	1.1	0.60	0.93	1.39	1.71	1.98	2.21	2.41
18	183.31 ± 7	1.1	0.80	0.53	0.78	0.99	1.19	1.36	1.51
19	183.31 ± 4.5	1.1	0.80	0.42	0.64	0.83	1.01	1.17	1.32
20	183.31 ± 3	1.1	0.80	0.37	0.57	0.74	0.91	1.06	1.20
21	183.31 ± 1.8	1.1	0.80	0.34	0.53	0.69	0.84	0.98	1.11
22	183.31 ± 1	1.1	0.90	0.28	0.46	0.60	0.72	0.83	0.94

Table 29: Scene Noise Amplification Factors relative to CrIS FOR (Left / Right Halves).

ATMS Properties				Scene Noise Amplification Factors											
Bands (Freq., Res., NedT)				FOR +1.1		FOR+2.2		FOR+3.3		FOR+4.4		FOR+5.5		FOR+6.6	
1	23.8	5.2	0.90	0.67	0.15	1.08	0.25	1.38	0.32	1.57	0.38	1.72	0.44	1.84	0.49
2	31.4	5.2	0.90	0.65	0.17	1.04	0.26	1.32	0.34	1.50	0.40	1.64	0.45	1.74	0.49
3	50.3	2.2	1.20	0.48	0.11	0.76	0.17	0.95	0.21	1.09	0.25	1.19	0.28	1.27	0.30
4	51.76	2.2	0.75	0.72	0.14	1.15	0.22	1.43	0.28	1.64	0.33	1.80	0.37	1.94	0.40
5	52.8	2.2	0.75	0.59	0.10	0.93	0.15	1.16	0.19	1.33	0.22	1.46	0.25	1.58	0.27
6	53.596	2.2	0.75	0.36	0.05	0.56	0.08	0.69	0.09	0.79	0.11	0.88	0.12	0.95	0.13
7	54.40	2.2	0.75	0.15	0.03	0.21	0.05	0.25	0.06	0.29	0.07	0.33	0.08	0.35	0.09
8	54.94	2.2	0.75	0.10	0.05	0.15	0.08	0.18	0.10	0.21	0.12	0.23	0.14	0.25	0.16
9	55.50	2.2	0.75	0.14	0.07	0.22	0.12	0.27	0.16	0.31	0.20	0.34	0.23	0.37	0.25
10	57.290	2.2	0.75	0.22	0.11	0.35	0.19	0.43	0.25	0.49	0.30	0.54	0.34	0.58	0.38
11	57.290	2.2	1.20	0.13	0.06	0.20	0.10	0.25	0.14	0.28	0.17	0.31	0.19	0.33	0.21
12	57.290	2.2	1.20	0.13	0.06	0.19	0.09	0.24	0.13	0.27	0.15	0.29	0.17	0.31	0.19
13	57.290	2.2	1.50	0.11	0.05	0.16	0.08	0.20	0.11	0.23	0.13	0.25	0.15	0.27	0.17
14	57.290	2.2	2.40	0.07	0.03	0.10	0.05	0.13	0.07	0.15	0.09	0.16	0.10	0.17	0.11
15	57.290	2.2	3.60	0.04	0.02	0.06	0.03	0.07	0.04	0.08	0.05	0.09	0.06	0.10	0.07
16	88.2	1.1	0.50	1.39	0.39	2.13	0.55	2.61	0.68	2.95	0.80	3.22	0.91	3.43	1.01
17	165.5	1.1	0.60	1.29	0.25	1.93	0.38	2.36	0.49	2.73	0.60	3.04	0.69	0.30	0.77
18	183.31	1.1	0.80	0.71	0.20	1.05	0.33	1.32	0.47	1.57	0.60	1.78	0.72	1.96	0.83
19	183.31	1.1	0.80	0.55	0.21	0.83	0.35	1.06	0.50	1.28	0.64	1.46	0.77	1.62	0.89
20	183.31	1.1	0.80	0.47	0.21	0.72	0.36	0.91	0.52	1.11	0.65	1.28	0.89	1.43	0.91
21	183.31	1.1	0.80	0.42	0.23	0.63	0.39	0.81	0.55	0.98	0.68	1.14	0.80	1.28	0.92
22	183.31	1.1	0.90	0.33	0.23	0.51	0.39	0.65	0.54	0.78	0.65	0.91	0.75	1.02	0.84

The truth for the simulations was computed by averaging the profiles from the MM5 scene that lie within each CrIS FOR in the scene. These profiles were also used to compute the IR SDRs where the variability between FOVs is ignored. To include FOV variability in the simulations, the individual FOVs in the scene were computed and the MM5 profiles were averaged to match these footprints (illustrated in Figure 112). The IR SDRs were not computed at 2 km resolution due to the time/space restrictions.

7.8.2.3 50 GHz Channels Spatial Resolution and Noise Trade

This section describes the results of the 50 GHz channels spatial resolution and noise trade. For this study we assume that ATMS bands 1 and 2 and 16 to 22 are exactly mapped to the CrIS

footprint. These channels are represented by the reference MW SDRs with added noise that includes a one-over-root-nine reduction. For bands 3 to 15 we consider 3 cases.

- ATMS mapped to CrIS FOR.
- ATMS mapped to CrIS FOR plus 1.1 degrees.
- ATMS mapped to CrIS FOR plus 2.2 degrees.

IR SDRs were computed from an averaged scene that includes FOV variability. The MW and IR SDRs were used as input in the CrIS retrieval code to derive MW and MW/IR retrievals of temperature and water vapor. These retrievals were compared against the true profiles for each FOR. Spatial averaging results in increased noise in channels 3 to 6 and decreased noise in channels 7 to 15 (see Table 27). The results presented in Figure 118 illustrate an improvement in both MW and MW/IR temperature retrievals at higher levels. The temperature near the surface and the water vapor profile are unaffected.

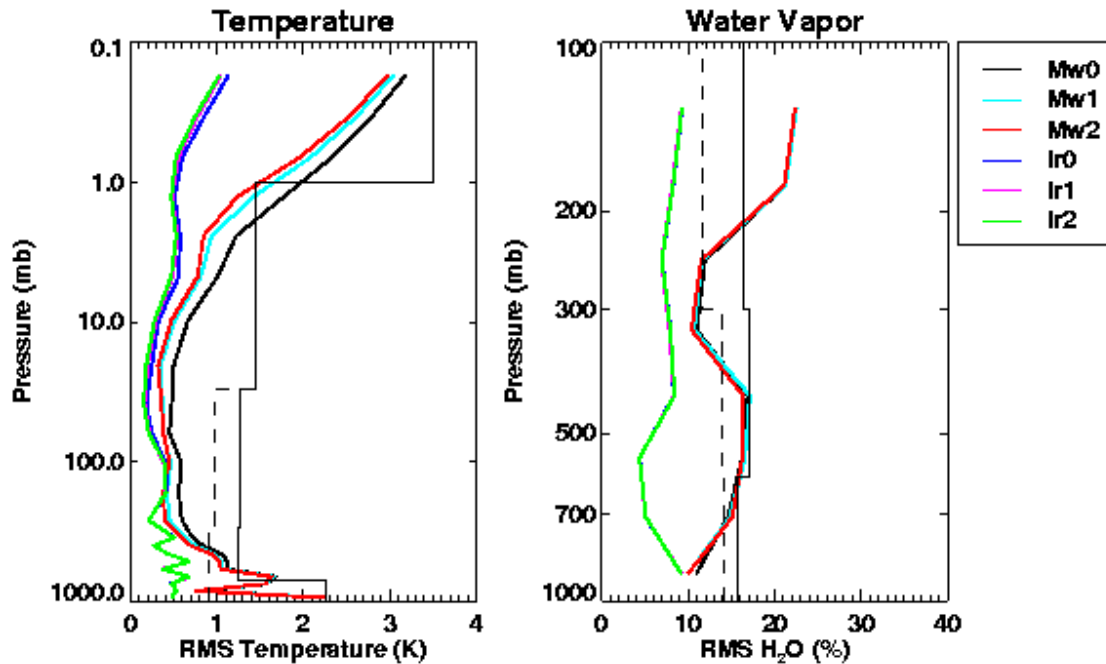


Figure 118: MW and MW/IR retrievals based on MM5 scene showing the effect of decreased resolution on 50 GHz ATMS bands. The lines labeled Mw0 and Ir0 correspond to retrievals based on ATMS SDRs matched to the CrIS FOR. The lines labeled Mw1 and Ir1 and Mw2 and Ir2 correspond to retrievals based on ATMS SDRs matched to the CrIS FOR + 1.1 degree and CrIS FOR + 2.2 degree footprints, respectively.

7.8.2.4 23/31 GHz Channels Spatial Resolution and Noise Trade

This section describes the results of the 28/31 GHz channels spatial resolution and noise trade. For this study we assume that ATMS bands 3 to 22 are exactly mapped to the CrIS footprint. These channels are represented by the reference MW SDRs with added noise that includes a one-over-root-nine reduction. For bands 1 and 2 we consider 3 cases.

- ATMS mapped to CrIS FOR.
- ATMS mapped to CrIS FOR plus 1.1 degrees.
- ATMS mapped to CrIS FOR plus 2.2 degrees.

IR SDRs were computed from an averaged scene that includes FOV variability. The MW and IR SDRs were used as input in the CrIS retrieval code to derive MW and MW/IR retrievals of temperature and water vapor. These retrievals were compared against the true profiles for each FOR. Spatial averaging results in increased noise in both channels 1 and 2 (see Table 27). However, the results presented in Figure 119 illustrate very little impact on the temperature and water vapor retrievals due to this increased noise. In fact, a slight improvement in the MW retrieval of near-surface water vapor is obtained for the larger footprints.

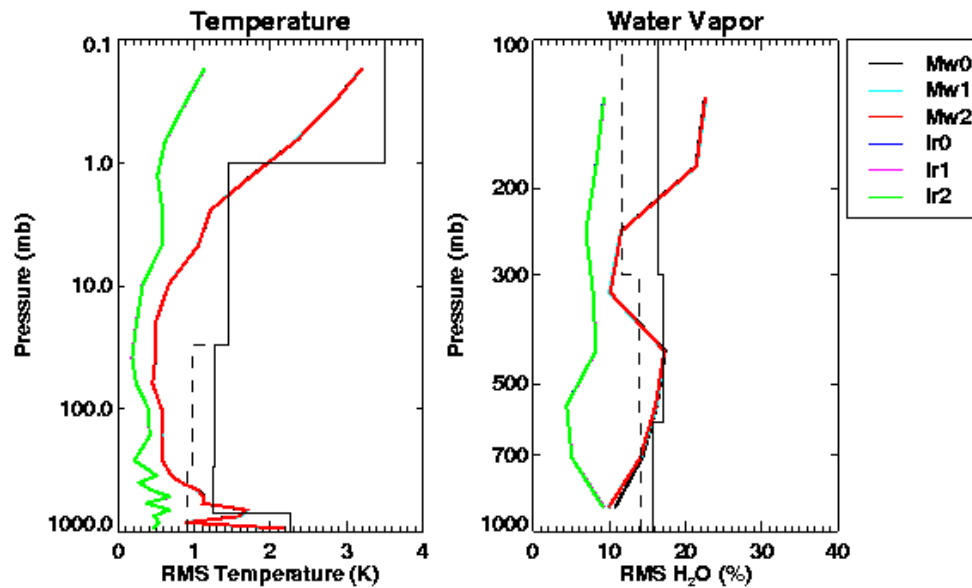


Figure 119: MW and MW/IR retrievals based on MM5 profiles showing the effect of decreased resolution on the 23 and 31 GHz ATMS bands. The lines labeled Mw0 and Ir0 correspond to retrievals based on ATMS SDRs matched to the CrIS FOR. The lines labeled Mw1 and Ir1 and Mw2 and Ir2 correspond to retrievals based on ATMS SDRs matched to the CrIS FOR + 1.1 degree and CrIS FOR + 2.2 degree footprints respectively.

7.8.3 ATMS Inhomogeneity Studies Using NOAA-88 Profiles

The objective of this trade study is to explore the impact of scene inhomogeneities within the ATMS footprint on CrIMS temperature and water vapor retrievals. Since the MM5 scene used above has limited atmospheric variability, NOAA-88 profiles are selected for this study. The footprint size for ATMS channels 1 and 2 is 5.2 degrees, compared to 2.2 degrees for ATMS channels 3 to 15, and 1.1 degrees for ATMS channels 16 to 22, and compared to the CrIS footprint size of 3.3 degrees. As a result, the process of matching the ATMS bands 1 and 2 to the CrIS FOR may include some contamination from outside the CrIS FOR. In this study, we investigate the impact of contamination from temperature, water vapor, cloud, skin temperature, and coastlines on the retrievals and evaluate the effectiveness of noise relaxation to compensate for the scene errors. The analysis is based on random samples from the NOAA-88 dataset, with perturbations introduced to simulate the effects of contamination.

7.8.3.1 Scene Contamination

In this study, we assume the ATMS channels 3 to 22 can be matched exactly to the CrIS FOR via a footprint matching algorithm, but ATMS channels 1 and 2 are matched to a FOR that is larger (i.e., 5.2 degrees) than the CrIS FOR. The worst case occurs when the scene characteristics outside the CrIS FOR (represented by areas B and C in Figure 120) differs from that inside the FOR (area A). In that case, the contribution from the area outside the FOR is 60% of the total signal for ATMS 1 and 2. This could result in significant inconsistencies with the other ATMS channels and the CrIS observations and contributes to the noise in the retrieval. While one can envision situations that in theory could give rise to this worst-case scenario (i.e., lake shorelines, islands, or broken cloud) such occurrences are unlikely.

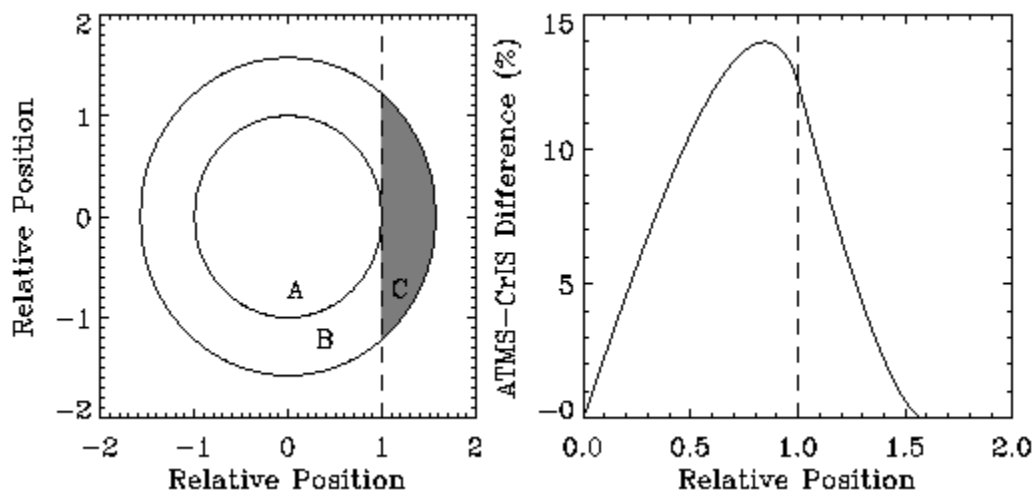


Figure 120: Circles representing the CrIS FOR (A: 3.3 degrees) and ATMS FOR (A,B,C: 5.2 degrees) are shown (left). The scene is bisected into two parts representing different conditions. The plot (right) shows the difference in contribution of the shaded area to the ATMS and CrIS footprints as a function of position in the scene.

Figure 120 shows a more typical case where the observed area is bisected into two parts that represent different conditions. The bisector could represent a cloud boundary, coastline, or weather front and could fall anywhere in the FOR. The plot shows the difference in relative contribution from the perturbed part of the scene (represented by area C) as a function of position

in the FOR. In this case, the difference in the contribution from area C to ATMS and CrIS footprints is less than 14%.

7.8.3.2 Scene Inhomogeneity Noise

The difference between signals originating from within the CrIS FOR and those measured from the extended ATMS footprint is a source of noise in the retrievals. To evaluate the magnitude of the resulting error, MW SDRs were computed based on a random sample of NOAA-88 profiles (L1), and based on the same sample but with a perturbation added to temperature, water vapor, skin temperature, cloud amount, or surface type (L2). For these calculations, the random sensor noise was set to zero. If the contribution to the observed ATMS SDR from the perturbation is 10%, then the noise is computed as the RMS difference of the measurements $0.1*(L2-L1)$. This value can be compared to the sensor noise. For a single ATMS FOV, this value is 0.90 but the exact noise value is a product of the ATMS-to-CrIS footprint-matching algorithm.

The impact of temperature inhomogeneities on ATMS SDRs is summarized in Table 30. In this case, the land and ocean temperature profiles at all levels were perturbed at random with an RMS amplitude of 1, 2, 5, and 10 K. The contribution to the observed SDR was 10%. The results illustrate that ATMS 1 and 2 contain very little information regarding the temperature profile. In addition, because temperature variations are gradual, the contribution of temperature inhomogeneities to the scene noise in ATMS 1 and 2 will be negligible compared to the random sensor noise.

Table 30: Scene Noise due to 10% Temperature Inhomogeneities.

Temperature Perturbation	Land		Ocean	
	ATMS 1	ATMS 2	ATMS 1	ATMS 2
1 K	0.013	0.006	0.019	0.004
2 K	0.026	0.011	0.037	0.008
5 K	0.066	0.028	0.093	0.020
10 K	0.132	0.058	0.187	0.041

The impact of water vapor inhomogeneities on ATMS SDRs is summarized in Table 31. In this case, the land and ocean water vapor profiles were perturbed at random with RMS amplitudes of 50%, 100%, 150%, and 200% (but limited to greater than -50%). The contribution to the observed SDR was 10%. Here, ocean profiles which are much wetter than land, result in a much larger error in ATMS 1 and 2. Water vapor is much more variable than temperature such that a gradient of 50% would not be unusual. Thus the contribution of water vapor inhomogeneities to the noise is comparable to the sensor noise for land profiles and may be a dominant effect for ocean profiles.

Table 31: Scene Noise due to 10% Water Vapor Inhomogeneities.

Water Vapor Perturbation	Land		Ocean	
	ATMS 1	ATMS 2	ATMS 1	ATMS 2
25%	0.131	0.062	0.727	0.413
50%	0.213	0.104	1.220	0.730
100%	0.307	0.168	1.863	1.291
150%	0.373	0.230	2.328	1.809

The impact of surface skin temperature inhomogeneities on the ATMS SDRs is summarized in Table 32. In this case, the skin temperatures for land and ocean scenes were perturbed at random with an RMS amplitude of 1, 2, 5, and 10 K. The contribution to the observed SDR was 10%. ATMS channels 1 and 2 are sensitive to the surface, so that gradients in skin temperature can produce moderate errors in the SDRs, i.e., comparable to the sensor noise. For example, in the region of the Gulf Stream the sea surface temperature can change by as much as 10 K.

Table 32: Scene Noise due to 10% Skin Temperature Inhomogeneities.

Skin Temp. Perturbation	Land		Ocean	
	ATMS 1	ATMS 2	ATMS 1	ATMS 2
1 K	0.073	0.077	0.047	0.051
2 K	0.146	0.153	0.095	0.102
5 K	0.364	0.384	0.237	0.254
10 K	0.728	0.768	0.473	0.509

The impact of cloud inhomogeneities on ATMS SDRs is summarized in Table 33. In this case, the baseline scenes were simulated for clear conditions to which was added a 10% contamination computed for the same scenes under cloudy conditions. The cloud-top and thickness were fixed at 600 and 100 mbar, respectively, and the cloud liquid water amount was varied with values equal to 0.01, 0.05, 0.10, and 0.20. The results indicate that the noise due to cloud inhomogeneities is comparable to or less than that due to the sensor.

Table 33: Scene Noise due to 10% Cloud Inhomogeneities.

CLW Perturbation	Land		Ocean	
	ATMS 1	ATMS 2	ATMS 1	ATMS 2
0.01	0.005	0.009	0.010	0.017
0.05	0.026	0.043	0.051	0.083
0.10	0.051	0.083	0.101	0.163
0.20	0.100	0.161	0.199	0.317

The impact of surface type inhomogeneities on ATMS SDRs is summarized in Table 34 for the extreme case of an ocean coastline. In this case, SDRs were computed for a random set of ocean profiles and for this same set with the surface emissivity replaced with that derived from a random sample of land profiles. Then the signals in ATMS 1 and 2 were computed based on a 5% and 10% contribution from the land simulations. The errors in ATMS 1 and 2 are shown to be significant compared to the sensor noise.

Table 34: Scene Noise due to 10% Coastline Inhomogeneities.

Coastline Perturbation	Land		Ocean	
	ATMS 1	ATMS 2	ATMS 1	ATMS 2
5%	N/A	N/A	1.974	2.064
10%	N/A	N/A	3.948	4.129

7.8.3.3 Performance

The performance of the MW and MW/IR temperature and water vapor retrievals was evaluated for selected cases representing the temperature, water vapor, skin temperature, cloud, and coastline inhomogeneities. In this case, all simulations were based on 200 random profiles from the NOAA-88 dataset. The construction of the simulated ATMS radiances was as described in Section 2 with a 10% contribution from the perturbed scene. In all cases, the performance is compared against the baseline retrievals.

7.8.3.3.1 Temperature

Figure 121 and Figure 122 show that a temperature inhomogeneity of 2 K has negligible impact on both the MW and MW/IR retrieval performance.

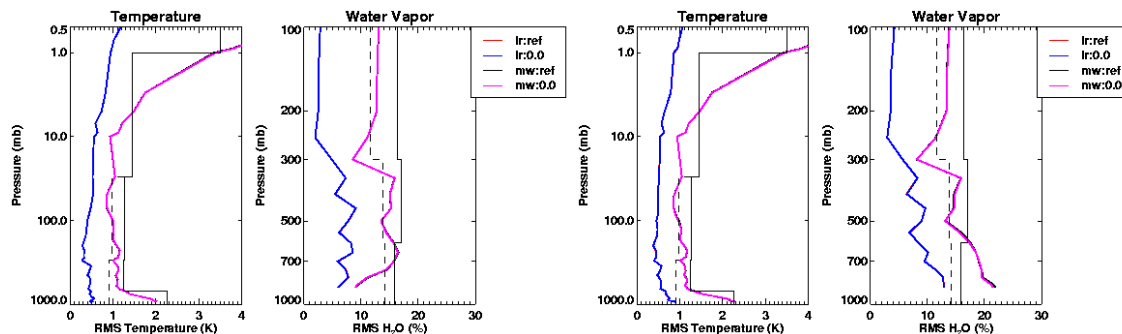


Figure 121: 2K Temperature inhomogeneity over land – clear (left), cloudy (right)

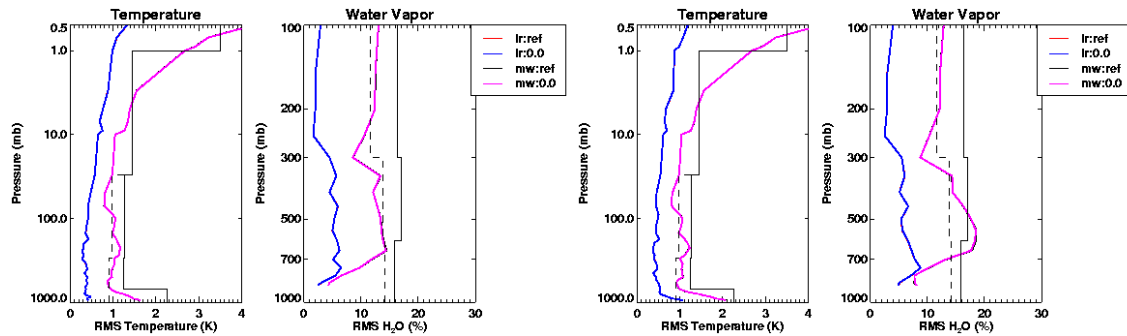


Figure 122: 2K Temperature inhomogeneity over ocean – clear (left), cloudy (right).

7.8.3.3.2 Water Vapor

The performance impact of a 50% water vapor inhomogeneity is illustrated in Figure 123 and Figure 124. In this case, a slight degradation in the performance of the clear-sky MW water vapor retrieval is observed in the 500-700 mbar region. However, in cloudy conditions over ocean the performance is improved in this region but degrades near the surface (800-900 mbar). The impact to MW temperature and MW/IR water vapor and temperature is negligible.

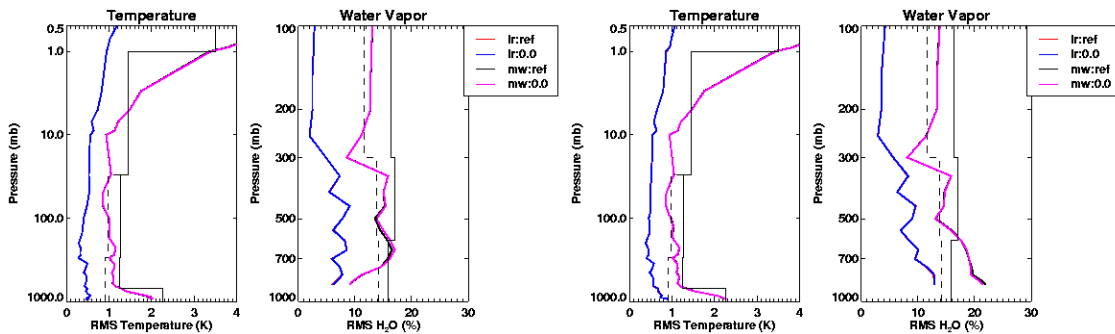


Figure 123: 50% Water vapor inhomogeneity over land – clear (left), cloudy (right).

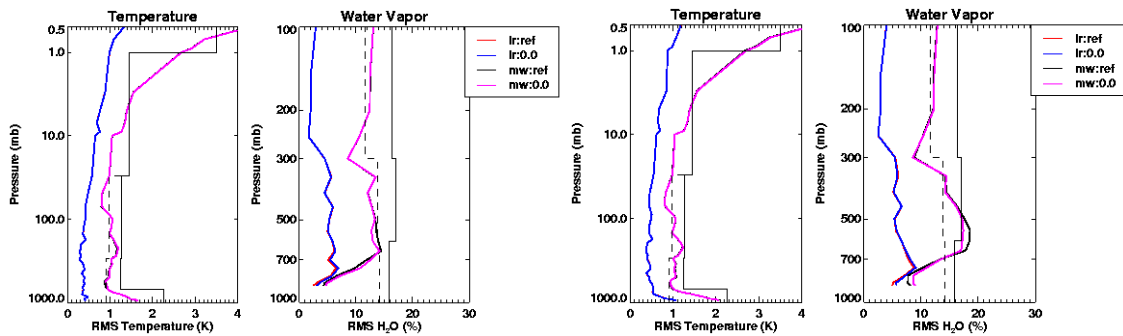


Figure 124: 50% Water vapor inhomogeneity over ocean – clear (left), cloudy (right).

7.8.3.3.3 Skin Temperature

The performance impact of a 5 K skin temperature inhomogeneity is illustrated in Figure 125 and Figure 126. In this case, negligible impact is observed from both the MW and MW/IR temperature and water vapor retrievals.

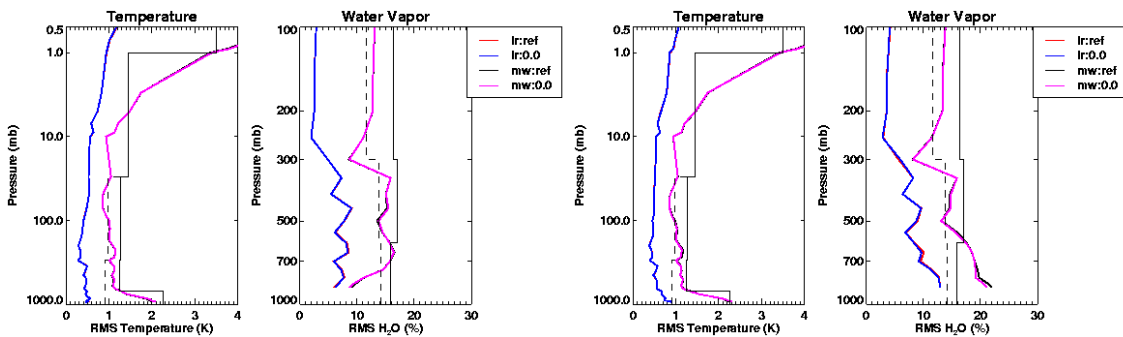


Figure 125: 5 K Skin temperature inhomogeneity over land – clear (left), cloudy (right).

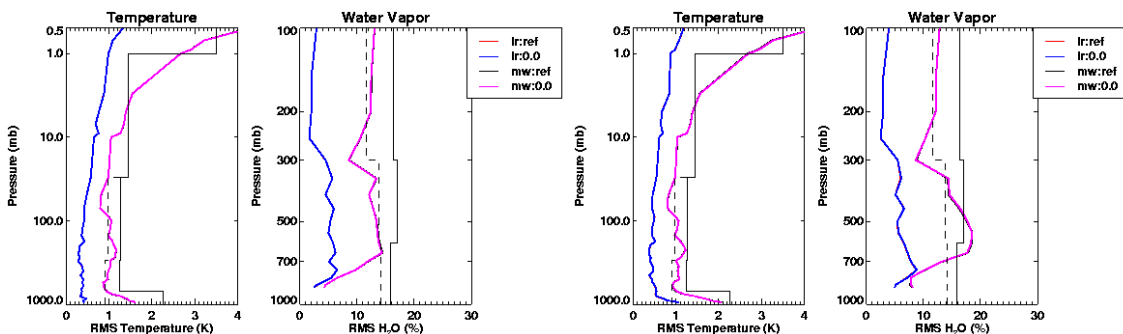


Figure 126: 5 K Skin temperature inhomogeneity over ocean – clear (left), cloudy (right).

7.8.3.3.4 Clouds

The contamination from a cloud at 600 mbar with cloud liquid water equal to 0.1 is shown to have minimal impact on clear sky retrievals in Figure 127 and Figure 128.

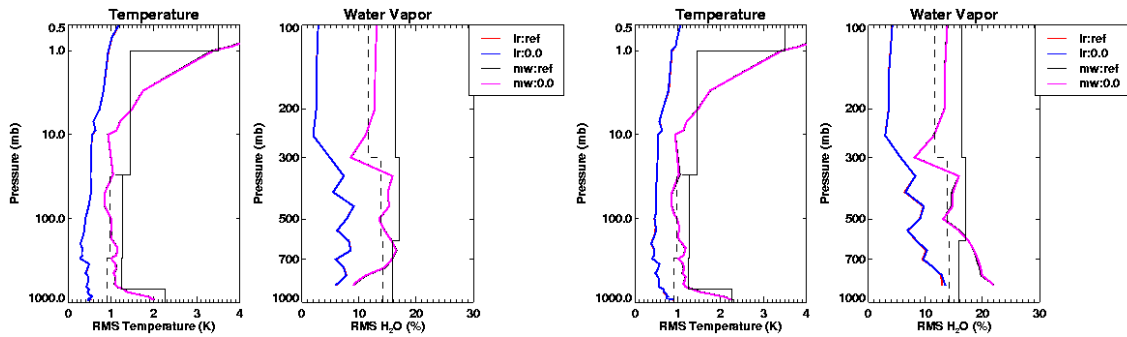


Figure 127: Cloud inhomogeneity over land – clear (left), cloudy (right).

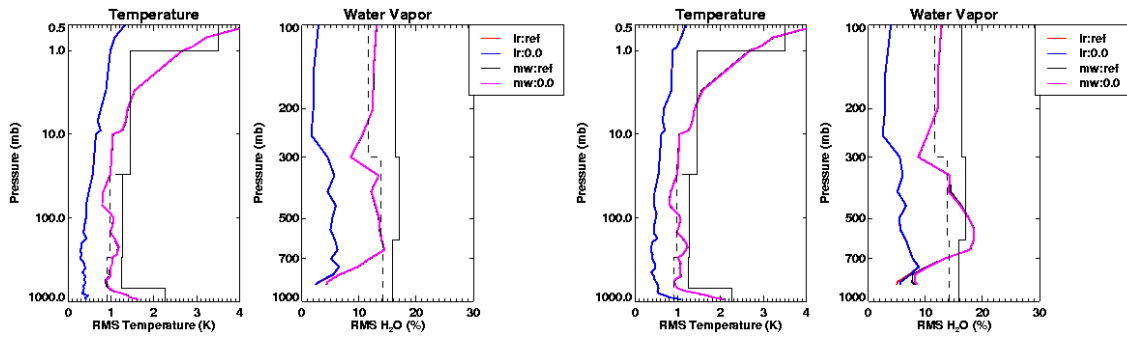


Figure 128: Cloud inhomogeneity over ocean – clear (left), cloudy (right).

7.8.3.3.5 Coastline

The performance impact due to coastline inhomogeneities is illustrated in Figure 129 and Figure 130. In this case, errors due to a 5% and 10% land contamination are considered. The impact on water vapor is significant in both cases, especially for the MW retrieval at altitudes between 400 and 700 mbars. Under cloudy conditions the performance may actually improve due to the perturbation. Difference near the surface are also observed both in the MW and MW/IR water vapor retrievals. MW temperature retrievals are also slightly impacted near 800 to 900 mbar. It should also be noted that the convergence is degraded for the coastline retrievals with 10% land contamination.

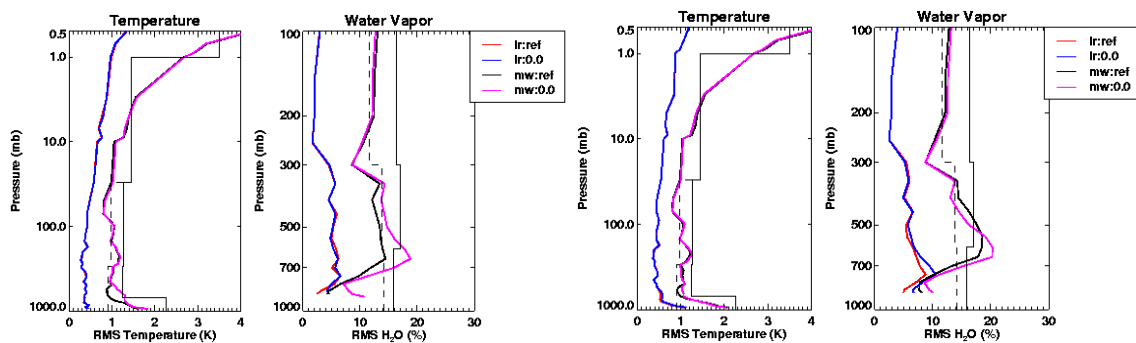


Figure 129: 10% Coastline inhomogeneity over ocean – clear (left), cloudy (right).

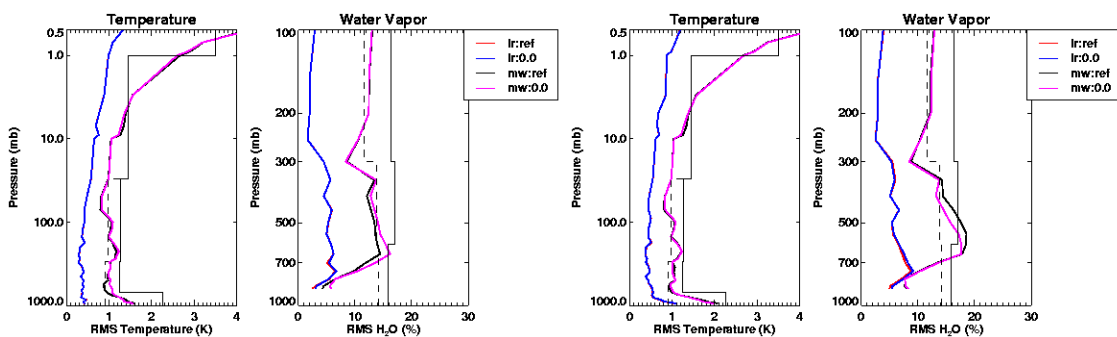


Figure 130: 5% Coastline inhomogeneity over ocean – clear (left), cloudy (right).

7.8.3.4 Discussion

Errors in ATMS 1 and 2 due to inhomogeneities in the scene tend to impact the MW water vapor retrieval if the magnitude of these errors is significant compared to the level of sensor noise. Two regions seem to be affected – near the surface, 800 to 900 mbar and at 400 to 700 mbars. The MW temperature retrieval may also be affected in the 800 to 900 mbar region. Under cloudy conditions, the degradation of MW retrieval with respect to the baseline does not necessarily correspond to degradation in performance for the combined IR+MW retrieval. For more extreme errors, the convergence of the retrievals is impacted. The impact to the MW/IR retrievals is minimal for most cases considered. The added scene noise generally only impacts the performance near the surface. Of all the factors considered, errors due to coastline inhomogeneities seem to cause the largest effect. Inhomogeneities in water vapor (with differences larger than 50%) can be expected to have a smaller impact on performance.

7.9 Impact of the Zeeman Effect on AMSU Radiances

At atmospheric pressures less than a few millibars, the oxygen lines near 60 GHz interact with the Earth's magnetic field through magnetic dipole moments, producing the Zeeman splitting. For the AMSU instrument, channels 13 and 14 have weighting functions that peak at higher altitudes and the Zeeman effect influences the radiance calculations. The impact of Zeeman effect has been studied by computing brightness temperatures with and without including this effect in the RT calculations. The computations have been made for each of the five latitude-stratified (tropical, mid-latitude summer and winter, sub-arctic summer and winter) standard atmosphere profiles (Anderson *et al.* 1986). This study has been conducted for AMSU channels, but the results are applicable to the ATMS configuration as well. For each profile, the AMSU scan angle, orbital equator crossing longitude, and position within the orbit were varied using 12-degree increments for each. The polarization of measurement rotated as a function of scan angle, consistent with the AMSU EOS/METSAT specification. The maximum error was found near the location on the Earth with the strongest magnetic field, and for maximum scan angle (where the weighting functions peak highest). The true maximum is probably a little larger, considering the 12-degree discretization of the search.

Figure 131 shows a global histogram of errors caused by the neglect of the Zeeman effect. Because it represents a frequency over AMSU samples, not per unit area over the globe, it does not represent the impact on a global analysis. The histogram is biased toward polar sampling, as is AMSU. The bars on the right-hand side represent the errors for AMSU channel 14 and the bars on the left-hand side represent the errors for AMSU channel 13. Apparently, the impact of the Zeeman effect on channel 13 is less than 0.25 K globally. This error is smaller than the instrument NeDT for this channel. For channel 14, the maximum error can be as large as 1.2 K, but the frequency of occurrences is very small (less than 1%). If AMSU is the only instrument to measure the stratospheric temperature, then the Zeeman effect for this channel should be included in the forward model RT calculation. For the CrIMSS instrument, the IR component (CrIS) provides independent channels for the upper atmospheric temperature sounding. We can

de-weight the contribution of AMSU channel 14 in the temperature retrieval by including the error due to the Zeeman effect in the noise error covariance.

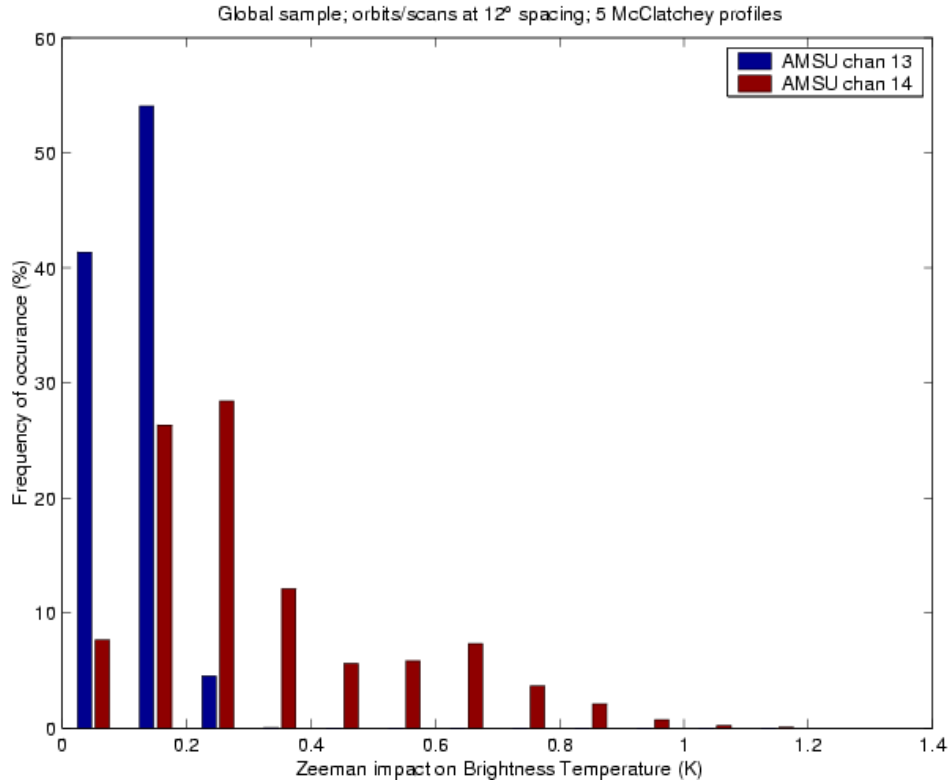


Figure 131: Histogram of errors caused by the omission of the Zeeman effect using the five latitude-stratified atmospheric profiles.

7.10 Impact of Sub-FOV Cloud Variability/Edge-of-Scan Effects

As a result of the finite spatial extent of a CrIS FOV (approx. 15 x 15 km at nadir), the radiance corresponding to an individual FOV is an ensemble average over a number of rays arriving within the FOV. The rays comprising the FOV travel on slightly different atmospheric paths and are reflected off different points at the Earth's surface or at the cloud-tops. While the differences in clear-sky atmospheric paths (i.e., temperature and humidity profiles) are assumed to be small (in fact, this assumption is fundamental to the CC method), the variations in the surface properties and cloud-top heights between individual rays within an FOV can be radiatively important. Effectively, these variations are manifested as a large number of cloud formations, which may not be properly estimated by the CC method, and this in turn may cause degradation in the retrieval results. The purpose of this study has been to analyze this effect using a realistic representation of natural cloud variability.

7.10.1 Cloud Data

We have analyzed a 3-dimensional data cube containing cloud-top height information for a 200 x 200 km region covering the Southern Great Plains ARM site. The cube has been generated for ITT by STC-METSAT and contains temperature, humidity, and cloud-top data derived from radiosonde and satellite measurements. The cube covers the altitude range from 0 to 30 km with a vertical resolution of 1 km (the horizontal resolution is also 1 km). In Figure 132a, we show the distribution of cloud-top height (in kilometers). The highest clouds have tops at altitudes exceeding 11 km (in the NE corner of the cube), while clouds with tops lower than 2 km are present at the edges of the cloud-covered region. In addition, within the same 200 x 200 km region, there exist significant cloud-free regions. The scene shown in Figure 132 corresponds to a specific geographic area at a specific time (the Southern Great Plains ARM site on June 23, 1997) and its position relative to the CrIS orbital track could be determined from the satellite orbital parameters. In this study, this complicated approach has been deemed unnecessary. Instead, the geometry of the satellite has been described in terms of only 2 parameters: the scan angle (between -45° and 45° relative to the local vertical) and an arbitrary angle (between 0° and

360°) by which the scene has been rotated around the local vertical. The introduction of the scene rotation angle provides an easy way to account for variations in the cloud scene without the need for more cloud data.

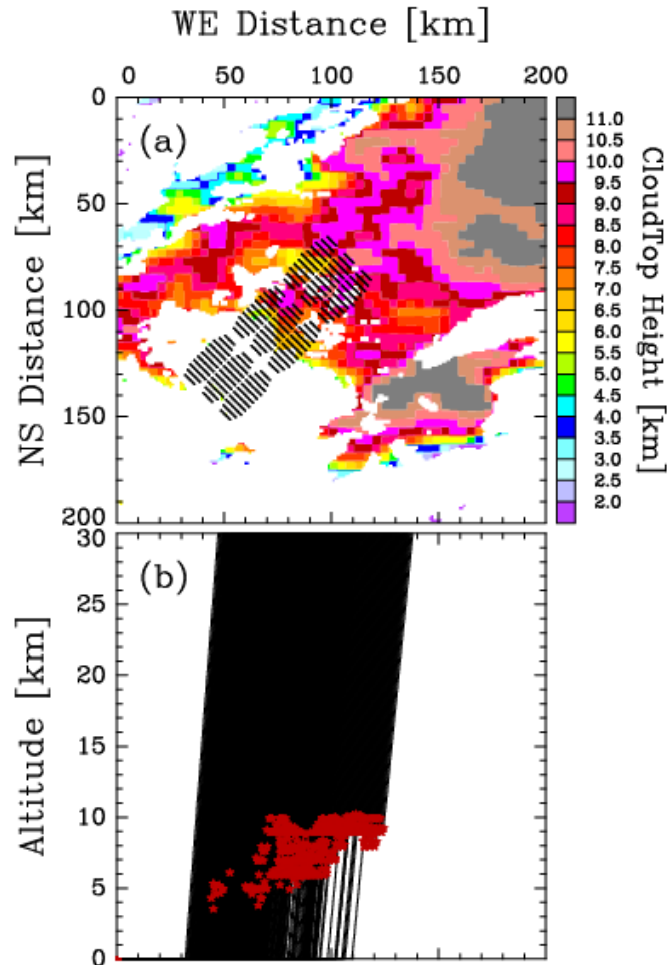


Figure 132: (a) Example of an inhomogeneous cloud scene from the Southern Great Plains ARM site on June 23, 1997. The color map represents the distribution of the cloud-top height in kilometers (with the scale given on the right). Ground footprints of 9 CrIS FOVs corresponding to the scan angle of 45° are represented by the black dots, with each FOV represented by approximately 100 individual dots (rays or pixels). (b) Positions of the rays in the vertical projection. The red crosses mark the points of intersection with the clouds.

7.10.2 Ray-tracing Model

To assess the impact of cloud-top inhomogeneities on the CrIS radiances, we have constructed a ray-tracing model. For each satellite viewing geometry (i.e., scan angle), the 9 CrIS FOVs are represented by a number of rays originating at the satellite and terminating at different points

within the elliptical footprints at the ground. In this representation, the radiance corresponding to a particular FOV is the mean over rays comprising the FOV (in Figure 132, each FOV is represented by approx. 100 rays). For each ray, we have determined the height of the point at which the ray intersects the cloud, taking into account the 3D structure of the cloud, i.e., considering both cloud-top and cloud base heights. The finite vertical extent of the cloud plays a progressively larger role as the scan angle increases, e.g., an overcast FOV can exhibit some clear pixels when the scan angle is changed from 45 to 0°. Since the cloud base height information is not contained in the data cube, the cloud thickness has been set to 1 km in Figure 132. In Figure 132*a*, the black dots represent the points of intersection between the rays and the ground. A great degree of variation exists between individual rays, with some rays travelling in cloud-free regions and others intersecting the cloud at various heights. For the particular viewing geometry adopted in Figure 132 (i.e., the satellite scan angle of 45° and the scene rotated by 45° around the local vertical), one FOV is completely cloud-free and one almost overcast. The positions of the rays in the vertical projection are shown in Figure 132*b*, with the points of intersection between the rays and the cloud marked by crosses. The cloud-top pressures within one FOV vary between 1000 mbar (i.e., rays that do not intersect the cloud) and 300 mbar. In contrast, variations in atmospheric temperature and humidity profiles are negligible from a radiative standpoint, probably as a result of the limited number of in-situ measurements at the ARM site. The variations in cloud-top pressure (and the corresponding variations in cloud-top temperature) will give rise to variations in the radiances computed for individual rays. These variations will be interpreted as multiple cloud formations within one FOV by the cloud-clearing algorithm and they will modify mean radiance contrasts between different FOVs.

7.10.3 Retrieval Results

The impact of sub-FOV cloud-top variability and the edge-of-scan effect on the CrIS retrievals are illustrated in Figure 133. Shown are the RMS errors in temperature and moisture for 200 profiles from the NOAA-88 database. In order to minimize the effect of surface variability, we have selected ocean profiles for this case study (the reference retrieval results for cloud-free ocean scenes are shown in the accompanying report on the implementation of the ASTER database). For each profile, the cloudiness is represented by the cloud-top pressure distribution

shown in Figure 132. This distribution reflects both sub-FOV cloud inhomogeneities as well as variability in cloud-top pressure caused by the edge-of-scan effect. In order to separate these two effects on the CrIS retrievals, we have also considered cloud-top pressure distributions for clouds with constant height at 10 and 5 km. This distribution reflects purely the scan geometry. It appears that the sub-FOV cloud-top variability causes a much larger degradation in the retrieval performance than purely geometrical effects. It should be noted that the results shown in Figure 133 have been obtained for scan angle equal to 45° . With fixed cloud-height, the degradation becomes very small at nadir, while with variable cloud-top height the errors are only slightly affected by the scan angle.

The relatively minor degradation in the moisture retrieval reflects the choice of ocean profiles for this study (over ocean, the MW-only retrieval provides an accurate first guess for the combined IR+MW retrieval). However, this degradation is significant in the variable cloud-top case. Both the moisture retrieval errors and the very large degradation in the temperature retrieval are caused by the FOV selection scheme used in this run. In this scheme, which is primarily employed to meet the EDR horizontal reporting requirement, the FOVs are grouped into four clusters using a geometrical constraint (see ATBD for more details). As can be seen in Figure 132a, in two of these clusters (located towards the NE corner of the domain), all FOVs contain significant ($> 50\%$) cloud fractions, which causes large degradation in the retrieval performance. The degradation caused by these clusters dominates the large errors evident in Figure 133. In contrast, the two clusters located toward the SW corner contain FOVs with small cloud fractions (one of the FOVs is completely cloud-free) and the algorithm performance for these clusters is significantly better (below the accuracy threshold for clear-sky retrievals). This good performance is the result of the application of the cloud-clearing algorithm, which weighs the cloud-cleared radiance toward the radiance observed in the cloud-free FOV. Consistently with this behavior, the retrieval performance is also much better when the retrieval is performed on clusters comprising all nine FOVs, as such clusters automatically contain the clear FOV, the presence of which provides an accurate estimate of the cloud-cleared radiance.

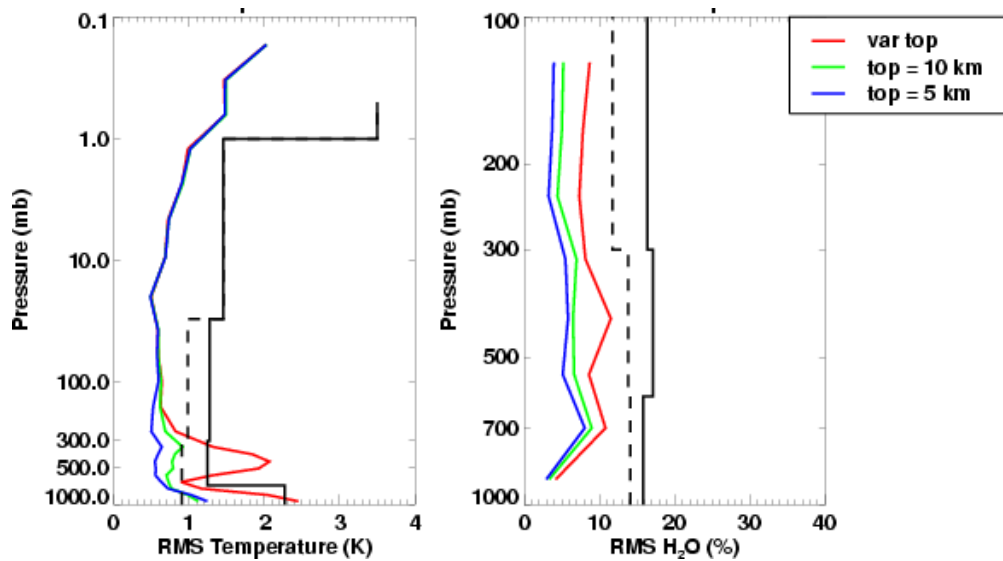


Figure 133: Impact of sub-FOV cloud-top variability and edge-of-scan effect. The three curves in this figure correspond to the case of variable cloud height (as in Figure 132), as well as cloud height fixed at 10 and 5 km (for these two cases, the variability in the cloud-top pressure results purely from geometrical effects at off-nadir scan angles).

Within the constraints provided by the particular cloud dataset available for this study, we have experimented with a somewhat larger set of cloud scenes obtained by varying the scene-rotation angle and the horizontal location of the FOR within the 200 x 200 km domain. This extended trade study has led to the following conclusions:

1. The sub-FOV variability in cloud height can cause large degradation in the retrieval, especially for temperature, for clusters in which none of the FOVs are clear and the cloud fractions are significant ($> 20\%$).
2. The variability in cloud height causes larger retrieval errors than purely geometrical effects caused by the interplay between scan geometry and the finite vertical extent of the cloud (it should be borne in mind, however, that we base this conclusion on a study in which cloud thickness was fixed to 1 km).

7.10.4 Summary

The results presented above demonstrate that sub-FOV cloud variability has the potential of seriously degrading retrieval performance. This degradation is largest in situations when none of the FOVs is cloud-free, the cloud fractions are large, and, for the particular cloud scene considered, it is caused primarily by the variability in cloud-top distribution rather than the off-nadir scan geometry. It is difficult to assess how representative this particular scene is of global cloud conditions, but based on this limited study it appears that for highly variable clouds, a mitigation of their impact on algorithm performance can only be achieved by attempting to include as many cloud-free FOVs as possible in the retrieval clusters (i.e., hole-hunting), or, more generally by reducing the CrIS footprint size so as to avoid cloud contamination.

APPENDIX A: Monte-Carlo Approach to the OSS Model

A.1 Introduction

The Monte-Carlo approach to the OSS method is especially efficient for a non-localized ILS. This will be illustrated using the *sinc* function as an example. The RMS error in the α -th channel can be written in the following form

$$RMS_{\alpha} = \sqrt{\frac{1}{N_s} \sum_{n=1}^{N_s} (\sum_i w_i^{(\alpha)} R_{n,v_i} - R_{n,c}^{(\alpha)})^2} . \quad (A.1)$$

Summation in n runs over N_s representative samples, i labels the selected points. $R_{n,c}^{(\alpha)}$ is used to denote the n -th component of the true radiance of the α -th channel. The RMS error is a key quantity defining the goodness of any search method, including the MC approach. Its application to the OSS model is schematically shown in Figure 134.

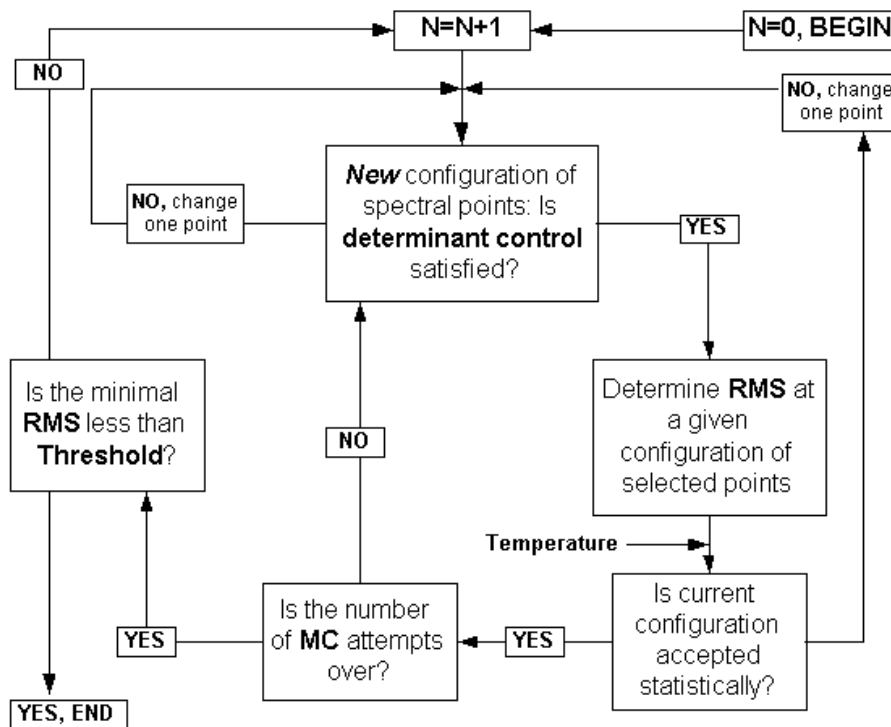


Figure 134: Flow diagram for the MC approach to the OSS model.

Let us consider in more detail how the MC search works with an ensemble of N selected points, and assign “slct” for their status. All other pre-selected points, which are confined to the channel region, get status “n/slct”. If the threshold condition is not satisfied with $(N - 1)$ “slct” points, a new, N -th, point chosen at random from the “n/slct” set will get the “slct” status. A new configuration should be checked as to whether the determinant control is satisfied (see below). If it is, then a statistical estimate should be done (see below under “Statistical Control”). The algorithm includes a pre-defined number of statistically accepted attempts. As long as this number is not exceeded, one point will be removed from the “slct” set and replaced by a point from the “n/slct” set, with both points selected at random. When the maximum number of MC attempts is reached, the RMS error is compared with the pre-defined threshold. If the former is smaller than the latter, the selection is finished. Otherwise, one proceeds to selecting the $(N + 1)$ -th point, etc.

It should be noted that the MC approach provides a high degree of duplication, i.e., the same wavenumbers can be utilized for different channels. For *Blackman*, the number of duplicated points can reach ~25% of the total number of selected points, while for *sinc* it can exceed 40%. This duplication can be used to improve the efficiency of the forward model.

The scheme shown in Figure 134 could be improved in cases when the set of selected points is overfilled, i.e., some of them could be removed from the selected ensemble without degrading the RMS error above the threshold. To eliminate these “overfilled” points, another selection among the selected points could be done. This would reduce the number of selected points for a given channel while keeping the RMS below the threshold. In contrast to the primary MC search, which may include a few thousand points for *sinc*, this secondary search deals with a maximum of a few tens of points and could be performed using either the sequential or the MC approach. The fraction of points eliminated during the secondary search in all CrIS bands is about 10% for *sinc*, but for some channels with 20 or more selected points after the primary MC search, the number of eliminated points can reach 40%.

A.2 Determinant Control

Let us suppose that a total of N_C wavenumbers and corresponding monochromatic radiances have been selected. Because of the constraint:

$$\sum_{i=1}^{N_C} w_i = 1 \quad (\text{A.2})$$

the RMS error of Equation (A.1) can be rewritten as

$$RMS = \sqrt{\left(\sum_{i=1}^{N_C-1} w_i (\vec{R}_i - \vec{R}_0) - (\vec{R}_C - \vec{R}_0) \right)^2} \quad (\text{A.3})$$

where \vec{R}_i , \vec{R}_0 and \vec{R}_C (vector of true radiance) are vectors in N_S -dimensional space. For example, the vector of radiance associated with the wavenumber ν_i is defined as:

$$\vec{R}_i = \frac{1}{\sqrt{N_S}} (R_{1,\nu_i}, R_{2,\nu_i}, R_{3,\nu_i}, \dots, R_{N_S,\nu_i}) . \quad (\text{A.4})$$

The system of linear equations for the weights is $w_i L_{i,j} = M_j$, where summation over repeating indices is assumed. Here $M_j = (\vec{R}_C - \vec{R}_0) (\vec{R}_j - \vec{R}_0)$ is a (N_C-1) -component vector, whereas the matrix $L_{i,j} = (\vec{R}_i - \vec{R}_0) (\vec{R}_j - \vec{R}_0)$ defines the determinant $D = \det(L)$ used in determinant control. The geometrical interpretation of D is that it is equal to the square of volume of the N -dimensional parallelepiped in N_S -dimensional space built on vectors $\vec{R}_i - \vec{R}_0$, $i = 1, \dots, N$. Note that the location of wavenumbers and their weights do not depend on the choice of \vec{R}_0 , i.e., the role of \vec{R}_0 can be played by any radiance vector among the N_C candidates.

The determinant control is implemented dynamically. The MC search begins with $N + 1$ points and a control that rejects configurations with determinants smaller than some $D(N)$. Rejected configurations are counted, and if the counter reaches a pre-defined number of accepted MC attempts, but the actual number of accepted MC attempts is below its limit, the determinant control is relaxed by multiplying $D(N)$ by some factor (0.1 in the current implementation). Simultaneously, the counter switches to zero. In addition, when the MC search with a new point begins, $D(N)$ may be further reduced (we used for such a reduction the factor of 0.1).

A.3 Statistical Control

Statistical control compares the current value of the RMS error with the value obtained for a preceding configuration of statistically accepted points. The comparison involves a parameter T called “temperature” which defines the probabilistic function:

$$P(RMS_{old}, RMS_{new}) = \frac{1}{1 + \exp(RMS_{new} - RMS_{old})/T} . \quad (A.5)$$

For T much larger than a typical RMS value, $P \approx 1/2$, i.e., statistically accepted and rejected attempts are equally probable. This is a sort of random selection, which is poorly convergent. In the opposite “low-temperature” limit, accepted are only those configurations for which $RMS_{new} < RMS_{old}$ and a majority of attempts will return $P \approx 0$. In this case, the MC search could be replaced by a sequential search, and this is in fact a reasonable choice for localized ILS functions. In general, something between these two limits is needed. In practice, if the numbers of rejected and accepted configurations differ by a factor of 2, the MC method shares the best features of sequential and random selections. It reveals the tendency to reduce the RMS error as in a deterministic sequential search method, and the ability to interrupt such a deterministic search in order to optimize it. There is no special equation to set a temperature, but it can be easily determined by a computational experiment. We set $T = RMS_{old}/3$. If the number of statistically rejected attempts reaches the doubled limit pre-defined for statistically accepted attempts, temperature grows by some factor (50% in our realization), which allows to get rid of

slowing down. As in the case of the determinant control, the counter of statistically rejected attempts switches to zero in this situation.

APPENDIX B: MM5 Simulations to Generate Realistic Scenes

B.1 Overview of MM5 Simulations

The Penn State University and NCAR (PSU/NCAR) mesoscale model, known as “MM5”, is a limited-area, nonhydrostatic, terrain-following sigma-coordinate model designed to simulate or predict mesoscale atmospheric circulation. This model has been applied to generate synthetic moisture, temperature, and pressure fields for use in an investigation into the impact of various aspects of scene inhomogeneity on the CrIS EDR retrievals. These fields have been computed at different spatial resolutions covering different domain sizes in order to provide adequate data for comprehensive testing.

In order to provide realistic scenes for simulated CrIS retrievals, 6-hour forecasts have been produced using two domains. The first, shown in Figure 135, is a 15 km resolution scene covering the continental U.S. (400 x 250 grid points horizontally, 30 vertical levels). This simulation took about 2 hours using 12 processors on a Linux cluster. The second domain, shown in Figure 136, is a 2 km resolution scene covering the U.S. Midwest (875 x 525 gridpoints horizontally, 30 vertical levels). This simulation took about 32 hours using 12 processors.

Both simulations have been run from 1800 UTC August 02 through 0000 UTC August 03, 2002, i.e., a day in summer. Distributions of selected meteorological fields at the end of the simulation period are shown in

Figure 137. These fields have been taken from an independent analysis performed by the NCEP Eta model and thus represent “observations” (in reality, an optimal blend of observations and model simulations). The MM5-simulated fields resemble the observations, as shown in

Figure 138 for temperature (note

Figure 138 shows the distribution of ground temperature, while

Figure 137 shows the distribution at 850 mbar). The cloudiness simulated by the MM5 is qualitatively consistent with the visible and infrared imagery obtained by the GOES-8 satellite, as shown in

Figure 140 and

Figure 141, respectively. In particular, both the 15- and 2 km simulation broadly reproduces the cloud field over the Rocky Mountains. The 15 km simulation also reproduces the convective clouds over Florida and Cuba and the marine stratocumulus clouds off the coast of California (the latter, owing to their low height, are only recognizable in the GOES visible image). As shown in Figure 142, there is a qualitative agreement in the cloud-top pressures (which are used in radiance simulations) in the area of overlap between the 2- and 15 km MM5 runs.

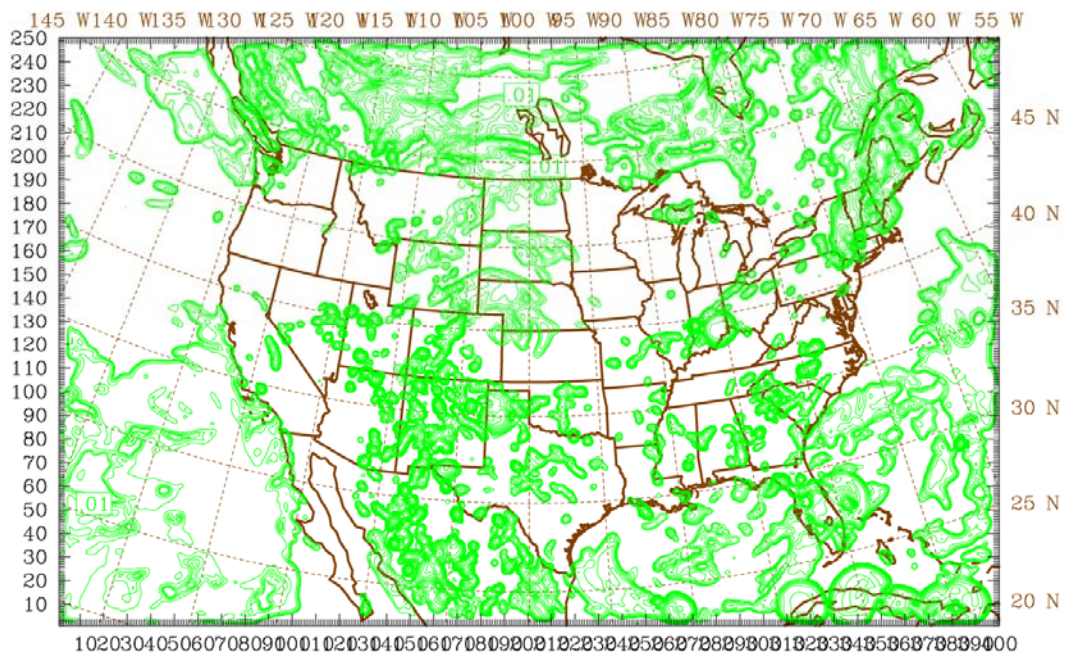


Figure 135: Horizontal domain for the 15 km run. The green lines represent the distribution of column-integrated hydrometeor amount (cloud water, cloud ice, snow, and graupel) used in the definition of cloudiness (see below).

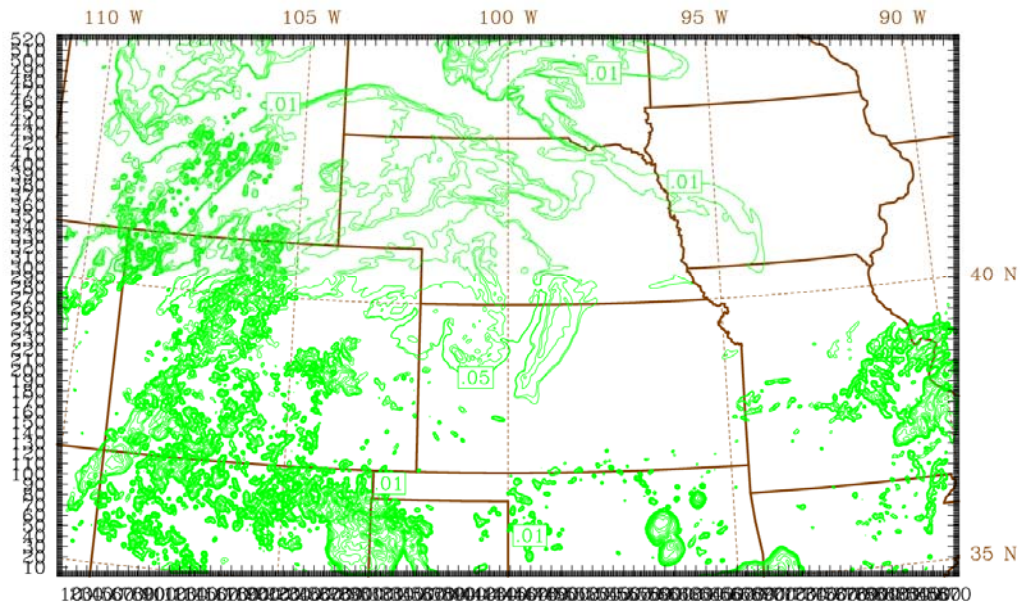


Figure 136: Horizontal domain for the 2 km run.

In addition to the summer case shown in Figure 135, two additional 15 km runs have been performed for periods in February and May 2002, but they have not been analyzed yet. Despite the availability of only one high-resolution scene, we believe that the heterogeneities generated by the MM5 at the 2 km resolution, especially evident in the cloud field, provide a good case for testing the performance of the CrIMSS retrieval algorithm on inhomogeneous scenes. On the other hand, being a summertime scene, the MM5 scene is not representative of the overall climatology represented by the NOAA-88 dataset. In particular, as shown in Figure 139, the MM5 scene is warmer, moister, and somewhat less variable than the full range of NOAA88 profiles.

The output from the MM5 run contains both 2D and 3D fields, as follows:

2D: terrain height [meters], temperature at 2 m [K], skin temperature [K], surface pressure [Pa], latitude [deg], longitude [deg], albedo [nondimensional], wind speed at the surface [m/s], and cloud-top [Pa].

3D: temperature [K], relative humidity [%], water vapor [kg/kg], cloud water [kg/kg], rain [kg/kg], cloud ice [kg/kg], snow [kg/kg], and graupel [kg/kg]. The temperature profiles have been interpolated to the CrIMSS 40-level grid [above 100 mbar, an extrapolation using a NOAA-88-based regression matrix has been applied (Eyre 1989)]. The profiles of water vapor have been interpolated in a similar way, except that a constant value has been used above 50 mbar (as described below, this has led to problems in the retrievals and necessitated a correction).

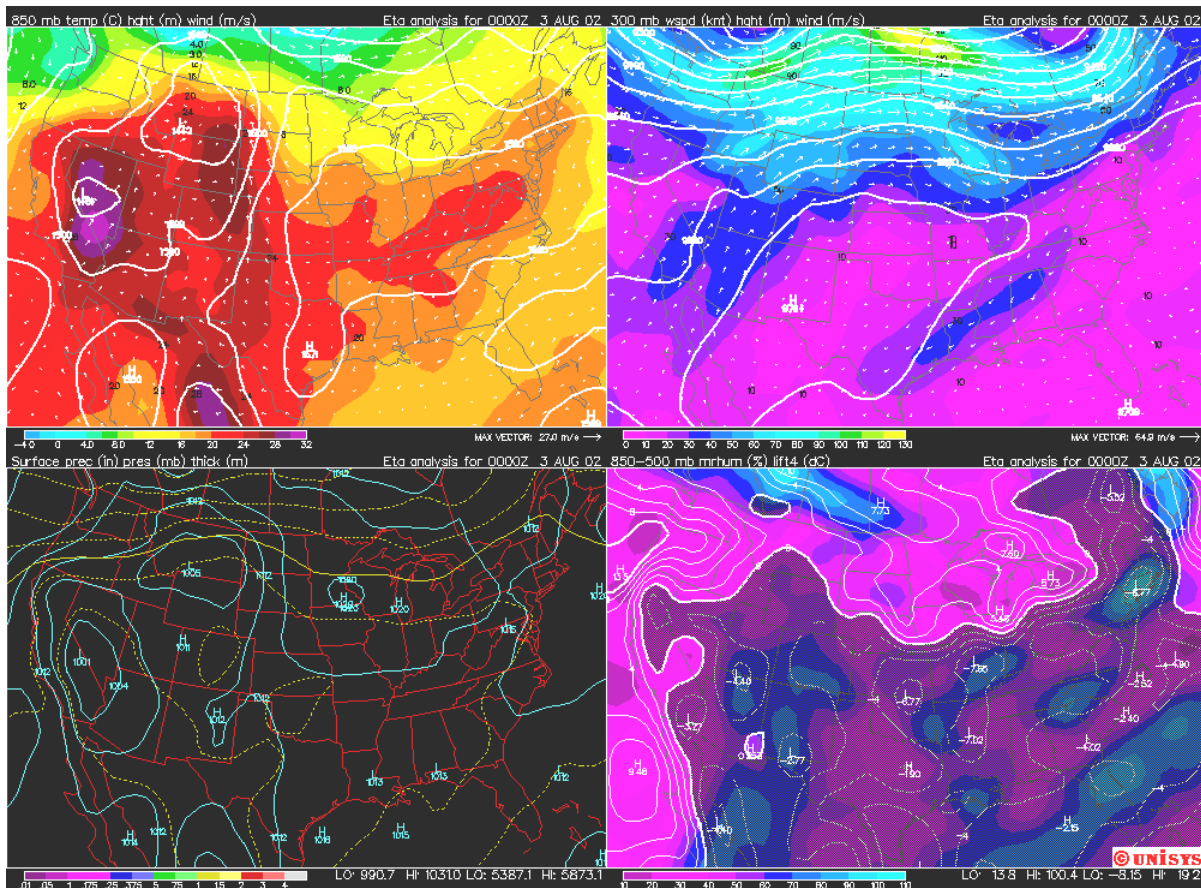


Figure 137: Fields of temperature at 850 mbar, wind speed and geopotential height at 300 mbar, surface pressure, and relative humidity at 0000Z, August 3, 2003, from the Eta analysis.

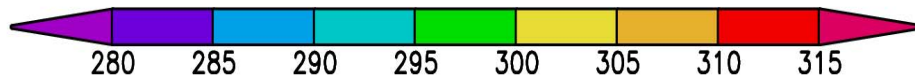
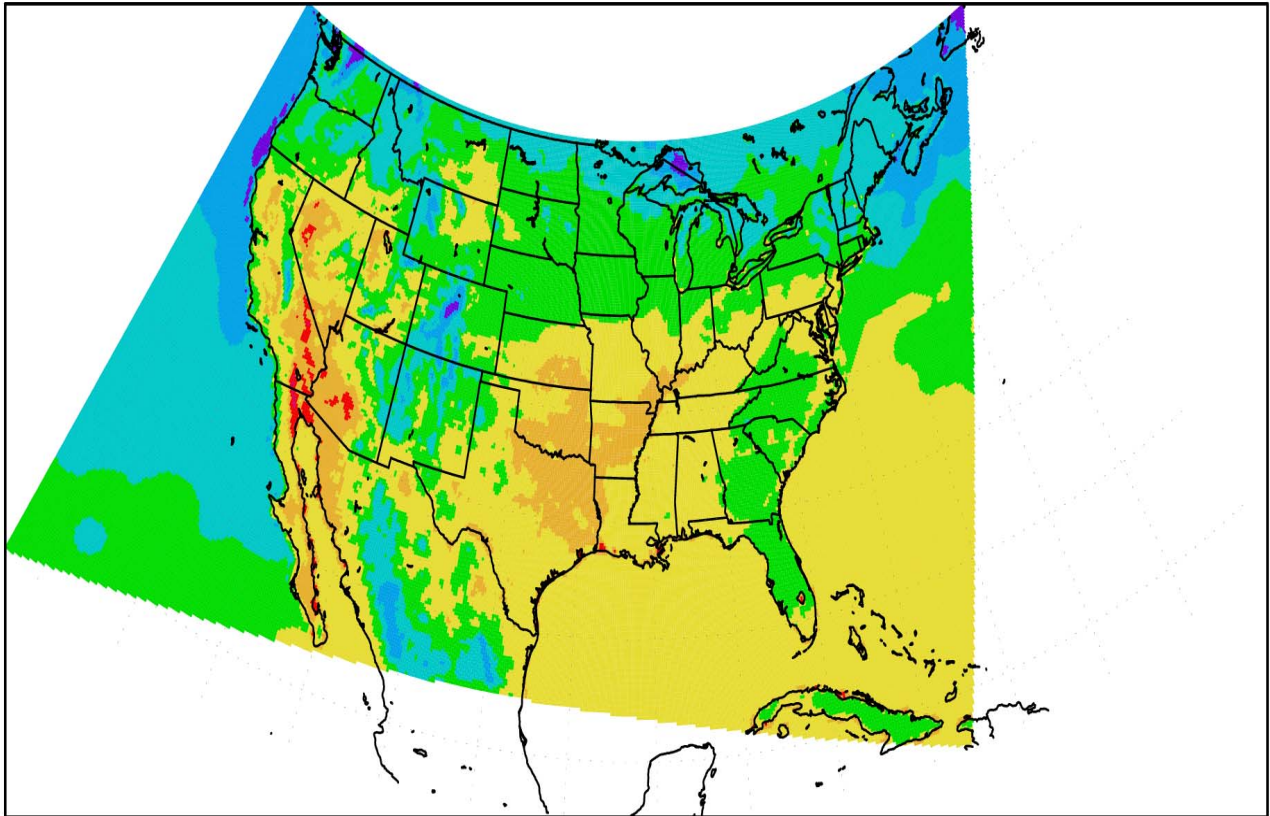


Figure 138: Ground temperature from the 15 km MM5 simulation.

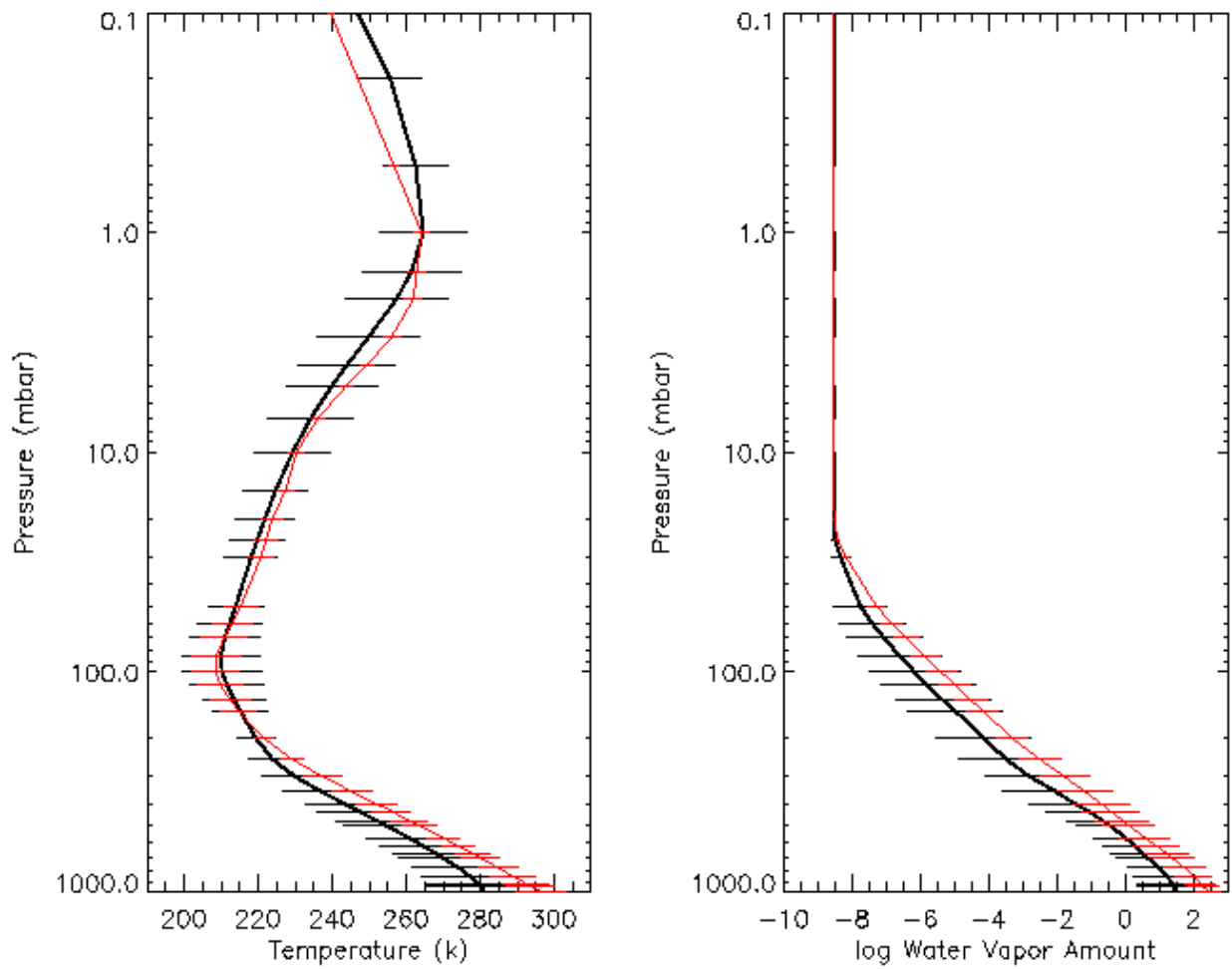


Figure 139: Mean profiles and standard deviation for temperature and water vapor in the NOAA-88 database (black) and the MM5 simulation (red).

GOES08 C1 VIS 02/08/02 18:00

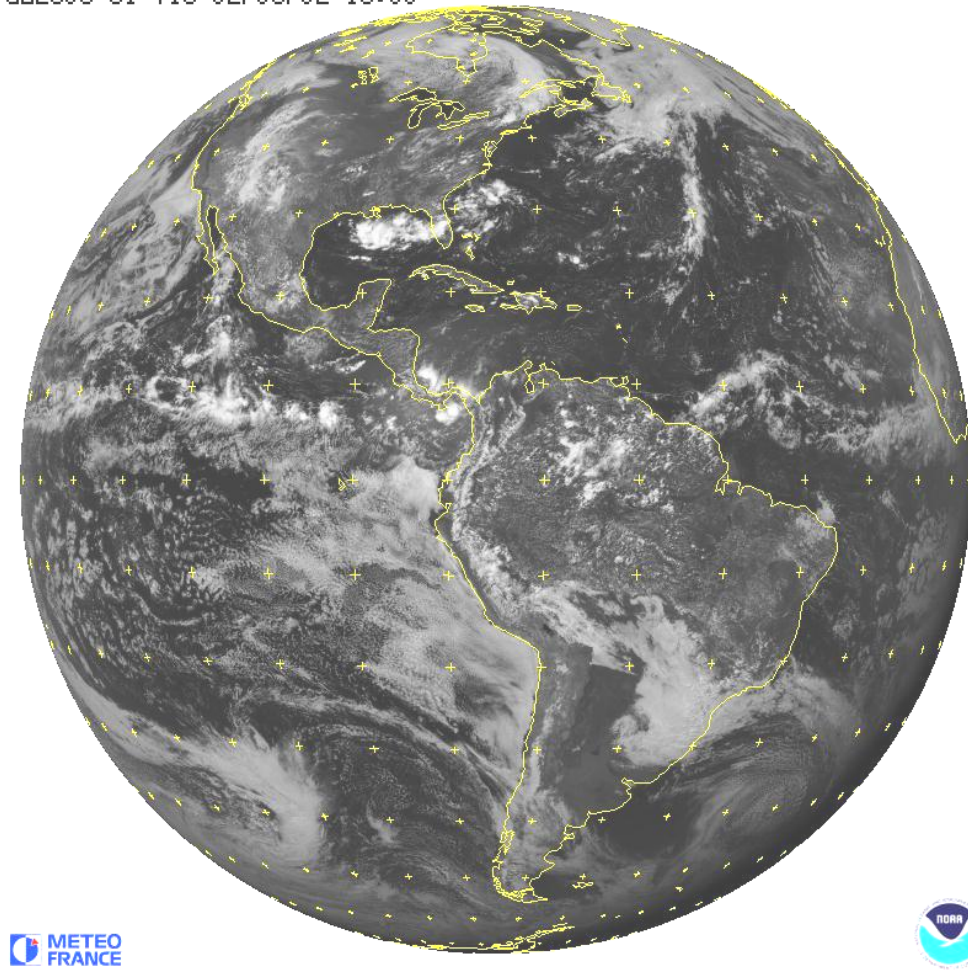


Figure 140: Visible image obtained by the GOES-8 satellite at August 2, 2002, 18 UTC (the beginning of the MM5 simulation).

GOES08 C4 IR 03/08/02 00:00

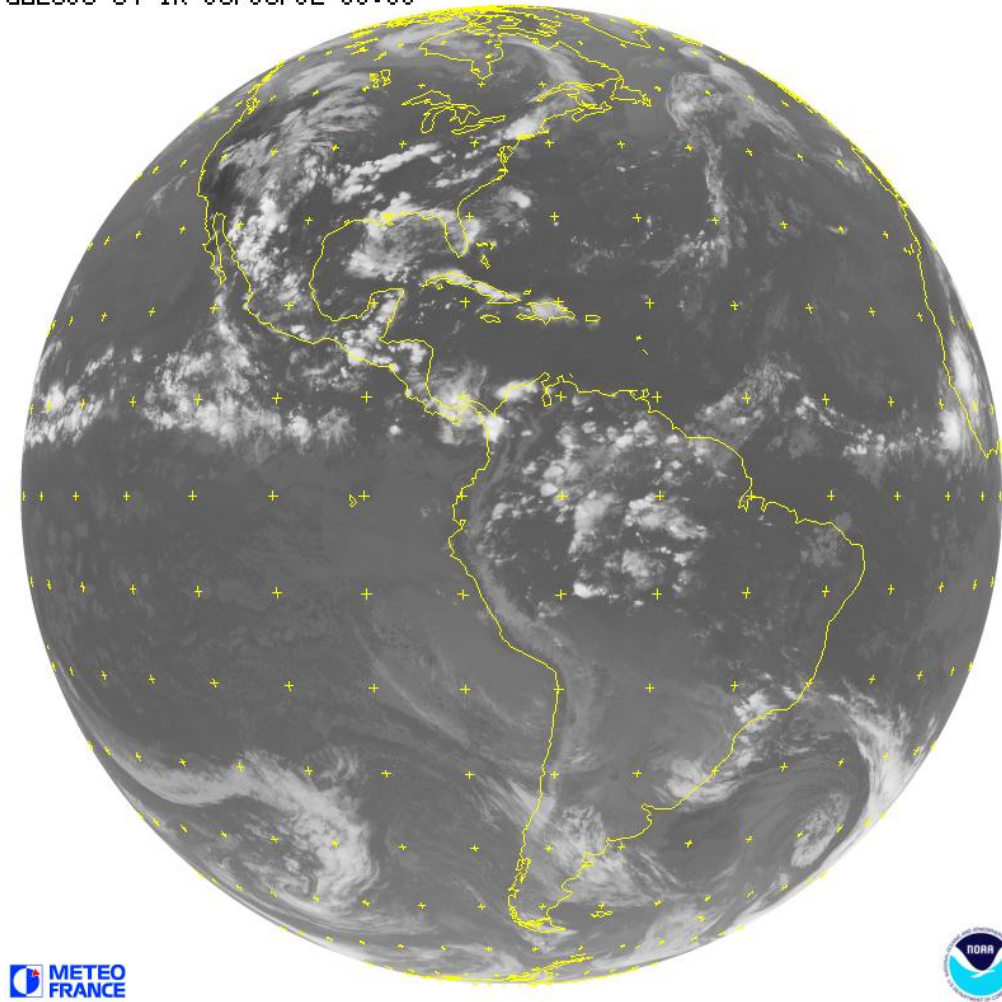


Figure 141: Infrared image obtained by the GOES-8 satellite at August 3, 2002, 00 UTC (the end of the MM5 simulation).

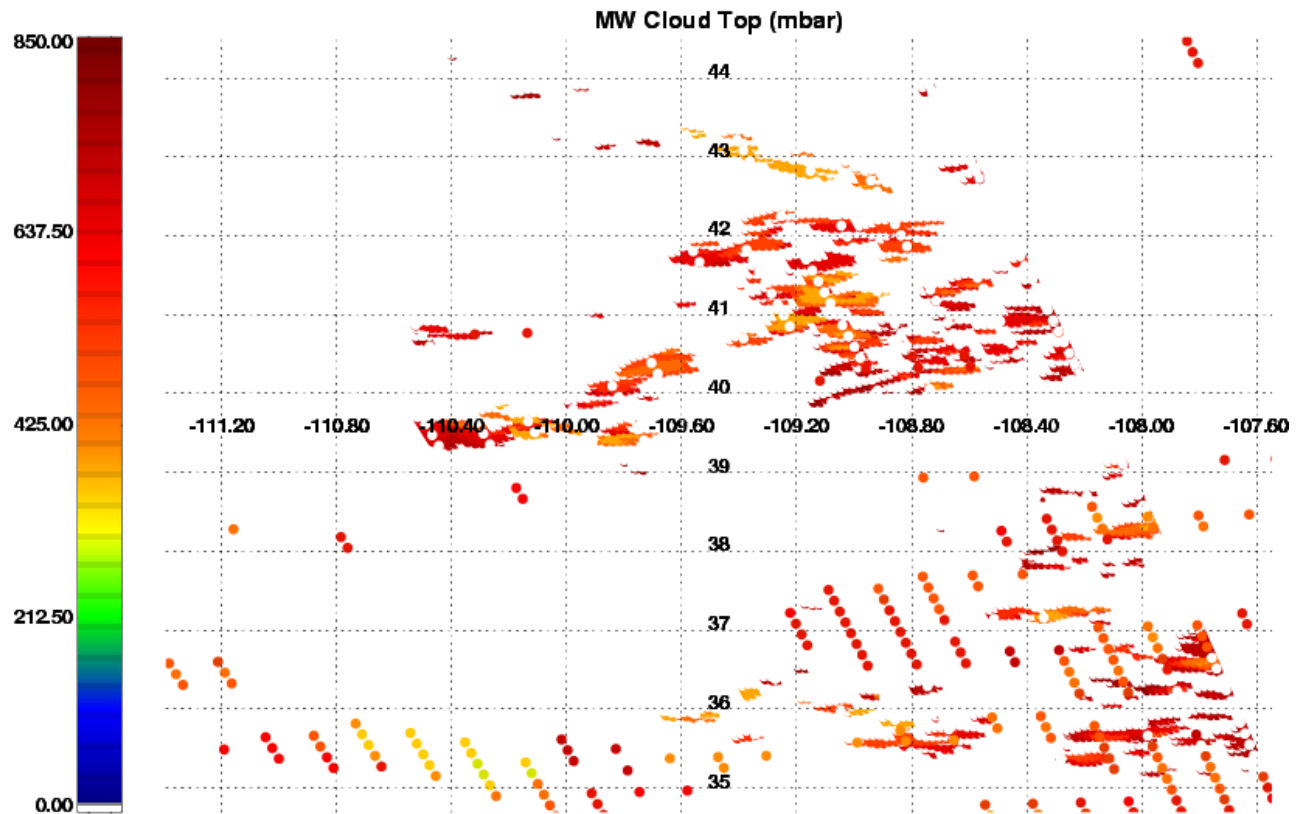


Figure 142: Cloud-top pressure in the 2- and 15 km MM5 simulations (color contours and circles, respectively).

B.2 Application to Simulated CrIS Retrievals

MM5 variables are read from files listed in `read_mm5_input_files` located in the root directory. MR/IR radiance simulations are performed using `sim_mm5` which is compiled as follows: `gmake DEVICE=ATMS_CrIS SIM_MM5` and executed subject to specifications in the namelist file: `bin/sim_mm5 < run/MM5/test.in`. The process of generating radiances also creates *simtruth.scene.nc* which contains all the scene information derived from the MM5 variables. Cloud properties (both MW and IR) are derived from the water and ice cloud profile amounts. For MW clouds, the top/bottom of the water cloud is calculated relative to a threshold amount and the integrated value gives the CLW amount. A single layer is permitted. For IR clouds, the cloud-top is determined from both the water and ice cloud profiles. Up to 8 layers is permitted if the clouds are partially transmissive. However, in the default mode all clouds are assigned a fraction equal to one, so that there is at most one cloud per pixel in the MM5 scenes. The MW

surfaces emissivities and IR emissivities/reflectivities are generated automatically during simulation using the Grody model and the ASTER database, respectively. The 50 MHz emissivity used as input to the Grody model is specified separately for water and land surfaces.

The 2 km scene is used to study the impact of ATMS footprint size and noise. The high-degree of sampling in this data is important for accurate representation of the radiances for different sampling options. An IDL code has been developed that will resample the simulated MW data for two different geometries:

1. Fixed grid - sampling and resolution for a specific CrIS FOR is fixed across the entire MM5 scene.
2. Scan grid - sampling and resolution is consistent with CrIS scan.

The 2 km MM5 scene is not large enough to cover the full set of 30 FORs from a CrIS scan. The IDL code simulates the ATMS MW data based on the (noise-free) MM5 scene, adds noise, then maps these radiances to the CrIS FORs. Currently the mapping is performed as a straight average and provides 3 outcomes corresponding to target sizes which are equal to the CrIS FOR, CrIS FOR + 1.1 degrees, and CrIS FOR + 2.2 degrees. In addition, the exact ATMS signal is computed directly from the 2 km MM5 scene for the CrIS FORs. The IDL code also generates the truth for each FOV within the FOR. In this step, cloud properties are assigned based on the properties at all 2 km gridpoints in the FOV. This leads to cloud fractions > 0 and < 1 , and multiple cloud layers in some cases.

The FOV mapping could be used to compute IR radiances for each FOV. However, this process is not practical since the simulated radiances must be generated each time for the geometry of the simulation. While the MW SDRs at 874 by 524 points can be computed fairly rapidly, the IR SDRs calculation is much more time consuming and requires much more storage space. Therefore, for this exercise, the IR SDRs are computed directly from the truth after the data has been mapped to the CrIS grid. This requires far fewer calculations. For example, the resulting nadir-fixed grid scene contains 18 x 32 FORs (after edge-trimming) or $18 \times 32 \times 9 = 5184$ FOVs.

The 15 km data is used to specify the covariance. This is necessary because the MM5 profiles are not consistent with the NOAA-88 covariances, especially for water vapor. Initial retrievals using the NOAA-88 covariances experiences problems only with the IR retrievals, not the MW retrievals. The reason for this is that at low altitudes to which the MW measurements are sensitive, the NOAA-88 water covariance is a reasonably good match to the data. However, at high altitude, the profile is quite different. This difference above 100 mbar propagates down in the IR retrievals resulting in large oscillations and poor performance. The new covariances are computed from the *simtruth.scene.nc* file generated using *sim_mm5*. When run in the MW-only mode, this file does not contain IR emissivities and reflectivities. So the final covariance gets updated using information from the NOAA-88 covariance for these variables.

- 1) Run MW-only simulations using *sim_mm5* based on 15 km data.
- 2) Add missing attributes to *simtruth.scene.nc* file.
- 3) Generate MM5 covariance.
- 4) Run MW-only simulations using *sim_mm5* based on 2 km data.
- 5) Process MW radiances through ATMS/CrIS simulations.
- 6) Generate IR radiances based on CrIS truth.
- 7) Run retrievals
 - cloud-free, cloudy
 - MW-only, MW/IR
 - ATMS = True CrIS, CrIS FOR, CrIS FOR + 1.1, CrIS FOR + 2.2.

APPENDIX C: CrIS FOV Naming Convention and Local Angles for Each FOV

This appendix describes the naming conventions for CrIS FOR and FOV according to the August 2002 ITT CrIS Sensor Specification.

Table 35 summarizes the nominal FOV and FOR parameters for the CrIS sensor. The values in the table have been updated to reflect the latest design specifications. This includes making the FOR footprint size, FOV sampling, and FOV footprint size equal in the cross-track and along-track directions. Also, the magnitude of the FOR rotation has been identified. Figure 143 shows an updated illustration of the FOV/FOR parameters. The convention adopted in the Sensor Specification assigns the maximum scan angle (+48.333 degrees) to FOR #1 and the minimum scan angle (-48.333 degrees) to FOR #30.

Table 35: Nominal FOV/FOR Parameters

Parameter	Value	CSS Reference
FOR numbering	1 to 30	CSS1657
FOR sampling	3 1/3 degrees	CSS1654
FOR footprint size	3.300 by 3.300 degrees	CSS819 ¹ , CSS1652 ¹
Maximum scan angle	+48.333 degrees (FOR 1)	CSS1657, CSS1683
Minimum scan angle	-48.333 degrees (FOR 30)	CSS1657, CSS1683
FOV numbering	1 to 9	CSS819
FOV sampling	1.100 by 1.100 degrees	CSS819 ¹ , CSS1718 ¹
FOV footprint size	0.963 by 0.963 degrees	CSS819 ¹ , CSS1718 ¹
Maximum FOV rotation	+48.333 degrees (FOR 1)	CSS818 ² , CSS1657 ²
Minimum FOV rotation	-48.333 degrees (FOR 30)	CSS818 ² , CSS1657 ²

¹ Modified based on discussions with ITT.

² Based on discussions with ITT.

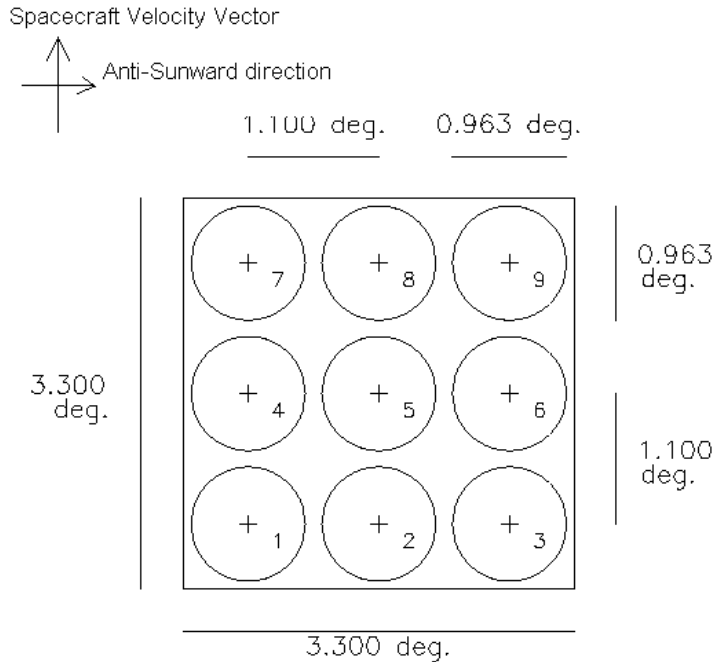


Figure 143: Nominal FOV/FOR parameters have been adopted from the August 2002 CrIS Sensor Specifications and based on discussions with ITT. In the current design, the extent of the FOR is equal in the in-track (indicated by the arrow) and cross-track directions (i.e., 3.300 degrees). The FOV footprint size (0.963 degrees) and FOV sampling (1.100 degrees) are also equal in the two directions. The numbering convention for the FOVs is indicated in the plot.

The convention for numbering FORs and FOVs is further illustrated in Figure 144. This figure also illustrates the direction of the FOV pattern rotation relative to the motion of the satellite. Table 36 lists the central scan angles for all FOVs and FORs following the convention illustrated in Figure 144. The Local Angle Adjustment algorithm is a regression-based algorithm that is trained to a specific set of angles. In the next release of the CrIS simulation/retrieval code, the coefficients of the algorithm will be tuned based on the angles listed in Table 36.

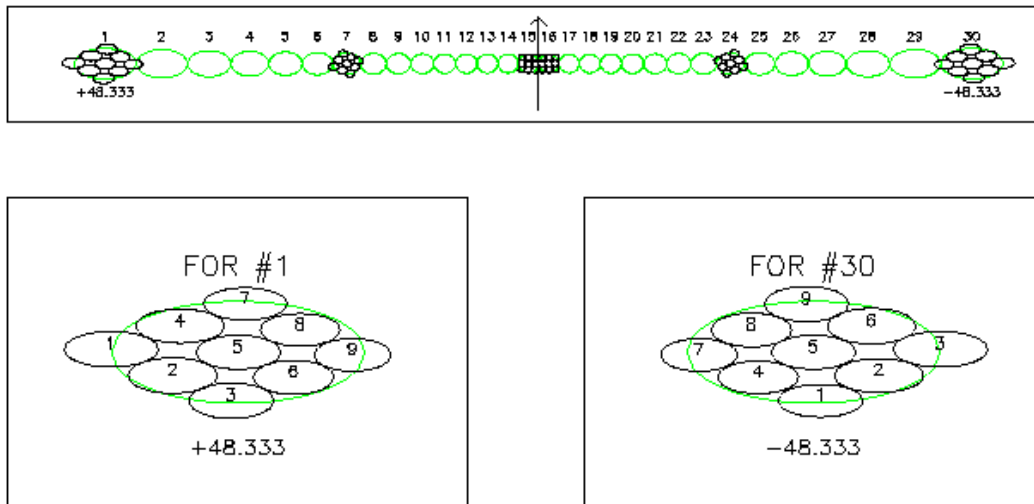


Figure 144: The top plot shows the numbering convention for the CrIS FORs as seen from above. The direction of the satellite is indicated by the arrow at zero scan angle (nadir). FORs are numbered 1 through 30 from left to right with scan angles ranging from +48.333 to -48.333 degrees. The FOV locations are shown for selected FORs in order to illustrate the rotation of the FOV pattern. The lower two plots show the FOV numbering convention at FOR #1 and #30. For these FORs, the FOV pattern is rotated by +48.333 and -48.333 degrees, respectively.

Table 36: CrIS Scan Angles

FOR	Scan Angle (degrees)									
	FOR	FOV 1	FOV 2	FOV 3	FOV 4	FOV 5	FOV 6	FOV 7	FOV 8	FOV 9
1	48.333	48.2512	47.5135	46.7805	49.0668	48.3333	47.6044	49.8862	49.1568	48.4320
2	45.000	45.0106	44.2249	43.4446	45.7804	45.0000	44.2249	46.5554	45.7804	45.0106
3	41.667	41.7702	40.9392	40.1139	42.4912	41.6667	40.8480	43.2195	42.4015	41.5895
4	38.333	38.5300	37.6563	36.7886	39.1992	38.3333	37.4738	39.8785	39.0205	38.1691
5	35.000	35.2895	34.3761	33.4688	35.9042	35.0000	34.1024	36.5324	35.6375	34.7498
6	31.667	32.0484	31.0984	30.1546	32.6062	31.6667	30.7340	33.1814	32.2529	31.3319
7	28.333	28.8066	27.8234	26.8459	29.3048	28.3333	27.3687	29.8257	28.8668	27.9157
8	25.000	25.5639	24.5508	23.5431	26.0001	25.0000	24.0066	26.4657	25.4798	24.5018
9	21.667	22.3200	21.2808	20.2463	22.6919	21.6667	20.6477	23.1015	22.0921	21.0907
10	18.333	19.0752	18.0138	16.9560	19.3802	18.3333	17.2922	19.7339	18.7046	17.6832
11	15.000	15.8297	14.7503	13.6734	16.0648	15.0000	13.9402	16.3637	15.3182	14.2807
12	11.667	12.5846	11.4922	10.4007	12.7458	11.6667	10.5916	12.9926	11.9351	10.8860
13	8.333	9.3431	8.2441	7.1450	9.4230	8.3333	7.2467	9.6244	8.5602	7.5064
14	5.000	6.1155	5.0239	3.9367	6.0966	5.0000	3.9054	6.2707	5.2112	4.1727
15	1.667	2.9584	1.9697	1.1941	2.7664	1.6667	0.5680	2.9943	2.0231	1.2803
16	-1.667	-1.1941	-1.9697	-2.9584	-0.5680	-1.6667	-2.7664	-1.2803	-2.0231	-2.9943
17	-5.000	-3.9367	-5.0239	-6.1155	-3.9054	-5.0000	-6.0966	-4.1727	-5.2112	-6.2707
18	-8.333	-7.1450	-8.2441	-9.3431	-7.2467	-8.3333	-9.4230	-7.5064	-8.5602	-9.6244
19	-11.667	-10.4007	-11.4922	-12.5846	-10.5916	-11.6667	-12.7458	-10.8860	-11.9351	-12.9926
20	-15.000	-13.6734	-14.7503	-15.8297	-13.9402	-15.0000	-16.0648	-14.2807	-15.3182	-16.3637
21	-18.333	-16.9560	-18.0138	-19.0752	-17.2922	-18.3333	-19.3802	-17.6832	-18.7046	-19.7339
22	-21.667	-20.2463	-21.2808	-22.3200	-20.6477	-21.6667	-22.6919	-21.0907	-22.0921	-23.1015
23	-25.000	-23.5431	-24.5508	-25.5639	-24.0066	-25.0000	-26.0001	-24.5018	-25.4798	-26.4657
24	-28.333	-26.8459	-27.8234	-28.8066	-27.3687	-28.3333	-29.3048	-27.9157	-28.8668	-29.8257
25	-31.667	-30.1546	-31.0984	-32.0484	-30.7340	-31.6667	-32.6062	-31.3319	-32.2529	-33.1814
26	-35.000	-33.4688	-34.3761	-35.2895	-34.1024	-35.0000	-35.9042	-34.7498	-35.6375	-36.5324
27	-38.333	-36.7886	-37.6563	-38.5300	-37.4738	-38.3333	-39.1992	-38.1691	-39.0205	-39.8785
28	-41.667	-40.1139	-40.9392	-41.7702	-40.8480	-41.6667	-42.4912	-41.5895	-42.4015	-43.2195
29	-45.000	-43.4446	-44.2249	-45.0106	-44.2249	-45.0000	-45.7804	-45.0106	-45.7804	-46.5554
30	-48.333	-46.7805	-47.5135	-48.2512	-47.6044	-48.3333	-49.0668	-48.4320	-49.1568	-49.8862

APPENDIX D: ATMS SDR Remapping Issues

A “noise amplification factor” NAF can be used under homogeneous scene conditions to estimate the noise level of ATMS after the footprints have been mapped to the CrIS grid. The goal is to establish nominal and worst-case values using a simple metric (rather than performing the actual footprint matching) so that the sensor noise values may be properly included for the ATMS portion of the CrIMSS algorithm. The operational algorithm will require a much more detailed algorithm for the ATMS/CrIS footprint matching. Most importantly, the algorithm will require the knowledge of actual ATMS antenna patterns (rather than the assumption of a Gaussian shape).

D.1 Relative Scan Geometry of CrIS and ATMS

The relative CrIS and ATMS field-of-view (FOV) geometry is given in Table 37 and illustrated in Figure 145. The CrIS retrievals are performed on a grid of 3x3 CrIS FOVs which comprise a single field-of-regard (FOR). A single CrIS scan is composed of 30 FORs (15 on either side of nadir), while a single ATMS scan has 96 FORs (48 on either side of nadir). ATMS makes 3 scans during the time it takes CrIS to make one scan (see Figure 146).

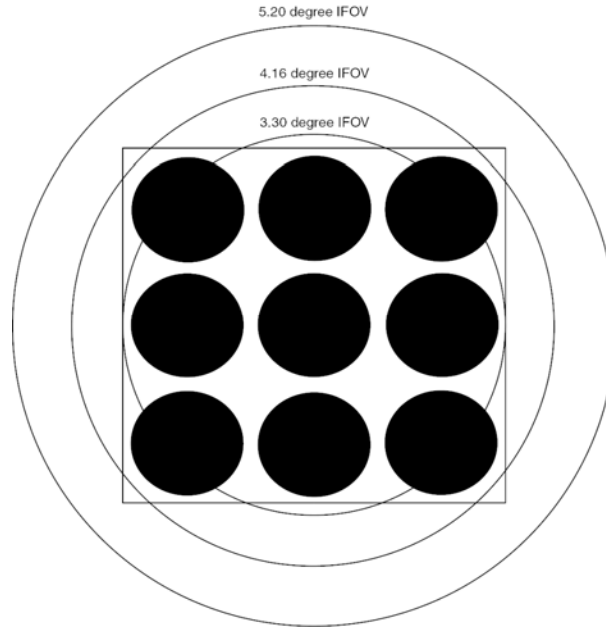


Figure 145: Comparison of beam diameters and CrIS FOR.

The grid of 3x3 CrIS footprints is measured using a 3x3 detector array. The sensor configuration and scanning geometry causes this grid to rotate as a function of the off-nadir scan angle.

Our analysis accounts for the rotation of the CrIS FOVs within the FOR as the sensor scans across the track. This rotation is assumed to be 1 degree for every 1 degree of off-nadir angle. This has minimal impact on the determination of ATMS footprint weights for the footprint matching (since we are matching to a circular pattern, not a square, the rotation is irrelevant), but it does impact the full CrIMSS retrieval studies for high spatial resolution, inhomogeneous scenes.

Table 37: Comparison of CrIS and ATMS Geometry Characteristics.

Parameter	CrIS	ATMS
Maximum Scan Angle (edge-of-scan)	+/- 49.395 degrees	+/- 52.725 degrees
FOV Spacing	1.11 degrees	1.11 degrees
FOV Beam Diameter	0.963 degrees	5.2 degrees (ch 1 & 2) 2.2 degrees (ch 3-16) 1.1 degrees (ch 17-22)
Scan Duration	8 seconds	8/3 seconds
FOR Rotation	49.395 degrees at EOS	N/A

A model of the CrIS and ATMS scan patterns has been developed to determine the degree of overlap between the two sets of FOVs. This calculation assumes a spacecraft altitude of 824 km, consistent with the NPP specification, in order to translate the FOV scan angles and beam diameter into the ground footprint size.

An example of the CrIS and ATMS footprint overlap is given in Figure 146. This figure shows the center positions of the ATMS scans along with a single CrIS FOR. The dotted overlay circles are the three ATMS FOV sizes corresponding to the ATMS scan most closely matched with this CrIS FOR. The ATMS footprint centers are shown with three different symbols to differentiate from three separate scan sequences (since the ATMS scans at three times the rate of CrIS). Because of this scan mismatch, the near-nadir CrIS FOV centers do not align along-track with the ATMS FOV centers, except for the first CrIS FOR where both CrIS and ATMS start their scan. However, because the incremental cross-track scan angle step size is the same, the FOVs do align in the cross-track direction. Also note that because this figure shows the near-nadir pixel, the FOVs are circular and there is very little FOR rotation.

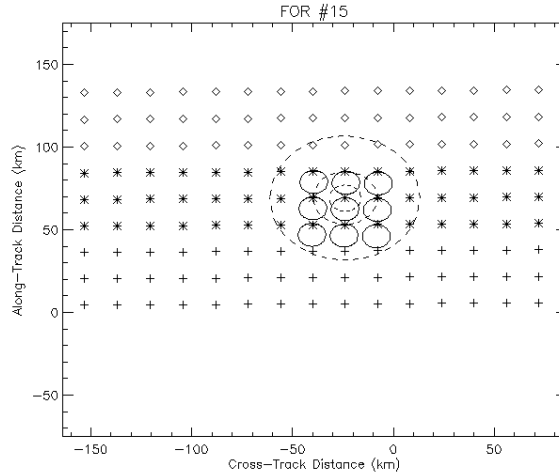
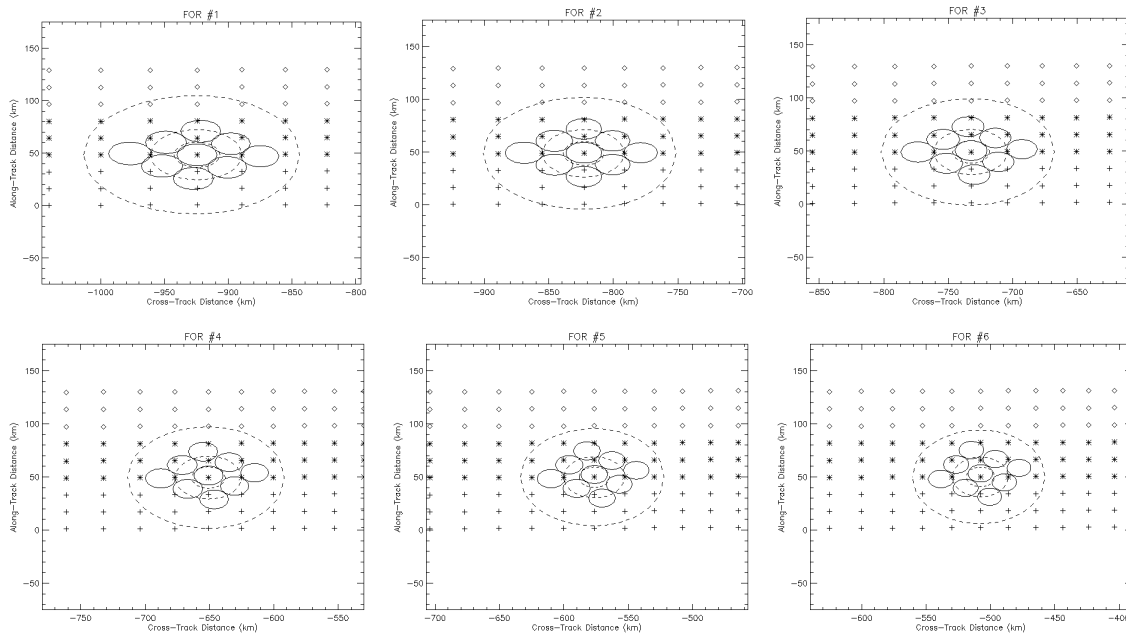
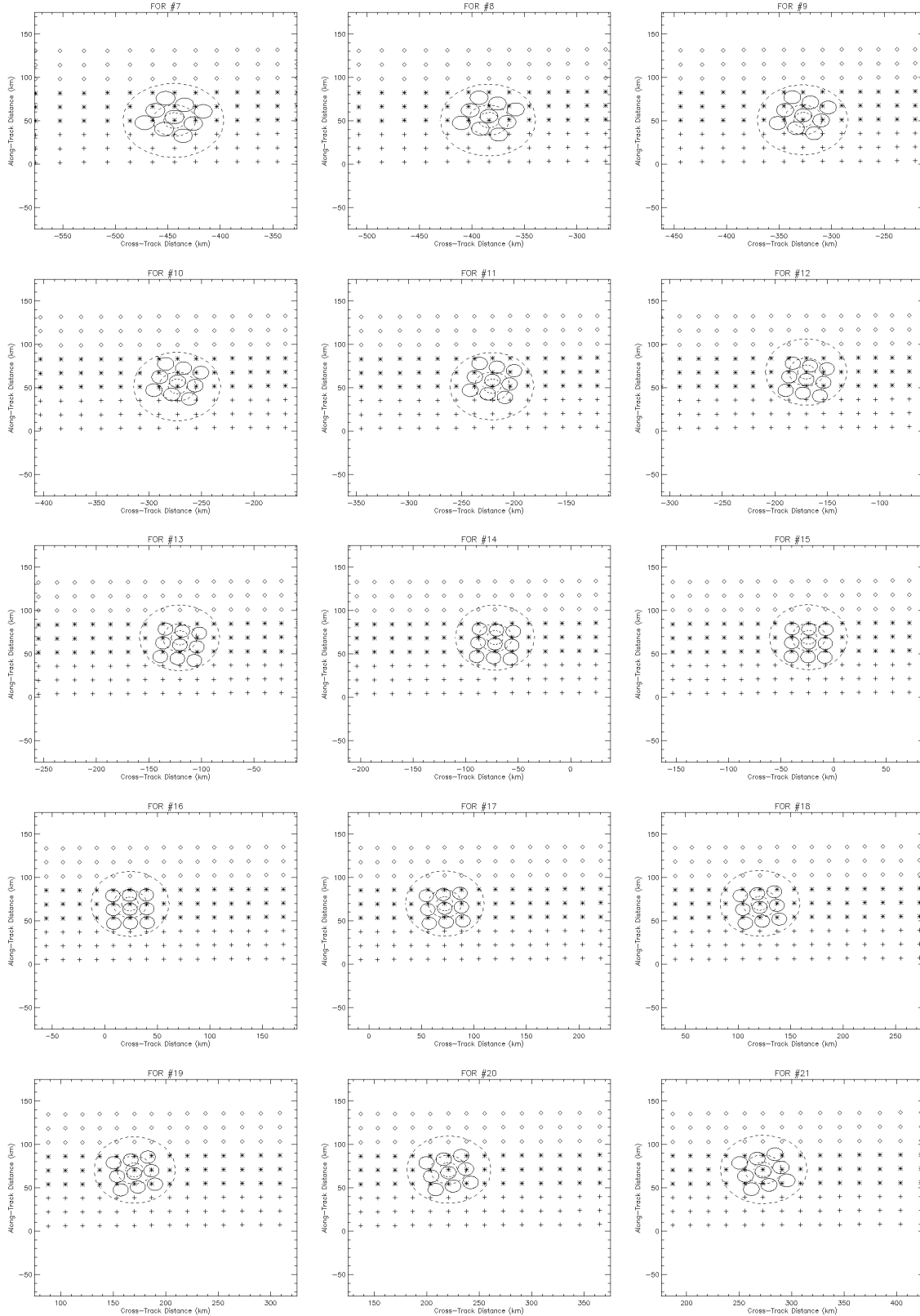


Figure 146: Example of CrIS FOR (FOR #15 corresponds to the 15th FOR and occurs just to the left of nadir relative to the along-track satellite velocity vector).

The relative ATMS and CrIS scan positions and FOV sizes for each of the 30 CrIS FORs is shown in Figure 147.





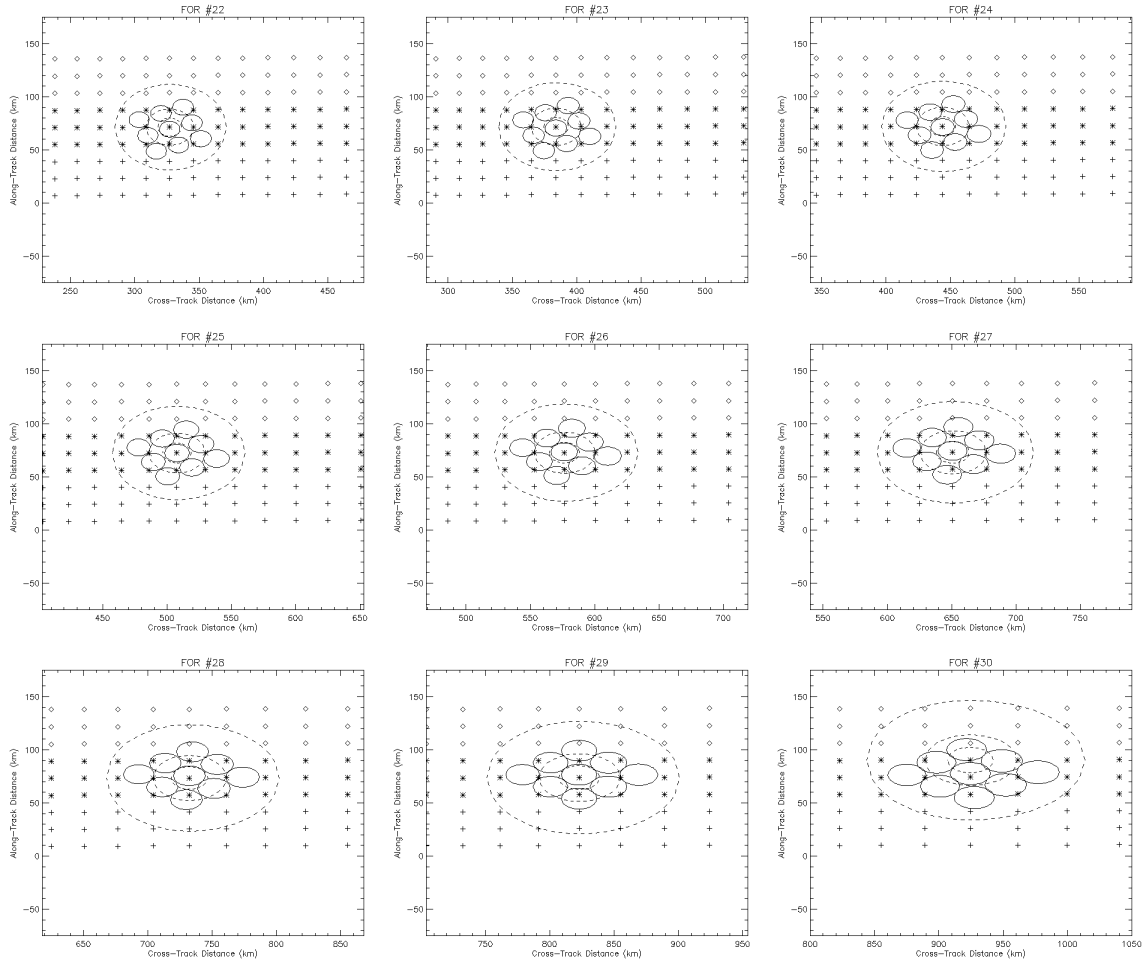


Figure 147: CrIS FORs.

D.2 Calculation of ATMS Noise Reduction Factor (NRF)

Comparison of the CrIS and ATMS FOVs used in a given retrieval indicate that there can be significant overlap in the FOV locations, particularly at the larger scan angles. Thus if the ATMS FOVs are mapped to the CrIS FOV grid there will be an effective reduction in the radiometric noise level of the ATMS radiances. While a detailed analysis of the footprint matching has yet to be carried out, an estimate of the resulting noise reduction factor can be obtained by assuming that the re-mapped footprint has the same size and shape as the largest ATMS footprint. In other words, we can calculate the NRF for the largest ATMS FOV centered on the CrIS FOR (this new ATMS FOV will be hereafter referred to as the ATMS FOR). However, the plots in Figure 147 indicate that the size and shape of the ATMS FOR is somewhat larger than the actual CrIS FOR. Consequently we also computed the NRF for a slightly smaller (80%) footprint that more closely approximates the CrIS FOR (this footprint was constructed by taking the dimensions of the ATMS FOV and shrinking them by 20%). This analysis was conducted for three scan angles – near-nadir, intermediate, and edge-of-scan, and the results are given in Table 38.

Table 38: NRF as a Function of FOR Size (relative to ATMS) and Scan Angle.

Field-of-Regard/ Scan Angle	ATMS Beam Diameter	Noise Reduction Factor (100% FOR)	Noise Reduction Factor (80% FOR)	Noise Reduction Factor (63.5% FOR)
1 / 48.28 deg	5.2 deg	0.292	0.441	0.68*
	2.2 deg	0.145	0.192	0.28
	1.1 deg	0.136	0.170	0.22
8 / 24.98 deg	5.2 deg	0.323	0.574	0.82*
	2.2 deg	0.170	0.223	0.31
	1.1 deg	0.159	0.200	0.25
15 / 1.67 deg	5.2 deg	0.343	0.613	0.93*
	2.2 deg	0.178	0.235	0.33
	1.1 deg	0.167	0.209	0.27

Note: The target size is defined by a modified Gaussian, with the exception of those marked with “*” (which use a Gaussian target).

The footprint characteristics for FOR #8 (24.98 deg scan angle) are shown in Figure 148. The axes indicate the cross-track and along-track distance from the center of the CrIS FOR. The “+” symbols indicate the ATMS FOVs contributing to the ATMS FOR, with the dotted line around the center FOV indicating the size of the contributing FOVs. The solid contours represent the near-Gaussian response of the ATMS FOR, where the 3 db contour indicates the 50% power point. The dashed circular line in the plots gives the target shape for the ATMS FOR (not visible in all figures due to the overlap with the 3 db contour).

A number of assumptions has been made in this study due to lack of specific details. These assumptions are summarized as follows:

- CrIS documentation gives FOR spacing as “1.100” degrees cross-track, while ATMS is 1.11 degrees. For convenience, in this study the CrIS spacing has been set to that of ATMS.

- ATMS beam diameter is given as the half-power point of the beamwidth. For this study we have assumed a modified Gaussian shape for the beam. In reality the beam will have a more-rapid fall-off past the half-power point and may contain side-lobes (side-lobes will decrease the fit capability and may increase the NRF).
- CrIS FOR rotation is assumed to be equivalent to the scan angle (e.g. a 20 degree rotation for a scan angle of 20 degrees).
- Plane-parallel geometry is used in the translation from angle-coordinates to distance-coordinates.
- NRF derived using statistics for independent samples. In reality, the noise is correlated and there will be less noise reduction than this study indicates. However, more information about the characteristics of the sensor is required before a complete analysis may be performed.

Now that we have the framework in place for studying footprint matching, it will be relatively easy to update any of our assumptions.

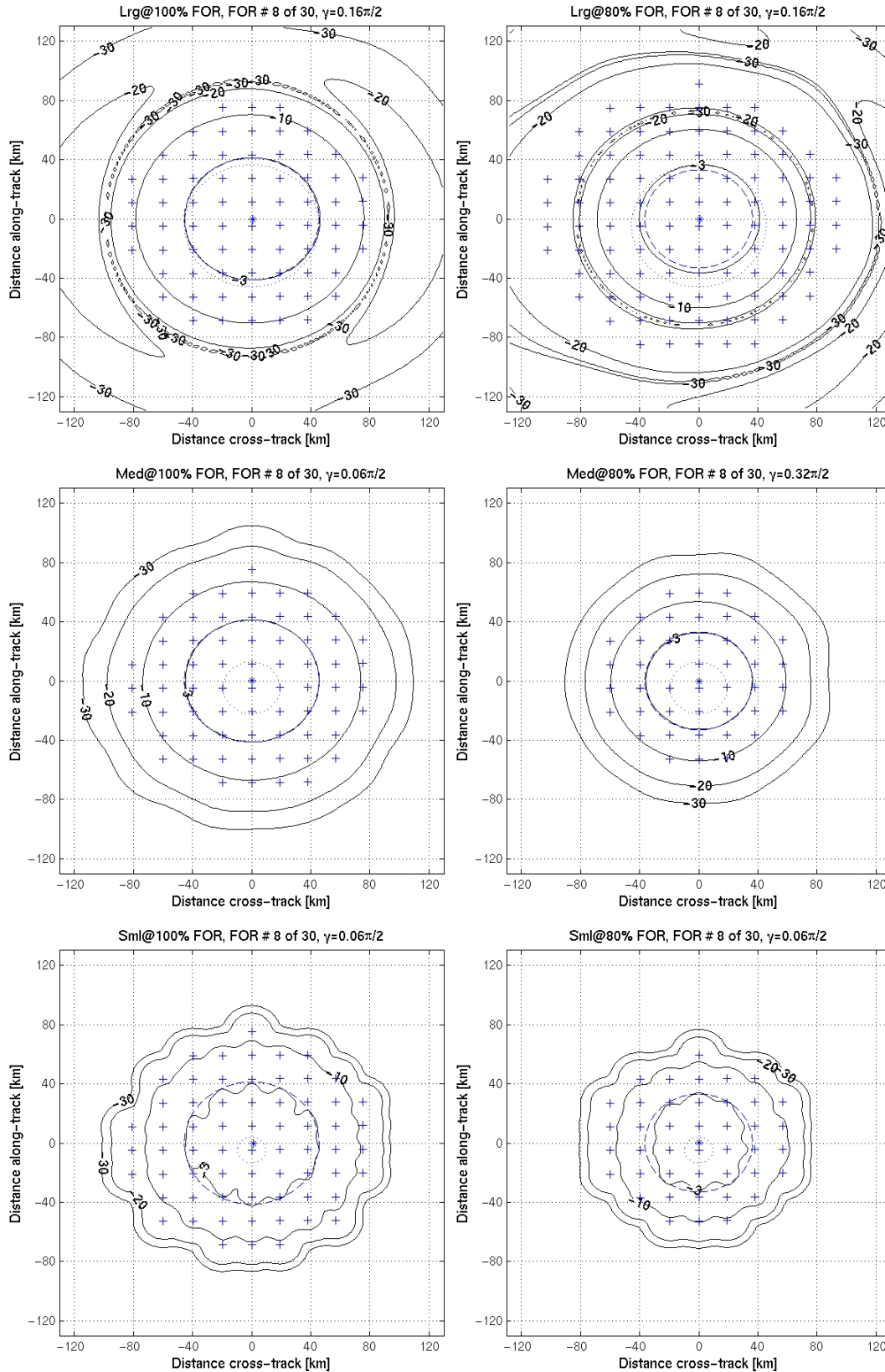


Figure 148: Footprint characteristics for FOV #8.

D.3 Differences from NGES Noise Amplification Memo

The memo from Barbara Burns to Kent Anderson titled “ATMS SDR Algorithm Description” (TM-01-380C, March 2003, hereinafter referred to as “the SDR-AD”) contains a detailed description of the ATMS/CrIS footprint matching procedure and results. In summary,

- Our analysis of the NGES report concludes that their spatial error metrics (matching error and HW error) underestimate the true mismatch between the effective (composite) patterns and the target (reference). As a result, for large (5.2°) sensor channels, it is likely that the noise amplification factor (NF) and spatial mismatch have not been simultaneously optimized and that significant numerical inversion error may remain in the solution. This may partially explain NGES’s large NF values that vary considerably across the scan.
- NGES’s limits on neighborhood size (3x3 to 7x7 samples) may also give larger NF for all channels and may cause large mismatch errors in the form of side-lobes for 5.2° channel matches. NGES’s matching error metric does not appear to measure some effective pattern side-lobes because the evaluation domain is limited to about 4 times the target pattern width at half-maximum (HW).
- Although 3.3° ATMS FOV is the specified goal for the resampling algorithm, it is too small a target to reach in practice with the 5.2° channels without introducing severe spatial noise (e.g., side-lobes) in the effective pattern in addition to amplifying noise. NGES’s HW and matching error metrics indicate the spatial error but appear to underestimate the magnitude. Valid, quantitatively significant metrics are needed to optimize both the noise and pattern of the resampled data. We recommend that maximum side-lobe level limits be set and that integrated main-beam weight (i.e., effective pattern weight within the target pattern’s half-power contour) be used as a spatial optimization metric.

Because NGES is the ATMS sensor developer, the trade studies presented in the following sections were conducted using both AER and NGES noise amplification values.

APPENDIX E: Simulation of Transparent Clouds

This Appendix details the addition of a transparent cloud module into the CrIMSS algorithm.

E.1: Introduction

The CrIMSS simulation code has been modified to allow the user to simulate transparent clouds. Previously delivered versions of the code have had the capabilities to simulate such clouds but the infrastructure to input the needed cloud properties were required. *Only absorbing clouds are simulated, the present version of OSS does not have scattering capabilities.* The CrIMSS retrieval algorithm does not model the clouds in the IR and this is the same basic code used for the simulations. In this Appendix we describe the expected inputs and modifications to the simulation procedure if transparent clouds are being modeled.

E.2: Input Files

The algorithm expects the frequency dependent cloud properties to be in the form of absorption coefficients with units m^2/gm . We have supplied several such cloud properties files for both ice and water clouds. In building these files we assumed spherical particles and used MIE code to generate the needed coefficients. The units for the absorption coefficient were set by dividing the output from the MIE code by the phase density. The files provided are temperature independent, besides for the phase considerations. A routine “*READMIE.f*” reads from ascii files the frequency and absorption coefficient(see end of memo). The routine is setup to load coefficients for both water and ice clouds. Figure 149 illustrates absorption coefficients for both water and ice particles

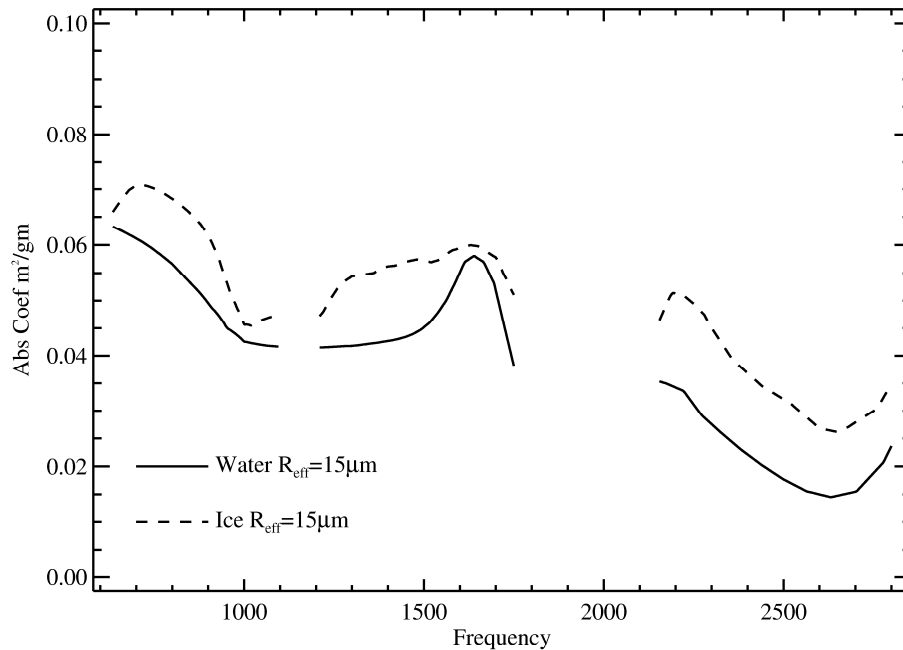


Figure 149: Absorption coefficients generated using MIE code for $R_{\text{eff}}=15\mu\text{m}$ for both water and ice.

E.3: Discussion

The simulator will still generate a weighted sum of the clear and cloudy scenes but the cloudy portion can have several layers of semitransparent clouds. Optical depths will be computed for a given the cloud top, cloud thickness, cloud amount and cloud absorption coefficients. Depending upon the temperature of the upper portion of the cloud, either ice or water phase absorption coefficient are used. Since only absorption is being modeled no attempt is made to account for solar reflection off the cloud top.

APPENDIX F: Radiative Transfer Model Upgrade

This Appendix describes the radiative transfer model upgrades that were performed in the creation of Version 4.0 of the CrIMSS EDR Algorithm Code. Note that prior versions of the code were used to produce the trade studies and results found in previous sections of this ATBD.

F.1: Introduction

The CrIMSS EDR algorithm relies on a fast RTM to compute microwave and infrared radiances and the associated Jacobians (the change in radiance with respect to geophysical parameters) for a given set of atmospheric profiles (temperature, water vapor, ozone, etc.), surface conditions (reflectivity and emissivity), viewing geometry, etc. The fast model (for both the microwave and infrared) is built upon the Optimal Spectral Sampling (OSS) approach. Because OSS is a mechanism by which the time required to compute the necessary radiative transfer is reduced by eliminating nearly redundant monochromatic information in the bandpass of each sensor channel, there is a specific error relative to the “perfect”, monochromatic calculation. This Appendix examines the differences between the monochromatic calculation and the fast model calculation and presents the changes to the software necessary to increase the overall accuracy while maintaining a reasonable computation time.

Note that much of the basis for the changes discussed below was previously presented and discussed at the International TOVS Study Conference (ITSC) in Sainte Adele, Canada (29 October 2003 – 4 November 2003) in paper 4.6 by Jean-Luc Moncet and Gennadi Uymin of AER.

F.2: Code Configuration for Testing

We have selected LBLRTM coupled with the HITRAN spectral line database as our reference radiative transfer model. For the tests described in this memo, and for the generation of the optical depth database for Version 4.0 of the CrIMSS code, we are using LBLRTM version 7. This is the same code and database used for previous versions of OSS, although the specific version of LBLRTM has changed (see <http://rtweb.aer.com/> for details).

The process of determining differences between the fast RT model and the line-by-line code is relatively straightforward, but care must be taken to ensure that the comparison is done in a fair manner. In particular, it is important to make sure that the following are done in a consistent manner: atmospheric layering and profile information (number and location of layers, same temperature and molecular profiles), surface term (emission and reflection), solar/thermal angles used for downwelling radiance, layer emission temperature calculation, solar source function (same Planck temperature or external file). When comparing the overall retrieval results obtained by two versions of the software it is also important that the sensor noise added to the simulated radiances be the same for both versions.

While LBLRTM was used to compute the optical depth tables used by the OSS-based forward model, a number of coding differences must be resolved between the ways in which the two models compute the top-of-atmosphere radiance. Previous tests have shown that the radiative transfer calculation is performed in a slightly different manner within OSS as compared to LBLRTM. While these differences are small in the context of sensor channel radiances, we have chosen to eliminate them completely by comparing the OSS result to LBLRTM optical depth calculations fed through the OSS radiance calculation module. By treating the radiative transfer in the same way the differences will be due only to the way in which optical depths are calculated for a specific test profile.

F.3: OSS Radiative Transfer Changes

A number of simplifying assumptions must be made in the calculation of molecular optical depths in order to design a fast radiative transfer model that has a significant computational advantage over line-by-line calculations. It is important to understand how these assumptions influence the final calculation results in order to reduce these errors to a level sufficient for the intended use of the model.

To date, i.e. through Version 3.0 of the CrIMSS code, we have identified a number of assumptions that are valid when using the OSS model for sensor simulation experiments, but will

likely cause unacceptable radiance errors when applied to actual measurement data. These assumptions include the following:

- Only 40 atmospheric layers
- Linear interpolation in temperature of absorption coefficients
- Treatment of absorption coefficients and total air mass of each layer relative to the water vapor concentration

The impact of all but the atmospheric layering is shown in Figure 150, a comparison of the OSS model brightness temperatures with those of the line-by-line code. Note that for this comparison the radiative transfer portion of the calculation was identical so that all errors may be attributed to the approximations inherent in the optical depth calculation. While details about each of these error sources and the error mitigation strategy are given in the following sections, Figure 151 shows the OSS model validation after making these changes. The errors are substantially reduced from those seen in Figure 150. For the following discussion we will refer to Version 4.0 of the CrIMSS code as having the “updated OSS”, while previous versions used “old OSS”.

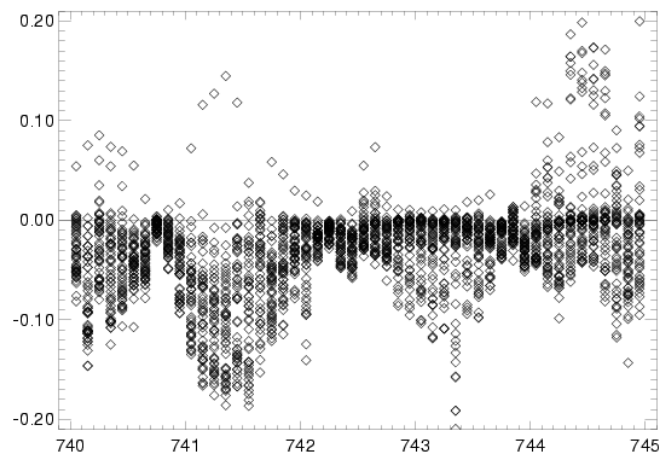


Figure 150: Total brightness temperature errors with old scheme

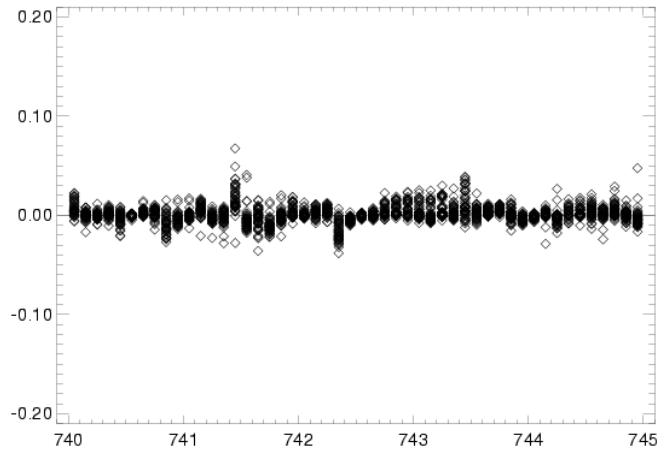


Figure 151: Total brightness temperature errors with new scheme

F.3.1: Impact of Layering

The original versions of the CrIMSS EDR algorithm (i.e. pre-version 4.0) used 40 atmospheric levels to specify the geophysical profile. The radiative transfer model used for these versions of the algorithm was designed for accurate and efficient calculations to support sensor and algorithm trade studies during the early phases of the project. It is recognized that this model is not sufficient for use with “real” data.

A major part of the effort to upgrade the radiative transfer involves the addition of atmospheric levels to reduce errors associated with the vertical averaging of temperature and molecular amounts (and thus the layer emission and absorption properties). We have selected a grid of 101 levels for the updated version of the model. This selection is based on several factors including trade-offs between the number of layers and the overall timing requirements of the algorithm, and recognition of work done within the overall science community to optimize the number of layers. The main drawback in using fewer than about 100 levels is that various approximations must be made, such as the Pade approximation to the effective layer emission. In general these approximations complicate the overall radiative transfer scheme, particularly the calculation of analytic derivatives, and have a rather significant timing penalty compared to more exact treatments using more layers.

The new vertical grid is given in Table 39.

Table 39: Pressure levels for 101 level vertical grid.

Level	p(mb)	Level	p(mb)	Level	p(mb)	Level	p(mb)
1	4.9999E-03	2	1.61E-02	3	3.84E-02	4	7.68998E-02
5	0.137	6	0.2244	7	0.3454	8	0.5064
9	0.714	10	0.9753	11	1.2972	12	1.6872
13	2.1526	14	2.7009	15	3.3398	16	4.077
17	4.9204	18	5.8776	19	6.9567	20	8.1655
21	9.5119	22	11.004	23	12.649	24	14.456
25	16.432	26	18.585	27	20.922	28	23.453
29	26.183	30	29.121	31	32.274	32	35.650

Level	p(mb)	Level	p(mb)	Level	p(mb)	Level	p(mb)
33	39.257	34	43.1	35	47.188	36	51.528
37	56.126	38	60.989	39	66.125	40	71.54
41	77.24	42	83.231	43	89.52	44	96.114
45	103.02	46	110.24	47	117.78	48	125.65
49	133.85	50	142.38	51	151.27	52	160.5
53	170.08	54	180.02	55	190.32	56	200.99
57	212.03	58	223.44	59	235.23	60	247.41
61	259.97	62	272.92	63	286.26	64	300.
65	314.14	66	328.67	67	343.62	68	358.97
69	374.72	70	390.89	71	407.47	72	424.47
73	441.88	74	459.71	75	477.96	76	496.63
77	515.72	78	535.23	79	555.17	80	575.53
81	596.31	82	617.51	83	639.14	84	661.19
85	683.67	86	706.57	87	729.89	88	753.63
89	777.79	90	802.37	91	827.37	92	852.79
93	878.62	94	904.87	95	931.52	96	958.59
97	986.07	98	1014.0	99	1042.2	100	1070.9
101	1100.	-	-	-	-	-	-

F.3.2: Impact of Temperature Interpolation

In the old version of OSS the temperature dependence of the molecular absorption for fixed and variable gases was modeled by storing the layer absorption data at 10 temperatures and by linearly interpolating to the actual layer temperature. The 10 temperature entries were evenly spaced with a difference of 10 K between adjacent entries, thus spanning a temperature range of 90 K. This range was centered on the US Standard profile. However, this choice of temperatures is clearly not optimal for some types of temperature profiles, as illustrated in Figure 152. Further, linear interpolation can result in large errors if the profile falls out of the range of the temperature node points.

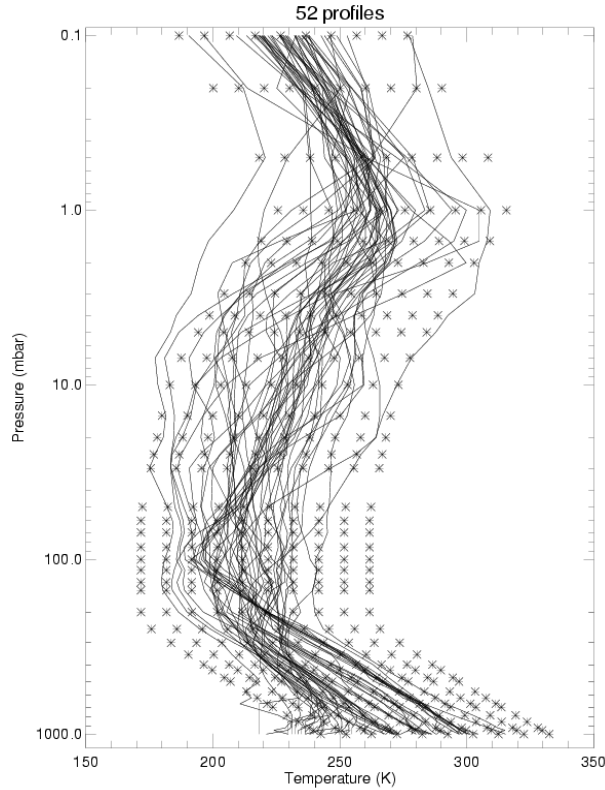


Figure 152: The OSS absorption coefficient temperature grid (*) superimposed on the set of 52 ECMWF standard temperature profiles.

The main driver behind the choice of the linear interpolation over higher order interpolation scheme was computational speed. However, this simple interpolation requires from 20 to 40 entries in order to bring numerical errors below 0.05 K, which would translate in an increase by a factor 2 to 4 in the size of the absorption table. Instead, in order to keep the table size below 100 Mbytes for a CrIS-like instrument, it has been decided to maintain 10 entries but adopt a 3-point Lagrange interpolation scheme (at the expense of computational time). The quadratic interpolation scheme used in the new OSS model for the function $f(i)$ defined on the set of points $x_i (i = 1, \dots, nT)$ follows the well-known Lagrange formula:

$$f(x) = f_{i-1} \frac{(x - x_i)(x - x_{i+1})}{(x_{i-1} - x_i)(x_{i-1} - x_{i+1})} + f_i \frac{(x - x_{i-1})(x - x_{i+1})}{(x_i - x_{i-1})(x_i - x_{i+1})} + f_{i+1} \frac{(x - x_{i-1})(x - x_i)}{(x_{i+1} - x_{i-1})(x_{i+1} - x_i)}$$

where x is within the interval $x_{i-1} < x < x_{i+1}$. Note that for $x < x_1$ or $x > x_n$, the function is extrapolated using the weights computed for $\{x_1, x_2, x_3\}$ and $\{x_{n-2}, x_{n-1}, x_n\}$, respectively. Note that in the new implementation, the index i is incremented when $x > \frac{(x_i + x_{i+1})}{2}$ and the resulting function displays a discontinuity at this point. However, unlike the linear interpolation, this scheme produces continuous first derivatives.

Figure 153 shows the brightness temperature errors incurred by reverting to the original interpolation scheme. Temperature interpolation errors with the linear scheme are of the same sign. Exceptions to that rule are due to profiles that fall out of the range of the tables. The profile with the largest error (with the linear interpolation scheme) corresponds to the coldest profile shown in Figure 152. By comparison, the higher order interpolation scheme is more robust with respect to out of range profiles (see Figure 151), although these profiles are responsible for the largest errors observed in the 741-742 cm^{-1} region.

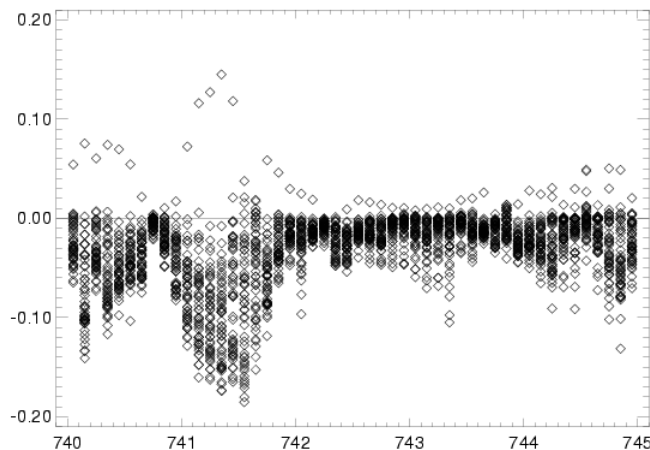


Figure 153: Brightness temperature differences between linear interpolation and the 3-point Lagrange interpolation.

F.3.3: Treatment of Absorption Coefficients

The infrared OSS model uses dry gas absorption data stored as a function of temperature only. In general, the computation of the pressure broadened half-width (α) for each molecule considers the self and foreign-broadening:

$$\alpha_m = (P - e_m)\alpha_m^f + e_m\alpha_m^s$$

where P is the total pressure, e is the partial pressure of the molecule (m) considered, and α is the half-width due to foreign or self-broadening effects. The impact of self-broadening is generally small, except for water vapor (see below), and is not explicitly treated in either LBLRTM or OSS, although it is included to some extent in the line halfwidth on the HITRAN spectroscopic database (used as input to LBLRTM). The small dependence of the dry gas optical depth on water vapor originates solely from the variations in the number of broadening molecules (w_{broad}) with water concentration:

$$w_{broad} = w_{total} - w_m = \frac{N_A}{M_{dryair}} \left[u_{total} - u_{water} \left(1 - \frac{M_{dryair}}{M_{water}} \right) \right]$$

where w is the molecular column amount (molecules cm^{-2}), N_A is Avogadro's number, M is the molecular mass, and u is the column mass (g cm^{-2}).

The treatment of the line broadening for water vapor is consistent with that of other molecules. However, for water vapor the self-broadened component is significant and cannot be neglected. In the old version of the OSS model water vapor optical depths were computed from the absorption coefficients of the self-broadened continuum and of the combined foreign-broadened continuum and spectral lines, with both stored as a function of temperature:

$$k_{water}(T) = k_{water}^{foreign+lines}(T) + k_{water}^{self}(T)$$

This approach neglects the influence of water vapor on the foreign broadened continuum and the line width. In order to quantify the impact of this approximation and improve the accuracy of the model, we compared this scheme with one in which the water vapor absorption is derived by linear interpolation from the total absorption coefficients (continuum and lines) for water vapor stored at two water vapor concentrations (for a dry and wet atmosphere):

$$k_{water} = aq_{water} + b$$

This new scheme is exact in the limit in which the absorption coefficient depends linearly on specific humidity. It is valid in the far wing but breaks down near the line center because of the non-linear relationship between line absorption and width. However, because the overall line strength remains unchanged, the error introduced quickly averages out to zero when integrated over the instrument line width (which is much wider than the spectral line width).

The accuracy of the old and new schemes is shown in Figure 155 and Figure 156, respectively for a boxcar filter of 0.1cm^{-1} in width (Figure 154 is provided as reference). As expected from the above discussion the largest residual errors are concentrated in the vicinity of the line centers. In the case shown here the maximum error is 0.05 K at 0.1 cm^{-1} spectral resolution. For an instrument with broader spectral resolution the error is less. Note that the spectral averaging to broader instrument line width is not done explicitly in OSS. However, the smaller contribution of line features to average radiances should be reflected in the weights so that errors decrease accordingly with increasing instrument line width.

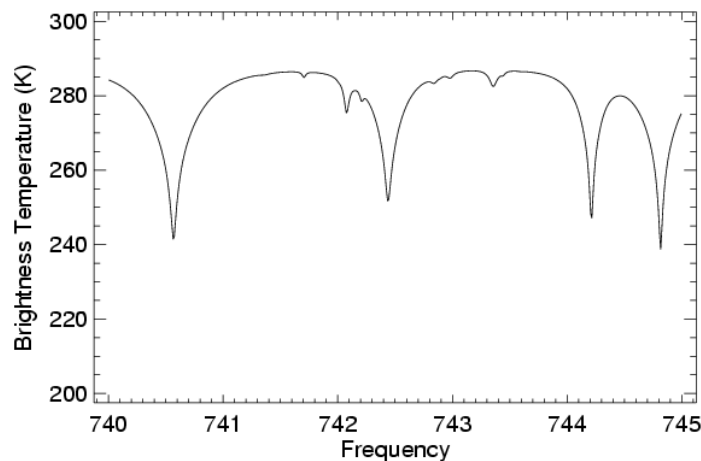


Figure 154: Sample spectral region for test.

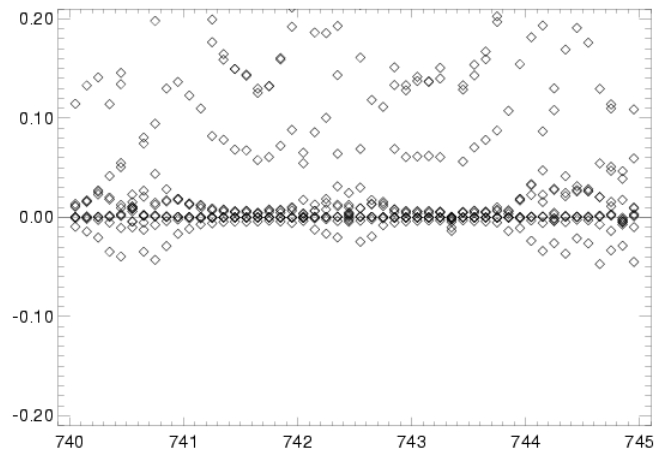


Figure 155: Brightness temperature errors for the "old" treatment of water vapor absorption. Note that for this test water was the sole absorber.

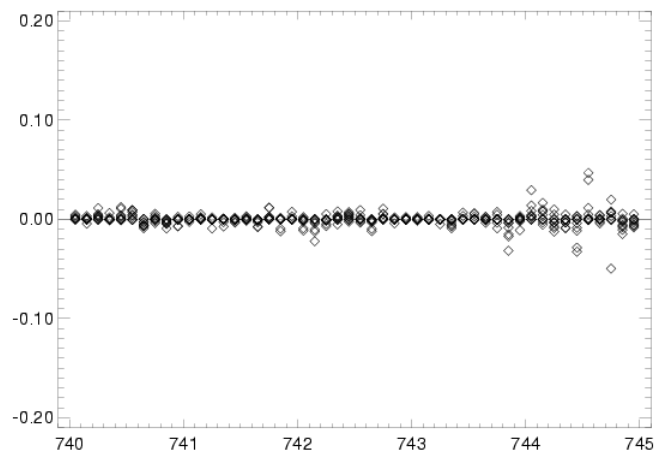


Figure 156: Brightness temperature errors for the "new" treatment of water vapor absorption. Note that for this test water was the sole absorber.

The input profile for OSS is defined as amounts at specific levels in the atmosphere. The model then converts these level amounts to layer amounts by vertically integrating the profile. The “old” version of the model neglects the impact of water on the total air mass. Further, for the fixed gases the OSS tables were stored directly as optical depth and neglected the contribution of water vapor to the total air mass within a layer. The errors due to this approximation are shown in Figure 157.

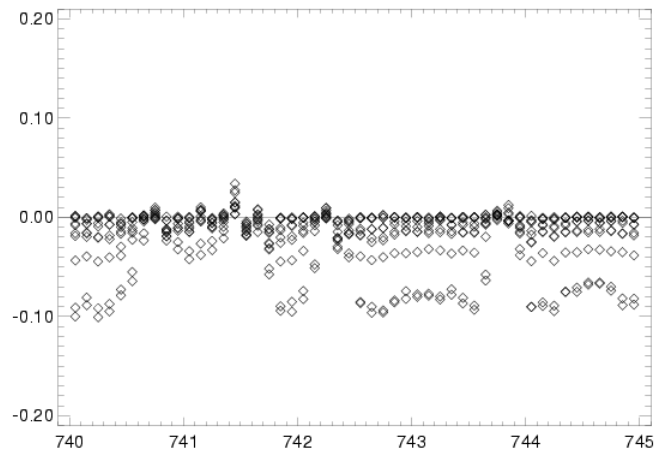


Figure 157: Error obtained when assuming that fixed gases optical depth does not vary with water vapor concentration.

For the “new” version of OSS the fixed gases are stored as absorption coefficients (instead of optical depth) for a reference profile amount:

$$\bar{k}_{fix} = \frac{\sum_{m-fixed-gases} \tau_m^{ref}}{\sum_{m-fixed-gases} u_m^{ref}} = \frac{\sum_{m-fixed-gases} \tau_m^{ref}}{\bar{u}_{fix}^{ref}}$$

For calculations, the fixed gas amount for a layer is then computed from the mixing ratio of the fixed gases, scaled by the new dry air amount:

$$k_{fix} = \bar{k}_{fix} u_{fix} = \bar{k}_{fix} \left(\frac{\bar{u}_{fix}^{ref}}{u_{dry}^{ref}} u_{dry} \right)$$

where u_{dry} is computed by accounting for the moisture present within the layer:

$$u_{dry} = \frac{\Delta P}{g} - u_{water}$$

The impact of the new treatment of fixed gases is shown in Figure 158. As expected, the spectral regions that are most affected by the original approximation are regions in between strong absorption lines that sense the troposphere. The profile used for computing is fairly dry. Therefore, the largest errors correspond to profiles with highest moisture content.

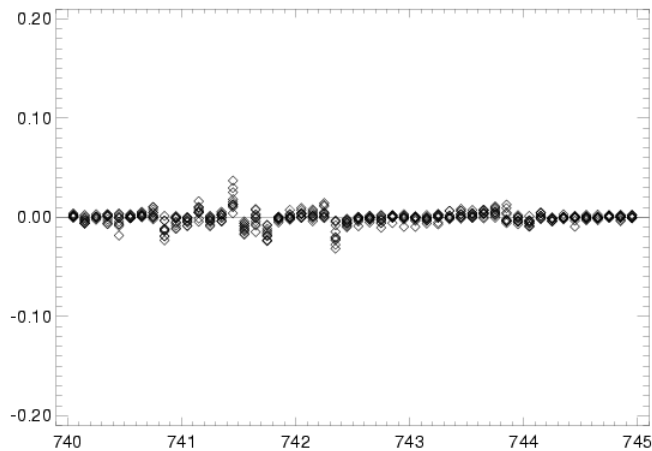


Figure 158: Error obtained when accounting for the impact of water vapor concentration on the fixed gases optical depth.

The above discussion has centered on the fixed gases. However, the new version of OSS treats both fixed and variable species in the same manner. Thus the subscript “fix” in the above equations can be replaced with a single gas name, and there is no longer a summation over all variable gases (each variable gas is stored individually).

F.3.4: Additional Changes to the Radiative Transfer

Some additional changes were made to the radiative transfer in order to increase the overall accuracy of the calculations:

- The model no longer neglects the temperature dependence of the absorption coefficient in the computation of temperature derivatives.
- In order to remain consistent with the new treatment of water vapor, the water vapor Jacobians are computed at constant air mass.

- The Planck function is computed for the actual layer temperature at 10 cm^{-1} intervals and linearly interpolated in wavenumber across the interval. This is faster than the use of a look-up table and interpolation scheme and does not require additional memory for storage of the table data.
- The OSS tables have been restructured so that the model loops over frequency nodes and then applies the weights, thus eliminating the redundant calculation of nodes that fall within the bounds of multiple channels. This is particularly advantageous for channel response functions that extend over a wide bandpass.
- The OSS tables now include molecular absorption by CFC-11, CFC-12, CCl_4 and HNO_3 .

F.4: OSS Node Selection and Validation

Given the changes to the radiative transfer code listed above, the OSS nodes and weights previously derived for the CrIS channels are no longer valid. This section discusses the selection and validation of OSS nodes using the new radiative transfer grid. Note that we provide new channel lineshape functions for the Hamming and Blackman apodizations (as described in technical memo P1197-TM-003-01-04). The reason for this is that the previous implementation of the CrIMSS algorithm considered only a finite spectral width for these apodizations, while the sinc-function (channels resulting from an un-apodized interferogram) extended throughout the band. A more realistic implementation of the Hamming and Blackman apodizations is to extend them to the full bandwidth. In this case, as for the sinc-function, the channel shape goes to zero at the edge of the band.

The OSS node selection begins with the calculation of total layer optical depth for a set of training atmospheres. The training set consists of 52 atmospheres and 5 view angles (where the atmospheres are shown in Figure 152). The optical depths are then combined by the radiative transfer module to construct monochromatic radiances for a range of view angles for use during

the node selection process. The monochromatic radiances are integrated over the sensor lineshape function to produce the “true” channel radiance against which the OSS selection regression is performed. The selection process adds frequency nodes until the error is minimized to within the threshold value. For the CrIMSS training we have set this threshold at 0.05K in RMS brightness temperature.

Validation of the OSS selection is performed in two different ways: comparison of the selection values using the training optical depths versus the training radiances, and comparison of the selection values using the OSS optical depth tables versus the training radiances. The former comparison ensures that the OSS selection is performed to within threshold values while the latter describes the overall error inherent in the system. Both types of validation results for each of the three CrIS apodization types indicate that we exceed this threshold in all cases.

The number of points selected for each of the lineshape functions is shown in Figure 159– Figure 163.

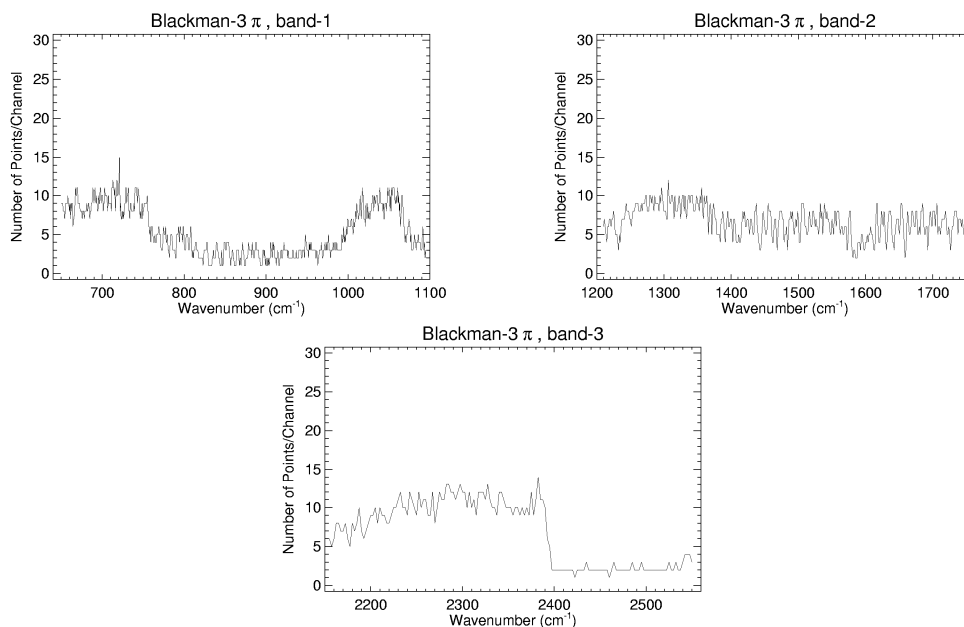


Figure 159: Number of points selected for finite-width Blackman apodization.

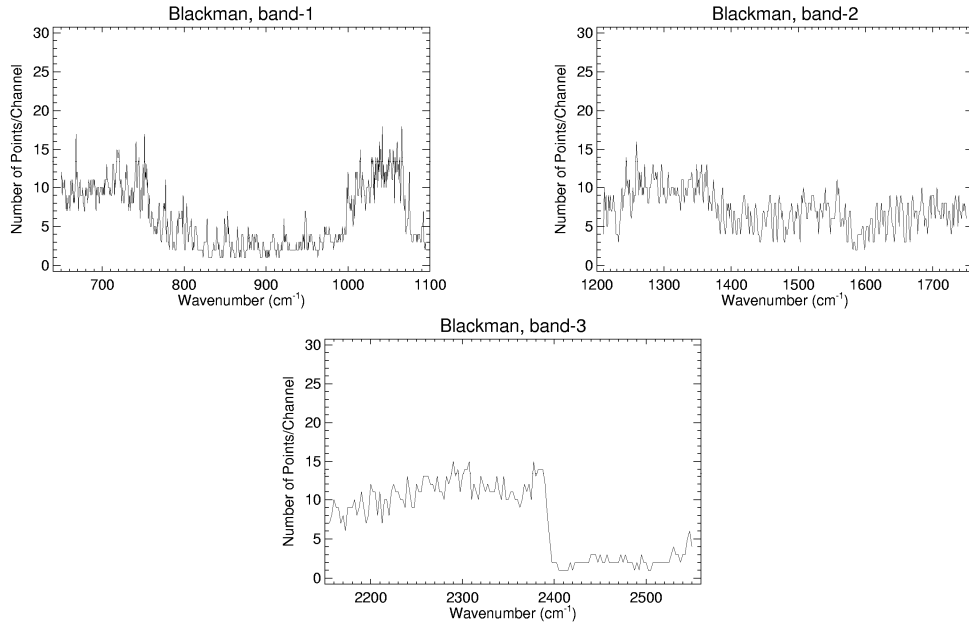


Figure 160: Number of points selected for Blackman apodization extending to the edges of the band.

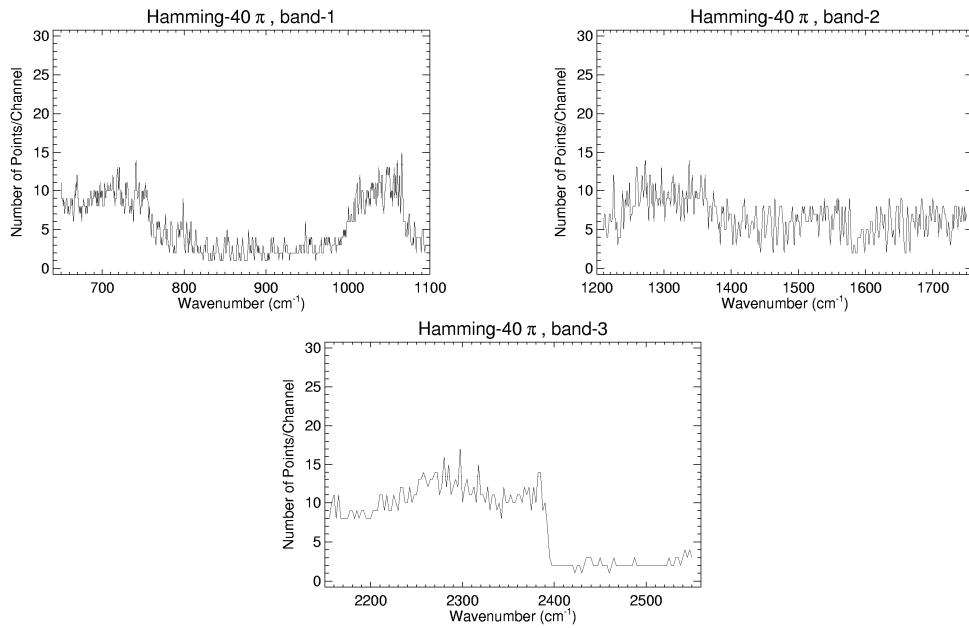


Figure 161: Number of points selected for finite-width Hamming apodization.

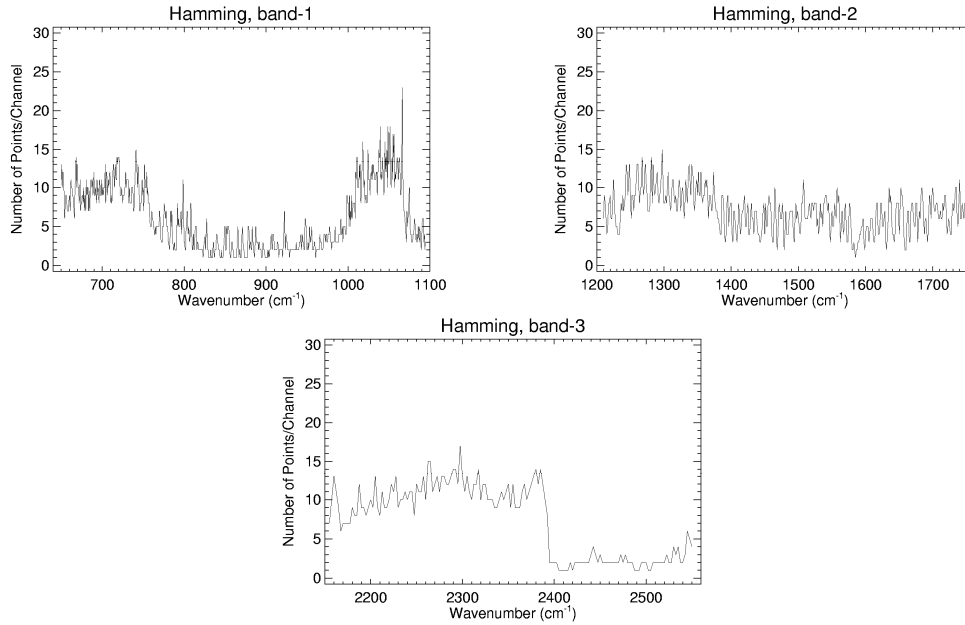


Figure 162: Number of points selected for Hamming apodization extending to the edges of the band.

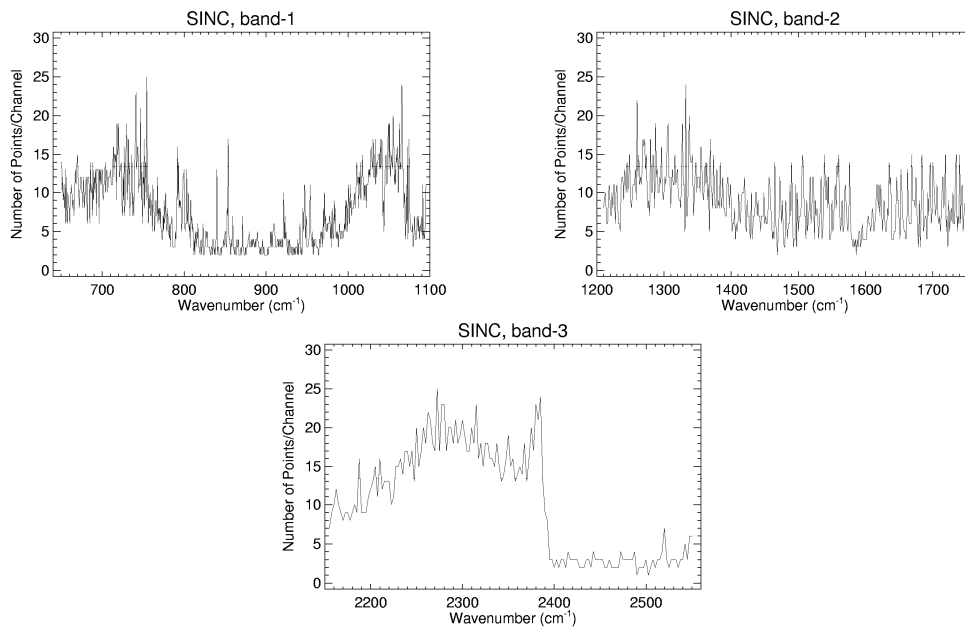


Figure 163: Number of points selected for sinc-function ILS extending to the edges of the band.

Results of the dependent validation, a comparison of the OSS node selection with the computed radiances, are given in Figure 164– Figure 168. A threshold RMS value of 0.05K was set for the difference between the monochromatic radiances integrated over the channel response function and the OSS selection.

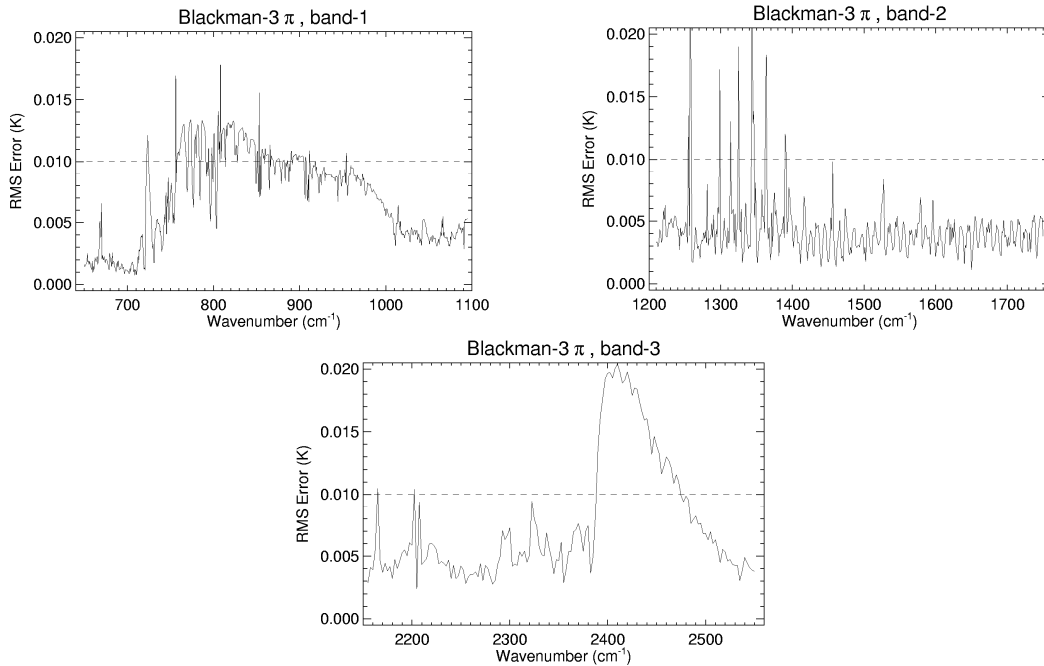


Figure 164: Dependent validation of OSS node selection for finite-width Blackman apodization.

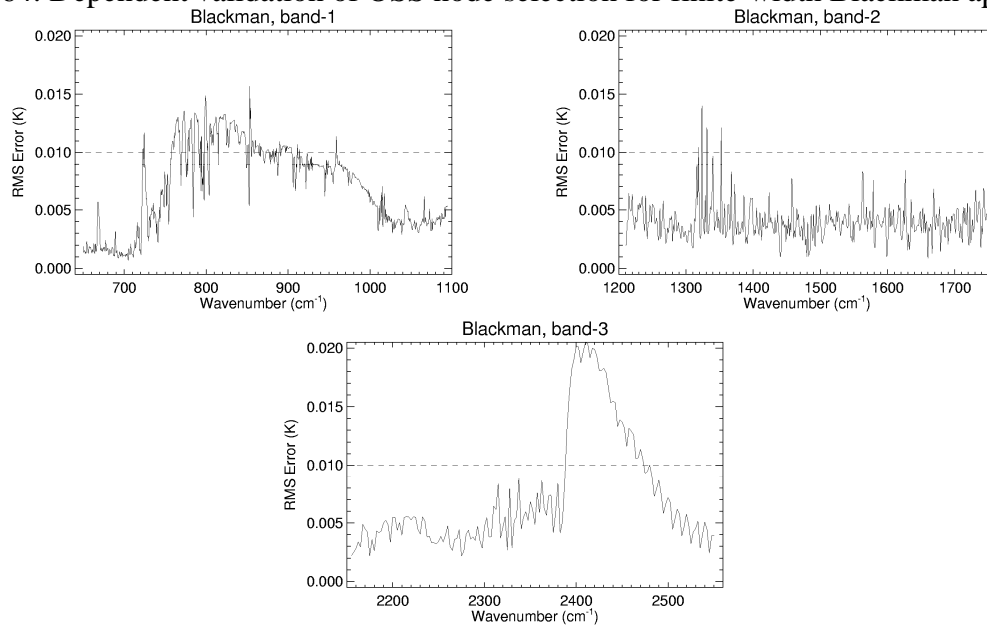


Figure 165: Dependent validation of OSS node selection for Blackman apodization extending to the edges of the band.

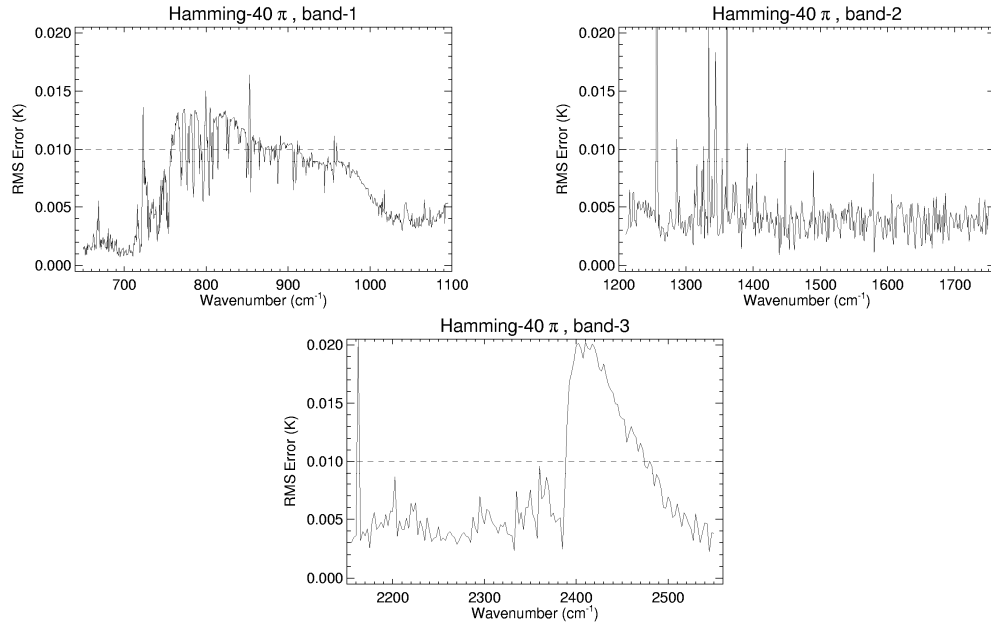


Figure 166: Dependent validation of OSS node selection for finite-width Hamming apodization.

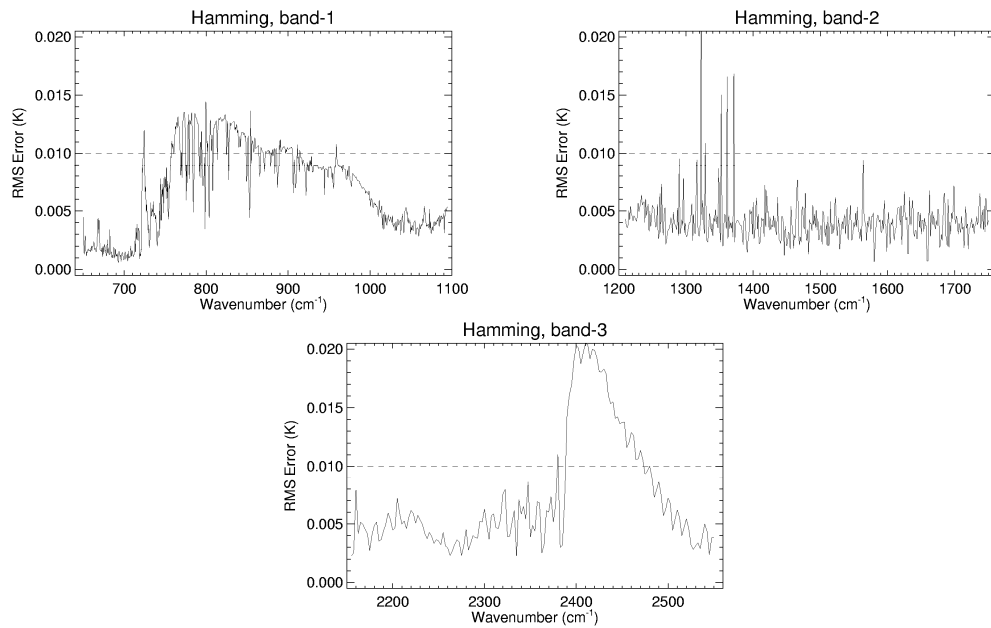


Figure 167: Dependent validation of OSS node selection for Hamming apodization extending to the edges of the band.

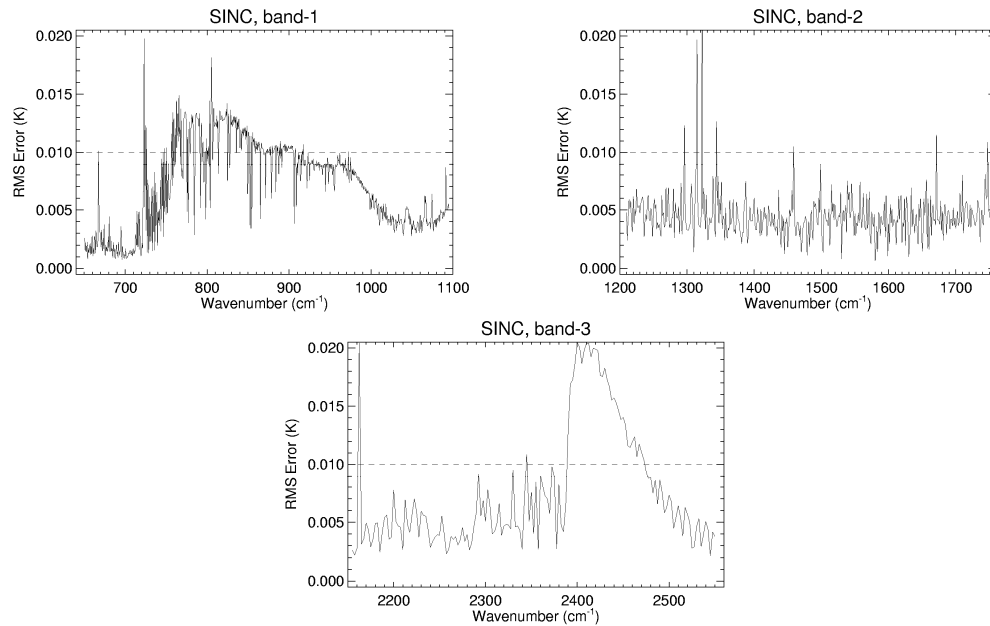


Figure 168: Dependent validation of OSS node selection for sinc-function ILS.

In addition to confirming that the OSS selection results in radiance differences below the threshold value, an additional independent validation was performed. For this case the final OSS optical depth tables were used to construct radiances for comparison with monochromatic radiances integrated over the channel bandpass. The results are shown in Figure 169– Figure 171. This test confirms that the RMS error is somewhat larger than the training error, but still reasonable compared to other noise sources.

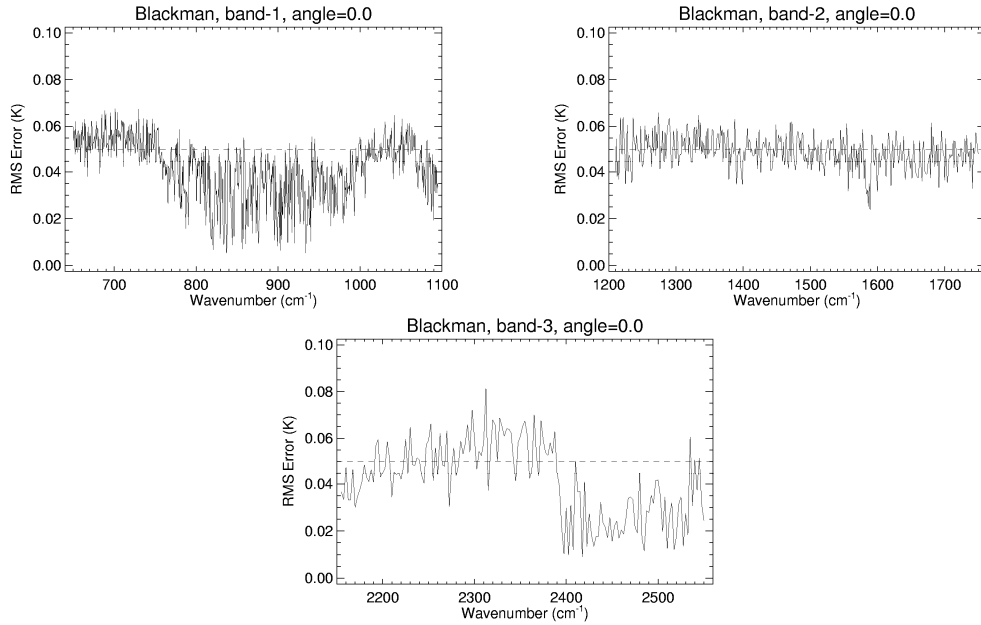


Figure 169: Independent validation of OSS node selection for Blackman apodization extending to the edges of the band.

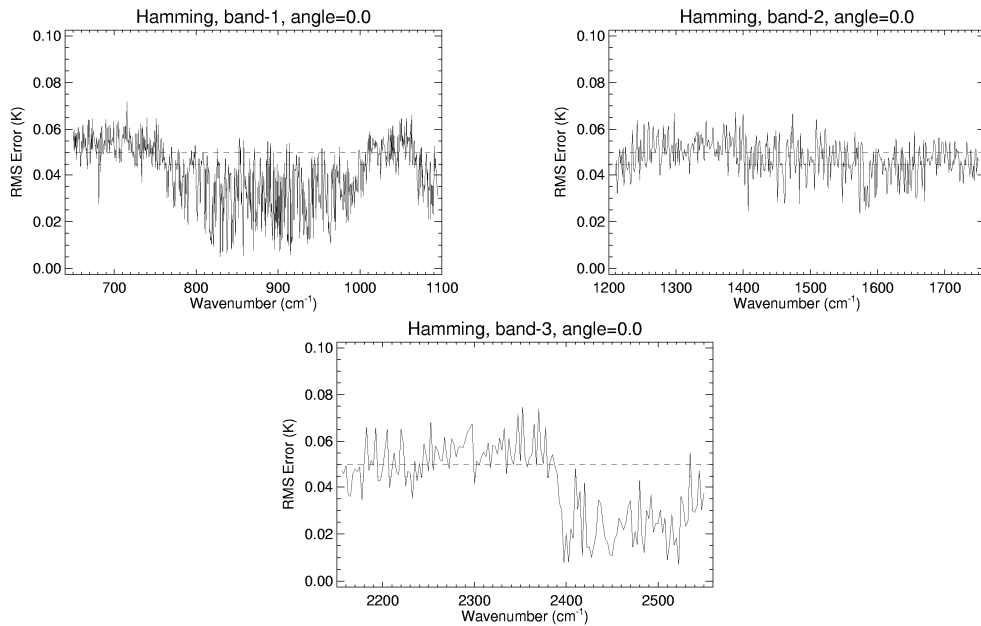


Figure 170: Independent validation of OSS node selection for Hamming apodization extending to the edges of the band.

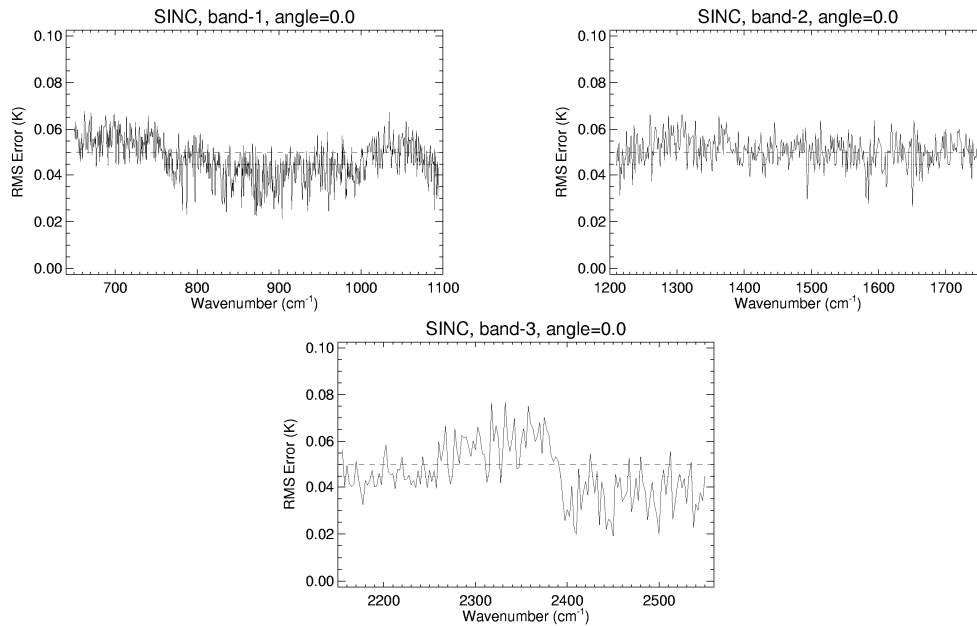


Figure 171: Independent validation of OSS node selection for sinc-function ILS.

F.5: Changes in Retrieval Results Due to RT Changes

In addition to examining differences in the OSS model (radiance, node selection, and training), an important part of validation process is to examine the overall impact on the CrIMSS EDR retrieval algorithm. Differences must be examined in the context of radiances and final EDR results. When comparing EDR results one must be careful to ensure that differences between the two cases are minimized. For example, because the code has been somewhat restructured, and the CrIS channel frequency file has been reduced to only those channels actually measured by the sensor, the noise added to the simulated radiances must be saved in an external file to be certain that both sets of radiances (100 layer and 39 layer) have exactly the same noise added.

Radiance differences between the 40 level and 101 level models occur for a variety of reasons. The difference in the placement of layers will impact the radiance observed at the top of the atmosphere. Another source of differences is the inclusion of additional molecular species in the 101 level model, namely HNO₃, CFC-11, CFC-12, and CCl₄.

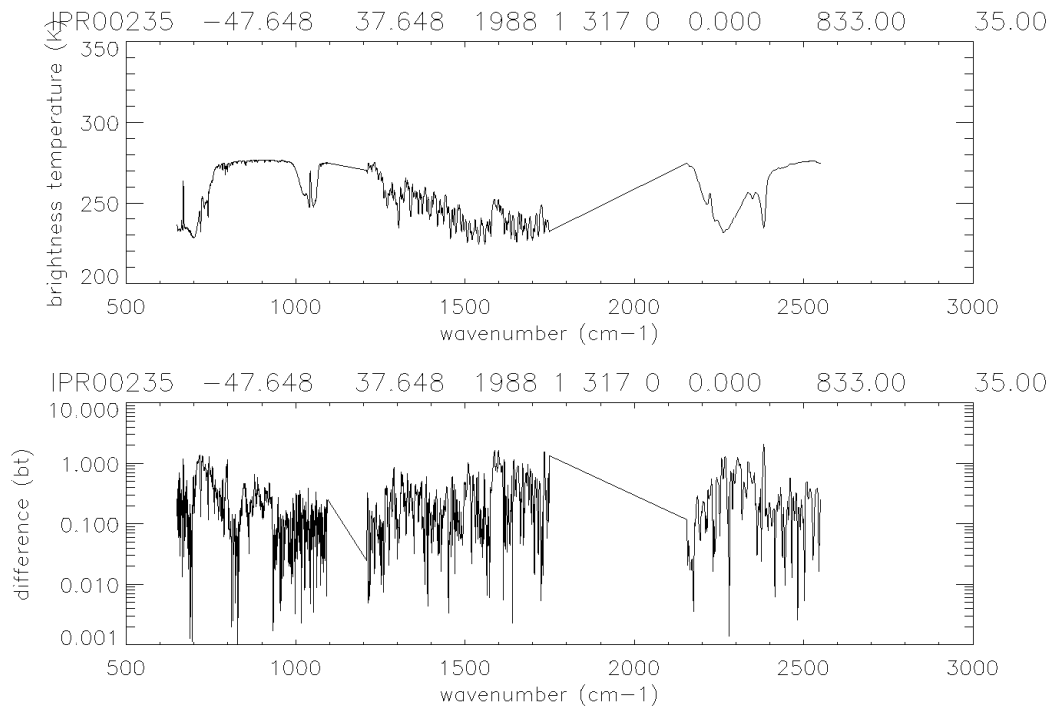


Figure 172: The top plot shows the brightness temperature and the bottom plot shows the radiometric differences (given in units of brightness temperature, K) between the 40-level model and the 101-level model for a single atmospheric profile.

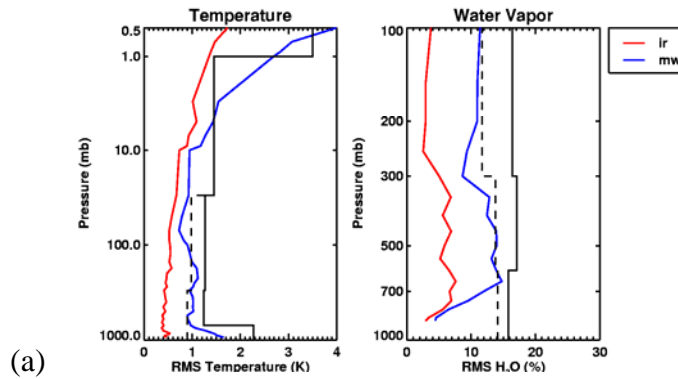
Comparisons of the actual EDR retrieval results are shown in Figure 173– Figure 174 for ocean and land scenes. *Differences are to be expected because the 101-level model contains more robust layering and more realistic physics than the 40-level model; the 101-level model provides a more accurate representation of the retrieval results that should be expected when the algorithm is applied to real data.* The resulting differences are generally small, except at the upper pressure levels, above about 10 mb. There are some additional factors that have not been considered that may contribute to the performance degradation (closer examination of these effects may also change the retrieval results):

- Most of the information above 10 mb is contained in the atmospheric covariance matrix. It is possible that the covariance used for these tests is not optimal compared to that used for the 40-level test.

- The retrieval is performed on empirical orthogonal functions (EOFs) rather than geophysical quantities. The number of EOFs was optimized for 40-levels. It is possible that the current number of EOFs does not capture the increased atmospheric structure present with the 101-level model.
- The convergence criteria and other tuning parameters were optimized for the 40-level model. Re-optimization may be required for the increased number of levels.

RMS Table (ChiSq: 1)
 (Fri Jan 30 09:10:52 2004)
 #Samples = 200 200
 Truth Files:
 run/cld0fov1/ocean/simtruth.scene.nc
 run/cld0fov1/ocean/simtruth.scene.nc
 Notes:
 RMS file: rms.ps
 100.000% 99.0000%

Tskin (K)	0.302788	2.10263
Pafc (mb)	0.00000	0.00000
Cloud Top (mb)	109.789	111.369
Cloud Thickness (mb)	0.00000	0.00000
Cloud H ₂ O(kg m ⁻³)	0.0138550	0.0237813
TPW (mm)	0.406164	0.696140
Lower Trop. Temp. (K)	0.272557	1.25859
Lower Trop. H ₂ O(g kg ⁻¹)	0.203944	0.363643



RMS Table (ChiSq: 1)
 (Fri Jan 30 11:07:47 2004)
 #Samples = 200 200
 Truth Files:
 run/cld0fov1/ocean/simtruth.scene.nc
 run/cld0fov1/ocean/simtruth.scene.nc
 Notes:
 RMS file: rms.ps
 100.000% 99.5000%

Tskin (K)	0.296682	2.11157
Pafc (mb)	0.00000	0.00000
Cloud Top (mb)	114.724	117.365
Cloud Thickness (mb)	1.26163	0.00000
Cloud H ₂ O(kg m ⁻³)	0.0156936	0.0241785
TPW (mm)	0.378995	0.525205
Lower Trop. Temp. (K)	0.353177	1.40749
Lower Trop. H ₂ O(g kg ⁻¹)	0.284440	0.473602

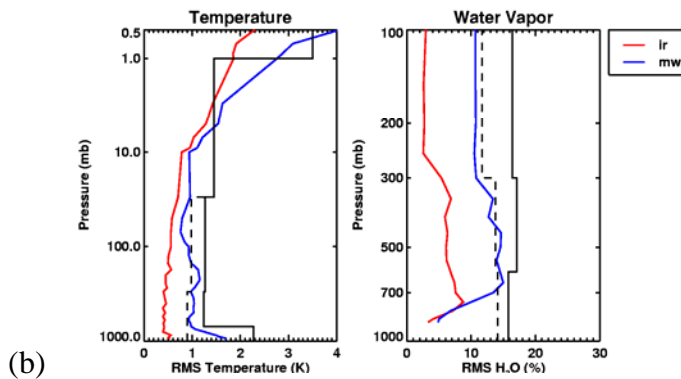
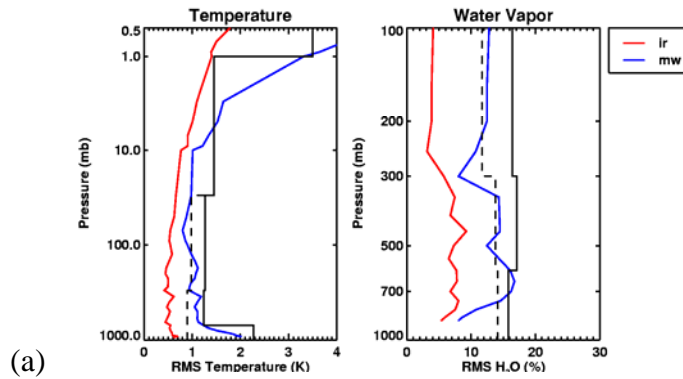


Figure 173: Ocean scenes: (a) 40-level retrieval results and (b) 101-level retrieval results.

RMS Table (ChiSq: 1)
 (Fri Jan 30 09:54:23 2004)
 #Samples = 200 200
 Truth Files:
 run/cld0fov1/land/simtruth.scene.nc
 run/cld0fov1/land/simtruth.scene.nc
 Notes:
 RMS file: rms.ps
 100.000% 98.5000%

Tskin (K)	0.241479	1.77389
Pafc (mb)	0.00000	0.00000
Cloud Top (mb)	120.096	116.711
Cloud Thickness (mb)	0.00000	0.00000
Cloud H ₂ O(kg m ⁻³)	0.0178073	0.0311191
TPW (mm)	0.602889	1.47486
Lower Trop. Temp. (K)	0.400075	1.67149
Lower Trop. H ₂ O(g kg ⁻¹)	0.303148	0.486735



RMS Table (ChiSq: 1)
 (Fri Jan 30 12:36:36 2004)
 #Samples = 200 200
 Truth Files:
 run/cld0fov1/land/simtruth.scene.nc
 run/cld0fov1/land/simtruth.scene.nc
 Notes:
 RMS file: rms.ps
 89.5000% 98.5000%

Tskin (K)	0.290031	2.14024
Pafc (mb)	15.0709	13.4397
Cloud Top (mb)	133.551	122.958
Cloud Thickness (mb)	5.00000	0.00000
Cloud H ₂ O(kg m ⁻³)	0.0208385	0.0302178
TPW (mm)	0.981897	1.49388
Lower Trop. Temp. (K)	0.772010	1.81521
Lower Trop. H ₂ O(g kg ⁻¹)	0.411974	0.526801

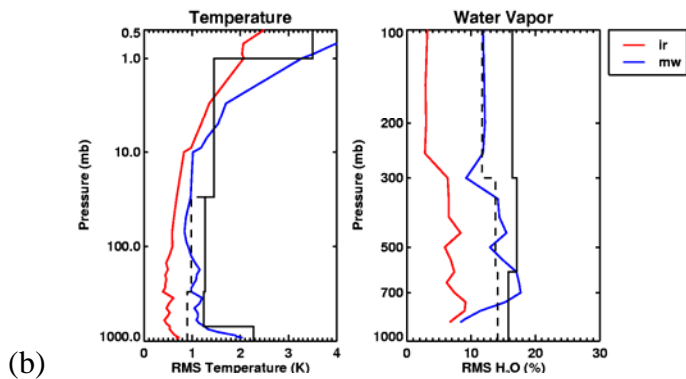


Figure 174: Land scenes: (a) 40-level retrieval results and (b) 101-level retrieval results.

F.6: Changes to Algorithm Computational Time

Estimates of the overall timing impact are best described on a per-iteration basis. This eliminates a number of initialization processes that only occur at the beginning of the program and helps to mitigate the impact of other computer processes on the timing estimate. It should be noted that even though the number of levels has increased, the changes made to the form and content of the OSS input files result in an overall decrease in the database load time at the beginning of the program.

Increasing the number of levels and improving the radiative transfer algorithm is expected to impact the algorithm run-time in a non-linear fashion. Two areas that contribute significantly to the overall execution time are as follows:

- Mapping from geophysical-space (profiles) to retrieval-space (eigenvectors) requires a larger matrix for the profiles even though the number of retrieval parameters is unchanged. This will increase the computation time.
- Calculation of molecular amounts, transmittances and radiances is now done for more vertical layers and will increase the overall time. However, taking advantage of redundant spectral points among channels has compensated for some of this increase.

Timing estimates were conducted on an SGI computer. *Note that this computer is several years old and rather slow – the timing results should be considered in a relative sense rather than looking at the absolute time for the run.* The two versions of the retrieval algorithm (V3.0 and V4.0) were run simultaneously for 25 profiles and the timing was computed using the system timing command (“dtime”). Care was taken to ensure that the number of CrIS spectral channels is the same for both cases.

The overall result is that the 101-level algorithm is approximately a factor of three slower than the 40-level algorithm (1.216 seconds/iteration for 101 levels; 0.419 seconds/iteration for 40

levels). Considering that there are about 2.5 times more layers in the new code, this is a very favorable result.

APPENDIX G: Mitigation against Detector Failure

This Appendix describes the modifications made to the CrIMSS code to make the code robust to detector failure in the CrIS instrument.

G.1: Description of Changes

The CrIS instrument is comprised of 27 detectors representing 3 bands and 9 fields of view. In the event that one of these detectors should fail, the CrIMSS algorithm is required to operate with limited impact to performance. Should multiple detectors fail, the algorithm should continue to operate with graceful degradation. The CrIMSS algorithm has been designed to address detector failure and the performance in the event of single detector failure has been evaluated based on a globally representative dataset.

Section 5.4 described the modes of operation for the algorithm. These modes are identified by the namelist variable “iClsMode”. When iClsMode = 1, the algorithm is designed to approach the NPOESS cell size requirements. Under clear conditions, retrievals are performed for every FOV. If the FOR is cloudy, then retrievals are reported for four clusters based on a subset of FOVs provided there is sufficient information available for cloud clearing; otherwise a single retrieval is reported for the FOR. For overcast FORs, one retrieval is reported based on channels that are unaffected by the cloud. When iClsMode=3, a single retrieval is reported for the FOR under all cloud conditions.

The state of the CrIS detectors should be updated for each granule and included with the SDRs. This information is represented in the CrIMSS algorithm as a detector quality flag with 27 elements. A value of 1 indicates that the detector is operating properly while a value of 0 is used to indicate that the detector has failed. Currently, this information is provided via the namelist

variable “detectorQF”. The first nine elements describe the status of the detectors contributing to band 1, the next nine to band 2, and the last nine to band 3. The detector quality is queried prior to processing each granule. There is no provision in the algorithm to monitor for detector failures on an FOR-by-FOR basis.

The consequence of detector failure is dependent on the bands that are impacted. Temperature and surface information are included through bands 1 and 3, while band 2 provides information about water vapor. Band 1 is critical for retrieval success because it is used for cloud layer identification and to provide the ranking the FOVs from warm to cold (i.e., clearest to cloudiest) used by the cloud clearing module. Cloud clearing channels from both band 1 and band 3 are used to evaluate cloud contrast and in the cloud clearing module. However, in the event that band 3 is not available, these steps can be adequately addressed using band 1 only.

Various strategies were considered for addressing detector failures. One solution is to eliminate any FOV impacted by a detector outage. However, in some instances this can result in a loss of information that could otherwise contribute to the retrieval. For example, under clear conditions single FOV retrievals are performed for iClssMode=1. If any of the 3 bands were not available in this case, the information in the remaining bands could still contribute to the retrieval when combined with the microwave. Alternatively, in the case when band 3 is impacted, it is possible to proceed with the retrieval using the information from band 1 and 2 only.

Clear

Cloudy (Option A)

Cloudy (Option B)

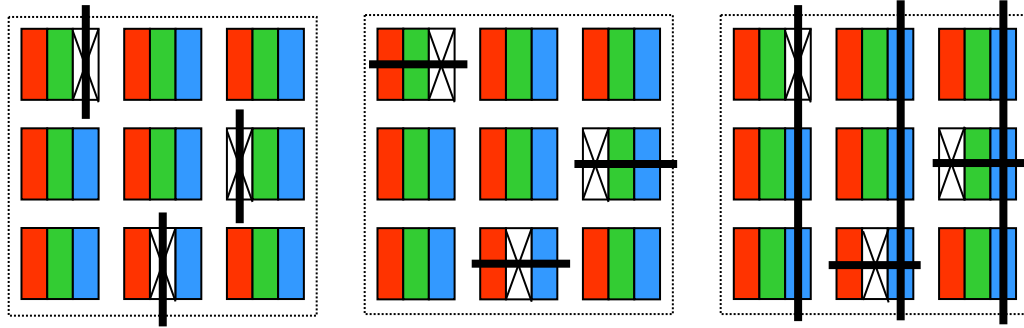


Figure 175: Left. In clear or overcast conditions, retrievals are based on the average of available information for all FOVs. Middle. Option A for cloudy conditions eliminates any FOV impacted by detector failure. Right. Option B for cloudy conditions eliminates FOVs that are impacted by failures in bands 1 or 2 and eliminates band 3 for all FOVs if a failure occurs in that band.

The strategy adopted for addressing detector failure is illustrated in Figure 175.

In clear conditions, for $iClssMode=1$, retrievals are performed based on the available information in each FOV. If in a given FOV, all bands are missing, then no retrieval is reported. For $iClssMode=3$, the retrieval is based on the average of channels for all available FOVs within the FOR.

In overcast conditions, retrievals are based on microwave only and not impacted by CrIS detector failure.

In cloudy conditions, FOVs impacted by band 1 or 2 detector failure are not used. For $iClssMode=1$ retrievals are reported for 4 clusters within the FOR provided the number of cloud formations within the FOR does not exceed 3 minus the number of FOVs impacted by detector failure. For example, if one FOV is unavailable because the detector corresponding to band 2 has failed then the retrievals are reported for 4 clusters only if the number of cloud formations is 2 or less, otherwise a single retrieval is reported for the FOR. If 3 or more FOVs are affected then a single retrieval is always reported for the FOR. Two options are available in the event of a detector failure in band 3. Option A is to eliminate the FOV as described above. Option B is to

omit band 3 from the retrieval and proceed using information from bands 1 and 2 only. This approach is justified by the fact that bands 1 and 2 together provide much of the temperature and moisture information required for the retrieval.

The scene classification procedure has been adapted to handle detector failure as follows.

Each FOV is identified as clear or cloudy based on a comparison of the observed minus model radiance from the band 1 cloud clearing channels and the noise amplitude. If band 1 is not available then the assignment defaults to cloudy. The number of cloud layers within an FOR is determined based on those FOVs for which band 1 is available via the principle components analysis. Finally, the FOVs with valid band 1 data are identified and ranked based on the total radiance in the cloud clearing channels.

For $iClassMode=3$, the thermal contrast between the warmest- and coldest-ranked FOVs is evaluated. This calculation is based on the cloud-clearing channels in band 1 and band 3 (if available). FORs with little contrast and with fewer than 2 cloud formations are identified as clear if the number of FOVs identified as clear is greater than or equal to 4; otherwise the FOR is identified as overcast. If the contrast is high or more than 1 cloud formation has been identified, then the FOR is identified as cloudy. For cloudy FORs, any FOV impacted by detector failure is eliminated from the retrieval since the cloud clearing scheme does not apply to FOVs with incomplete band information.

For $iClassMode=1$, FOVs not impacted by detector failure are identified and ranked based on the total radiance from the band 1 cloud clearing channels. If no cloud formations are identified and at least 5 FOVs are identified as clear, then the FOR is deemed clear and retrievals are performed based on individual FOVs. In this case if no bands are available for any of the FOVs, then flags are set to specify no retrieval for this FOV. If no cloud formations are identified and fewer than 5 FOVs are identified as clear then the FOR is identified as overcast, and a single cluster is formed. The FOR is otherwise identified as cloudy. Four clusters are created if the number of cloud formations in the FOR plus the number of FOVs with failed detectors is less than 3; otherwise one cluster is formed. Within each cluster, the FOVs associated with the dominant

land type (i.e., land or ocean) are identified. If number of FOVs is less than the number of cloud formations then no retrieval is reported for this cluster. If at least two FOVs include information from band 1 then the cluster is analyzed to determine if it is clear, overcast, or cloudy. The determination that the cluster is clear or overcast is based on the results of the contrast test which is carried out using the cloud clearing channels of band 1 and band 3 (if available) and is based on the number of clear FOVs within the cluster. If fewer than 2 FOVS include information from band 1 then the cluster is identified as overcast. Clusters are identified as cloudy if the contrast is high. In that case, FOVs with incomplete band information are eliminated. If the band information is incomplete for all FOVs in the cluster, then the cluster is processed as though it was clear by averaging whatever information is available from the FOVs. Otherwise cloud-clearing is applied based on the FOVs ranked from warm to cold.

Several safeguards are included in the algorithm in order to ensure the functional performance of the algorithm in the event of substantial detector loss. Foremost of these is the requirement that band 1 be available for a minimum number of FOVs. This value is currently set to 4. If this requirement is not met, then the algorithm will terminate without producing any retrievals.

G.2: Performance Analysis

The impact of single detector failure affecting band 1, 2, and 3 has been evaluated for iClassMode=1 and 3 based on a globally representative dataset. The scene provided by NGST is identified as 010701_2130. The analysis of performance was based on layer-averaged temperature and moisture profile. The control case (all detectors active) was shown to be consistent with the NGST results. The impact of the detector failure was evaluated as a degradation in performance relative to this control case. The results were based on 9 instances of detector failure, i.e., band 1 FOV 1, 5, and 8, band 2 FOV 1, 5, and 8, and band 3 FOV 1, 5, and 8. The results are presented in the CrIMSS Detector Failure Task: Final Report (Document # P1198-PR-2005-10-14) and are summarized here. Unless otherwise stated, Option A method is used for handling partly cloudy cases (see Figure 175).

For $iClassMode=3$, the failure of a detector has minimal effect on the overall performance when the FOV impacted by the failure is omitted. The results are consistent with the small increase in noise owing to the elimination of one FOV. For those FORs identified as clear, there is a small degradation in performance when detector failure affects band 1. This error is attributed to the possible misclassification of FORs as clear which would otherwise be identified as cloudy if the band 1 detector had not failed. In the case when band 3 fails, the performance was also evaluated based on the alternate Option B scheme whereby band 3 is eliminated for the retrieval and results are obtained using bands 1 and 2 only (option B). The results indicate that retrievals performed without band 3 are significantly degraded relative to the baseline. Thus Option B is not recommended. Results showing the impact of single detector failure in band 1 are shown in Figure 176. Results for band 2 and 3 (with Option A) are similar. Results showing the impact of detector failure in band 3 based on the alternate scheme to eliminate the band (Option B) are shown in Figure 177.

The statistics for $iClassMode=1$ are not as straightforward. In this case, the occurrence of a detector failure can change how the scene is classified and therefore how the performance statistics are computed. In particular, the baseline case with all detectors active may report retrievals for 4 clusters in the FOR while the case with detector failure may result in the reporting of a single retrieval for the FOR. In this example, the performance with detector failure may be better than that reported for the 4 clusters. For this reason, the overall performance derived in this study based on option A is improved when detector failure impacts any of the bands. While not a definitive measure of the performance difference, the results do not imply any significant performance degradation owing to the detector failure. For those FORs, identified as clear, a small degradation in performance is identified when detector failure impacts bands 1 and 3 in particular. Results showing the impact of detector failure on band 1 are shown in Figure 178. Results for bands 2 and 3 (with Option A) are similar.

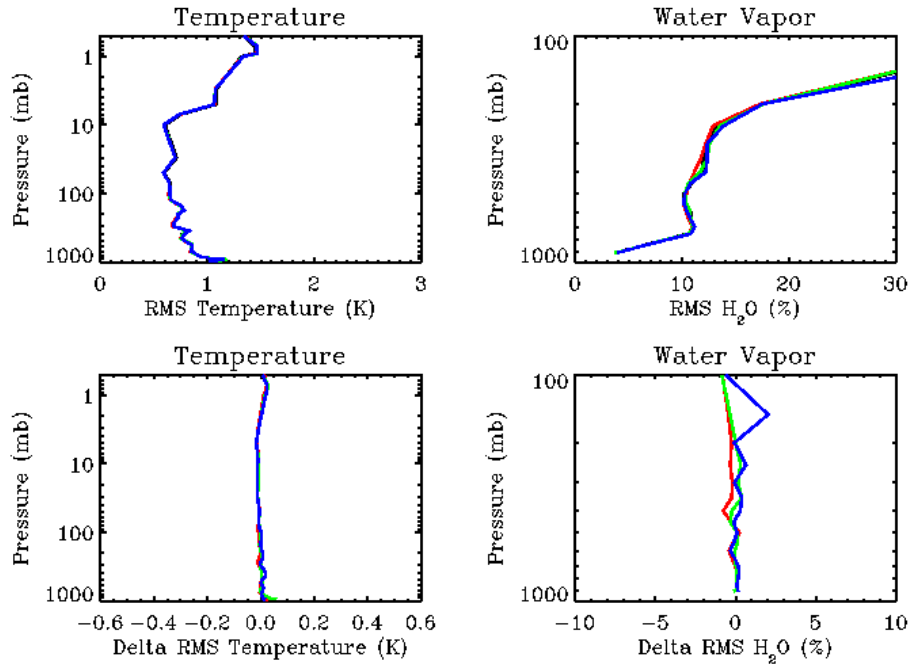


Figure 176: Performance degradation owing to Band 1 detector failure for FOV 1, 5, and 8 with iClsMode = 3. Results are based on the scheme to eliminate FOVs impacted by detector failure.

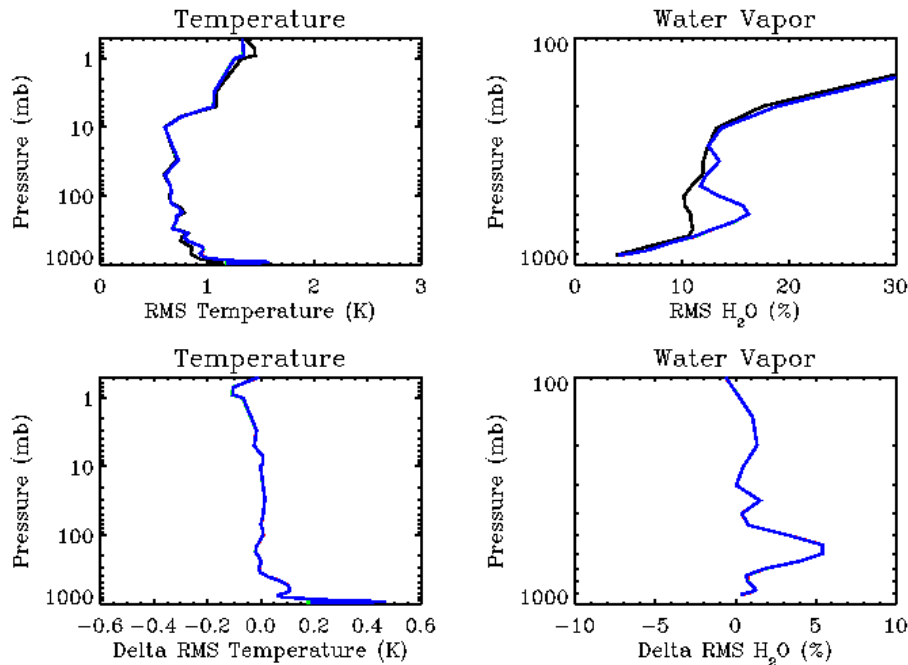


Figure 177: Performance degradation owing to Band 3 detector failure for FOV1, 5, and 8 with $iClssMode = 3$. Results are based on the option to eliminate band 3 and perform retrievals using bands 1 and 2 only (Option B).

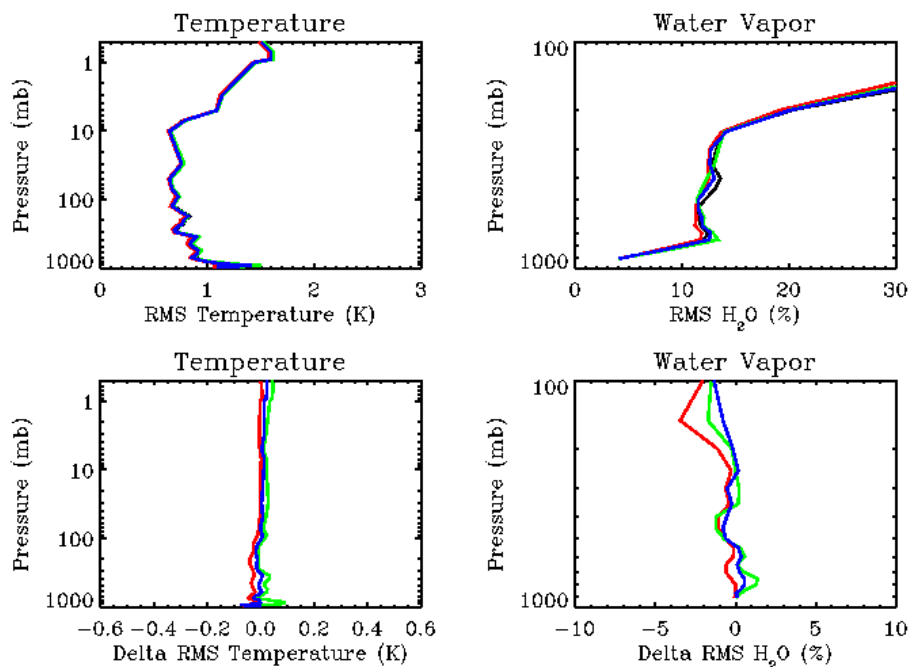


Figure 178: Performance degradation owing to Band 1 detector failure for FOV 1, 5, and 8 with $iClssMode = 1$. Differences in performance relative to the baseline are largely due to differences in scene classification (i.e. FOV clustering).

G.3: Modifications to Local Angle Adjustment

Local Angle Adjustment (LAA) corrects SDRs for the 9 FOVs for the path difference relative to the center FOV. The coefficients used by the correction are determined via a regression based on an EOF-decomposition of the observed SDRs (see Section 5.2.2.1). Previously, this regression combined information from all three bands from the CrIS instrument. In order to make the algorithm compatible with detector failure strategies, the LAA correction algorithm was retrained using data available from individual bands.

REFERENCES

- Amato, U., D. De Canditiis, and C. Serio, 1998: Effect of apodization on the retrieval of geophysical parameters from Fourier-transform spectrometers. *Appl. Optics.*, **37**, 6537-6543.
- Anderson, G.P., S.A. Clough, F.X. Kneizys, J.H. Chetwynd, and E.P. Shettle, AFGL atmospheric constituent profiles (0-120 km), *Tech. Rep. AFGL-TR-86-0110, Phillips Lab., Hanscom Air Force Base, Massachusetts*, 1986.
- Barnes, S.L., 1964: A technique for maximizing details in numerical weather map analysis. *J. Appl. Meteor.*, **3**, 396-409.
- Barnet, C.D., J.M. Blaisdell, and J. Susskind, 2000: Practical methods for rapid and accurate computation of interferometric spectra for remote sensing applications. *IEEE Trans. Geosci. Remote Sensing*, **38**, 169-182.
- Black, T.L., 1994: The new NMC mesoscale Eta Model: Description and forecast examples. *Wea. Forecasting*, **9**, 265-278.
- Brasseur, G.P., D.A. Hauglustaine, S. Walters, P.J. Rasch, J.-F. Muller, C. Granier, and X.X. Tie, 1998: MOZART: A global chemical transport model for ozone and related chemical tracers. 1. Model description. *J. Geophys. Res.*, **103**, 28,265-28,289.
- Burns, B. and K. Anderson, ATMS SDR Algorithm Description, NG Technical Memo, TM-01-380C, March, 2003.
- Chahine, M.T., Remote sounding cloudy atmospheres. I. The Single Cloud Layer, *J. Atmos. Sci.*, **31**, 233-243, 1974.
- Chahine, M.T., Remote sounding cloudy atmospheres. II. Multiple Cloud Formations, *J. Atmos. Sci.*, **34**, 744-757, 1977.
- Chahine, M.T. and J. Susskind, Fundamentals of the GLA physical retrieval method, *Report on the Joint ECMWF/EUMETSAT Workshop on the Use of Satellite Data in Operational Weather Prediction: 1989-1993*, Vol. 1, 271-300, T. Hollingsworth Editor, 1989.
- Chedin, A., N.A. Scott, C. Wahiche and P. Moulinier, The Improved Initialisation Inversion (3I) method: A high resolution physical method for temperature retrievals from the TIROS-N series, *J. Clim. Appl. Meteor.*, **24**, 128-143, 1985.
- Clough, S.A., F.X. Kneizys, and R.W. Davies, Line shape and the water vapor continuum, *Atmos. Res.*, **23**, 229-241, 1989.
- Clough, S.A., M.J. Iacono, and J.-L. Moncet, Line-by-line calculation of atmospheric fluxes and cooling rates: Application to water vapor, *J. Geophys. Res.*, **97**, 15761-15785, 1992.

Clough, S.A., C.P. Rinsland, and P.D. Brown, Retrieval of tropospheric ozone from simulations of nadir spectral radiances as observed from space. *J. Geophys. Res.*, **100**, 16579-16593, 1995.

Cuomo, V., R. Rizzi, and C. Serio, An objective and optimal estimation approach to cloud-clearing for infrared sounder measurements, *Int. J. of Rem. Sensing*, **14**, 729-743, 1993.

Daley, R., 1991: Atmospheric Data Analysis. Cambridge University Press.

Devenyi, D. and T.W. Schlatter, Statistical properties of three-hour prediction errors derived from the Mesoscale Analysis and Prediction System, *Mon. Wea. Rev.*, **122**, 1263-1280, 1994.

Eyre, J.R., Inversion of cloudy satellite sounding radiances by nonlinear optimal estimation: Theory and simulations for TOVS and application to TOVS data, *Quart. J. Roy. Meteor. Soc.*, **115**, 1001-1037, 1989a.

Eyre, J.R., Inversion of cloudy satellite sounding radiances by nonlinear optimal estimation. II: Application to TOVS data, *Q. J. R. Meteorol. Soc.*, **115**, 1027-1037, 1989b.

Eyre, J.R., The information content of data from satellite sounding systems: A simulation study, *Q. J. R. Meteorol. Soc.*, **116**, 401-434, 1990.

Goerss, J.S. and P.A. Phoebus, The multivariate optimum interpolation analysis at the Fleet Numerical Oceanography Center. *FR 7531-92-9413*, Navy Research Laboratory, Monterey, CA, 1993.

Grody, N.C., Surface identification using satellite microwave radiometers, *IEEE Trans. Geosci. and Remote Sensing*, **26**, 850-859, 1988.

Halem, M., M. Ghil, R. Atlas, J. Susskind, and W. Quirk, The GISS sounding temperature impact test, *NASA Tech. Memo. 78063*: 2.9-2.82, 1978.

Hamilton, K., R.J. Wilson, J.D. Mahlman, and L.J. Umscheid, 1995: Climatology of the SKYHI troposphere-stratosphere-mesosphere general circulation model. *J. Atmos. Sci.*, **52**, 5-43.

Harris, F., On the use of windows for harmonic analysis with the Discrete Fourier Transform, *Proc. IEEE*, **66**, 51-83, 1978.

Hayden, C.M. and R.J. Purser, 1988: Three-dimensional recursive filter objective analysis of meteorological fields.

Hayden, C.M. and R.J. Purser, 1995: Recursive filter objective analysis of meteorological fields: Applications to NESDIS operational processing, *J. Appl. Meteor.*, **34**, 3-15.

Ingleby, N.B., The statistical structure of forecast errors and its representation in The Met. Office Global 3-D Variational Data Assimilation Scheme, *Quart. J. Roy. Meteor. Soc.*, **127**, 209–231, 2001.

Kurucz, R.L., 1992: Synthetic infrared spectra. In *Infrared Solar Physics*, edited by D.M. Rabin and J.T. Jefferies, Kluwer Acad., Norwell, Mass.

Lachance, R., *et al.*, Algorithm Theoretical Basis Document (ATBD) for the Cross-Track Infrared Sounder (CrIS), Volume I, Sensor Data Records (SDR), BOMEM / ITT Document, 1999.

Levenberg, K., A method for the solution of certain problems in least squares, *Q. Appl. Math.*, **2**, 164-168, 1944.

Liebe, H.J., G.A. Hufford, and T. Manabe, A model for the complex permittivity of water at frequencies below 1 THz, *Intern. J. Infrared Millimeter Waves*, **12**, 659–675, 1991.

Lorenc, A., 1992: Iterative analysis using covariance functions and filters, *Quart. J. Roy. Meteor. Soc.*, **118**, 569-591.

McMillin, L.M. and C.A. Dean, Evaluation of a new operational technique for producing clear radiances, *J. Appl. Meteor.*, **21**, 1005-1014, 1982.

McMillin, L.M., M.D. Goldberg, H. Ding, J. Susskind, and C.D. Barnet, 1997: A forward calculation for interferometers: method and validation, *Appl. Opt.*, **37**, 3059-3068.

Marquardt, D., An algorithm for least squares estimation of nonlinear parameters, *SIAM J. Appl. Math.*, **11**, 431-441, 1963.

Mesinger, F., Z.I. Janjic, S. Nickovic, D. Gavrillov, and D.G. Deaven, 1988: The step-mountain coordinate: Model description and performance for cases of alpine lee cyclogenesis and for a case of an Appalachian redevelopment, *Mon. Wea. Rev.*, **116**, 1493-1518.

Miller, S.M., H.E. Snell, and J.-L. Moncet, Simultaneous retrievals of middle atmospheric temperature and trace gas species volume mixing ratios from Cryogenic Infrared Radiance Instrumentation for Shuttle (CIRRIS 1A), *J. Geophys. Res.*, **104**, 18697-18714, 1999.

National Aeronautics and Space Administration, *Joint Polar Satellite System Cross-track Infrared Sounder Sensor Data Records Algorithm Theoretical Basis Document*, 474-00032, Released 21 October 2011.

Press, W.H., S.A. Teukolsky, W.T. Vetterling, and B.P. Flannery, Numerical Recipes in C: The Art of Scientific Computing, *Cambridge University Press, Cambridge*, 681-689, 1992.

Prigent, C., Rossow, W.B., and Matthews, E., Microwave land emissivities estimated from SSM/I observations, *J. Geophys. Res.*, **102**, 21867-21890, 1997.

Reuter, D., Susskind J., and Pursch A., First guess dependence of a physically based set of temperature-humidity retrievals from HIRS2/MSU data, *J. Atmos. Ocean. Tech.*, **5**, 70-83, 1988.

Rizzi, R., C. Serio, G. Kelly, V. Tramutoly, A. McNally, and V. Cuomo, Cloud-clearing of Infrared Sounder Radiances, *J. Appl. Meteor.*, **33**, 179-194, 1994.

Rodgers, C.D., Retrieval of atmospheric temperature and composition from remote measurements of thermal radiation, *Rev. Geophys.*, **14**, 609–624, 1976.

Rodgers, C.D., Information Content and Optimization of High-Spectral-Resolution Measurements, *Proc. SPIE*, **2830**, 136-147, 1996.

Rosenkranz, P.W., A Rapid Atmospheric Transmittance Algorithm for Microwave Sounding Channels, *IEEE Trans. on Geo. and Remote Sensing*, **33(5)**, 1135-1140, 1995.

Smith, W.L., An improved method for calculating tropospheric temperature and moisture from satellite radiometer measurements, *Mon. Wea. Rev.*, **96**, 387-396, 1968.

Smith, W.L., H.L. Huang, and J.A. Jenney, An advanced sounder cloud contamination study, *J. Appl. Met.*, **35**, 1249-1255, 1996.

Snell, H.E. *et al.*, OMPS ATBD, 1999.

Snell, H.E., G.P. Anderson, J. Wang, J.-L. Moncet, J.H. Chetwynd, and S.J. English, Validation of FASE (FASCODE for the Environment) and MODTRAN3: Updates and Comparisons with Clear-Sky Measurements, in *Passive Infrared Remote Sensing of Clouds and the Atmosphere III*, *Proc. SPIE 2578*, pp 194-204, David K. Lynch and Eric P. Shettle, Editors, 1995.

Snyder, W.C., Z. Wan, Y. Zhang, and Y.-Z. Feng, Classification-based emissivity for land surface temperature measurement from space, *Int. J. Remote Sensing*, **19**, 2753-2774, 1998.

Susskind, J., Water vapor and temperature. *Atlas of Satellite Observations Related to Global Change*. Edited by R. J. Gurney, J. L. Foster, and C. L. Parkinson. Cambridge University Press, Cambridge, England, 89-128, 1993.

Susskind, J. and D. Reuter, Retrieval of sea-surface temperatures from HIRS2/MSU, *J. Geophys. Res.*, **90C**, 11602-11608, 1985.

Susskind, J., J. Rosenfield, D. Reuter, and M.T. Chahine, Remote sensing of weather and climate parameters from HIRS2/MSU on TIROS-N, *J. Geophys. Res.*, **89**, 4677-4697, 1984.

Susskind, J., C. Barnet, and M. Goldberg, Final Report to the Integrated Program Office on the Interferometer Thermal Sounder Study: Part II Comparative Performance of Interferometers/AIRS, 1998.

Tan, C. A. Gambacorta, M. G. Divakarla, S. Kizer, E. Maddy, G. Guo, M. Wilson, X. Xiong, X. Liu, and C. D. Barnett, On Empirical Bias Corrections of NPP CrIMSS OSS Forward Model. 93rd AMS Annual Meeting, Jan. 6-10, Austin Texas, Poster #438

Thiebaux, H.J. and M.A. Pedder, 1987: Spatial Objective Analysis with Applications in Atmospheric Science. Academic Press, London.

Wilheit, T.T., The effect of winds on the microwave emission from the ocean's surface at 37 GHz, *J. Geophys. Res.*, **84**, 4921-4926, 1979.

Wiscombe, J.W. and J.W. Evans, Exponential Sum Fitting of Radiative Transmission Functions, *Journal of Computational Physics*, **24**, 416-444, 1977.

Wu, X. and W.L. Smith, Emissivity of rough sea surface for 8-13 μm : modeling and verification, *Appl. Opt.*, **36**, 2609-2619, 1997.

LIST OF ACRONYMS

AER	Atmospheric and Environment Research, Inc.
AERI	Atmospheric Emitted Radiance Interferometer
AIRS	Advanced Infrared Sounder
AMSU	Advanced Microwave Sounding Unit
ASTER	Advanced Spaceborne Thermal Emission and Reflection Radiometer
ATBD	Algorithm Theoretical Basis Document
ATMS	Advanced Technology Microwave Sounder
BRDF	Bi-directional Reflectance Distribution Function
CC	Cloud-clearing
CMIS	Conical Microwave Imaging Sounder
CrIMSS	Cross Track Infrared and Microwave Sounder Suite
CrIS	Cross Track Infrared Sounder
DEM	Digital Elevation Map
EDR	Environmental Data Record
EOF	Empirical Orthogonal Function
ESFT	Exponential Sum Fitting Technique
FOR	Field Of Regard
FOV	Field Of View
FWHM	Full Width at Half Maximum
HH	Hole Hunting
HIRS	High-Resolution Infrared Sounder
HIS	High-Resolution Interferometric Spectrometer
HSB	Humidity Sounder Brazil
ILS	Instrument Line Shape
IPO	Integrated Program Office
IR	Infrared
LA	Lower Atmosphere
LAA	Local Angle Adjustment
LBL	Line By Line
LBLRTM	Line By Line Radiative Transfer Model
LOS	Line Of Sight
L-M	Levenberg-Marquardt
LWIR	Longwave IR band
MC	Monte-Carlo
MHS	Microwave Humidity Sounder
ML	Maximum Likelihood
MPD	Optical Path Difference
MSU	Microwave Sounding Unit
MW	Microwave
MWIR	Midwave IR band
NASA	National Aeronautics and Space Administration
NAST	NPOESS Atmospheric Sounder Testbed

NDVI	Normalized Difference Vegetation Index
NEDN	Noise Equivalent Difference
NESDIS	National Environmental Satellite, Data, and Information Service
NGES	Northrop Grumman Electronic Systems
NGST	Northrop Grumman Space Technologies
NOAA	National Oceanic and Atmospheric Administration
NPOESS	National Polar-orbiting Operational Environmental satellite System
NRF	Noise Reduction Factor
NWP	Numerical Weather Prediction
OSS	Optimal Spectral Sampling
PCA	Principal Component Analysis
PDR	Preliminary Design Review
QC	Quality Control
RDR	Raw Data Record
RMS	Root Mean Square
RT	Radiative Transfer
RTE	Radiative Transfer Equation
SCPR	Simultaneous Cloud Parameter Retrieval
SDR	Sensor Data Record
SGI	Silicon Graphics, Inc.
SRD	Sensor Requirement Document
SRF	Sensor Response Function
SSM/I	Special Sensor Microwave/Imager
SSSR	System Sub-System Review
SST	Sea Surface Temperature
SWIR	Shortwave IR band
TIGR	TOVS Initial Guess Retrieval
TOA	Top Of Atmosphere
TOVS	TIROS-N Operational Vertical Sounder
UA	Upper Atmosphere
USGS	United States Geological Survey
VIIRS	Visible/Infrared Imager/Radiometer Suite